REPORT DOCUMENTATION PAGE

Form Approved
OMB No. 0704-0188

Public reporting burden for this collection of information is estimated to average 1 hour per response, including the time for reviewing instructions, searching existing data sources, gathering and maintaining the data needed, and completing and reviewing this collection of information. Send comments regarding this burden estimate or any other aspect of this collection of information, including suggestions for reducing this burden to Department of Defense, Washington Headquarters Services, Directorate for Information Operations and Reports (0704-0188), 1215 Jefferson Davis Highway, Suite 1204, Arlington, VA 22202-4302. Respondents should be aware that notwithstanding any other provision of law, no person shall be subject to any penalty for failing to comply with a collection of information if it does not display a currently valid OMB control number. PLEASE DO NOT RETURN YOUR FORM TO THE ABOVE ADDRESS.

1. REPORT DATE (DD-MM-YYYY)	2. REPORT TYPE	3. DATES COVERED (From - To)
08/22/00	FINAL TECHNICAL REPORT	7/15/94 - 7/14/98

4. TITLE AND SUBTITLE
AASERT: "Development of Pulse-Burst Laser Source and Digital Image Processing for Measurements of High-Speed, Time-Evolving Flow"

5a. CONTRACT NUMBER

5b. GRANT NUMBER
F49620-94-1-0372
P00002

5c. PROGRAM ELEMENT NUMBER

5d. PROJECT NUMBER

5e. TASK NUMBER

5f. WORK UNIT NUMBER

6. AUTHOR(S)
Miles, Richard B.

Department of Mechanical & Aerospace Engineering
Princeton University

7. PERFORMING ORGANIZATION NAME(S) AND ADDRESS(ES)

Princeton University
Department of Mechanical &
Aerospace Engineering
Princeton, NJ 08544

8. PERFORMING ORGANIZATION REPORT NUMBER

9. SPONSORING / MONITORING AGENCY NAME(S) AND ADDRESS(ES)

Air Force Office of
Scientific Research (AASERT)

10. SPONSOR/MONITOR'S ACRONYM(S)

11. SPONSOR/MONITOR'S REPORT NUMBER(S)

12. DISTRIBUTION / AVAILABILITY STATEMENT
Unlimited

13. SUPPLEMENTARY NOTES

14. ABSTRACT

This AASERT Grant on the development of a "Pulse-Burst Laser Source and Digital Image Processing for Measurements of High-Speed, Time evolving Flow" was originally paired with Grant #F49620-92-J-0217 entitled, "Quantitative Imaging of Time-Evolving Structure in Supersonic and Hypersonic Flows." That grant ended in December 1994. The students have more recently been working in conjunction on the development of diagnostics in association with "Shock Propagation and Supersonic Drag in Low Temperature Plasmas (#F49620-97-1-0497) which began June 1, 1997. Major accomplishments achieved under this AASERT Grant were the fabrication of a cavity-locked, injection-seeded Ti:Sapphire Laser and the demonstration of UV filtered Rayleigh scattering imaging in a supersonic jet, the fabrication/ characterization of a narrow passband transmission filter, and the development of a new concept for a line imaging Raman spectrometer for flow field, combustion, and plasma diagnostics.

15. SUBJECT TERMS
Pulse burst lasers, passband transmission filters, Rayleigh scattering imaging

16. SECURITY CLASSIFICATION OF: Unclassified			17. LIMITATION OF ABSTRACT	18. NUMBER OF PAGES	19a. NAME OF RESPONSIBLE PERSON
					Richard B. Miles
a. REPORT	b. ABSTRACT	c. THIS PAGE			19b. TELEPHONE NUMBER (include area code)
UU	UU	UU	UU	1485	609-258-5131

Standard Form 298 (Rev. 8-98)
Prescribed by ANSI

20000829 163

"DEVELOPMENT OF PULSE-BURST LASER SOURCE AND DIGITAL IMAGE PROCESSING FOR MEASUREMENTS OF HIGH-SPEED, TIME-EVOLVING FLOW"

FINAL TECHNICAL REPORT
For the Period 7/15/94 - 7/14/98

AFOSR Grant #F49620-94-1-0372 P00002
(Report dated 8/22/00)

AASERT STUDENTS:
Noah Finkelstein, Vincent Chiravalle, and Alan Morgan

INTRODUCTION:

This AASERT grant on the development of a "Pulse-Burst Laser Source and Digital Image Processing for Measurements of High-Speed, Time-Evolving Flow," was originally paired with Grant #F49620-92-J-0217, entitled, "Quantitative Imaging of Time-Evolving Structure in Supersonic and Hypersonic Flows." This grant ended in December 1994, and the students then began working in conjunction with the AFOSR University Research Initiative (URI) in Aerothermochemistry, entitled, "Turbulent Reacting Flows at High Speed" (Grant #F49620-93-1-0427). Since the URI program encompassed the development of advanced diagnostics and the application of the pulse-burst laser, this pairing was appropriate. That grant officially ended June 30, 1997. Students associated with the AASERT continued to work on the development of diagnostics and related matters in association with "Shock Propagation and Supersonic Drag in Low Temperature Plasmas" (Grant #F49620-97-1-0497), which began June 1, 1997. The AASERT grant supported Noah Finkelstein, Alan Morgan, and Vincent Chiravalle. Noah Finkelstein successfully completed his Ph.D. in December 1997 under this support and a copy of his Thesis is appended. Alan Morgan left the University, and Vincent Chiravalle is continuing his Ph.D. program with support form other sources.

Major accomplishments include the development of a new concept for a line imaging Raman spectrometer for flow field, combustion, and plasma diagnostics, and the exploration of a new thruster concept based on laser energy addition downstream of the nozzle throat.

The work has been reported in the following papers (please note that papers noted with a "*" were attached to previous progress reports, while papers noted with a "#" are attached to this final report:

*N.D. Finkelstein, W.R. Lempert, R.B. Miles, A. Finch, G.A. Rines, "Cavity-Locked, Injection-Seeded, Titanium:Sapphire Laser and Application to Ultraviolet Flow Diagnostics," AIAA-96-0177, 34th Aerospace Sciences Meeting & Exhibit, Jan. 15-18, 1996, Reno, NV.

DTIC QUALITY INSPECTED 4

*N.D. Finkelstein, W.R. Lempert, and R.B. Miles, "A Narrow Passband, Imaging, Refluorescence Filter for Nonintrusive Flow Diagnostics," AIAA-96-2269, 19th AIAA Advanced Measurement and Ground Testing Technology Conference, June 17-20, 1996, New Orleans, LA.

#R.B. Miles, W.R. Lempert, J. Forkey, N.D. Finkelstein, and S.R. Harris, "Optical Diagnostics for Flows with Density Variations," IUTAM Symposium on Variable Density, Low Speed, Turbulent Flows, Institut de Recherche sur les Phenomenes Hors Equilibre, Marseille, France, July 8-10, 1996.

#N.D. Finkelstein, W.R. Lempert, and R.B. Miles, "Mercury Vapor Filter Technology and Ultraviolet Laser Source for Flow Field Imaging," AIA-97-0157, 35th Aerospace Sciences Meeting & Exhibit, Jan. 6-10, 1997, Reno, NV.

#W.R. Lempert, P.F. Wu, and R.B. Miles, "Filtered Rayleigh Scattering Measurements Using a MHz Rate Pulse-Burst Laser System," AIAA-97-0500, 35th Aerospace Sciences Meeting & Exhibit, Jan. 6-10, 1997, Reno, NV.

#N.D. Finkelstein, W.R. Lempert, and R.B. Miles, "Narrow Linewidth Passband Filter for Ultravioelt Rotational Raman Imaging," Optics Letters, Vol. 22, No. 8, April 15, 1997, pp. 537-539.

#W.R. Lempert, P. Wu, N. Finkelstein, P. Erbland, and R.B. Miles, "Imaging Fluid Phenomena with Atomic and Molecular Filters," AIAA-97-2520, 32nd Thermophysics Conference, June 23-25, 1997, Atlanta, GA.

#A.P. Yalin, N.D. Finkelstein, W.R. Lempert, R.B. Miles, "Ultraviolet Rotational Raman Spectroscopy with an Atomic Resonance Filter," AIAA-98-0311, 36th Aerospace Sciences Meeting and Exhibit, Jan. 12-15, 1998, Reno, NV.

#V.P. Chiravalle, R.B. Miles, and E.Y. Choueiri, "Laser Propulsion Using a Molecular Absorber," AIAA-98-3932, 34th AIAA/ASME/SAE/ASEE Joint Propulsion Conference & Exhibit, July 13-15, 1998, Cleveland, OH.

#N.D. Finkelstein, A.P. Yalin, W.R. Lempert, and R.B. Miles, "Dispersion Filter for Spectral and Spatial Resolution of Pure Rotational Raman Scattering," Optics Letters, Vol. 23, No. 20, October 15, 1998, pp. 1615-1617.

Filtered scattering refers to a class of nonintrusive optical techniques in which atomic and molecular vapor filters are used as spectral discriminators in order to extract global velocity and/or temperature and density data form laser sheet scattering images. Prior to Mr. Finkelstein's thesis research, all known filtered scattering has been performed using visible laser sources, principally, second harmonic of Nd:YAG at 0.532 microns, or argon-ion at 0.514 microns (green), in combination with molecular iodine vapor cells. Mr. Finkelstein's thesis focused on the exploration of the properties of the exceedingly strong absorption/fluorescence resonance of atomic mercury vapor at 0.254 microns (ultraviolet). Associated with this research was the

development of a new, high power, precision-controlled, all solid-state laser system based on Ti:Sapphire. A block diagram of this system is shown in Fig. 1.

SIGNIFICANT ACHIEVEMENTS

i. Fabrication of a Cavity-Locked, Injection-Seeded Ti:Sapphire Laser

A program of laser development was initiated in collaboration with Schwartz Electro-Optics (SEO), Inc., Research Division Concord, Massachusetts. The major component of this work was the development of a new optical scheme for what is termed "injection seeding." Injection seeding refers to an approach in which a small quantity (order mW) of cw light is injected into a pulsed laser cavity. Due to a preferential nonlinear amplification, the resulting pulsed output is spectrally narrowed, compared to the output in the absence of the seed. In order to obtain precise frequency control, however, the length of the pulsed laser cavity must be controlled to with $\lambda/2$ where λ is the wavelength of the laser output (in this case, on the order of 0.7microns). This precise control was accomplished using a new "ramp and lock" feedback system, the details of which are described in detail in Paper AIAA-96-0177, which was presented by Dr. Finkelstein at the 34th Aerospace Sciences Meeting in Reno, NV, January 1996 (a copy of this paper was included with Technical Progress Report I).

ii. Demonstration of UV Filtered Rayleigh Scattering Imaging in a Supersonic Jet

In order to verify the performance of the new cavity locking scheme, mercury vapor FRS imaging experiments were undertaken in a Mach 2 free jet, existing directly into the laboratory. . The acoustic noise level was estimated to be in excess of 100 dB, therefore providing an excellent test of system robustness. Figure 2 shows a collage of three single shot images of the Mach 2 jet illuminated at three different laser frequencies. The field-of-view in all three images includes the exit of the nozzle as well as a portion of the jet. The laser sheet was aligned to illuminate both the flow and the nozzle. Illustrations below the images give the relative position of the laser frequency (marked *l*), and the Doppler-shifted flow scattering frequency (marked *f*), with respect to the absorption resonance of the atomic mercury vapor filter. In Fig. 2a, both the laser and flow scattering occur outside the absorption band of the filter. As a result, both the Doppler-shifted flow scattering and the unshifted scattering from the nozzle surface reach the imaging camera. In Fig. 2b, the laser has been tuned such that the nozzle scattering falls within the filter absorption band, but the Doppler-shifted flow scattering is still outside the band. Finally, in Fig. 2c, the laser has been tuned such that the flow is absorbed by the filter, while the nozzle scattering is not.

iii. Fabrication/Characterization of Narrow Passband Transmission Filter

A vapor transmission filter is one which transmits in a narrow wavelength band and absorbs at all other wavelengths. It is essentially the inverse of the more common absorption filter. The new filter is based on the absorption and subsequent refluorescence of light by atomic mercury vapor. This concept is illustrated in Fig. 3, which is taken from paper AIAA-96-2269 which was presented by Dr. Finkelstein at the 19th Advanced Measurement and Ground Testing Technology Conference, June 1996, in New Orleans, LA (a copy of that paper was attached to Progress

Report II). A laser or light source is used to illuminate a target volume. Scattering from the volume is imaged onto the front surface of a cell containing mercury vapor. If the incident light on the cell surface is spectrally outside the absorption band, it passes through the cell and is rejected. If the light scattering frequency is coincident with the mercury absorption band, the scattering is absorbed in a very thin region (order 25 microns) near the cell front surface. Virtually all of the absorbed light then re-radiates out the front surface of the cell. This re-radiation is then imaged onto a camera. The net effect is that only the light within the mercury absorption band reaches the detector and is imaged. Figure 4 (also taken from the paper cited above) shows both a transmission spectrum (upper trace) and absorption spectrum (lower trace) from an atomic mercury vapor cell. To first order, they are the inverse of one another, although they are not identically so.

iv. Image Preservation

Since the mercury vapor cell can be made with exceedingly high absorption, the subsequent refluorescence will originate from a well defined plane of minimal thickness (order 25 microns) very close to the cell entrance window. Therefore, the filter is image preserving as well as very narrow bandwidth. Figure 5 show an example of this imaging capability. The experimental arrangement is similar to that of Fig. 3, except that the scattering source is a business card. The illumination source is the third harmonic output of the cavity-locked, injection-seeded Ti:Sapphire laser. In Fig. 5a the illumination laser is tuned to spectrally coincide near the center of the filter passband. In Fig. 5b the laser is tuned to reside on the edge of the filter passband, resulting in decreased image brightness and resolution. Finally, in Fig. 3c the laser is tuned out-of-band and no image appears.

v. Rotational Raman Spectrum

The spectral resolution of the filter is approximately 30 GHz, due chiefly to the presence of multiple isotopes with overlapping absorption wavelengths. Further refinements suggest that the filter linewidth can be reudced to on the order of 5 GHz or less using isotopically-enhanced mercury vapor. The 30 GHz resolution is high enough, none the less, to permit the separate detection of individual rotational-vibrational states of molecular species. For example, Fig. 6 is a preliminary spectrum showing the separate detection of nitrogen and oxygen rotational states observe din room air. This approach has the potential of instantaneously imaging selected species in complex environments such as in combusting media and reacting flows. Since Raman scattering is linear in laser energy and is not affect by quenching or saturation, higher signal levels can be obtained by higher energy lasers.

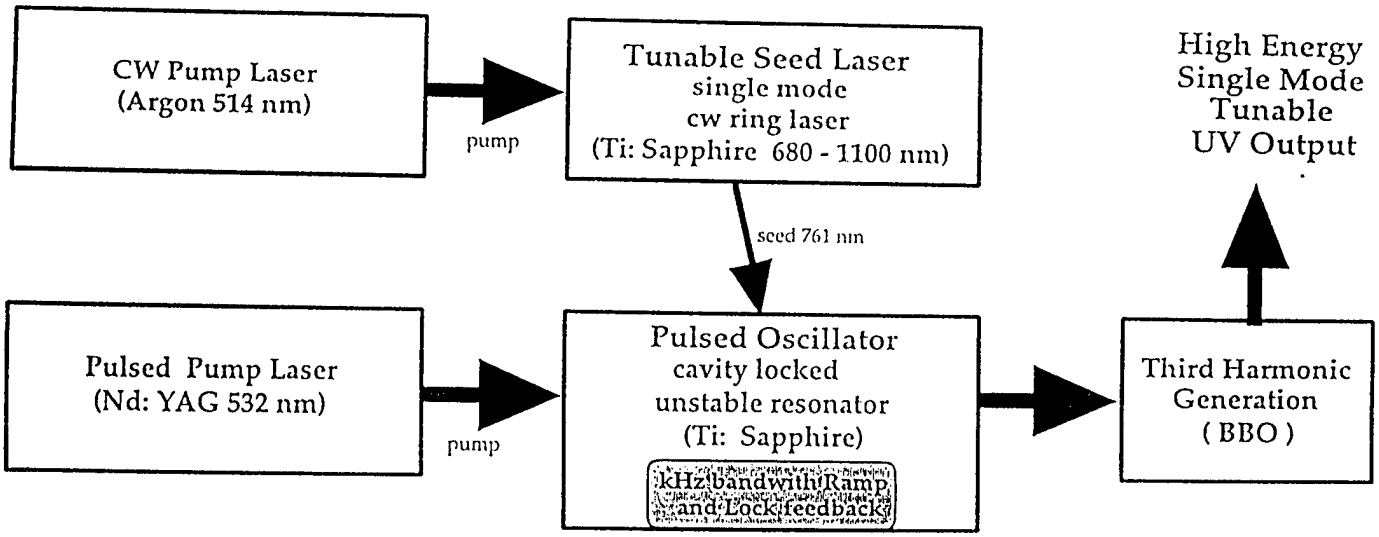

Figure 1. Block diagram of injection-seeded, cavity-locked, UV laser system.

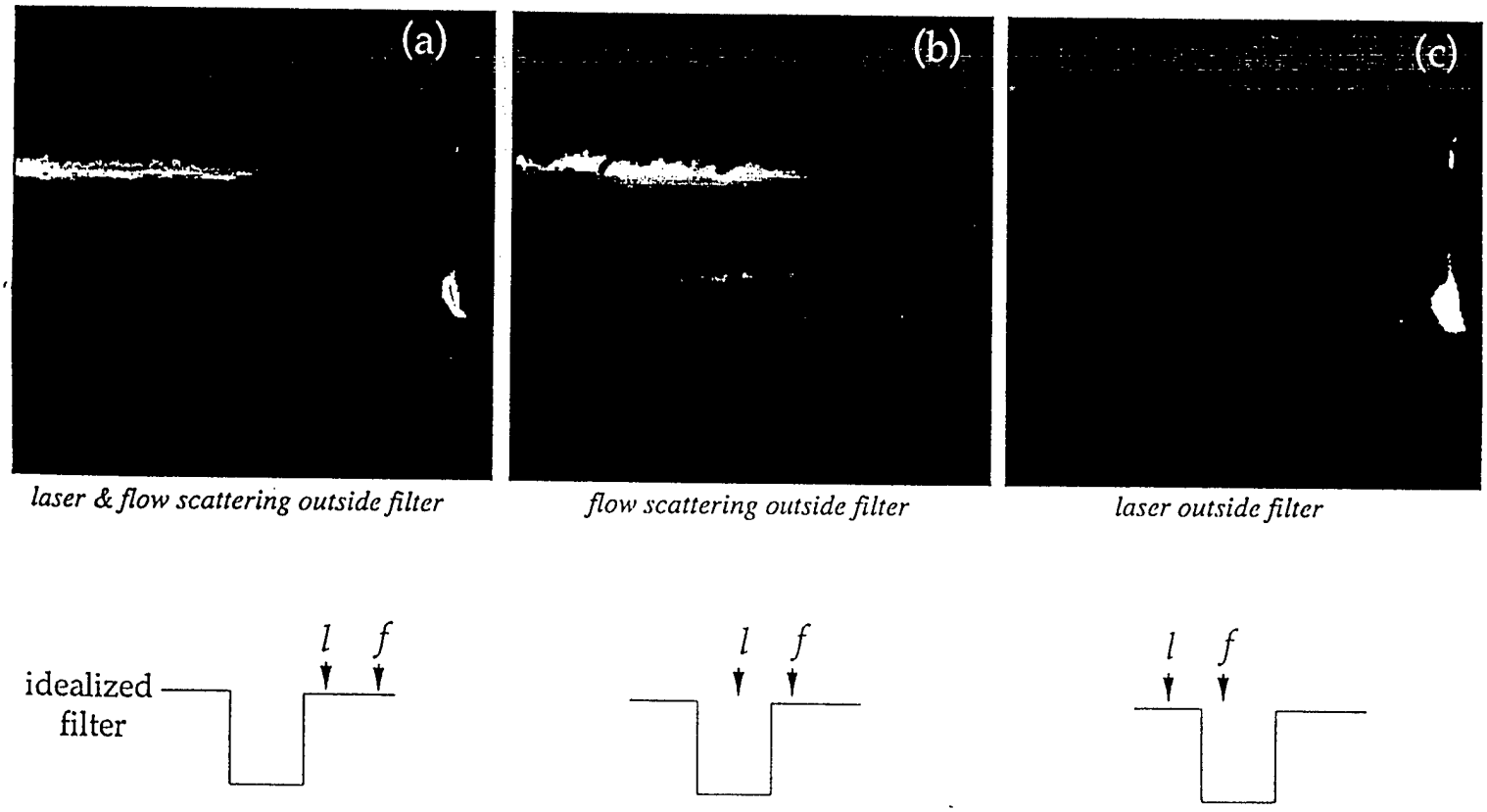

Figure 2. Instantaneous FRS images using mercury vapor cell.

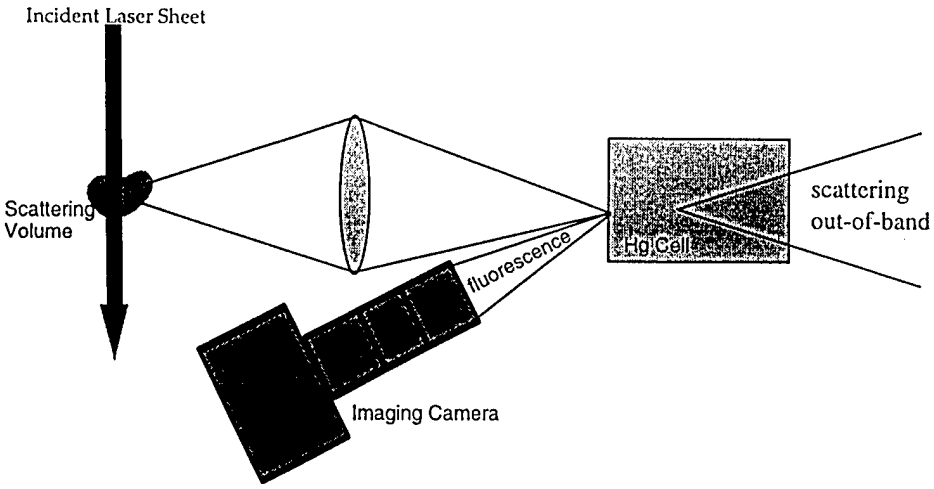

Figure 3

Schematic Diagram of Refluorescence Cell

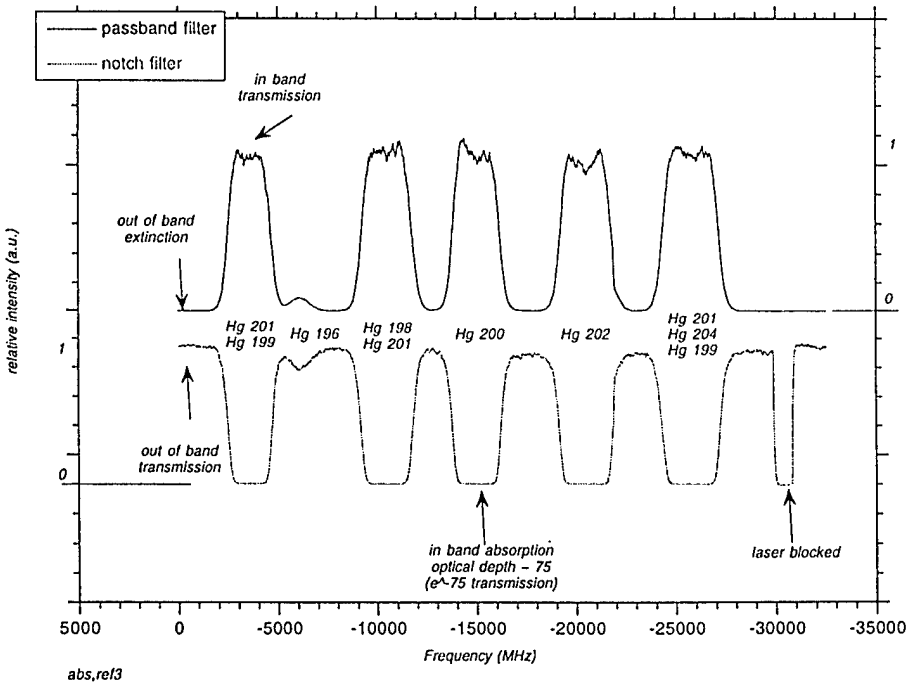

Figure 4

Simultaneous Spectral Scan of Mercury Vapor Filter Absorption (lower trace) and Transmission (upper trace).

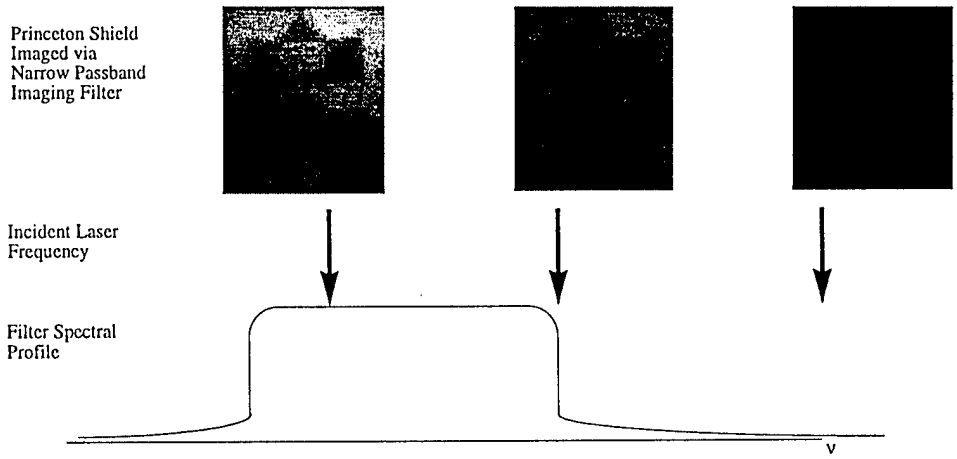

Figure 5

Demonstration of Refluorescence Cell Image Preservation

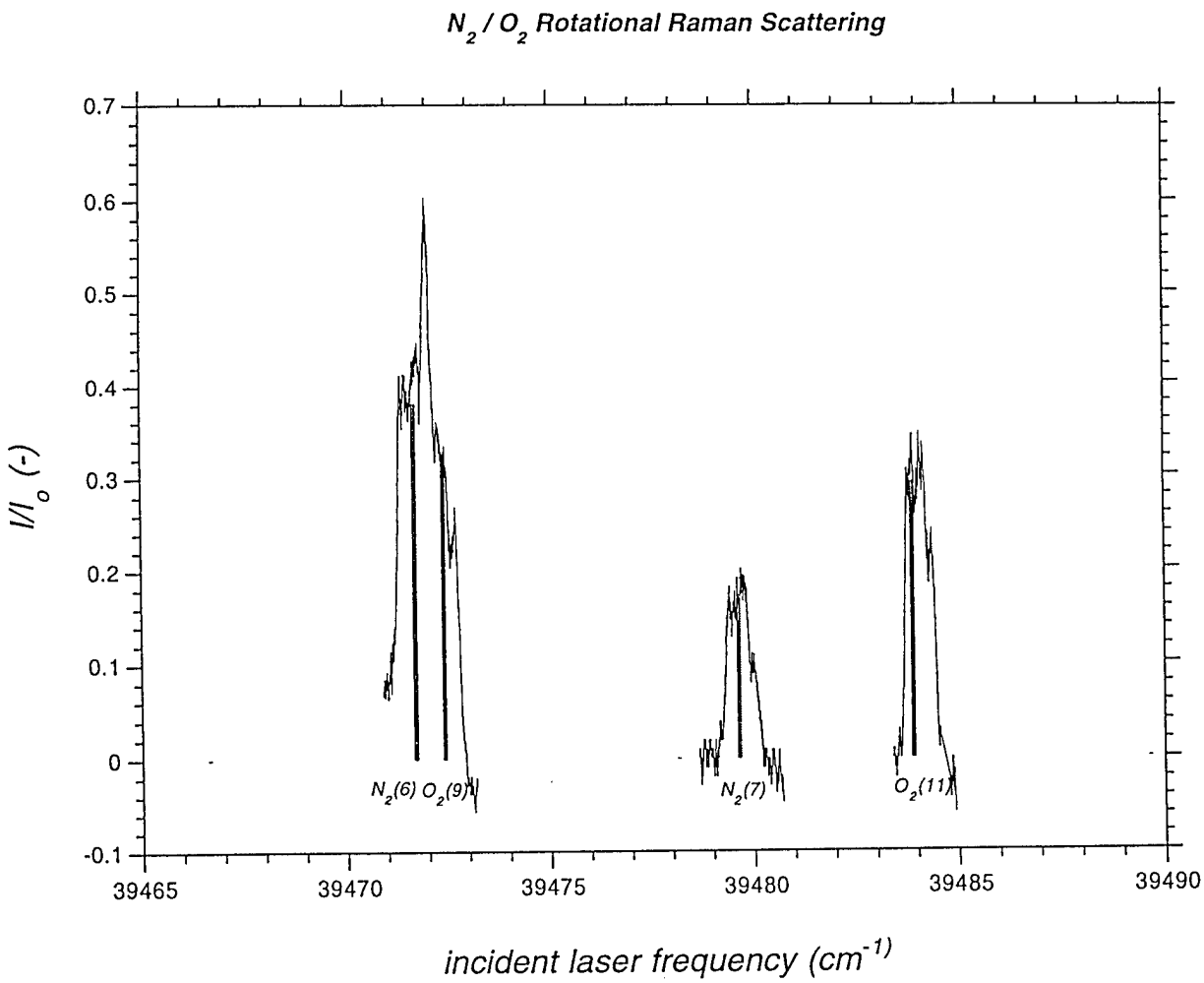

Figure 6

Rotational Raman Spectrum Obtained using Hg Vapor Refluorescence Cell

AN ULTRAVIOLET LASER SOURCE AND SPECTRAL IMAGING FILTERS FOR NON-INTRUSIVE LASER-BASED DIAGNOSTICS

Noah D.M. Finkelstein

A DISSERTATION
PRESENTED TO THE FACULTY
OF PRINCETON UNIVERSITY
IN CADIDACY FOR THE DEGREE
OF DOCTOR OF PHILOSOPHY

RECOMMENDED FOR ACCEPTANCE
BY THE DEPARTMNET OF
MECHANICAL AND AEROSPACE ENGINEERING

JANUARY, 1998

© Copyright by Noah D.M. Finkelstein, 1997. All rights reserved

Abstract

This dissertation details the development of new state-of-the-art tools which enable ultraviolet non-intrusive laser based diagnostics. A laser source and three new optical filters are developed, characterized, and demonstrated in application to flowfield diagnostics. The laser produces high power (50mJ/pulse), spectrally near transform limited, spatially near diffraction limited, tunable output in the vicinity of 250 nm. A notch absorption band and two narrow passband spectral filters feature exceptional spectral resolution, high throughput, and maintain imaging capabilities. Pairing the laser and filters makes possible unique spatially resolved flowfield measurements via ultraviolet Rayleigh and Raman scattering based techniques.

The laser source is an injection-seeded, frequency-tripled, cavity-locked, titanium: sapphire source. It features a new cavity locking scheme, which allows it to be tuned rapidly and discontinuously without losing its narrowband spectral profile.

The first spectral filter is a narrow band, notch absorption filter that is based upon a ground state absorption of mercury. The filter acts to strongly suppress a narrow spectral band (on a GHz scale), while efficiently passing light spectrally shifted by a GHz or less. The filter is characterized, modeled, and combined with the laser to demonstrate ultraviolet filtered Rayleigh scattering for flowfield visualization and velocity measurements of a Mach 2 free jet.

The second filter is a narrow passband imaging filter, designed for rotational Raman scattering based measurements. It features an ultranarrow passband (less than

$1cm^{-1}$) and has the ability to suppress strong background scattering (Rayleigh scattering and surface reflections) while maintaining 2-D imaging capabilities. This filter is characterized, modeled, and applied in measurements of individual pure rotational Raman lines of oxygen and nitrogen in room air.

The third filter, also for rotational Raman imaging, simultaneously discriminates multiple rotational Raman lines, while maintaining 1-D imaging and suppressing strong out-of-band scattering. The filter is a vapor prism based on the anomalous dispersion of mercury near resonance. The filter is characterized, modeled, and demonstrated capturing rotational Raman scattering signals from CO_2.

Acknowledgments

In my tenure as a student at Princeton, I have strived to engage in and to add to various communities. It is my belief in collaborative learning, and the purposefulness of communities that has led me to approach my graduate career at Princeton as I did. Owing to the nature of collaborative efforts, I am indebted to many people, who I hope believe as I do that the whole is greater than the individual efforts comprising it. I am still stunned that through the direction and guidance of my advisor, Richard B. Miles, I was propelled to the forefront of a rich and exciting discipline. Through his support and drive to research, publish and attend conferences, I have become fluent in this discipline.

Another mentor, Walter R. Lempert, was critical in my development as a scientist. Walter kindly, patiently, and expertly served to teach me the nitty-gritty of laser based research. A host of others served to teach and support me in my research. Joan Gambogi of physical chemistry, and Joseph Forkey in the applied physics group were my earliest graduate student collaborators, from whom I learned the practice. The rest of the applied physics group students including Barry Zhang, Joe Forkey, George Williams, Scott Harris, Peter Erbland, Pingfan Wu, Zhen Tang, and Azer Yalin have served as coaches, sounding boards, teachers, and comrades through my studies and research. Others in our research group, Peter Barker, Debbie Brown, and Phil Howard have added valuably in their vast support and ability. Over the last couple of years, my greatest research has been achieved with the collaboration our post-doctoral fellow, Jay Grinstead who is a model of what I aspire to become as scientific researcher.

I have had the pleasure of collaboration with many others throughout and outside the university. Each has added to my education and capability. My early laser work in the physical chemistry labs was graciously supported and tolerated by Giacinto Scoles and Kevin Lehmann. Also, in chemistry, the campus glassblower, Michael Souza has provided both amazing talent in producing the optical filters, and friendship. Similarly, my collaborators at Schwartz Electro Optics, Inc. Research Division, have taught me of lasers, research, and the industry. Andy Finch, Richard Schwarz, and especially Glenn Rines have been outstanding role models, as amazingly talented laser physicists, and friends.

I am proud that my education extended beyond the walls of the Engineering School. It is fitting that my first contact a Princeton be Etta Recke. She has served valuably to make the incompressible workings of the university manageable. One of my great joys at Princeton has been to participate in the development and implementation of the Summer Scholars Institute. The director of the program, Dean Hal McCulloch, is both inspiring, and remarkable. Other teaching responsibilities led me to associate with Dean Peter Bogucki - whom I pleased to know as boss and colleague. In other roles on campus, I was honored to work with colleagues at the Center for Jewish Life, which hosts a wonderful and welcoming community.

As to my friends, they are the ones who kept me here, and have made the daily routine pleasurable. The talented individuals whom I call friend mark my greatest achievement. To hold the company of individuals such as these throughout the world is humbling, and inspiring. Those individuals know who they are. They include, but by no means are limited to: Scott, Blake, Stacey, Chetan, Will, Lan, Peter, Cheryl, Shroder, Lump, Eric, Kara, Steve, Gary, Mel, Cindy, Bex, Bruce, Jeff, Joe, Goeff, the Scotts, Jill,

Rose, Shane, Jo, Chaim, Ethan, Greg, Steve, Erika, Art and Mark. A wise man once suggested that owing to his friends his thesis was half as long, and twice as fun. I am pleased to say that my thesis is twice as long, and well, fun - owing to my friends.

My family, I am honored to posses their love and friendship. Truly my greatest lifelong mentors have been my parents. To them, I am ever indebted for growing up as well as I have - for my courage, wisdom, and peace - To my brother, I am grateful for his support, wisdom, assistance, humor, and company. Being the youngest in the family, I suppose it is acceptable to be the last to become a doctor.

Many thanks to my thesis readers, official (Walt Lempert, Mike Littman, Richard Miles) and unofficial (you).

I wish to acknowledge the funding sources for my research and support: the Air Force Office of Scientific Research, NASA Ames, Schwartz Electro-Optics, Inc., and the International Society for Optical Engineering (SPIE).

This thesis carries the number 3015-T in the records of the Department of Mechanical and Aerospace Engineering at Princeton University.

Table of Contents

CHAPTER 1: INTRODUCTION **1**

CHAPTER 2: THE LIGHT SOURCE **9**

Approach of UV tunable system 10

Development of tunable cw source 10

Alternative approaches to cw Ti: sapphire locking 17

Injection seeding of pulsed resonators 17

The Ti: sapphire pulsed resonator 18

Cavity locking (Ramp and Lock) 22

Cavity locking alternatives 30

Experimental Characterization 31

UV generation (Third harmonic generation) 37

CHAPTER 3: MERCURY **45**

Introduction and spectroscopy 45

Model 50

Model predictions 51

Experiment and comparisons 54

Fitting data sets & parameter extraction 62

CHAPTER 4: A NOTCH ABSORPTION FILTER AND ULTRAVIOLET FILTERED RAYLEIGH SCATTERING **69**

Introduction 69

FRS concept 70

The laser 72

The filter 73

FRS theory 79

Experimental setup 81

Background suppression 83

Velocity measurements 85

Comparison of UV to visible FRS 90

CHAPTER 5: A WORD ABOUT RAMAN SCATTERING **95**

Introduction and background 95

Raman scattering (theory) 102

CHAPTER 6: A NARROW PASSBAND IMAGING FILTER APPLIED TO ROTATIONAL RAMAN SCATTERING **111**

Filter description and background 111

Filter characterization 116

spectral characteristics and rejection 116

model 118

temporal characteristics 123

spatial resolution 131

efficiency 141

Imaging constraints 144

Diagnostic applications 146

Rayleigh 146

Raman 148

CHAPTER 7: DISPERSION FILTER **155**

Introduction and concept 155

Background 157

Theory 159

Design 166

Experimental verification 168

Predictions 169

CO_2 rotational Raman scattering 171

Comparison of dispersive prism with diffraction spectrometer 173

Improvements 175

CHAPTER 8: CONCLUDING REMARKS **177**

APPENDICES:

A: Hg model absorption co-efficient and transmission vs. frequency

B: Hg fitting routine - Powell's method fitting of Hg spectra

C: Monte Carlo simulation of narrow passband fluorescence filter

List of Figures

CHAPTER 2

II.1	Lasing band of Ti: sapphire	9
II.2	Block laser diagram	10
II.3	CW system	11
II.4	Pulsed laser	20
II.5	NIST mount design of pzt	23
II.6	Ramp and lock signals	26
II.7	Ramp and lock: locking electronics	27
II.8	Timing diagram (ramp and lock)	28
II.9	Laser output: single dual mode output (temporal)	33
II.10a	Laser output: single mode etalon scan	34
II.10b	Laser output: dual mode etalon scan	34
II.11	Pulsed single mode output scans of Hg	35
II.12	Discontinuous spectral jumps of pulsed laser	36
II.13	Spectral location of discontinuous pulsed laser jumps	37
II.14	BBO tripling efficiencies	39

CHAPTER 3

III.1	Hg energy level diagram	46
III.2.a	Hg absorption co-efficient vs. frequency	52
III.2 b	Hg transmission vs. frequency	52
III.3	Hg cell construction	54
III.4	Experimental spectral scans setup	55
III.5	Experimental data 0.002 Torr	57
III.6	Experimental data 10^{-5} Torr	58
III.7	Experimental data 0.05 Torr	58
III.8	Experimental data and model	59
III.9	Isotopically enhanced Hg 202 experiment & model 0.002 Torr	61
III.10	Isotopically enhanced Hg 202 experiment & model 0.05 Torr	61
III.11	Pressure broadening co-efficient from naturally occurring Hg at 1.5 Torr	65

Table III.1 Hg parameters for naturally occurring isotopes 47

CHAPTER 4

IV.1 Filtered Rayleigh Scattering concept 71

IV.2 Ideal spectral filter 74

IV.3 Single Hg 202 line detail 77

IV.4 Doppler shift and FRS angles directions 80

IV.5 Experimental setup: geometry 82

IV.6 Experimental setup: field of view 83

IV.7 Background suppression 84
a. nozzle and flow
b. flow only
c. nozzle only

IV.8 Velocity measurements: nozzle scattering signal vs. video frame 86

IV.9 Velocity measurements: nozzle & flow scattering vs. frequency 88

CHAPTER 5

V.1 Raman scattering concept 96

V.2 Boltzmann plot of N_2 rotational levels at STP 104

V.3 O_2/N_2 rotational Raman scattering signal vs. Rayleigh signal (STP) 107

Table V.1 Raman scattering co-efficients/parameters 106

CHAPTER 6

VI.1 Narrow passband fluorescence filter concept 114

VI.2 Hg cell absorption and transmission: experimental scans 117

VI.3 Model: Monte Carlo flow chart 119

VI.4 Model and experiment of passband filter 122

VI.5 Model: multiple pressures 122

VI.6 Temporal response of filter: experimental data 125

VI.7 Temporal response of filter: various optical depths 127

VI.8 Temporal response of filter: various incident frequencies 127

VI.9 Temporal response of filter: exponential fits 128

VI.10 Temporal response of filter: Monte Carlo simulation and experiment 129

VI.11 Temporal response of filter: Monte Carlo simulation and experiments II 130

VI.12 Spatial response of filter: Princeton University shield, 3 spectral locations 131

VI.13 Filter penetration depth vs. cell vapor pressure 132

VI.14 Spatial resolution of filter: pin scattering 134

VI.15 Spatial resolution of filter: ruled grating vs. temporal gate 136
VI.16 Spatial resolution of filter: ruled grating vs. spectral location 137
VI.17 Modeled atomic transport: distance vs. cell temperature 139
VI.18 Modeled atomic diffusion: diffusion length vs. cell pressure 141
VI.19 Experimental setup Rayleigh/ Raman measurements 146
VI.20 Rayleigh data and model 147
VI.21 Raman data and model 149
VI.22 Raman data and model:
a. detail $N_2(6)/O_2(9)$ line 150
b. detail $N_2(7)$ line 151
c. detail $O_2(11)$ line 151

Table VI.1 Parameters for Raman measurements 149

CHAPTER 7

VII.1 Vapor prism filter concept: index of refraction / geometry 156
VII.2 Prism geometry 160
VII.3 Index of refraction for multiple isotopes 161
VII.4 Model: deviation angle vs. input angle and index of refraction 162
VII.5 Model: reflection co-efficient vs. input angle 163
VII.6 Model: deviation & absorption vs. frequency at two vapor pressures 164
VII.7 Prism construction/design 167
VII.8 Experimental scans and model predictions 170
VII.9 Model predictions for rotational Raman measurements 171
VII.10 CO_2 rotational Raman scattering demonstration 172

Table VII.1Comparison of spectrometer to vapor prism filter 174

Chapter 1: Introduction

A quantitative understanding of flowfield velocity, temperature, density, and species mole fraction are the goals of aerodynamic flowfield measurements.[Miles 1994] Early work in flowfield imaging relied upon shadowgraph, schlieren, or interferometry to image index-of-refraction based effects in high speed flow. Intrinsically, these techniques are path integrated, leaving limited applicability in complex flowfields. Planar measurements of flowfields have been made with particle seeding (e.g. particle image velocity); however, there are cases in which flow seeding is impractical or cannot yield desired information. Two approaches for non-intrusive planar flowfield imaging are feasible: laser induced fluorescence (LIF), which is a resonant process, and Rayleigh/ Raman scattering techniques which are non-resonant. Because it is a resonant process, laser induced fluorescence can produce high signal yields, an attribute desirable in low density flowfields.[Miles 1997] In fact, LIF is generally applied to measurement of trace or low density species. It is capable of species specific measurement of temperature, concentration, and velocity, based on the measurement of the absorption profile and the fluorescence signal of the species under investigation. However, quantifying the LIF signal can pose significant difficulty because of quenching, saturation effects, laser attenuation, and laser-induced chemistry. Further, because of the resonant nature of LIF, the light source is constrained by the species under investigation — the resonance band of the fluorescing species determines the operating wavelength of the light source. As a result, only those species that are both photoactive *and* coincide spectrally with existing light sources may be interrogated.

By utilizing a non-resonant process, Rayleigh or Raman scattering, the frequency of interrogation is not pre-determined, the process is instantaneous (and not subject to quenching), and the signal is linear with both interrogation intensity and species number density. The challenge with both Rayleigh and Raman scattering is that the processes are weak and often occur in a strong and spectrally complex background. As a result, Rayleigh and Raman based diagnostics require high energy interrogation sources and specialized spectral filters for signal resolution. The filtered Rayleigh scattering technique is based on resolving the spectral profile of Rayleigh-Brillouin scattering from high speed flows.[Forkey] By appropriately measuring the spectral profile of the scattering, two dimensional measurements of temperature, density, and velocity may be made with accuracies of a few percent. Because it is an elastic scattering process, Rayleigh scattering does not contain the species specific information of the Raman scattering process. Raman scattering is like Rayleigh in that it is instantaneous and linear, but the Raman signal is species resolved and orders-of-magnitude weaker. The Raman scattering based diagnostics developed here are capable of maintaining spatial resolution while measuring species specific density and temperature.

This thesis details the development of a laser source and spectral filters optimized for Rayleigh and Raman based diagnostics. A high power laser system compensates for the weak scattering signals. Both the Rayleigh and Raman scattering signals increase strongly with frequency, and hence, it is desirable to operate in the ultraviolet. Further, because the spectral content of the light scattering depends upon both the laser profile and the flow parameters under investigation, a spectrally pure laser source is desirable. Narrow band operation of the interrogation source allows for high resolution measurements of

parameters that would otherwise be obscured by a broadband illumination source. A tunable interrogation source changes the traditional paradigm for these diagnostic measurements. Traditionally, a fixed frequency laser source is used for illumination, and the scattering is spectrally resolved through tunable filters (spectrometers). However, conventional filters such as spectrometers or thin-film dielectrics suffer from inherent trade-offs among spectral resolution, efficiency, and imaging ability. By using an ultraviolet, narrowband, tunable laser source, new fixed frequency filters can be developed which simultaneously achieve high spectral resolution, high efficiency (throughput) and maintain desired imaging capabilities.

Rayleigh and Raman based diagnostics require spectral filters to determine the spectral profile of scattered light which contains the desired flowfield information. The filters must also serve to reject unwanted background scattering which interferes with measurement. For Rayleigh scattering based measurements, a notch absorption filter is used to reject light in one narrow band, while passing all other frequencies. Pairing this fixed notch filter with the tunable laser source, the unwanted elastic scattering from walls and windows may be made coincident with the filter notch, and hence removed from the measurement. The desirable scattering may be thermally broadened and Doppler shifted (for moving flows) so that it is passed by the filter. For Raman based diagnostics, in order to resolve individual spectral features amidst a strong and spectrally complex background, a filter with a narrow passband is preferable. A narrow passband filter must be able to pass the low light levels characteristic of Raman scattering while rejecting the nearby stronger Rayleigh line. For both Rayleigh and Raman scattering, in order to determine the spectral profile of the flowfield scattering, the filters must also have the ability to discriminate small

spectral shifts. As will be described in successive chapters, each of the filters is based on the properties of optically thick mercury vapor. Because of the strong, ground state transition of mercury, the filters achieve high spectral discrimination, large out-of-band rejection, and maintain imaging capabilities for both Rayleigh and Raman scattering measurements. In addition to developing these new devices and diagnostics, each of the following chapters includes relevant background and review of related work.

Chapter Two describes the development of the new ultraviolet laser source. The light source is a frequency tripled, injection seeded, cavity-locked titanium: sapphire laser. The laser achieves 50 mJ/pulse of tunable, near transform limited (spectrally), near diffraction limited (spatially) output at 250 nm. This high power, tunable, ultra-narrow band output in the ultraviolet is unique. By comparison, the laser community has recently pushed forward in the development of optical parametric oscillators (OPOs), which with significant engineering have reached broadly tunable ultraviolet output with bandwidths orders of magnitude greater at a fraction of the output energy.[Coherent] Narrow band operation of the Ti: sapphire laser is achieved by injection seeding a cw Ti: sapphire laser into a pulsed resonator. A new cavity locking mechanism, Ramp and Lock, gives single shot cavity locking which allows the pulsed laser to tune rapidly and discontinuously, making the system frequency agile. A description of the customized cw seed source and cavity locking is given in addition to a review of alternative approaches. The chapter concludes with a discussion of the frequency tripling, its merits and limitations. The ultraviolet laser source is paired with each of three new spectral filters for the development and demonstration of new diagnostic techniques. These techniques are discussed in subsequent chapters as are the relevant features of the light source to these diagnostics. To highlight some of these, the ultra-narrow band tunable laser produces precision controlled

output which resolves Rayleigh broadening, Raman shifts, and Doppler shifts all of which are measurable to the MHz scale. Because of the strong ultraviolet enhancement of Rayleigh and Raman scattering an ultraviolet laser is desirable. Finally, by operating in the UV, the laser may be paired with mercury vapor based spectral filters, which provide nearly ideal filtering capability.

Because mercury vapor forms the basis for each of the spectral filters, Chapter Three reviews basic mercury spectroscopy. The relevant parameters of mercury vapor are detailed in order to develop a computer model for the ground state absorption at 253.7 nm. Experimental high resolution (MHz) absorption measurements of naturally abundant and isotopically enhanced mercury are used to validate the computer model. The modeling is extended to include a data fitting routine to account for unknown parameters such as instrument linewidth and mercury self-broadening coefficient. This model is incorporated in the development of the three new vapor filters: notch absorption, narrow passband, and refraction.

UltraViolet Filtered Rayleigh Scattering (UVFRS), a natural coupling of the laser and notch absorption filter, is developed in Chapter Four. UVFRS is an extension of visible filtered Rayleigh scattering, previously characterized and demonstrated with an iodine vapor cell and frequency doubled Nd: YAG laser.[Forkey] The diagnostic technique is capable of planar measurements of temperature, density and velocity fields with accuracy of a few percent for static to supersonic fluid flows. The chapter characterizes the basic concept and theory of filtered Rayleigh scattering. The mercury vapor notch absorption filter is detailed, and its nearly ideal characteristics highlighted. Imaging and velocity measurement of a Mach 2 free jet are made via UVFRS. Finally, the merits of an ultraviolet

source and mercury vapor filter are discussed.

Because species specific information is necessary in many flowfield measurements, Raman scattering based diagnostics are motivated. Chapter Five discusses the concept and basic theory behind rotational Raman scattering, and its benefits over the vibrational counterpart. Because rotational Raman scattering has a spectral shift significantly smaller than that of the vibrational analog, strong background interference from Rayleigh scattering poses significant challenge for spectral filtering. The discussion articulates the spectral filter's features necessary for resolving individual rotational Raman lines while simultaneously suppressing the Rayleigh signal and maintaining imaging capabilities.

Chapter Six describes the development, characterization and implementation of a new ultra-narrow passband imaging filter for rotational Raman scattering based diagnostics. The filter is based upon the resonant fluorescence of the mercury 253.7 nm absorption, and features a spectral passband less than 1 cm^{-1}. The filter is capable of spatially resolving individual lines from rotational Raman scattering. Experimental characterization and analysis of the spectral, temporal, and spatial response of the filter is given together with measurements and a discussion of efficiency and limitations of the filter. A Monte Carlo model of the filter is developed and validated. Finally, the filter is demonstrated in high resolution Rayleigh and Raman scattering measurements of room air.

An alternative approach to rotational Raman imaging is developed in Chapter Seven. A filter capable of making simultaneous measurements of multiple rotational lines, while preserving one dimensional imaging capability, complements the spatially resolved narrow passband filter. This filter is based on the anomalous dispersion of mercury vapor and somewhat analogous to an imaging spectrometer. Light scattering spectrally close to

the mercury resonance is refracted by imaging through a vapor prism. The filter simultaneously achieves the high background suppression of the notch absorption filter (for removing the Rayleigh line), and spectrally discriminates rotational Raman scattering. Spectral discrimination occurs in one dimension spatially, and spatial information is preserved in the other. Chapter Seven details the concept, theory, and construction of this filter. Model predictions and characterization of the filter are given. Finally, the filter is demonstrated by imaging rotational Raman scattering from CO_2.

Chapter Eight concludes by discussing the future directions and application of each of these devices and techniques. The appendices contain the detailed computer code developed in each of the models described in the thesis. Portions of the work presented in this thesis have appeared in various papers listed in the following references section.

References:

Coherent Laser Group, *Product Catalog*, Optical Parametric Oscillator Specifications, Santa Clara, CA (1997).

Finkelstein, N.D., Lempert,W.R., and Miles, R.B., "Rotational Raman Scattering Measurements with a Single Mode Laser Source and Narrow Passband Filter," *Optics Letters*, **22**(8), 537, (1997).

Finkelstein, N.D., Lempert,W.R., and Miles, R.B., "Narrow Linewidth Passband Filter and UV Laser Source for Rotational Raman Imaging," SPIE paper 3172-88, *Annual Meeting: Optical Science, Engineering and Instrumentation,* San Diego, CA, (1997).

Finkelstein, N.D., Lempert,W.R., and Miles, R.B. "Mercury Vapor Filter Technology and UltraViolet Laser Source for Flowfield Imaging," AIAA paper 97-0172, *35th*

Aerospace Sciences Meeting and Exhibit, Reno, NV, (1997).

Finkelstein, N.D., Lempert,W.R., and Miles, R.B., "A Narrow Passband, Imaging, Refluorescence Filter for Non-Intrusive Flow Diagnostics," AIAA paper 96-2269, *19th Advanced Measurement and Ground Testing Technology Conference*, New Orleans, LA, (1996).

Finkelstein, N.D., Lempert,W.R., and Miles, R.B., "Cavity Locked, Injection Seeded Titanium: Sapphire Laser and Application to UltraViolet Flow Diagnostics," AIAA paper 96-0177, *34th Aerospace Sciences Meeting and Exhibit*, Reno, NV, (1996).

Finkelstein,N.D., Gambogi,J., Lempert, W.R., Miles, R.B., Rines,G, Finch,A., and Schwarz, R.A., "The Development of a Tunable Single frequency UltraViolet Laser Source for UV Filtered Rayleigh Scattering," AIAA paper 94-0492, *32rd Aerospace Sciences Meeting and Exhibit*, Reno, NV, (1994).

Forkey, J.N., "Development and Demonstration of Filtered Rayleigh Scattering - A laser based Flow Diagnostic for Planar Measurement of Velocity, Temperature and Pressure," doctoral thesis #2067-T, Princeton University, Princeton NJ (1996).

Miles, R., Lempert, W., Forkey, J., Finkelstein, N., Erbland, P., "Quantifying high speed flows by light scattering from air molecules," *25th AIAA Fluid Dynamics Conference*, AIAA 94-2230, Colorado Springs, CO (1994).

Miles, R.B., and Lempert, W.R., "Quantitative flow visualization in unseeded flows," *Annual Review of Fluid Mechanics*, **29**, 285-326, (1997).

Chapter 2: The Light Source

Approach of the ultraviolet tunable system

The high power narrow linewidth, tunable, ultraviolet source is a frequency-tripled, injection-seeded, cavity-locked titanium: sapphire laser. Because the gain bandwidth of the titanium-sapphire is quite broad (680-1100 nm, shown in Figure 1), it serves as an excellent medium for tunable laser sources. Figure 2 gives a schematic of the laser source, comprised of two pump lasers, a seed source, an unstable resonator, and frequency tripling stage. The seed source is a narrow band, tunable, continuous wave (cw) ring Ti: sapphire, pumped by an argon ion laser running broadband. Single longitudinal mode output is used to seed the Nd: YLF pumped high power unstable resonator. A novel cavity-locking mechanism, Ramp and Lock, insures the pulsed resonator cavity length tracks the input seed frequency, so the output of the pulsed resonator is single longitudinal mode. A pair of frequency mixing crystals triple the pulsed output. The laser system generates 50 mJ/pulse of tunable, spectrally near transform limited, spatially near diffraction limited output at 250 nm.

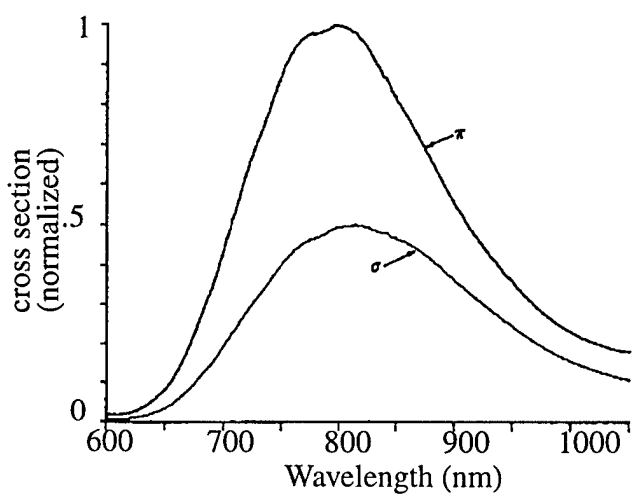

Figure 1: Titanium: sapphire lasing cross-section (normalized to π polarization)

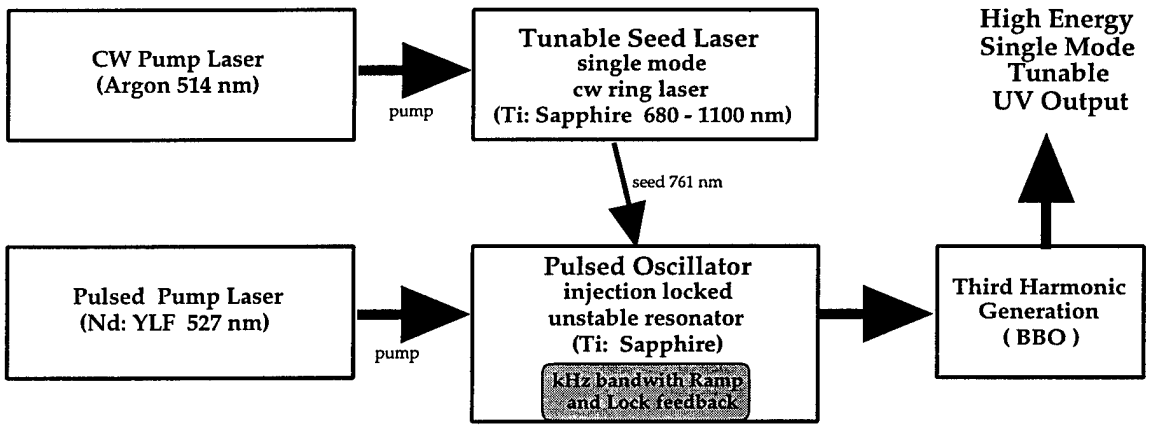

Figure 2: Schematic of injection-seeded, cavity-locked, frequency tripled titanium: sapphire laser system. An agron ion pumped cw ring Ti: sapphire injection-seeds an Nd: YLF pumped unstable resonator. Cavity-locking electronics insure single longitudinal mode output. A pair of BBO crystals frequency triple the infra red to produce tunable, narrow band, ultraviolet output

Development of tunable CW source:

The goal of the cw source development effort was to generate continuously tunable, narrow linewidth (single-mode) near infrared laser light at 760 nm. The laser was required to operate in both a high power (1-3 Watt) and low power (microWatt) regime for its two different tasks: cw mercury vapor spectroscopy, and high power pulsed oscillator seed source. Both tasks are described in following sections.

Addressing the more taxing of these goals, the multi- Watt level tunable output, assured success in operation as a spectroscopic tool and application as a seeder for the pulsed system. Figure 3 shows the schematic of the cw system. The laser is a modified version of the Schwartz Electro-Optics Titan CW laser system. The ring configuration of the cavity was selected for its broad and continuous tuning capability. The sapphire crystal is 0.2% doped with Titanium $^{3+}$ ion. The ring cavity is formed by a pump mirror and fold mirrors, PMIR and FMIR (dichroic concave mirrors), a high reflector FLAT mirror, and

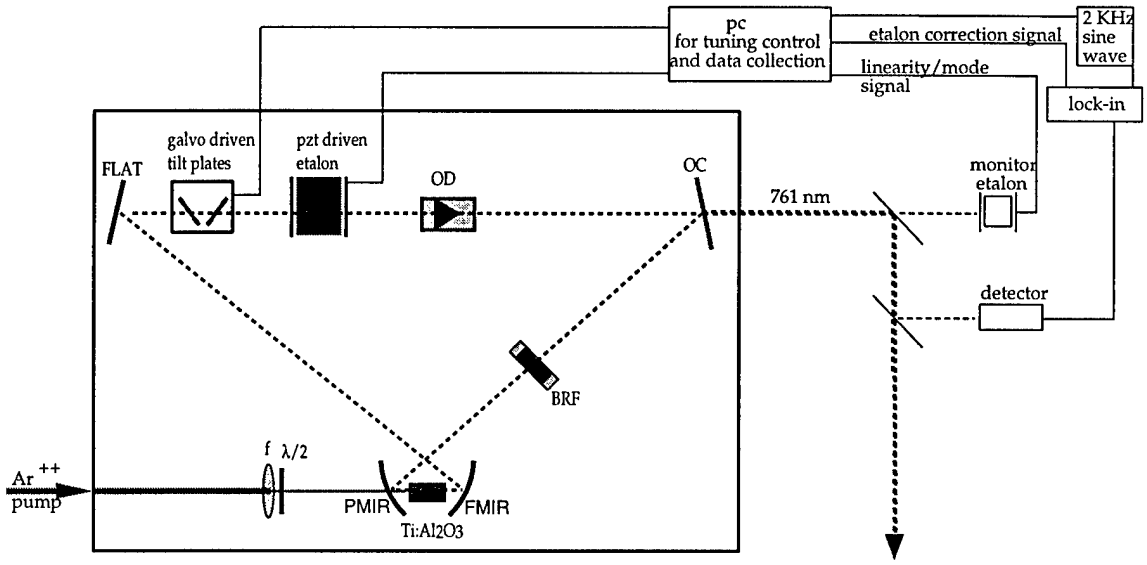

Figure 3: CW titanium: sapphire laser. An argon ion laser pumps the ring configured Ti: sapphire cavity. An optical diode (OD) insured unidirectional lasing. An intracavity etalon provides single-mode operation, while galvanometer driven tilt plates tune the output by changing the effective cavity length. External monitoring detectors and electronics provide feedback to continuously tune while maintaining single longitudinal mode operation.

output coupler OC. Additional standard intracavity components are the BRF, 3 plate bi-refringent filter, and OD, optical diode. As discussed later, the birefringent filter is the coarse tuning element, while the optical diode insures unidirectional lasing, by inducing a polarization loss by coupling a Faraday rotation with a birefringent quartz flat. The titanium: sapphire is pumped by an argon ion laser, running on all lines. A half wave plate ($\lambda/2$) provides the necessary p-polarization for pumping. The pump is focussed to a beam waist of nominally 50 μm at the Ti: sapphire crystal. The higher power operation utilized a Coherent Inova 200 full frame argon ion laser, pumping in excess of 12 Watts, while the lower power case has used a Lexel -95 4 Watt source. The pump mode of the laser is critical, of course. Initial difficulties with deformation of the steering mirrors for the pump

induced spatial mode variation in the Ti: Sapphire output. Similarly, f-centering (color center absorption) of the Brewster mirrors inside the argon ion cavity produced doughnut mode pump output, which prevented the Ti: sapphire from lasing. However, pumping the Ti: sapphire crystal with good spatial mode, p-polarized light reliably produces tunable infrared output. The ring laser system achieved 2.8 Watts of multi-mode output with 10 Watts of pump input, and 1 Watt output for 5 Watts of pump. The cavity modes are spaced 250 MHz apart and the spatial mode is TEM_{00}. Though Ti: sapphire is described as a homogeneous gain material, line narrowing optics are required to insure single longitudinal mode output.

To achieve single frequency, continuous scanning, the laser is operated with the addition of a galvanometer-driven dual tilt plate assembly, and a piezo-electrically controlled scanning etalon. These components complement the standard coarse tuning element, the three plate bi-refringent filter, which allows the laser to operate on one or more modes over a 15 GHz range. Since this is broader than our desired application, no effort was made to modify / control the birefringent filter's operation.

The addition of a piezo-electric transducer (pzt) driven etalon ensures single-mode operation. The confocal air spaced etalon (Spectra Physics 761) is low finesse (approximately two, mirror reflectivity of 20%), and has a free spectral range of 75 GHz. By suppressing all other cavity modes below lasing threshold, the etalon acts to select the single, highest gain, longitudinal mode of the cavity. The single-mode output is stabilized by adding a small 2 kHz sinusoidal dither to the etalon offset voltage, and by using a standard first derivative nulling to provide feedback in the form of a quasi-dc bias voltage.[Bjorkland] The voltage applied to the internal etalon determines the spectral

location of its peak transmission. If the peak of the etalon transmission is spectrally coincident with the laser cavity mode, maximal output is achieved. Detuning the peak of the etalon transmission introduces slight loss and thereby decreases the laser output power (not its spectral location). Thus an amplitude modulation (AM) locking scheme may be achieved by applying the relatively small 2kHz sinusoidal voltage on top of the larger 600 Volt etalon offset voltage. The amplitude of the applied dither is 1 Volt, corresponding to a 100 MHz frequency modulation of the etalon, which produced less than one milliWatt modulation of the laser power. The small resulting fluctuations in output power of the laser are detected on a photodiode and beat with the 2kHz driving signal on a Thorlabs LIA 100 lockin amplifier. If the etalon peak lags the spectral location of the cavity mode, the AM modulation is in phase with the 2kHz driving voltage and the dc output of the lockin is positive. If the etalon leads the laser cavity mode, the modulation is out of phase, and the lockin output is negative. The magnitude of the dc lockin output correlates linearly (to first order) with the spectral offset between the etalon and laser cavity mode, because of the changing slope of the etalon transmission profile. Thus, the dc lockin output is used as the feedback in a simple proportional-integral (PI) control circuit to lock the etalon transmission peak to the laser cavity mode. A proportional-integral control circuit was built (10-100ms integration time, variable gain 1-1000) and offers continuous locking capability as the laser is tuned.

Continuous tuning is achieved by changing the laser's effective cavity length by tilting a set of dual quartz plates held at nearly Brewster's angle. The walk off compensating configuration of these galvanometer mounted (0.25 inch thick) fused silica flats insures that the beam maintains a constant path even as the plates rotate.[SEO 'notes'].

The overall travel of the plates is 1.2° and corresponded to 12 GHz tuning. For continuous scans greater that 12 GHz, the tilt plates are reset, while the etalon is held fixed. Computer control allows the overlap of the new cavity mode to match the etalon peak. Discrete steps of 4 MHz are the resolvable digital increments of the galvanometer controller. For the majority of experiments, the tilt plates are held fixed, or given a ramp voltage for continuous scanning. However, for precision measurements in the infra-red, a feedback control loop (proportional integral) was used to lock the tilt-plates to a known reference (potassium D1 line at 770 nm).[Grinstead] Such a lock loop is required to compensate for real cavity length modulation due to thermal cycling of the room and laser optics mounts. For frequency stabilized operation of the cw laser as a seed source, the oxygen A bands at 760 nm also may be used.[Kroll] (A thorough description of an appropriate locking scheme is given by Forkey. [Forkey, pg 127]) The continuous tuning rate and locking bandwidth of the cw laser are limited by the physical travel of the tilt plate assembly. The system is limited to 18Hz by the mechanical response of the galvanometer assembly — fast enough for thermal fluctuations, but not necessarily acoustic vibration.

The laser is scanned in one of two operating modes: continuous (4 MHz steps), or mode-hop (250 MHz steps). In the continuous scanning mode, the effective cavity length is modified via the tilt plates, and single-mode operation maintained by actively tracking the etalon mode with the cavity. In the mode hop scan (a coarser and faster scanning method), the cavity modes are fixed (by fixing the tilt plate position) and the etalon offset voltage ramped, to 'hop' from one cavity mode to the next.

While independent control electronics for the etalon and tilt plate assemblies reliably allow the laser to continuously tune, the addition of computer control makes the

system more robust. A Keithley 1601 (100 kHz) data acquisition board is used to digitize and store up to 8 input channels, and produced 2 analog signals for control of the etalon and tilt plate assembly, respectively. Home built data acquisition software and laser control were written in Turbo Pascal and run on an ATT 6386/sx personal computer. Some of the computer control enhancements included: a synchronized data collection with laser scan step (data are not collected while feedback issued to the intracavity etalon, or while the tilt place assembly resets at 12 GHz), a variable feedback dead-band (user specified levels of acceptable mismatch between the internal etalon and cavity mode), discontinuous, programmable, and manual tuning.

While advertised as a continuously tunable system, further modification must be made to truly scan uninterrupted through the infrared: oxygen free conditions. The weak and classically forbidden oxygen A-band transitions in the vicinity of 760 nm provide enough intracavity absorption to suppress lasing in those regions. The laser cavity 'hops' to another longitudinal mode, which has higher gain (despite the lower throughput of the low finesse intracavity etalon). By purging the cavity with nitrogen, continuous tuning through these bands has been achieved. Measurements of the oxygen absorption at 761 nm and 769 nm were made, placing the absorption as high as 2%/ meter which is in good agreement with the expected absorption.[Bruce]

Calibration and linearity of the laser scan are essential for accurate spectroscopic measurements. An external etalon was used to monitor the behavior of the laser. For the mercury absorption spectroscopy, we used a 1.5 GHz Fabry-Perot interferometer with custom built comparator circuit to monitor spectral continuity and linearity. A normal saw tooth ramp voltage was applied to the external monitoring etalon at a much faster rate than

the tuning of the laser. The comparator electronics consist of an analog sample and hold, which was triggered by the occurrence of an etalon transmission peak. The voltage applied to the etalon, proportional to the relative frequency change, was measured each time an etalon transmission occurred. Each point of the recorded offset voltages varied from a linear fit by less than 2 percent. Thus, we could verify a constant scan rate. The etalon traces also revealed any discontinuities, mode hops, or multi-mode behavior of the laser. In less critical measurements, the laser output was measured with a 2 GHz free spectral range Fabry-Perot interferometer. Etalon peak transmission was monitored on an oscilloscope, rather than captured. The absolute frequency of the system was determined by an external Burleigh wavemeter (WA - 10, accurate to 1 part in 10^6).

The addition of internal tuning elements, the single etalon and tilt-plate combination was found to reliably produce single frequency tunable output. The laser system achieved 2.2 Watts single longitudinal mode tunable output at 761 nm, with 10 Watts of ion laser pump power. It could be reliably tuned, continuously, in excess of 15 GHz without adjustment of the bi-refringent filter. With appropriate tuning of the bi-refringent filter (micro-motor attachment and control), we anticipate that the system could be tuned for much greater (order of nanometer) intervals. In lower pump powers, for injection-seeding applications, 4 Watts pump produce over 500 milliWatts tunable light. The spectral line width is approximately 1 MHz over milliseconds, and approximately 10 MHz over minutes.

This thesis will focus on the application of this laser as seed source for a high power pulsed oscillator. However, as mentioned, this laser has been used independently as a spectroscopic tool (for measurement of Hg described in chapter 3, and C-H stretch

overtones, [Gambogi]), and for diagnostics application.[Grinstead] As a seed source, the laser produces well in excess of the necessary power, and under appropriate conditions could ultimately be replaced by a diode laser source.

Alternate approaches to CW Ti: sapphire locking

Because of the robust and versatile nature of Ti: sapphire, it has been used in a variety of contexts as a cw source. For high resolution spectroscopic measurements, active stabilization of a ring Ti: sapphire cavities has been demonstrated with linewidths of 1.0 kHz or less [Boyd; Vassen]. In these cases the slow response of the galvanometer driven tilt plate assembly is not sufficient to stabilize the Ti: sapphire ring cavity to an external reference. Tuning and stabilization is achieved by placing the HR mirror on a piezo-electric transducer mount. Such adaptation is necessary for rapid feedback and narrow linewidth operation. In other cases, as ours, where the linewidth is not critical, the galvanometer driven tilt plates are sufficient for slower locking and tuning. In conditions where cavity length variation and vibration is not an issue, independent control of the tilt-plate and etalon assemblies has demonstrated continuous scanning without feedback.[Sasada] However, when mode hops (changes in longitudinal mode of the resonator) must necessarily be avoided, a feedback mechanism must be employed.

Injection-seeding of pulsed resonators

The ultimate purpose of the scanning cw system is to act as a seed source for a high power, pulsed, injection-locked system, used for diagnostic techniques such as UV Filtered Rayleigh Scattering. As described above, Ti: sapphire offers the advantage of being a tunable, high power, narrow band source, yielding spectral densities matched only perhaps

by pulse-dye amplifier (PDA) systems. Titanium: Sapphire was demonstrated as a laser material by Moulton in 1982.[Moulton (1982)] Since then Ti: sapphire has been operated cw, mode-locked, and narrow band pulsed. As background to this work, a discussion of similar efforts to produce narrow linewidth high power output of Ti: sapphire is given. The first appearance of injection control of a Ti: sapphire system is by Brockman, in 1986 as a prospect for remote differential absorption lidar (DIAL).[Brockman] Injection-seeding of the Ti: sapphire with a narrow band dye laser produced 2.5 pm spectral width pulses. Subsequently cw diode seeding was reported by the same group.[Bair] However, not all energy was extracted at the seed frequency, leaving a spectral background too broad for narrow band work. True single-mode output of Ti: sapphire is reported by Rines and Moulton by seeding with a cw Ti: sapphire system.[Rines (1990)] Shortly thereafter, Raymond and Smith produced a single-mode Ti: sapphire system injected via diode seeding, with as little as 100 μWatts.[Raymond] An alternate approach has also been pursued by workers at Spectra Technology, Inc. (STI) of Bellevue, Washington.[Kangas] By using a Littman configuration for a pulsed Ti: sapphire resonator, tunable, single-mode operation was achieved. A glancing incidence grating was used in zero order as output coupler, and in first order as feedback for the pulsed cavity. Meeting both the cavity condition and the grating equation assured single-mode operation. The drawback of this pulsed configuration is limited output power, 1-3 mJ, due to walk off of the beam from the gain media and the grating, and grating damage.

The effort to produce several hundred milli-Joules of narrow linewidth laser is limited. Collaborators at Schwartz Electro-Optics, report a variety of configurations yielding high energy output, maximally in the standing wave configuration described

below. For a 1 Joule (532nm) Nd: YAG pump pulse, the Ti: sapphire resonator has achieved 430 mJ/pulse.[Rines (1990)] Barnes and co-workers have developed a power oscillator based on this design, and with a 1.5 mJ seed source achieved a spectrally pure, tunable 155 mJ/pulse system for DIAL measurements.[Barnes] Finally, frequency mixing of an injection-seeded Ti: sapphire laser with an Nd: YAG has produced a tunable blue source.[Brown] Brown and co-workers at STI used a cw-seeded unstable resonator design of Rines and Moulton, to achieve 200 mJ narrow band pulse. The addition of a single pass amplification stage (YAG pumped) yielded 350 mJ of narrow band infra-red output for their mixing work.

The Ti: sapphire pulsed resonator

The schematic of our injection-seeded Ti:sapphire system is given in Figure 4. The unstable resonator design is a modified version of the Schwartz Electro-Optic Titan-P pulsed laser system, based on the original design of Moulton and Rines.[Rines (1990)] Because of the short 3.2 μs natural lifetime of the excited state of Ti: sapphire, [Rapoport] pumping is traditionally achieved with another pulsed laser system. Successful operation has been demonstrated with both an Nd: YAG (Continuum YG 661), and an Nd: YLF (custom Schwartz Electro-Optic) - each frequency doubled, running at 532nm and 527nm, respectively. A significant feature of the pump laser is that a uniform top-hat mode reach the Ti: sapphire crystals. Since the Nd: YAG mode is a good TEM_{00}, it is necessary to pump in the intermediate field of the focussing lens (to avoid high peak intensities and the crystal damage threshold of roughly 12 J/cm^2 for a 8.5 ns pump pulse).[Rines (1997)] For this particular YAG system, 130 cm focal length lenses were placed 70 cm before the two Ti: sapphire crystals (pumping 140 mJ/pulse in a 2.7 mm diameter spot on each of the front

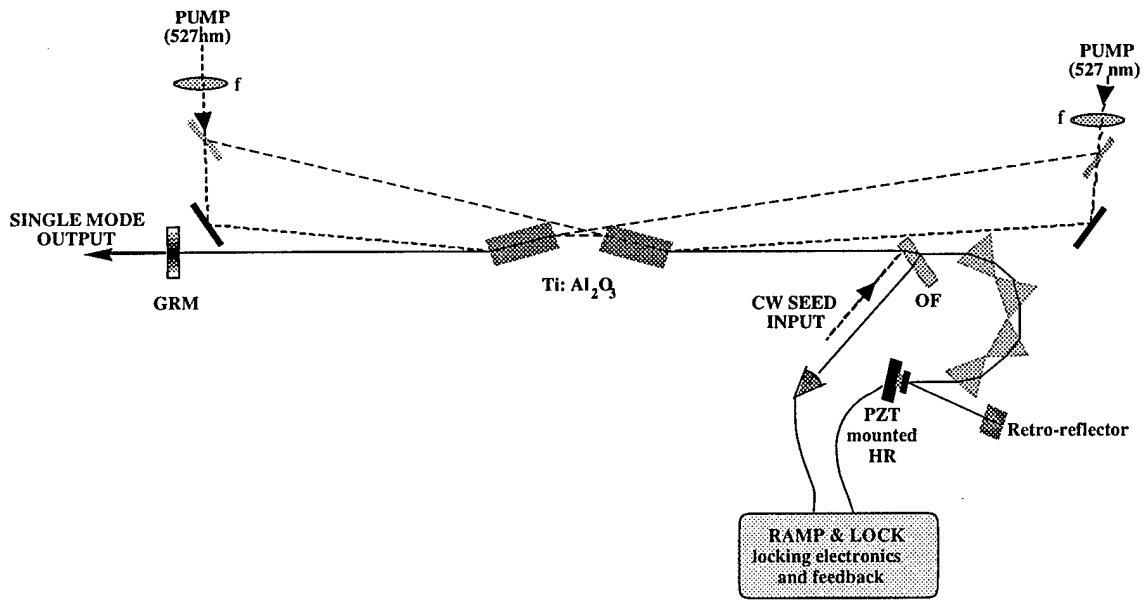

Figure 4: Pulsed titanium: sapphire resonator. Nd: YAG/YLF pumped folded mirror cavity design with four turning prisms for coarse tuning. Injection-seeded with an optical flat (OF), and cavity-locked with custom Ramp and Lock cavity-locking and pzt mounted high reflector. Output, on left, through a graded reflectivity mirror, GRM.

two surfaces). The Nd:YAG pumped system achieved nominally 100mJ/pulse. A higher power Ti: sapphire system used the Nd: YLF to pump the four surfaces of the two Ti: sapphire crystals. The Nd: YLF pump has a more divergent multi-mode beam, focusing at the beam waist of 130cm focal length lenses. This produced the more uniform top-hat pump mode desired. Each of the four surfaces is pumped by a 220 mJ/pulse, 3.5 mm beam, yielding 300mJ/pulse in the infrared. The short pump pulse (7 - 10 ns) operating at 10Hz (YAG) up to 30Hz (YLF) produced similarly short output pulses in the Ti: sapphire.

Two Ti^{3+} doped sapphire crystals are placed in series in the folded mirror cavity design, shown in Figure 4. The output coupler, shown left, is a graded reflectivity mirror

(GRM) with 37% reflectivity at center, AR coating at a 2 mm radius. The reflectivity is:

$$R = R_o\left[1-\left(\frac{r}{1.3}\right)^3\right]\ldots(r \le 1.24mm)$$

$$R = \exp[-13(r-0.9mm)]\ldots(r \ge 1.24mm) \qquad \text{II.1}$$

and radius of curvature of -4m. The two Ti: sapphire crystals are Brewster-cut and placed with opposing chirality. The Brewster cut is aligned with the c-axis of the bi-refringent sapphire, to take advantage of the greater absorption and emission cross sections of π-polarized light.[Rapoport] The Brewster angle achieves a broadband, low loss surface for both pump and lasing wavelengths. Further, the dispersion between these two wavelengths in Ti: sapphire allows correct alignment of the pump and laser paths without the use of dichroics. As seen, the small angular deviation of the pump beam from the lasing path increases overall efficiency, and precludes pump-beam damage to Ti: Al_2O_3 mirrors. The use of two Ti: sapphire crystals increases output power, while simultaneously compensating for dispersion of differing lasing wavelengths. The opposing chirality of the two wedged Ti: sapphire crystals ensures the beam path between the output coupler and the first crystal is constant, independent of wavelength. The dispersion between the four BK7 turning prisms and the high reflector assembly gives a means of coarse tuning, and line narrowing (approximately 1 nm at peak gain). As the high reflector (HR 6m radius of curvature) is angled in the horizontal plane, the laser tunes to a wavelength band that is in resonance with the cavity. Thus, by adjusting one axis of a single mirror the wavelength of the laser is tuned, while the (dispersion compensated) output remains spatially fixed. For cavity-locking discussed below, the traditional concave HR is replaced by a flat pzt

mounted reflector and poro retro-reflecting prism. While the confocal cavity condition is altered, the slight divergence is offset by gain guiding, thermal lensing, and seeding to maintain near TEM_{00} output mode. The Ti: sapphire crystals are housed in copper heat sinks, cooling the crystals to room temperature, but not below (to avoid surface condensation). This cavity design is limited in output power by the Ti: sapphire crystal damage, and has produced 430 mJ/pulse of nearly diffraction limited, tunable infrared output. [Rines (1990)]

Cavity-locking

It is relatively straightforward to injection-seed a high power oscillator. However, without active feedback to adjust the pulsed laser cavity length, the output frequency will fluctuate between one and two longitudinal mode output.[Rahn] When the seed laser frequency closely matches the resonance condition of the pulsed oscillator, the output is single longitudinal mode. When the frequency of the seed beam lies between two cavity modes of the pulsed oscillator, the pulsed laser operates on both cavity modes. In the single-mode case, the spectral output is near the transform-limit of the temporal width; whereas, in the dual-mode case, the output is several times the transform-limit. For many diagnostic applications it is desirable to continuously scan, while maintaining single-mode output. Other experiments are enhanced by the use of a frequency agile laser — a system which may discontinuously, and rapidly scan, maintaining single-mode, near transform limited operation. To this end, in collaboration with Schwartz Electro-Optics, a control system has been developed to acquire and maintain single longitudinal mode operation, while scanning rapidly, discontinuously and in harsh acoustic environments.

An optical flat (OF, Figure 4) placed in the cavity provides two ports, for seeding

and locking the pulsed resonator. For cavity-locking, the traditional high reflector has been replaced by a piezo-electric transducer (pzt) mounted high reflector, and retroreflecting assembly (shown in Figure 4). The custom built pzt mounted high reflector modifies the length of the 1.3 m cavity, while the retroreflector compensates for angular deviation (tilt) of the pzt stack during translation. The pzt-stack and mount are designed to translate the high reflector in excess of 3 microns, while allowing high bandwidth (10's kHz) feedback. The mechanical resonance of the high reflector mount is the limiting factor in the bandwidth of the cavity-locking feedback. Based on a NIST design, the mechanical mount (shown in Figure 5), has its first mechanical resonance at approximately 40 kHz.[Finch]

Injection-seeding of the cavity is achieved using one of the surface reflections of the optical flat placed in the pulsed resonator. Varying the angle of the optical flat changes input coupling efficiency from zero to 4 percent. An angle corresponding to nominally 2

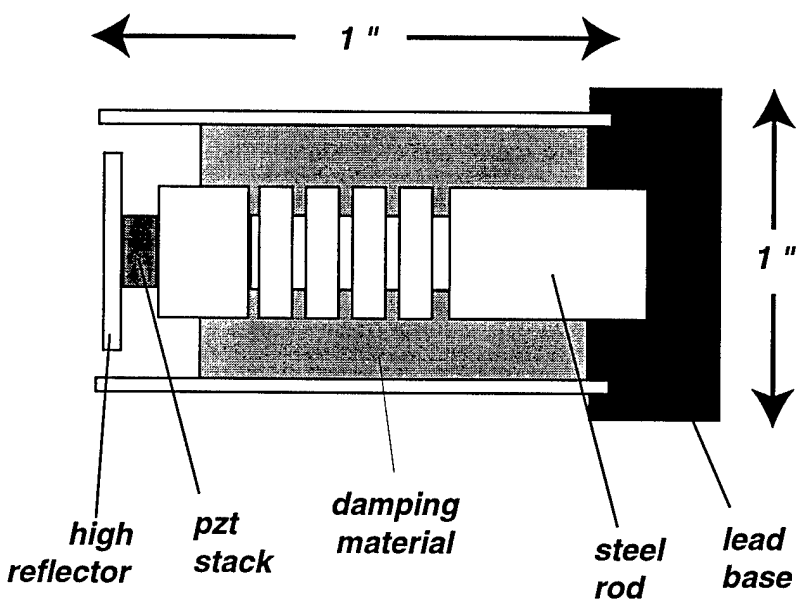

Figure 5: Custom high reflector mount. Designed for high bandwidth operation of Ramp and Lock cavity-locking, the mount has its first mechanical resonance at 40 kHz. The lead base acts as a low pass filter due to large inertial mass. The steel rod acts as a high-pass filter for acoustic noise. Damping material (putty), further acoustically isolates the high reflector from the laser optical bench to which it is rigidly attached.

percent coupling is more than sufficient to provide the necessary 100 μW for seeding.[Raymond] Increasing the injected seed power to several milliWatts provides enough signal to monitor the seed beam as it passes back out of the pulsed resonator (necessary for locking purposes). To further isolate the cw seed source from pulsed feedback, an optical isolator providing 30 dB attenuation in the reverse direction is inserted between the seed and pulsed lasers. To insure good spatial mode and stability of the seed beam, a pinhole spatial filter is also placed in the beam path between seed and pulsed lasers. Ultimately, if the system is to be injection-seeded with a laser diode, a second optical isolator would be required to provide approximately 60 dB attenuation of feedback.[Schwarz]

The cavity-locking mechanism is based on a novel approach, termed "Ramp and Lock," which provides the capability of tuning the laser frequency rapidly. The technique is based on monitoring the cw seed beam as it passes through the pulsed resonator. Feedback is given to insure a resonance between the pulsed cavity length and the input seed frequency. For each laser pulse, approximately 10 ms prior to the pump laser firing, the pzt mounted high reflector is given a ramp voltage that corresponds to roughly a 2.0 micron displacement. As the high reflector is displaced, a photodetector which monitors the cw seed beam passing through the unstable resonator detects fringes in time (modulation depth of approximately 50%). The monitor photodiode is an amplified HUV-1100 EG&G detector, terminated to give 100kHz bandwidth. The temporal fringes occur because the pulsed cavity acts as a low finesse Fabry-Perot cavity. Each new fringe corresponds to an increment of the pulsed cavity length by one half the seed wavelength.

Maximal transmission occurs when the pulsed resonator meets the cavity condition:

$$L = m\frac{\lambda}{2} \qquad \text{II.2}$$

L is the length of the pulsed cavity; m is an integer; λ is the wavelength of the injected-seed laser. Figure 6 illustrates the photodiode voltage versus time and pzt ramp voltage versus time. Labeled are the *Ramp*, *Lock*, and *Fire* segments of the cavity-locking scheme. After several fringes have been collected, the ramp voltage applied to the pzt stack is allowed to decay, thus reversing the translation of the pzt displacement. The fringes continue, but spaced further apart in time. During the ramp portion of the cycle, the sample and hold electronics determine the photodiode voltages corresponding to the minimum and maximum points of the fringes. After a specified delay, the locking electronics are applied. Feedback is given to the pzt to insure the photodiode voltage remains locked at a constant proportion of the fringe height. This feedback compensates for any cavity drift or acoustic vibration. The fringe position set point, defined as a fraction between minimum and maximum fringe signal, is variable and manually optimized. For single frequency operation, the optimum lock point is not at the peak of the fringe (the resonance condition), because of cavity length chirping induced by the pump laser. This lock point offset compensates for the pump induced change in the pulsed cavity's effective length.[Wall] With the two cavities (pulsed and cw) simultaneously matching the cavity condition, single-mode output of the pulsed laser is ensured. The ramp and lock technique acquires lock before *every* pulse. As a result, regardless of how the cw frequency changes, the pulsed system tracks and remains single-mode.

A schematic of the locking electronics is given in Figure 7. The main features are the input sample and hold, min/max detect and comparator, logic and timing, feedback

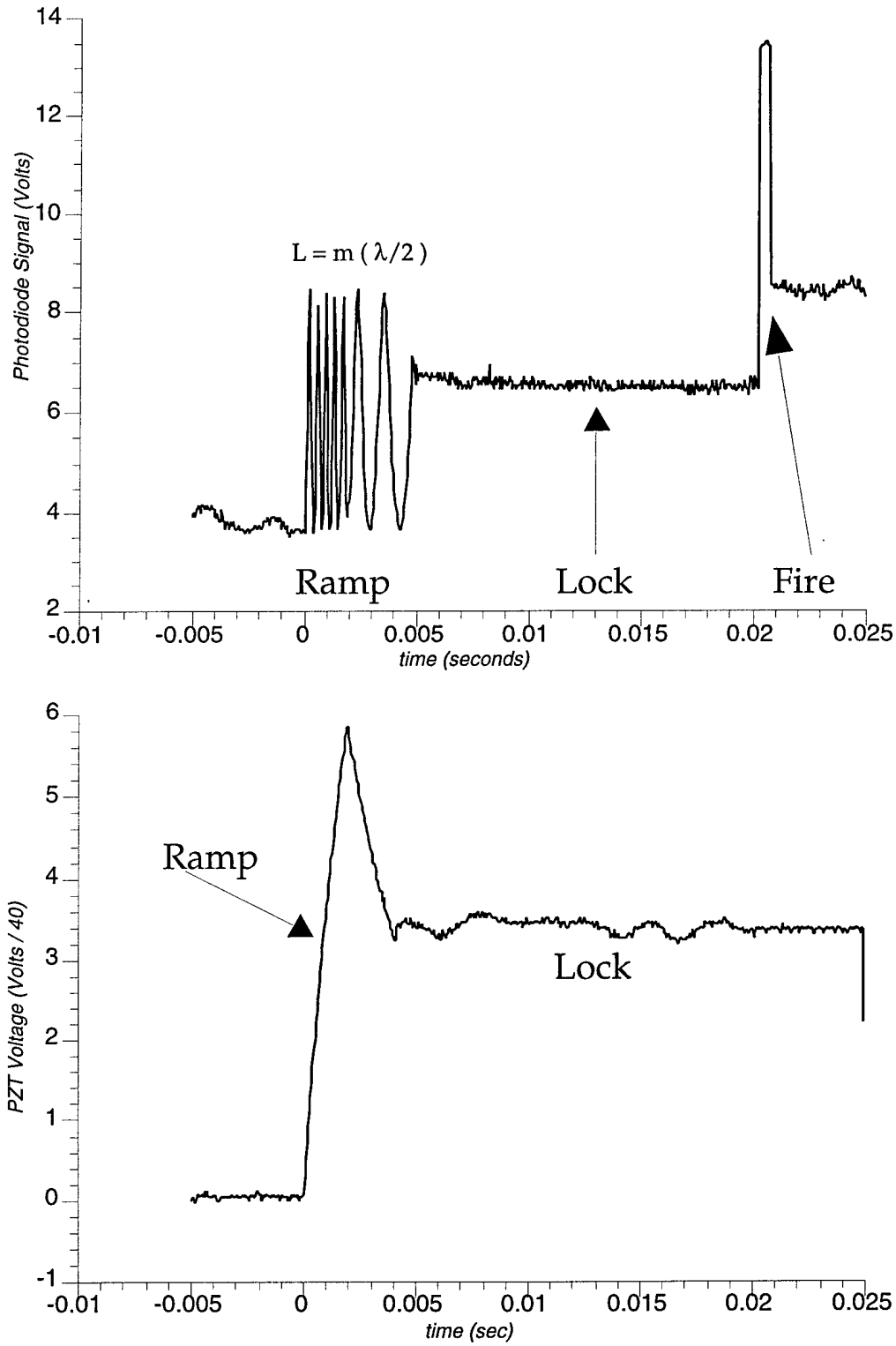

Figure 6: Ramp and Lock cavity-locking. Above, photodiode signal versus time. Below, voltage applied to the pzt stack (translating the high reflector). Fringes are observed above, as the seed frequency falls into and out of resonance with the pulsed cavity. Feedback ensures cavity match between the seed and pulsed cavities during lasing.

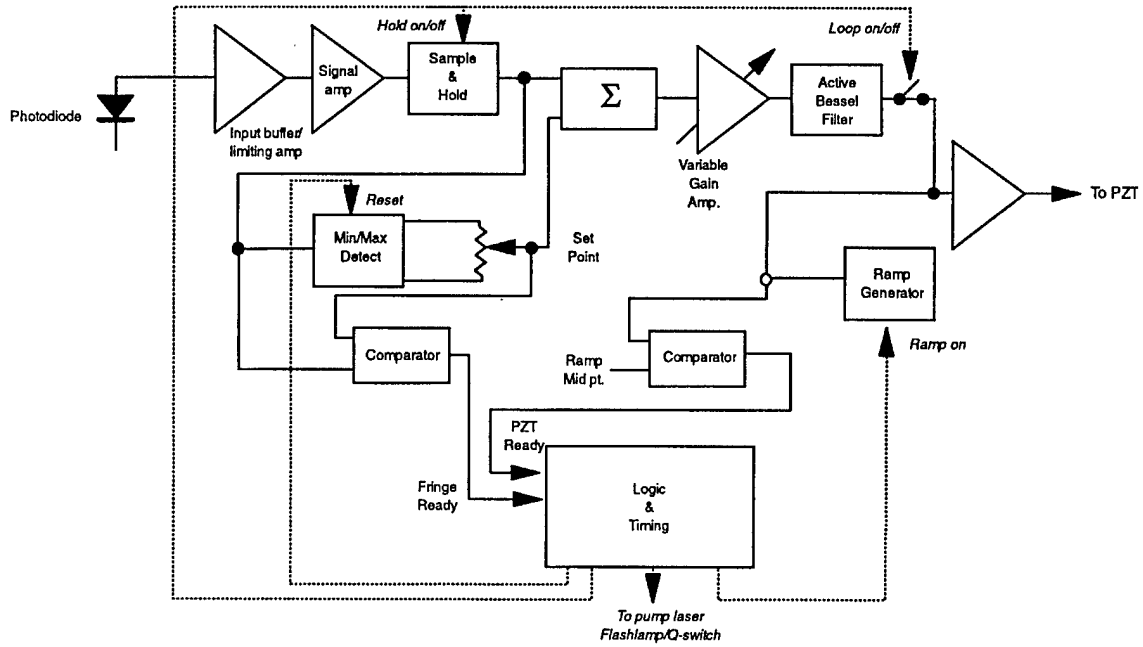

Figure 7: Ramp and Lock cavity-locking electronics. Key elements are the input sample and hold, min/max fringe detection, logic, and proportional-integral feedback and filter. Input arrives from an amplified, high speed photodiode. Output is given to an amplifier which produces 0-240V to translate the piezo-electric transducer stack mounted high reflector.

and filter. The signal from the amplified photodiode (monitoring the cw seed beam as it passes through the pulsed resonator) is buffered and sampled (in 100 ns segments). During the *Ramp* portion, this signal is used by the minimum and maximum detectors to determine the fringe peak height and depth. A potentiometer is used to vary the lock set-point as a fraction of the max-min height. During the *Lock* portion of the cycle, the photodiode signal is summed with an inverted lock set-point value, giving the difference between the actual and desired voltages on the photodiode. A variable gain proportional-integral (PI) control loop varies the voltage applied to the pzt stack to null the difference between the photodiode signal and set-point. Depending upon the environment that this locking circuit is operating in, additional filtering mechanisms may be added to

the lock-loop. A predetermined amount of time, 100ns-1μs, before the pump laser is *Fired*, the voltage applied to the pzt stack is clamped to a constant value. The output voltage of the control circuit (ramp, lock, and fire stages) is amplified through an Apex PA85A power amplifier to produce the 0-240Vpotential required to translate the pzt stack. A series of clocking and logic circuits monitor and control the stages of cavity-locking cycle.

A simplified sample timing diagram is given in Figure 8. A master clock pulse is issued at the repetition rate of the laser, 10-30Hz. This initiates a 2 ms ramp pulse trigger, during which a voltage ramp is applied to translate the pzt stack. A mid range comparator is used to determine that the pzt has translated approximately 1 micron. After the ramp pulse ends, the pzt voltage is allowed to decay (the travel of the pzt stack is in excess of 2 microns, corresponding to several fringes). As the ramp voltage decays past the mid-range set point, the locking circuitry is activated. The feedback lock signal requires that the pzt decays past the mid range and the monitor photodiode signal voltage is equivalent to the lock setpoint. The photodiode signal resonance with the lock setpoint is determined by a fringe comparator trigger. Once the lock-loop is activated, the error signal is fed back to the pzt voltage to null the difference between the photodiode monitor signal and the lock setpoint. In the event that the lock loop is not activated, the ramp is still applied, but feedback not applied.

It should be noted that the system may also be locked to dual-mode output. Instead of locking to match the pulsed cavity length to the cw seed frequency Equation II.2, the pulsed cavity length may be locked (accounting for chirp) to the trough of the fringe pattern given in Figure 6. In this way, the cw seed is halfway between two cavity modes of

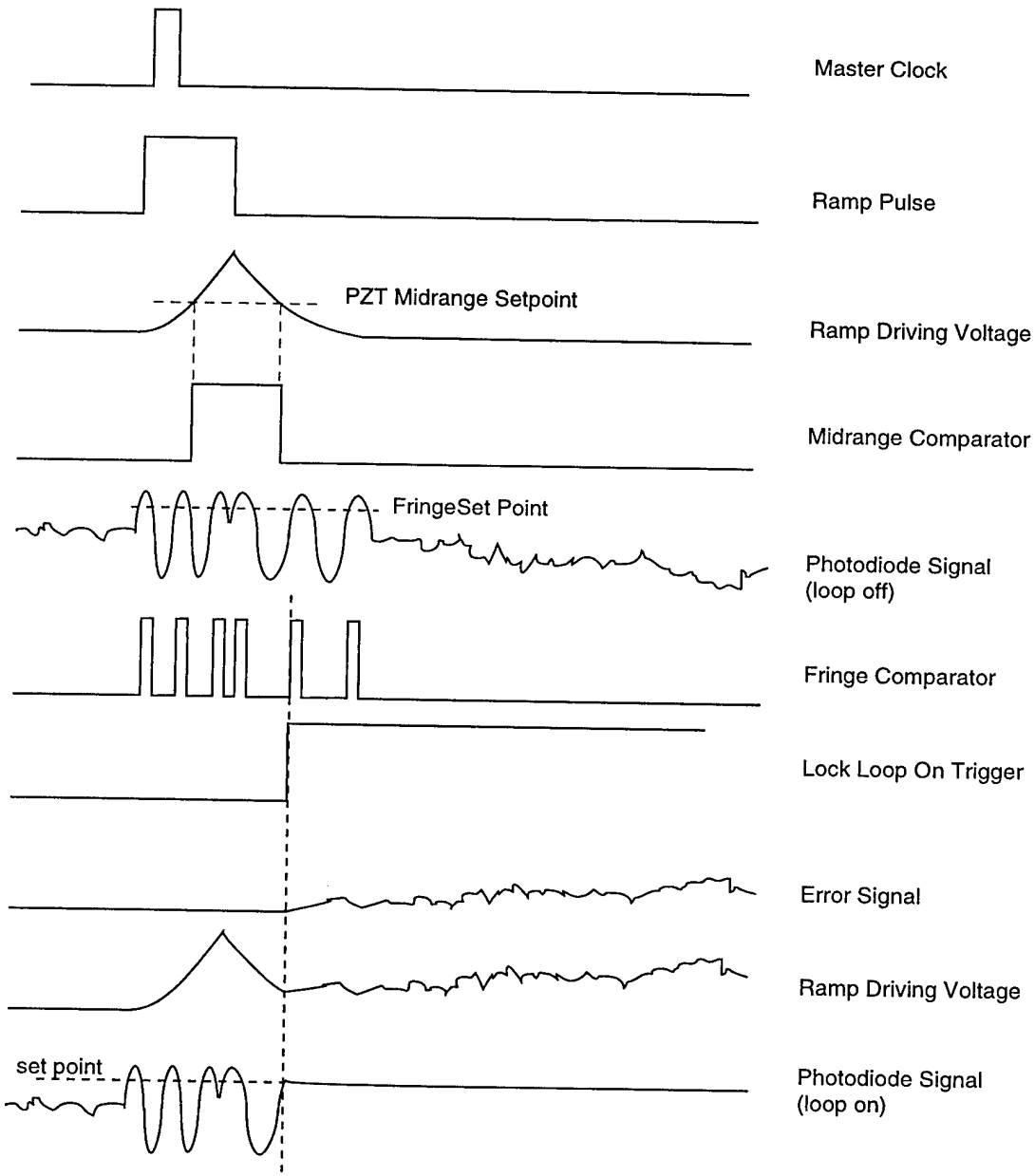

Figure 8: Ramp and Lock timing diagram. A master (10Hz) clock pulse triggers the pzt ramp voltage. After mid-range comparator level is reached the voltage applied reverses the translation of the pzt stack, until a manual set-point is reached. Locking electronics are applied, and feedback issued to maintain constant fringe height on the photodiode monitor.

the unstable resonator, and both are seeded. Such dual-mode output capability is useful, since the dual-mode output power is roughly 10 to 15 percent higher than single mode operation.[Rines (1990)] The corresponding higher fractional conversion for harmonic generation would motivate the dual-mode operation; however, for our diagnostics applications the single mode operation is used.

Cavity-locking alternatives

For our purposes, there are distinct advantages of the fringe locking mechanism over the standard pulse build-up time reduction technique.[Rahn] The main difference between these two control systems is that the fringe, cavity resonance system offers shot to shot cavity-locking, while the pulse build-up minimization issues feedback based on the history of many pulses. The build up time minimization technique measures the time between the opening of the Q-switch (the gain spoiler in the pulsed laser system) and the laser output. If the system is well seeded, and cavity-locked, the system will lase sooner than in the unseeded/ poorly seeded case. The feedback for a given laser shot is derived from information from previous laser pulses. Hence, the feedback control is most accurate when the laser conditions are not rapidly changing; spectral scanning must be very slow. Further, the effects of unstable ambient noise are not accounted for. In an open loop control, it is possible to predict where the pzt mounted high reflector should be for a given input seed frequency. Current work examines the potential for this method to increase scan rates, and discontinuously tune.[Farrow] However, unpredictable rapid deviations in cavity length (as with acoustic vibration) may not be predicted.

While the Q-switch build up time reduction technique is predominant, there exist a host of other cavity-locking and injection-seeding techniques for narrowing the output of

pulsed laser sources. Early work demonstrated the injection-locking of an Nd: YAG to a pulsed seed source. Byer stabilizes and monitors the output pulses of each laser, temporally and spectrally.[Park (1984)] Teets monitors the master oscillator output and the effect of optical feedback from the slave oscillator.[Teets] Injection-seeding with a cw source, Fry demonstrates single mode output of an Nd: YAG system in acoustically harsh environments (up to115dB).[Fry] Dubbed *ramp and fire*, the cavity length of the YAG is swept, while monitoring the input seed beam. As before, fringes are observed, and at a predetermined fringe height the laser lamps and Q-switch are fired. Similar in design, the systems lacks a feedback system, which requires that the laser be the master timing source in any experiment. In a ring cavity design, Raymond, demonstrated that the ratio of forward to backward propagating seed beam energies can exceed 1000:1, and hence gives an effective means of cavity-locking.[Raymond] Alternatively, Hamilton has demonstrated injection-seeding and cavity-locking of a Ti: Sapphire ring oscillator by dithering the high reflector and using phase sensitive detection of the cw beam through the pulsed cavity.[Hamilton] He demonstrates both single mode operation, and high temporal stability.

Experimental characterization

The injection-seeded, cavity-locked titanium: sapphire system yields high energy, single longitudinal mode output over a widely tunable range in the near infrared. The spatial quality is near TEM_{00} and nearly diffraction limited. Four surface crystal pumping by an Nd: YLF 850 mJ/pulse at 527 nm, the laser achieves in excess of 300 mJ/pulse at 760nm. The lasing band of Ti: sapphire is given in figure 1; however, limitations in mirror reflectivities constrain cw (seed) to tuning 710 - 840nm, and the pulsed resonator to

730-790 nm, due to a specialized high reflector.

A series of measurements were performed to experimentally characterize the laser's spectral linewidth, its tuning capabilities, and its ability to maintain lock with large changes in seed laser frequency. Two means of assessing the laser's spectral profile were employed. First, the temporal profile of the laser output was monitored on a shot to shot basis. When cavity-locked to single spectral mode, the temporal output is approximately Gaussian in time. When locked to dual-mode, the temporal profile is fringed, reflecting beating of the two closely spaced longitudinal modes. The measured beat frequency of 7 ns corresponds to the 140 MHz spacing of the pulsed cavity modes. Temporal traces of the laser system operating single, and dual-mode are presented in Figures 9a and b. The temporal width dictates the minimum spectral width given by the transform limit of the temporal profile, but does not necessarily dictate the actual spectral profile of the laser. The time-averaged spectral width and purity of the pulsed laser output was assessed with a confocal 2 GHz free spectral range etalon, with finesse 100. By fixing the etalon spacing and slowly scanning the laser (10 MHz/second), a spectral linewidth of 28 MHz (FWHM) was measured as given by Figure 10a. This represents a time averaged lineshape of the pulsed linewidth convolved with the 20 MHz resolution of the etalon. Deconvolved, the laser spectral linewidth is close to the 19.5 MHz transform limit of the 22.5 ns fwhm pulse. As indicated by the long temporal pulse, the laser is running relatively low power, emitting 20mJ/pulse. Similar scans were also collected for the Ti: Sapphire laser locked to dual-mode output, Figure 10b. Higher pump powers produced shorter output pulses with broader spectral width (40MHz). The still narrow laser linewidth allows for discrimination between the two closely spaced peaks of the etalon trace. The adjacent

peaks reflect different pulsed cavity modes and are separated by 140 MHz, in agreement with the fringe spacing in the temporal trace (Figure 9b). Note that the lock point of the cavity-locking mechanism was altered mid-scan, which changes the relative strength of the two cavity modes.

To evaluate the tuning capabilities of the pulsed system, the near infra-red output

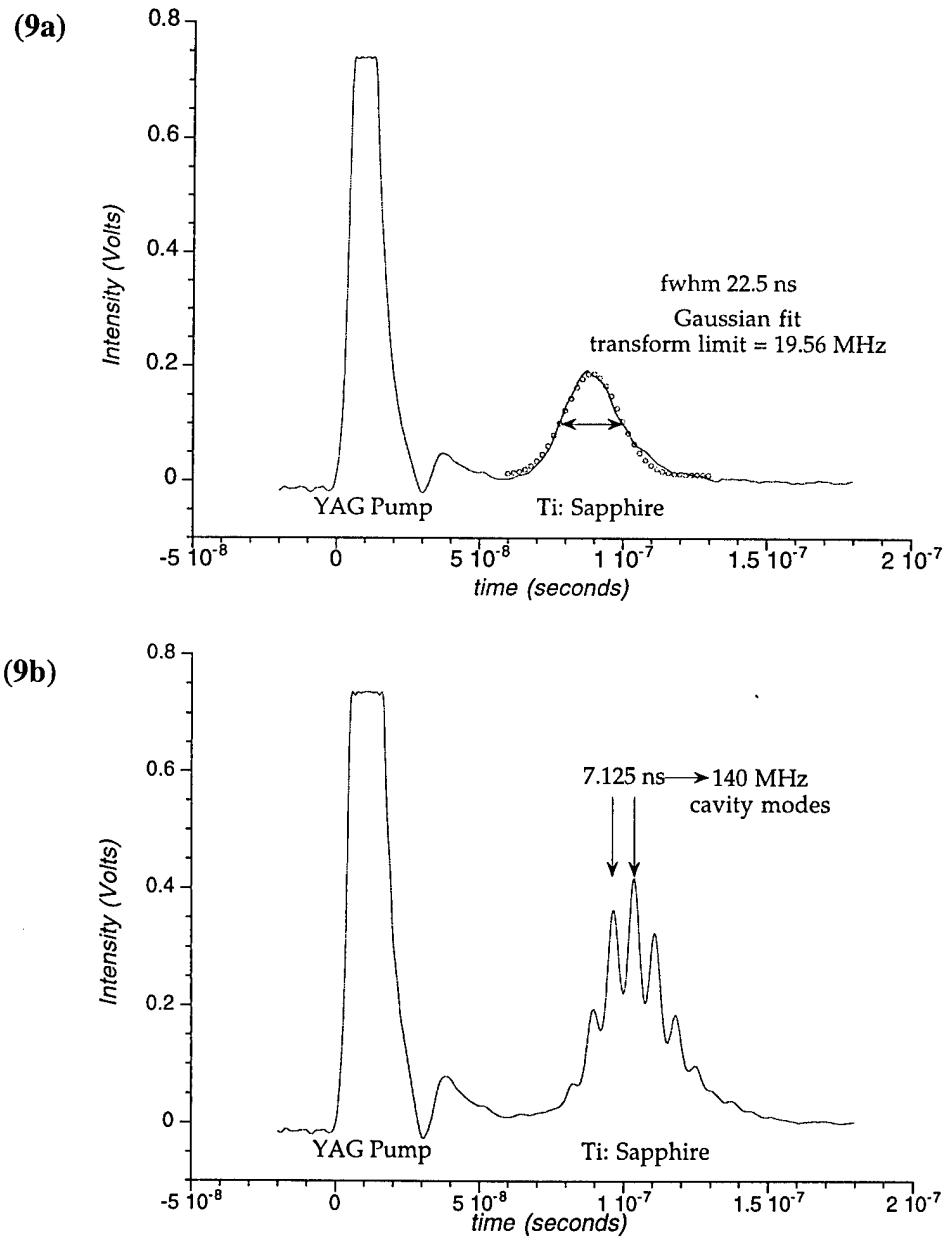

Figures 9a and 9b: Temporal output of Ti: sapphire laser. Above (9a), single longitudinal mode output and Gaussian fit. Below (9b), dual-mode output and temporal beating reflecting cavity mode spacing.

(10a)

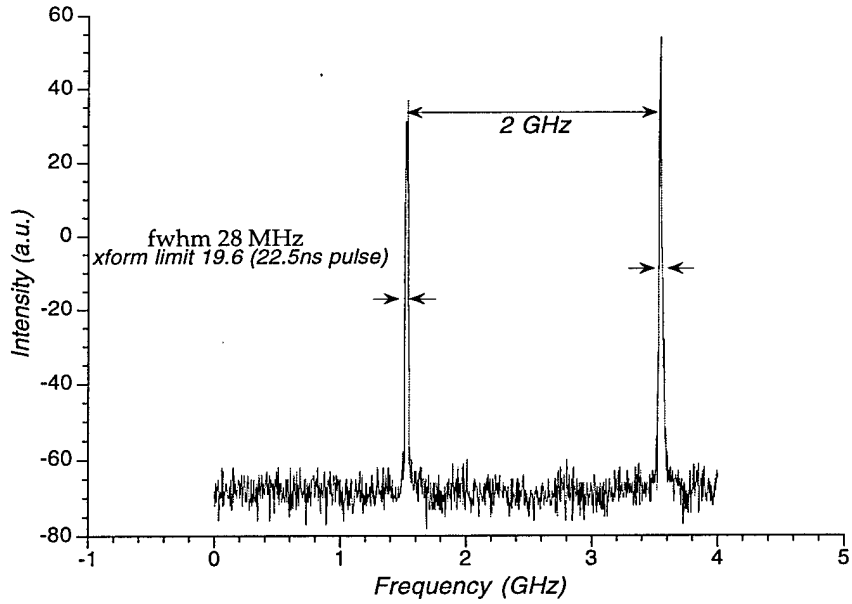

(10b)

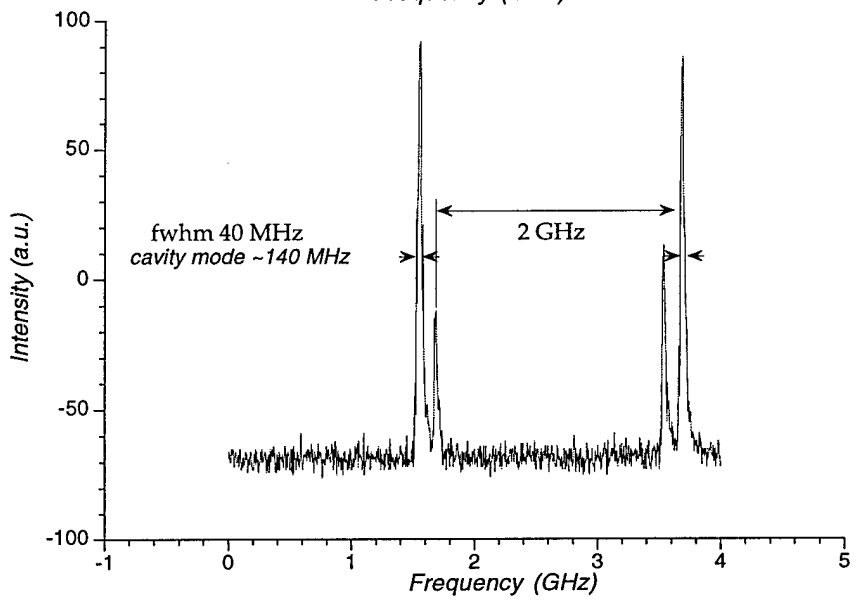

Figures 10a and 10b: Spectral profile of Ti: sapphire laser. Above (10a) time averaged single longitudinal mode output. Below (10b) time averaged dual longitudinal mode operation (n.b. mid-scan the relative weights of the two cavity modes are altered).

of the Ti: Sapphire was frequency tripled to interrogate the mercury ^3P-^1S transition at 253.7 nm. Frequency tripling efficiency and mercury vapor spectroscopy are discussed in subsequent sections. However, shown in Figure 11 is a pulsed measurement of the

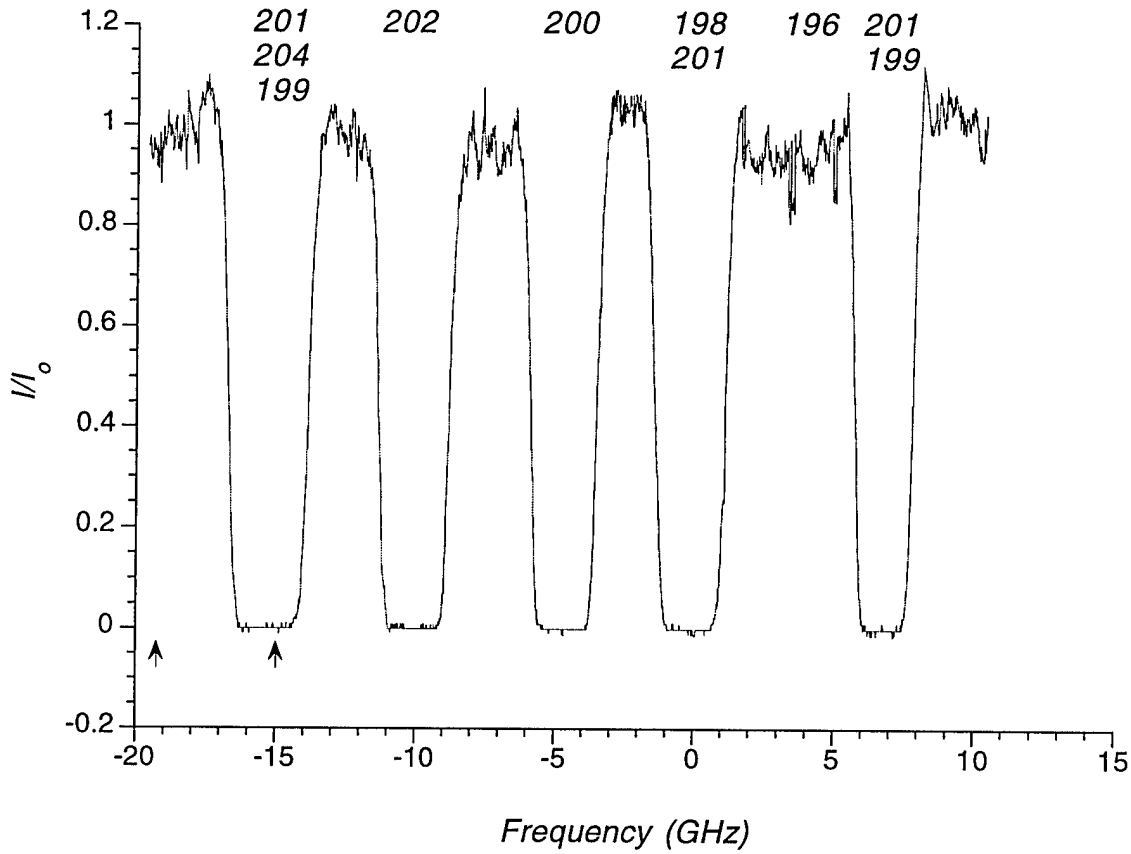

Figure 11: Spectral transmission profile of the mercury 6^3P_1-6^1S_0 transition at 253.7nm as interrogated by the frequency tripled Ti: sapphire laser operating single longitudinal mode. Natural isotopes are listed above the absorption bands.

transmission through a 5 cm path of mercury vapor at 1.5 mTorr. Clearly defined are the individual absorption lines of differing isotopes listed at the top of the figure. While a more detailed discussion of mercury vapor spectroscopy is given in chapter 3, a good agreement between the experimental scans made with the pulsed laser and the cw source highlight both the narrow linewidth and tuning control of the high power, pulsed system. Continuous scan rates are limited by the cw seed source, varying from a few MHz/ sec (limited by cavity thermal drift), to hundreds of MHz/sec (limited by computer control).

In order to examine the frequency agility of the Ramp and Lock scheme, the

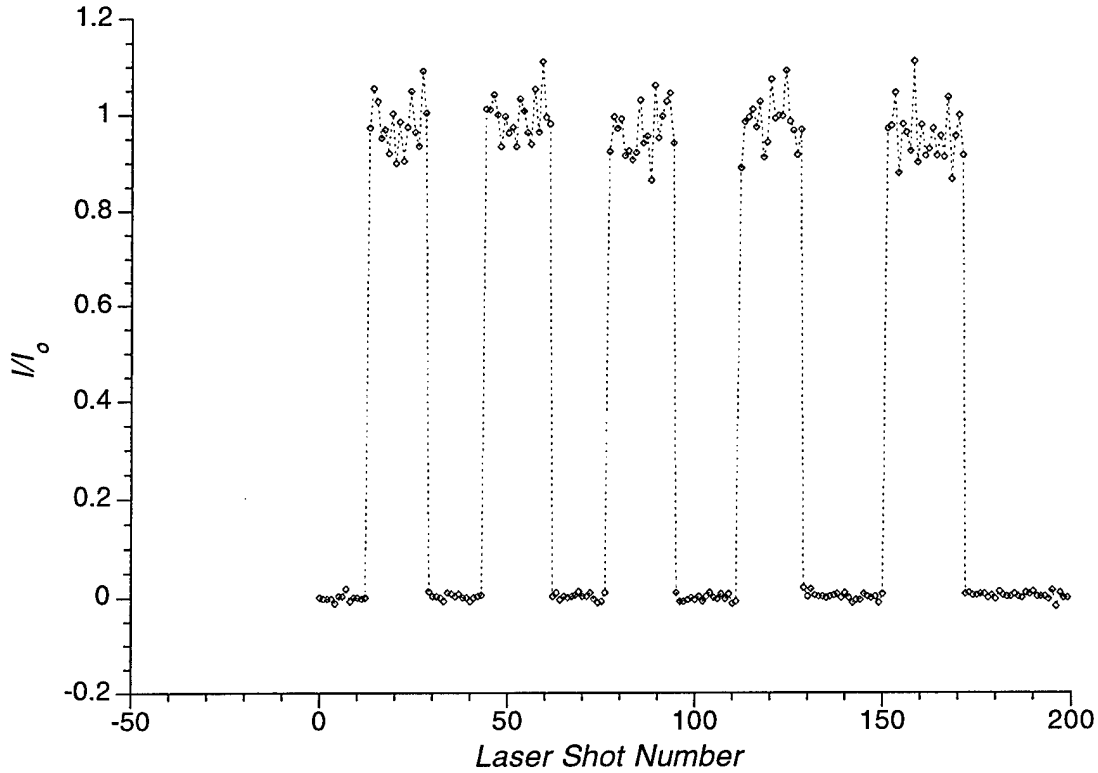

Figure 12: Frequency agility of Ti: sapphire laser system. Plot of intensity of laser scatter seen through the mercury vapor filter as function of laser shot. Between laser shots (after approximately 20), the laser is toggled into and out of the absorption band (shown spectrally as two arrows on Figure 11).

frequency of the cw seed source was toggled between two different spectral locations corresponding to the absorption-band and pass-band of the Hg cell. Approximately every twenty shots of the pulsed system, discontinuous 1.68 GHz jumps of the seed source (corresponding to 12 cavity modes) were induced by altering the intracavity etalon. The frequency tripled output of the system jumped 5.04 GHz. The absolute positions of the two ultraviolet light frequencies are denoted by the arrows on the bottom left of Figure 11. One arrow (at -15 GHz) is inside an absorption band of mercury, while the other arrow (at -20 GHz) is outside. A plot of signal versus laser shot is given in Figure 12. While the laser frequency was changed only every twenty shots, the important feature to note is that in all cases the in-band/ out-of-band transition occurs *between* two laser shots. That is, the pulsed

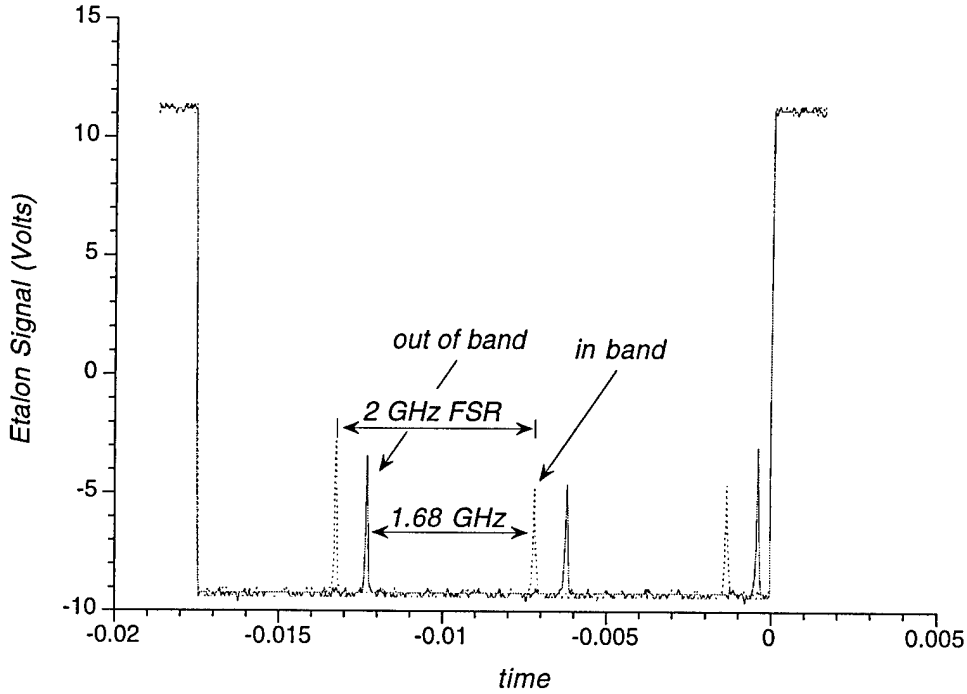

Figure 13: Frequency agility of Ti: sapphire laser system. Spectral location of seed laser (cw in the infra-red), as monitored by a scanning interferometer. Discontinuous jumps of 1.7 GHz in the infrared, or 5.1GHz in the UV are achieved on a shot-by-shot basis of the pulsed laser.

laser cavity tracked the cw seed between pulses and remained locked. Single-mode operation was verified by observing the temporal envelope of the pulsed laser. Simultaneously, the cw seed frequency was monitored on a 2 GHz free spectral range scanning interferometer. The relative spectral locations of the cw seed input are shown in Figure 13.

Third harmonic generation

A comprehensive examination of harmonic generation in Ti: sapphire guided the decision to obtain 250 nm tunable light via frequency tripling with β-Ba_2BO_4 (BBO).[Rines (1995)] This study details the characteristics of BBO versus KH_2PO_4 (KDP) and LiB_3O_5 (LBO) for our application. In summary, for optimal efficiency in second

harmonic generation both KDP and LBO require long crystal lengths (on the order of 30mm). For both type I and type II doubling, KDP was less efficient than BBO in the Ti: sapphire tuning range, a 25mm long type II KDP yielding 25% conversion versus 41% conversion of a 6mm BBO(I) at 911nm. Further, optimized KDP crystals have a narrow temperature acceptance (2 C), and require large input aperture (12 mm) to cover the Ti: sapphire tuning range. LBO is attractive because of a high surface damage threshold, and the material is not hygroscopic. However, limited size of high quality LBO prevents a thorough investigation of its promise for Ti: sapphire harmonic generation. It is anticipated LBO(I) may exceed the 60% conversion of BBO(I) doubling.

By type II mixing in the third harmonic generation (THG) stage, we take advantage of the orthogonal polarization of the fundamental and doubled output from the initial BBO type I doubling. A type I THG would require a waveplate rotator to align the polarizations of the fundamental and second harmonic inputs to the mixer. Furthermore, spectral tuning is significantly complicated with the addition of a chromatic rotation stage. Due to its simplicity and relatively high conversion efficiency, we have optimized third harmonic generation using type I doubling in BBO, followed by type II mixing in BBO. Figure 14 gives the conversion efficiency for doubling and tripling stages, in both the seeded and unseeded cases. The benefits of seeding are clearly evident. Seeding improves the spatial mode quality and reduces the bandwidth, both of which enhance the harmonic generation. A lower saturated efficiency in the unseeded case is observed because the broad spectral linewidth exceeds the spectral acceptance of 0.5 nm. Further, greater dephasing in the BBO results from the larger diameter and greater divergence of the input beam. In the seeded case, the second harmonic generation is near the optimum of 67% internal conversion by

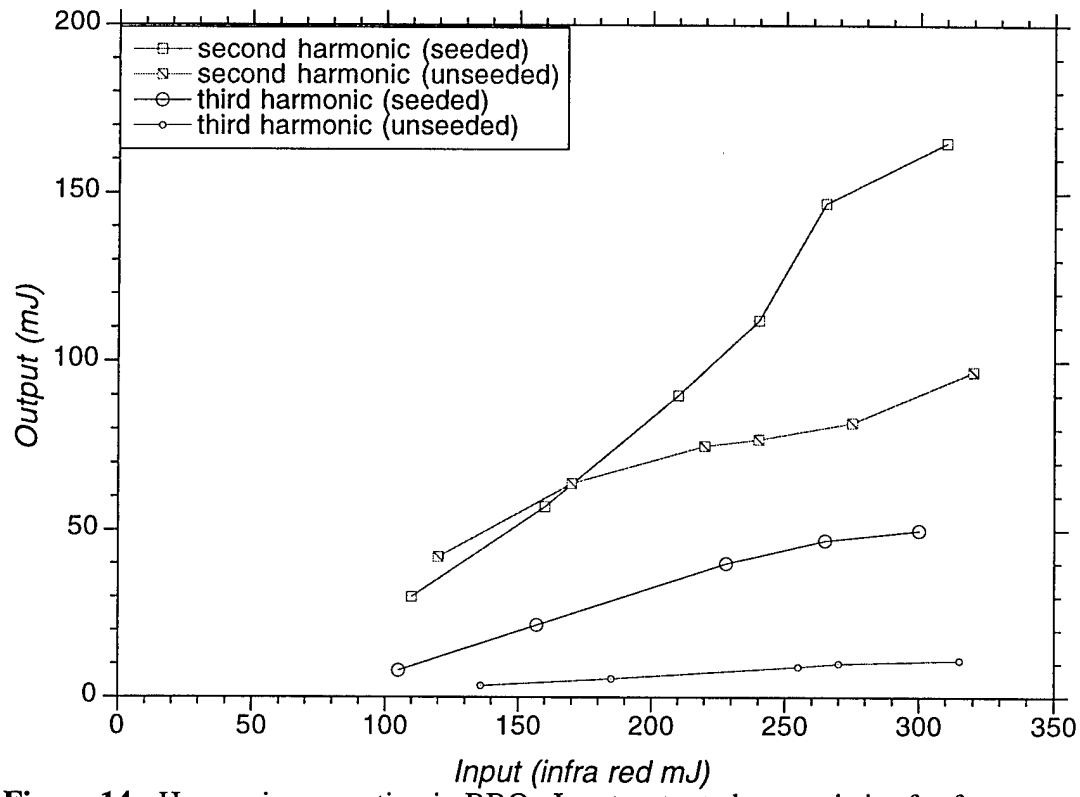

Figure 14: Harmonic generation in BBO. Input-output characteristics for frequency doubling and tripling (type I and II, respectively) of infrared light. Effects of seeding are evident in the higher conversion efficiencies achieved.

power, or 50% conversion by photon. The conversion from the second to third harmonic is lower, and results in a net conversion to third harmonic of 14 to 18%, external conversion by power. That is the 18% conversion does *not* account of surface reflections at the 4 surface interfaces or loss at the dispersive element surface. A rough estimate of the reflection loss yields a conversion efficiency in excess of 20%.

The lower than anticipated frequency conversion is suspected to be due to lack of spatial and temporal overlap of the fundamental and second harmonic beams. Because the infrared beam is close to Gaussian spatially and temporally, the intensity is dramatically higher at temporal and spatial line center than in the wings. Highly efficient second harmonic conversion produces 2ω output that is narrower spatially and temporally than the

fundamental. The residual fundamental that is left to mix with the 2ω light is no longer spatially or temporally overlapped with the up-converted beam. Poor overlap of the two beams leads to poor third harmonic conversion. Experimentally, the highest 3ω conversion efficiencies occur when the second harmonic is detuned from optimal performance. Such behavior is consistent with the theory of spatial and temporal mismatch. Ideally, the fundamental input beam would appear as a top hat spatially and temporally. Equivalent conversion at all spatial and temporal locations would produce 2ω and residual beams that were well overlapped. However, given the near TEM_{00} output of the fundamental, two other approaches warrant exploration. To improve the spatial overlap of the second harmonic with the fundamental, either beam shaping optics or two non-optimized second harmonic crystals could be employed. In the first case, beam shaping optics using dichroics and focusing lenses would allow for the residual fundamental to be re-shaped to produce better spatial overlap. Such an approach requires several additional optical components to separate, shape and recombine the two beams. Alternatively, it may be possible to place an additional second harmonic crystal before the mixing stage. For appropriately matched crystal lengths, back conversion from 2ω to fundamental would occur in the high intensity center of the beam. Simultaneously, in the wings, longer crystal lengths would yield greater conversion. The resultant beam would appear flattened in spatial profile, closer to the optimal top-hat. The additional effect of opposing the orientation of the crystal axes would allow for longer conversion lengths without walk-off of the power from the propagation vector.

As observed, the increase ultraviolet generation with input intensity promotes high intensity beams. A fundamental trade-off exists between conversion efficiency and crystal

damage. It is the nature of BBO that the highly efficient conversion region is proximate to the damage threshold. BBO damage threshold is currently being detailed, but estimates place it at 200 MW/cm^2 for nanosecond pulses at 266 nm.[Catella] Further, anti-reflection coatings which simultaneously minimize reflections at multiple wavelength (ω,2ω,3ω) and sustain high power beams are in development stages. The state-of-the-art hybrid sol-gel coatings of Cleveland Crystals combine the standard hard dielectric AR coating under a high damage threshold gel coating of silicon-dioxide micro-spheres.[Catella] The sol-gel sustains higher power than standard coatings, and gives good index-matching characteristics with quartz and BBO in the ultraviolet. Finally, a limiting factor in harmonic conversion in the ultraviolet appears to be a non-linear, intensity and wavelength dependent broadband bulk absorption by BBO. Estimates place this absorption as high as 25%/cm in BBO at 266nm for intensities of 50 MW/cm^2.[Catella]

References

Bair, C.H., Brockman, P., Hess, R.V., and Modlin, E.A., "Demonstration of frequency control and cw diode laser injection control of a titanium-doped sapphire ring laser with no internal optical elements," IEEE Journal of Quantum Electronics, **24**(6), 1045, (1988).

Barnes, J.C., Barnes, N.P., Wang, L.G., and Edwards, W., "Injection Seeding II: Ti: Al_2O_3 Experiments," *IEEE Journal of Quantum Electronics*,**29**(10), 2684,(1993).

Bjorkland, G.C., *Optics Letters*, **5**,15, (1980).

Boyd, T.L. and Kimble, H.J., "Frequency stabilization of a continuous -wave Ti: sapphire laser," *Optics Letters*, **16**(11), 808, (1991).

Brockman, P., Bair, C.H., Barnes, J.C., Hess, R.V., and Browell, E.V., "Pulsed injection control of a titanium-doped sapphire laser," *Optics Letters*, **11**(11), 712, (1986).

Brown, A.J.W., Fisher, C.H., and Kangas, K., "Efficient, high-energy, narrow-band, blue-light source," *Optics Letters*, **18**(14), 1177, (1993).

Bruce, D.M., and Cassidy, D.T., "Detection of oxygen using short external cavity GaAs semiconductor diode lasers," *Applied Optics*, **29**(9), 1327-1332, (1990).

Catella, G., Cleveland Crystals, Cleveland, OH, personal communication, (1997).

Farrow, R. Sandia National Labs, Combustion Research Facility, Livermore, CA, private communication, (1997).

Finch, A., Schwartz Electro-Optics, Inc., Bedford, MA, private communication, (1997).

Forkey, J.N., "Development and Demonstration of Filtered Rayleigh Scattering - A laser based Flow Diagnostic for Planar Measurement of Velocity, Temperature and Pressure," doctoral thesis #2067-T, Princeton University, Princeton NJ (1996).

Fry,E.S. Q. Hu, and X. Li, *Applied Optics*, "Single frequency operation of an injection -seeded Nd; YAG laser in high noise and vibration environments," **30**(9), 1015, (1991).

Gambogi, J.E., "Eigenstate resolved spectroscopic studies of intramolecular vibrational redistribution using single and double resonance methods," doctoral thesis, Princeton University, Princeton NJ (1995).

Grinstead, J.H., Finkelstein, N.D., and Lempert, W.R., "Frequency Locked Light Scattering: real-time Doppler velocimetry with closed-loop feedback control," *Applied Optics*, in press (1997).

Hamilton, C.E., "Single Frequency, injection seeded Ti: sapphire ring laser with high temporal precision," *Optics Letters*, **7**(10), 728, (1992).

Hamilton, C.E. Kangas, Muller, Lowenthal, and Raymond, "Fully stabilized single frequency Ti: Al_2O_3 laser oscillator," SPIE Solid State Lasers, Volume 1223, 208, (1990).

Henderson, S.W., Yuen, E.H., and Fry, E.S., *Optics Letters*, **11**(11),715, (1986).

Kangas, Lowenthal, and Muller, "Single-longitudinal mode, tunable pulsed Ti: sapphire laser oscillator," *Optics Letters*, **14**(1), 21, (1989).

Kroll, M., McClintock, J.A., and Ollinger, O., "Measurement of gaseous oxygen using diode laser spectroscopy," *Applied Physics Letters*, **51**(18), 1465, (1987).

Littman, M.G., *Applied Optics,* **23**, 4465 (1984).

Littman, M.G., and Metcalf, H, *Applied Optics*, **17**, 2224, (1978).

Moulton, P.F., 12th International Quantum Electronics Conference, Munich (June 1982).

Park, Y.K., Guiliani, G. and Byer, R.L. *Optics Letters*, **5**(3), 96, (1980)

Park, Y.K., Guiliani, G. and Byer, R.L., "Single Axial Mode Operation of a Q-Switch Nd: YAG Oscillator by Injection Seeding," *IEEE Journal of Quantum Electronics*, **QE-20**(2), 117, (1984).

Rahn, L.A., *Applied Optics*, **24**(7), 940, (1985)

Rapoport, W.R., and Khattak, C.P, "Titanium sapphire laser characteristics," *Applied Optics*, **27**(13), 2677, (1988).

Raymond, T.D., and Smith, A.V., *Optics Letters*, **16**(1), 33, (1991).

Rines, G.A. and Moulton, P. F., "Performance of Gain Switched Ti: Al_2O_3 Unstable Resonators Lasers," *Optics Letters*, **15**(8), 434, (1990).

Rines, G.A. and Moulton, P. F., "Performance of Gain Switched Ti: Al2O3 Unstable Res-

onators Lasers," OSA Proceedings on Advanced Solid-State Lasers, Volume 6, Salt Lake City, UT, 88 (1990).

Rines, G.A., Zenzie, H.H., Schwarz, R.A., Isyanova, Y. and Moulton, P.F. "Nonlinear Conversion of Ti: Sapphire Laser Wavelengths," *IEEE Journal of Selected Topics in Quantum Electronics*, **1**(1),50-57, (1995).

Rines, G.A., I.R. Sources, Brookline, NH, personal communication, (1997).

Rosasco, G.J. Bowers, W.J, and Hurst, W.S. private communication. Nation Institute of Standards and Technology, Process Measurements Division, Gaithersburg, MD(1994).

Sasada, T., T. Tsukamoto, Y.Kuba, N. Tanaka, and K. Uehara, "Ti: sapphire laser spectrometer for Doppler-limited molecular spectroscopy," *Journal of the Optical Society of America B*, **11**(1), 191, (1994).

Schwarz, R.A., Schwartz Electro-Optics, Inc. Research Division, Concord, MA, personal communication, (1997).

Schwartz Electro Optics, Inc., "Notes on Galvo Mounted Etalon and Tilt-Plates," Technical Notes, Schwartz Electro-Optics, Research Division, Concord, MA (1993).

Teets, R.E., "Feedback to Maintain, Injection Locking of Nd: YAG lasers," *IEEE Journal of Quantum Electronics*, **QE20**(4), 326, (1984).

Vassen, W., C. Zimmermann, R. Kallenbach, and T.W. Hänsch, "A frequency-stabilized titanium sapphire laser for high resolution spectroscopy," *Optics Communications*, **76**(5,6), 435, (1990).

Wall, K.F., Aggarwal, R.L, Sciacca, M.D., Zeiger, H.J., Fahey, R.E., and Strauss, A.J., "Optically induced nonresonant changes in the refractive index of Ti: Al_2O_3," *Optics Letters*, **14**(3), 181, (1988).

Chapter 3: Mercury

Atomic mercury has long been used for both producing and filtering light. Mercury discharge lamps provide a light source emitting from the orange (577nm), green (546 nm), blue (435 nm, 365 nm) to the ultraviolet (254 nm).[Herzberg, pg 6] Similarly, the absorption characteristics of mercury vapor have been utilized to provide spectral filtering since the early part of this century.[Rasetti] This research focuses on mercury vapor as medium for spectrally filtering light scattering. Differing properties of mercury vapor are used to create three types of spectral filter: a notch absorption filter, a narrow passband transmission filter, and a refraction filter. Each of the filters is fully described in ensuing chapters which detail the utility of the filters for various diagnostic applications. While distinct in their properties and features, each of these filtering technologies relies upon the same electronic transition. To appropriately understand and model the filters, it is necessary to fully characterize the 6^3P_1-6^1S_0 transition of Hg at 253.7 nm.

An energy level diagram of the lower lying mercury states is shown in Figure 1. The ground state $^3P_1$-$^1S_0$ transition is strong (oscillator strength, f, of 0.024), despite its being classically spin-forbidden. The $\Delta S=0$ selection rule holds rigorously for light atoms, where Russell Saunders (L-S) coupling is observed. However, the larger the atomic number, the larger the multiplet splitting, and the stronger the intercombinational transitions.[Herzberg, pg. 155] While considered strong, the intercombinational $^3P_1$-$^1S_0$ transition is about fifty times weaker than the 'allowed' singlet-singlet $^1P_1$-$^1S_0$ transition.[Kuhn, Radzig] This behavior does not hold true for the emission spectrum of

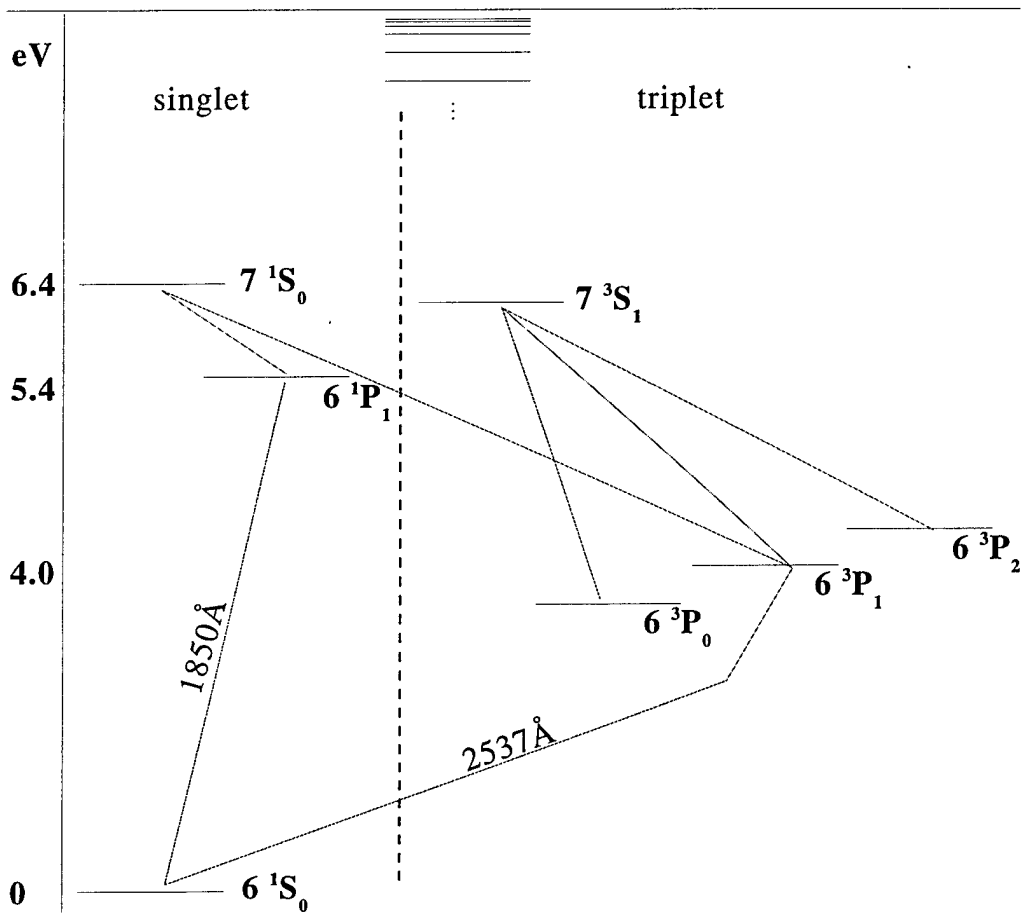

Figure 1: Energy level diagram for mercury. The ^3P-^1S ground state transition at 2537 Å is the transition explored in this thesis. The triplet - singlet selection rule does not apply.

pen-lamps and plasmas, however. Often, it is the *emission* spectrum of the 253.7 nm line that is reported as the dominant line (15 times that of the 185nm counterpart).[Reader] Finally, it is worthy of note that the selection rule $\Delta J = 0,\pm 1$ (J=0 does not couple to J=0) is observed.

Mercury exists in seven naturally occurring isotopes, each of which has a slightly different ground state energy transition. Table 3.1 gives a list of each of the isotopes and their relative energy ground state shift, as observed by Bitter. [Bitter]. While the radioactive isotopes Hg 197 and Hg 197* are included for completeness, they are not studied in this work.

Isotope	Hyperfine Level	Nat. Isotopic Abundance	Resonance Frequency (GHz)
196	—	.0016	4.107
197	$^{3}/_{2}$	—	10.4
197	$^{1}/_{2}$	—	-12.7
197*	$^{15}/_{2}$	—	-13.1
197*	$^{13}/_{2}$	—	5.13
197*	$^{11}/_{2}$	—	19.4
198	—	.1002	0
199	$^{3}/_{2}$	.1684	6.728
199	$^{1}/_{2}$	.1684	-15.409
200	—	.2313	-4.805
201	$^{5}/_{2}$	.1322	-14.662
201	$^{3}/_{2}$	.1322	-0.676
201	$^{1}/_{2}$	.1322	6.872
202	—	.2980	-10.106
204	—	.0685	-15.313

Table 3.1: Mercury isotopes. Hyperfine levels, naturally occurring abundance, and energy shift.

In addition to isotopic energy shifts, hyperfine splitting shifts the energy levels of the odd isotopes. The even isotopes have a net nuclear spin of zero, and hence, exhibit no hyperfine splitting. The odd isotopes 199, 201 have a nuclear spin, I, of 1/2 and 3/2

respectively. Hence, hyperfine levels, F = I + J, are observed and splitting shifts the energy level transitions, as listed in table 3.1. The lifetime of the 6^3P_1 excited state of mercury is 120 ns [Migdalek]. The relatively long lifetime of this excited is important and will be explored later with its role in resonant fluorescence. The oscillator strength *f*, of the $^3P_1$ - $^1S_0$ transition is given by:

$$f = \frac{m_e c}{8\pi^2 e^2} \frac{g_u}{g_l} \lambda^2 A_{21} \qquad \text{III.1}$$

where in cgs, m_e is the mass of an electron, c the speed of light, e the charge of an electron, g_u and g_l the degeneracy of the upper and lower states, λ the wavelength, and A_{21} the Einstein A coefficient ($1/\tau$). Evaluating Equation III.1 yields f=0.024, the same as experimental measurement.[Radzig]

With knowledge of these basic parameters— resonance frequency, mass, oscillator strength and natural lifetime— a model of the absorption lineshape of mercury can be made for a given temperature and pressure. The absorption lineshape is taken to be the Voigt profile, a convolution of Lorentzian and Gaussian components.[Steinfeld, pg 21] The Lorentzian profile, the homogeneous component due to natural lifetime and pressure broadening, is given by:

$$l(\nu) = \frac{1}{\pi} \frac{\frac{\gamma}{2}}{(\nu - \nu_0)^2 + \frac{\gamma^2}{4}} \qquad \text{III.2}$$

where ν_0 is the resonance frequency. γ is the Lorentzian full-width-at-half-maximum (FWHM) linewidth. The Lorentzian linewidth is the sum of natural broadening (due to a finite excited state lifetime) and collisional broadening, experimentally determined (due to

a pressure dependence). The Gaussian, or inhomogeneous component is due to thermal broadening, given by:

$$g(\nu) = \frac{2}{\Delta\nu}\sqrt{\frac{\ln 2}{\pi}}\exp\left[-4\ln 2\left(\frac{\nu-\nu_0}{\Delta\nu}\right)^2\right] \qquad \text{III.3}$$

where ν_0 is the resonance frequency, and $\Delta\nu$ is the fwhm Gaussian linewidth given by:

$$\Delta\nu = \frac{1}{\lambda}\sqrt{\frac{8kT\ln 2}{m}} \qquad \text{III.4}$$

where λ is the resonant wavelength; c is the speed of light; k Boltzmann's constant; T the temperature (K); m the mass (amu). Convolving the Lorentzian and Gaussian components yields the Voigt profile:

$$V(\nu) = \frac{2}{\Delta\nu}\sqrt{\frac{\ln 2}{\pi^3}}\int_{-\infty}^{\infty}\left(\frac{\frac{\gamma}{2}}{y^2+\frac{\gamma^2}{4}}\cdot\exp\left[-4\ln 2\left(\frac{\nu-\nu_0-y}{\Delta\nu}\right)^2\right]\right)dy \qquad \text{III.5}$$

Despite the dominance of the inhomogeneous broadening (the Gaussian linewidth generally exceeded the Lorentzian by 2-6 orders of magnitude), the features of both lineshapes are necessary to adequately predict the behavior of mercury in our various applications. Particularly, the Lorentzian profile dominates far from resonance due to its $1/\nu^2$ behavior versus the exponential decay of the Gaussian.

The absorption co-efficient, $\Gamma(\nu)$, is a measure of the absorption per centimeter.

$$\Gamma_i(\nu) = \frac{\pi e^2}{mc}N_i f_i V(\nu) \qquad \text{III.6}$$

where, in cgs, e is the charge of an electron; m is the electron mass; c is the speed of light; N is the number density; f the oscillator strength; V(ν) the normalized Voigt lineshape

described above. The subscript i is used to denote isotope and hyperfine splitting effects. First, each naturally occurring isotope will exhibit a different absorption co-efficient due to a shift in spectral resonance, and a varying number density (listed in Table 3.1). Second, the subscript is used to modify the oscillator strength, f, to appropriately weight the likelihood of transition to hyperfine levels. For all isotopes the oscillator strength is given by Equation III.1, for the ^3P-^1S transition. For the even isotopes f is equivalent. However, for odd isotopes the likelihood of transition is distributed among the split hyperfine levels according to degeneracy. The degeneracy of the hyperfine levels m_f is 2F + 1. To first approximation, the likelihood of transition to each hyperfine sublevel is equivalent (owing to small shifts in energy levels), and thus the overall oscillator strength may be divided equally among hyperfine sublevels. This results in a statistical weighting for the oscillator strength, such as 2:1 for Hg 199 (F=3/2): Hg 199 (F=1/2).

A computer model predicting $\Gamma_t = \Sigma_i \Gamma_i$ as a function of frequency, temperature, and vapor pressure is listed in Appendix A. Because the Voigt convolution integral (III.5) cannot be solved in closed form, it is necessary to approximate it, or to solve it numerically. The Whiting approximation to the Voigt profile yields a closed form equation well suited for our application.[Whiting]. The residual error from the approximation is of order percent or better, in our typical operating conditions. The first application of this model is to predict the transmission of light of a fixed path length through mercury vapor. The output of the Hg absorption model is a table of ν, $\Gamma(\nu)$, and $T(\nu)$, where $T(\nu)$, the transmission, is given by Beer's Law:[Steinfeld, p19]

$$T(\nu) = \frac{I(\nu)}{I_o} = Exp[-\Gamma_t(\nu)z] \qquad \text{III.7}$$

where $I(\nu)$ is the transmitted intensity; I_0 is the incident intensity; z is the pathlength of the mercury vapor. As discussed below, the model is validated by comparing to known experimental conditions. The model may be further used both as a predictive tool, and as a tool for extracting unknown parameters by fitting to given data sets.

Model predictions

Figures 2a and 2b show model predictions of absorption co-efficient $\Gamma(\nu)$ and transmission, $T(\nu)$, for 3 vapor pressures and temperatures, in a 5 cm path of mercury vapor. The upper plot, 2a, plots a normalized absorption co-efficient as a function of frequency, $\Gamma_{ot}(\nu)$. For Figure 2a only, $V(\nu)$ is scaled only by each isotope's relative population fraction N_i/N, and oscillator strength f_i/f, not overall number density in order to compare lineshape effects. The relative population density, and relative oscillator strength (for odd isotopes) is reflected in the variation in isotope peak absorption. Note that these plots do not differ significantly in the peak of the absorption bands, due to normalization. While the Gaussian and Lorentz widths increase slightly (1.07GHz-1.3 GHz for the dominating Gaussian), the dominant effects are in the number density term (normalized out for these plots), and the behavior in the wings of the absorption profile. At the higher vapor pressure of 2 Torr, the individual lines blend slightly more. Most notably however, the Lorentz component of the absorption profile dominates in the wings, changing noticeably with increased vapor pressure.

The transmission profile, given by Equation III.7, accounts for total number density (varying with vapor pressure), and is plotted in Figure 2b (below). The effect of number density is readily seen by the dramatically changing shape of the transmission profile. At the lowest vapor pressure, 0.002 Torr, five strong and one weak absorption

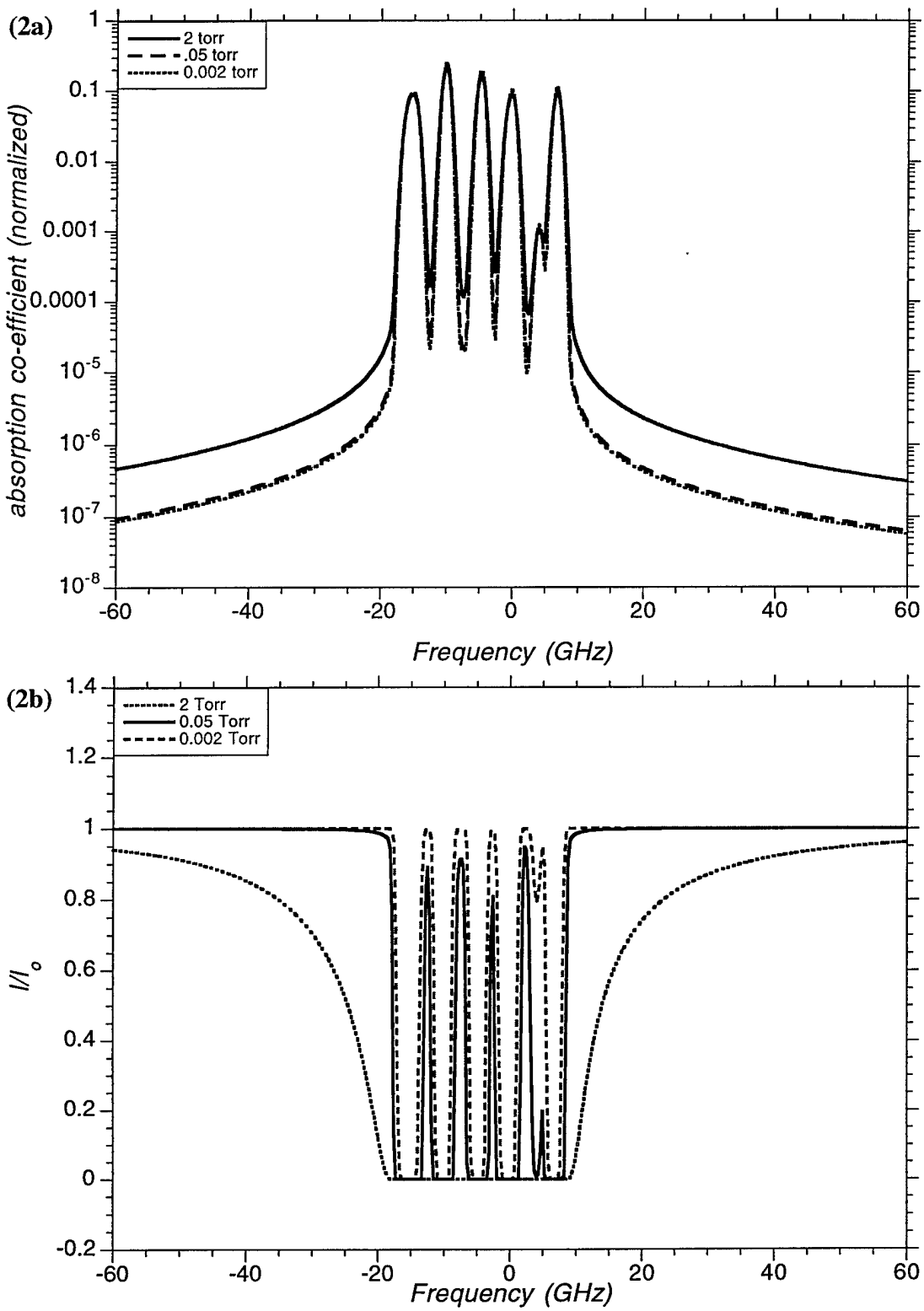

Figures 2a and 2b: Above (2a) plot of mercury absorption co-efficient normalized by number density (note the semi-log scale). Below (2b) transmission profile of light through 5 cm path of mercury vapor.

lines are evident. These different lines arise from the seven different naturally occurring isotopes of mercury listed in Table 3.1 Five of the absorption bands feature sharp walls and flat bases which are characteristic of high optical depth ($\Gamma_t(\nu) * z \gg 1$). The Hg 196 absorption profile is not optically thick because of its low natural abundance of 0.16%. As the vapor pressure increases to 0.05 Torr, the individual absorption bands are no longer fully resolved, and the optical depth has dramatically increased (as evidenced by the Hg 196 line). Even though the absorption co-efficient doesn't broaden significantly (Figure 2a), the width of the absorption band in the transmission profile is observed to increase. As the vapor pressure is further increased to 2 Torr (still only 1/380 of an atmosphere!), the transmission profile changes dramatically. The individual absorption bands of differing isotopes are no longer distinguishable. Further, the bandwidth of this single absorption feature has increased to 38.5 GHz, almost one and a half times the extent of all the absorption bands in the lower vapor pressure plots. The broader absorption band is a result of the Lorentzian 'wings' on the absorption profile. This model demonstrates the non-negligible Lorentzian component of the Voigt profile — a modest 20 MHz Lorentz width, 1.5% of the 1.3 GHz Gaussian full-width-half-max, causes the broad sloping walls of the transmission profile. The Lorentzian contribution dominates in the wings of the very optically thick Voigt profile where its polynomial decay overwhelms the exponential decay of the Gaussian component. The significance for diagnostic measurements is that this represents a fundamental parameter for the use of mercury vapor as an optical filter. As will be discussed in future chapters, the sharpness of the absorption wall will determine the spectral discrimination of the notch filter, the background suppression of the narrow bandpass filter, and the deviation and absorption parameters of the dispersion filter.

Experiment and comparison

To verify the predicted transmission of mercury vapor, a cell 5 cm in length with 5 cm diameter windows and side-arm cold-tip containing the liquid mercury was constructed of quartz (Figure 3). The cell body, excluding the side arm portion, is wrapped in conventional heating tape which controls the body temperature to +/- 1 C. A Haake Fe 2 water bath encloses the side arm and maintains constant temperature to +/- 0.1C. Prior to sealing, a small quantity (approximately 5 gms) of electronic grade mercury was inserted and the cell evacuated. The ambient pressure (an inert gas, argon) inside the cell is estimated to be less than 0.05 Torr. Since the heating tape maintains the cell body at a temperature higher than that of the water bath, the side arm temperature controls the vapor

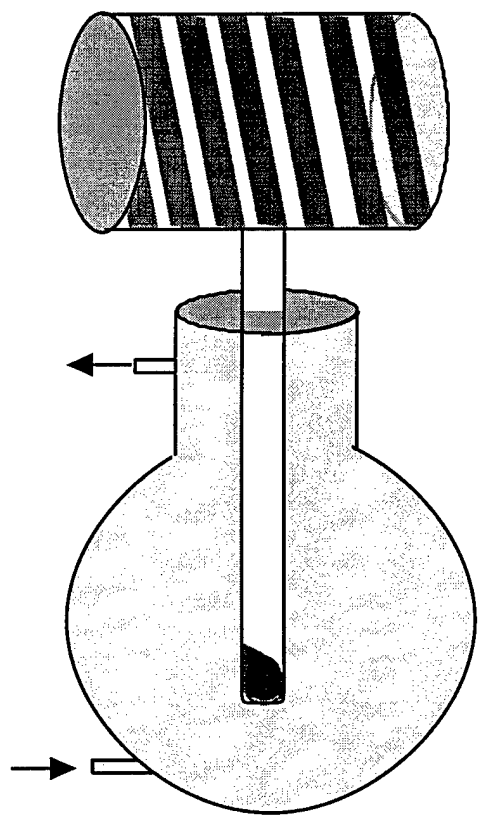

Figures 3: Mercury vapor cell. All quartz construction, the 2" diameter windows seal a 5 cm length cell. A side arm cold-tip sits in a water bath to control the vapor pressure of the cell. Heating tape ensures the mercury does not condense on the windows.

pressure of the mercury. Experiments were run characterizing the mercury cell transmission for side arm temperatures of approximately 25 C, 70 C, and with the water bath replaced by a CO_2 slurry. These corresponds to vapor pressures of 0.002 Torr, 0.05 Torr, and ~ 10^{-5} Torr, respectively.[CRC, D161]

The experimental setup for the absorption experiments is depicted in Figure 4. The tunable output of the cw Ti: sapphire laser, described in Chapter 2, was used. The output of the cw source was frequency tripled by a series of BBO crystals, for type I doubling and type II mixing, similar to the pulsed setup described in Chapter 2. However, due to the low input intensity, a pair of BBO crystals, aligned in a wedged walk-off compensating geometry, were used for the second harmonic generation. The dual crystal arrangement

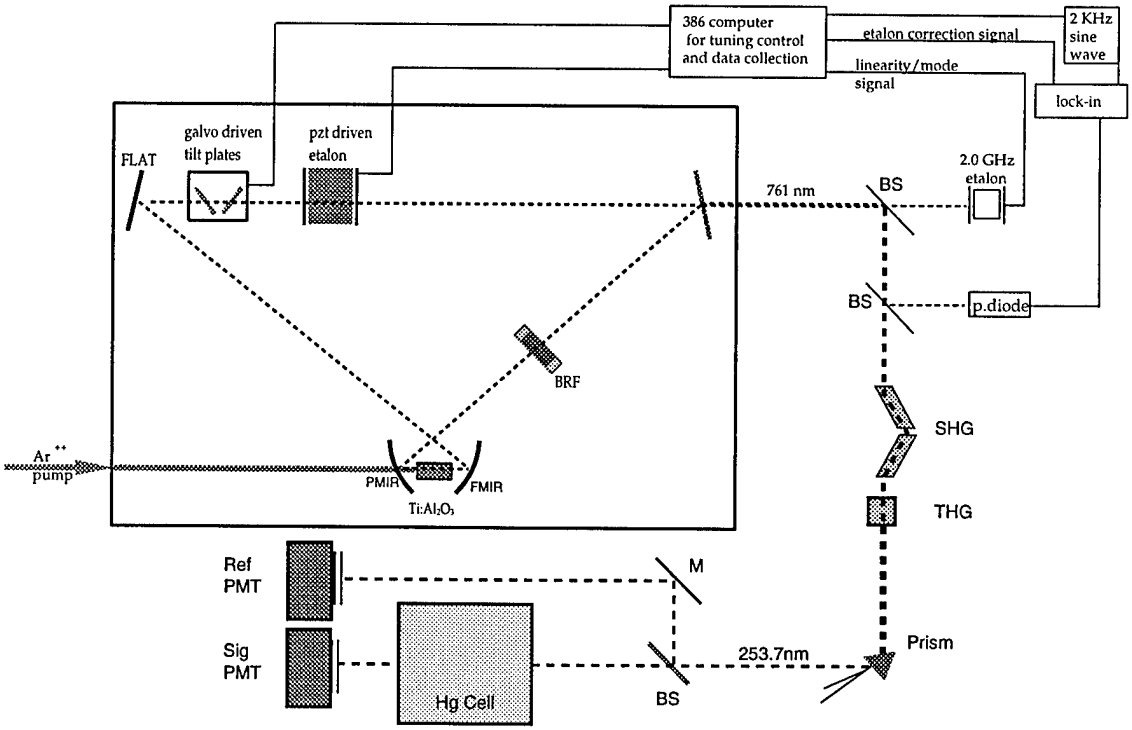

Figures 4: Experimental setup Hg cell transmission profile. The cw Ti: sapphire is frequency tripled via BBO crystals. A pair of photomultiplier tubes monitor intensity of two paths: one through the Hg vapor cell, and the other through reference leg. Data are collected as the cw source is scanned in frequency.

increased the second harmonic conversion by creating a longer effective interaction length, without walk-off of the power (Poyting) and propagation ($\bar{k}$) vectors. Because of the low cw input power (nominally 1 Watt at 761nm) and the non-optimized harmonic generation, minimal amounts (on the order of 10^{-10} Watts) of 253.7 nm light was created. However, these low light levels were still readily detectable for the mercury vapor spectroscopy. As shown, a prism separated the fundamental and second harmonic from the 253.7 nm which was 50:50 split into reference and absorption legs. Twenty nanometer bandwidth thin film interference filters (.25 transmission) were used in combination with solar blind photomultiplier tubes (Hamamatsu R166) to avoid interference from scattered second harmonic light. The signal from the photomultiplier tubes was filtered through a low band-pass RC circuit (time constant of 0.01 seconds), and digitized with the previously described Keithly A/D system. The computer also collected a relative frequency axis, as described in chapter two. A normalization to complete (100%) transmission was made by removing the cell from the transmission beam path.

Figure 5 is a transmission profile of the mercury cell at a vapor pressure of approximately 0.002 Torr. For this experimental scan, the side-arm cold-tip was not actively stabilized but kept at ambient temperature (nominally 25 C). This scan represents a sweep of approximately 30 GHz in the UV, or 10 GHz in the fundamental. Between the discrete absorption bands we see an approximately flat transmission, at about 70% of the signal without the cell present. The 30% loss is due to the four uncoated window surfaces of the cell. Two other experimental scans verify baseline and Lorentzian contributions, see Figures 6 and 7. Transmission measurements at the coldest side-arm temperature, -90 C (10^{-5} Torr or less), verified that the 70% baseline transmission is due to window losses, as

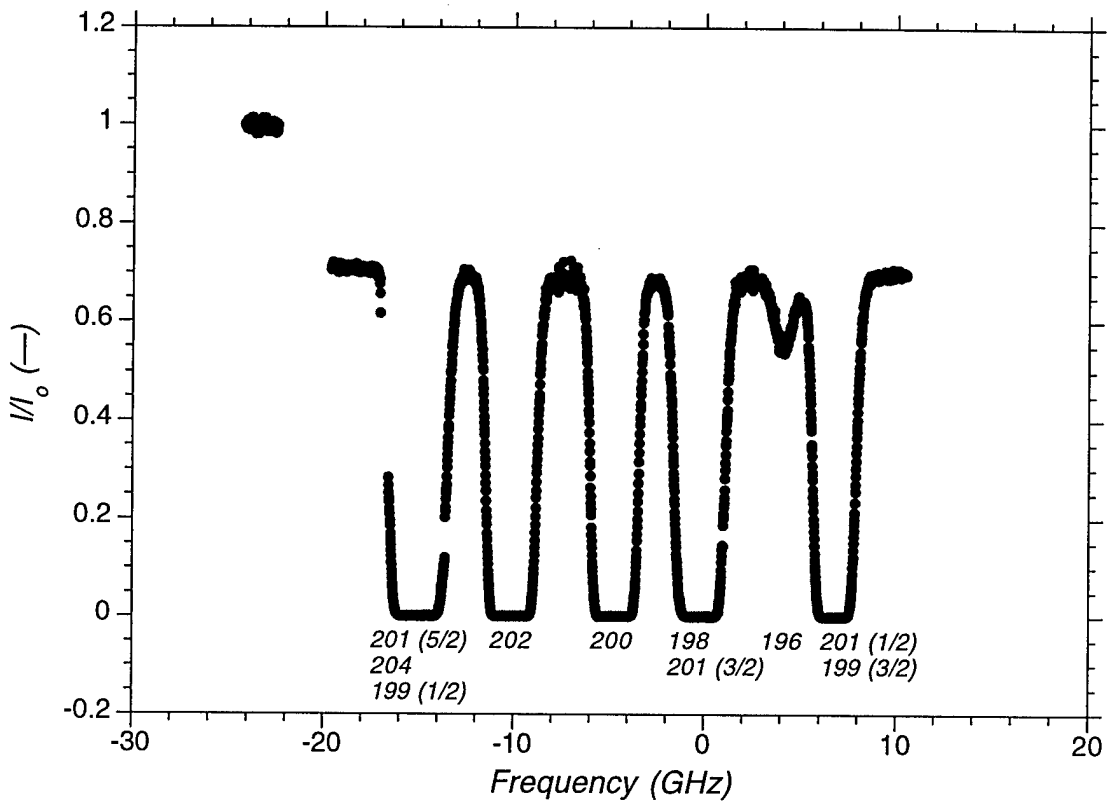

Figures 5: Experimental scans of mercury ground state absorption at 253.7 nm. Transmission of light through a 5 cm cell of mercury vapor (at 0.002 Torr). Individual isotopes are listed below each transition. On the far left, the cell is removed to give a measure of cell transmission out-of-band, for normalization.

opposed to continuum absorption which appears in iodine vapor based cells.[Forkey] A scan at a higher vapor pressure, 0.05 Torr (side arm heated to 70 C) reveals the onset of the Lorentzian wings. The cell temperature was kept at 105 C, corresponding to an inhomogeneous linewidth of 1.19 GHz (fwhm). The low vapor pressure implies the homogeneous broadening still arises from the natural lifetime ~ 1.33 MHz. As can be seen this figure, the width of the absorption band also increases; the once separate absorption lines are no longer fully resolved. The fwhm of an individual absorption line increases from 2.76 GHz at 25 C, to approximately 4.4 GHz at 70 C.

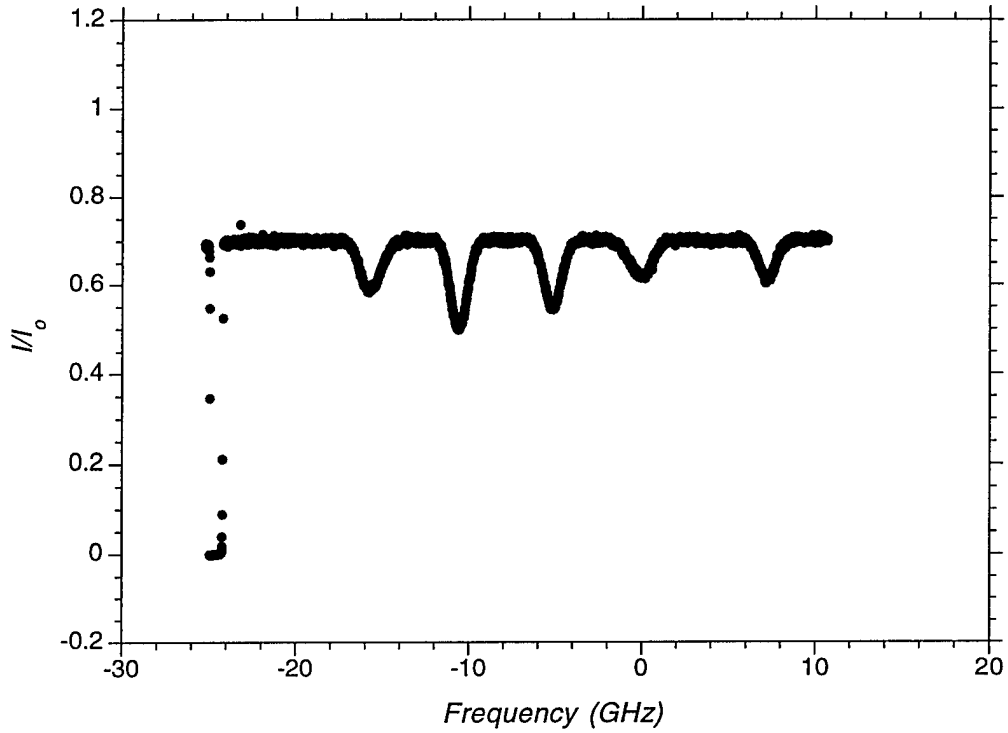

Figures 6: Transmission through 5 cm mercury vapor cell at 10^{-5} Torr.

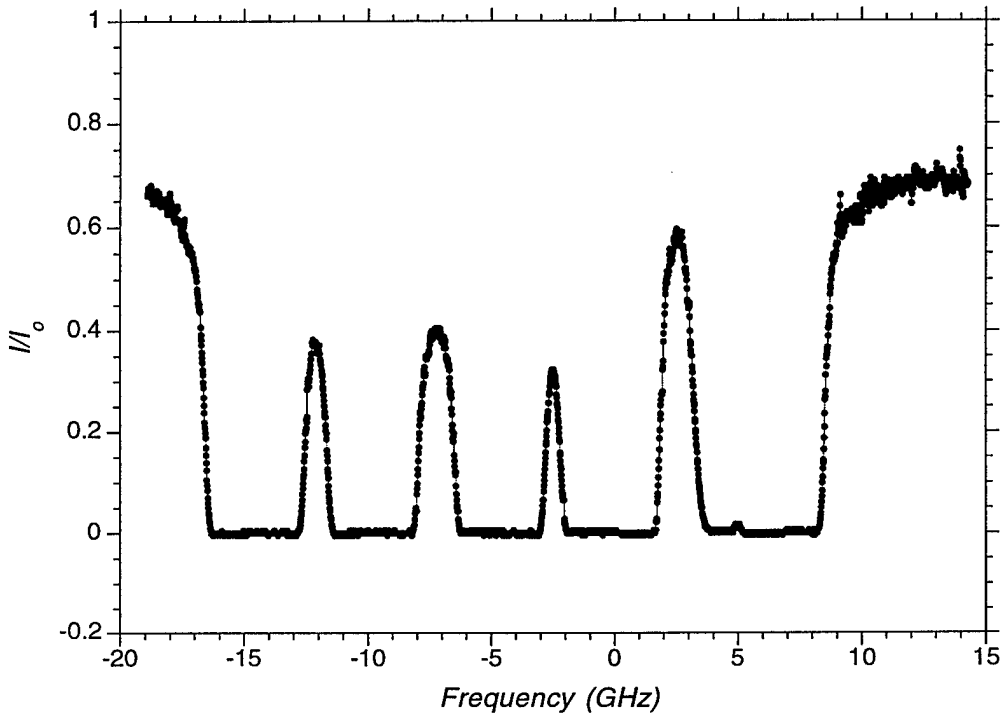

Figures 7: Transmission through 5 cm mercury vapor cell at 0.05 Torr.

To verify the computer model, the experimental data collected above was compared with the modeled profiles. Figure 8 shows a comparison plot of model and experimental data from Figure 5 (0.002 Torr). The experimental data has been rescaled to remove reflection losses, and the frequency axis rescaled to remove anomalies such as mode-hops. The model was run at various vapor pressures (0.0015 - 0.0022 Torr) until the best fit was observed. Best match to the data was observed with the vapor pressure of 0.0020 Torr, or 26° C. Other than the modification in vapor pressure, the model parameters were set independently of the experimental data, giving confidence in the model.

Another test case for the model was experimental data collected from a cell filled with isotopically enhanced mercury. A 1 cm pathlength cell contained in excess of 96%

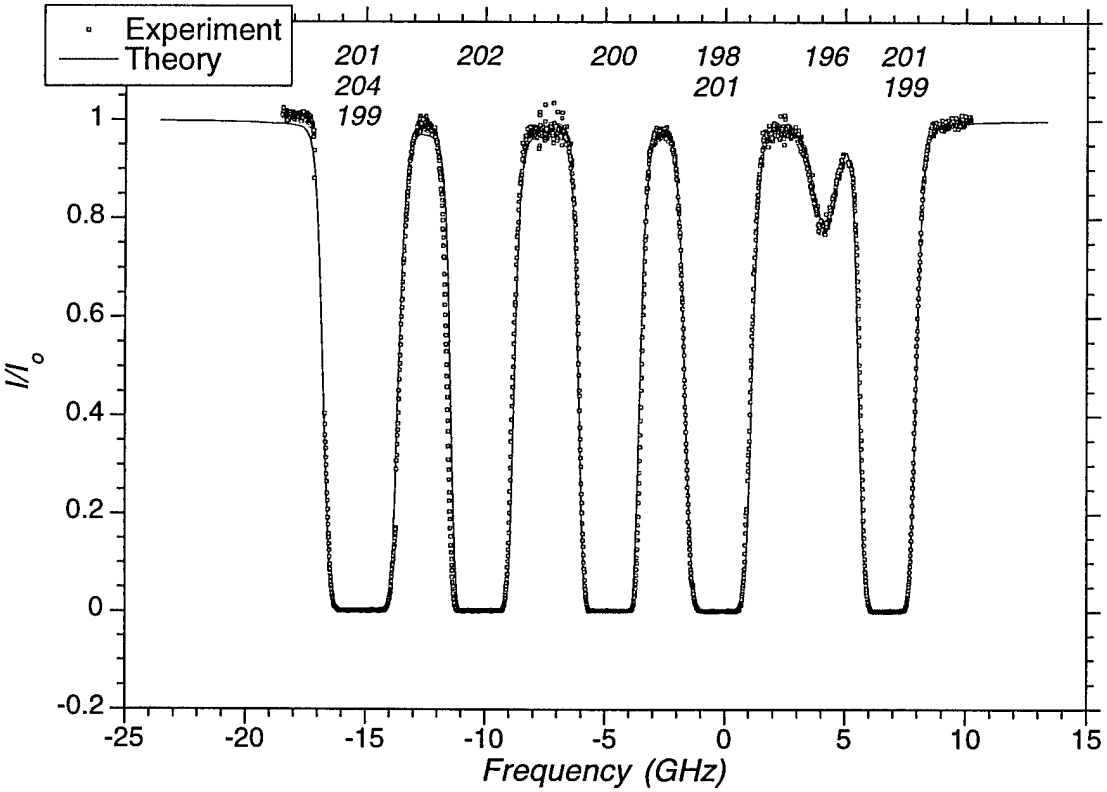

Figures 8: Experiment and Model predictions of transmission through a 5 cm path of mercury vapor at 0.002 Torr.

Hg 202, and percent orders of the rest of the isotopes. In this case the temperature (and hence vapor pressure) was controlled to ±0.5 C by a resistance heater and PI control feedback temperature controller (Omega CN76000). With the exception of the cell, the experimental set-up was identical to the previous experiment. Figure 9 contains a plot of the experimental scan at near room temperature (analogous to Figure 5). The increased optical depth of the Hg 202, and simultaneous decreased optical depth of the other lines are evident. Replacing the appropriate isotopic abundances, and experimental conditions, the model predicts the dashed line in fig 9. While the line location and relative absorption strengths are correct, the lineshape is does not capture the experimental measurements (most notable on the Hg 202 line). A relatively large (50 MHz) Lorentzian component in the mercury absorption recovers the experimental lineshape. However, such homogenous broadening is not physical (see discussion below on mercury self-broadening). By modeling a broader instrument function (laser linewidth), the experimental lineshape is also recovered. The broad instrument function (broader than the quoted 10 MHz fundamental or 17-30MHz frequency tripled) is consistent with a second spatial mode of the laser which was occasionally observed during the scans of the isotopically enhanced mercury. (Note that the an instrument function is not included in the earlier plots of naturally abundant mercury because the laser was well behaved, contributing negligibly to the transmission profile). The model including the instrument function is shown as the solid line and matches the experimental data significantly better. To verify the consistency of the model and the effect of the laser, the same model was used to predict a higher vapor pressure case (0.05 Torr, or 70 C). With and increased Gaussian width (due to temperature), and a constant Lorentz width (due to the instrument function), the model and experimental data are shown in Figure 10.

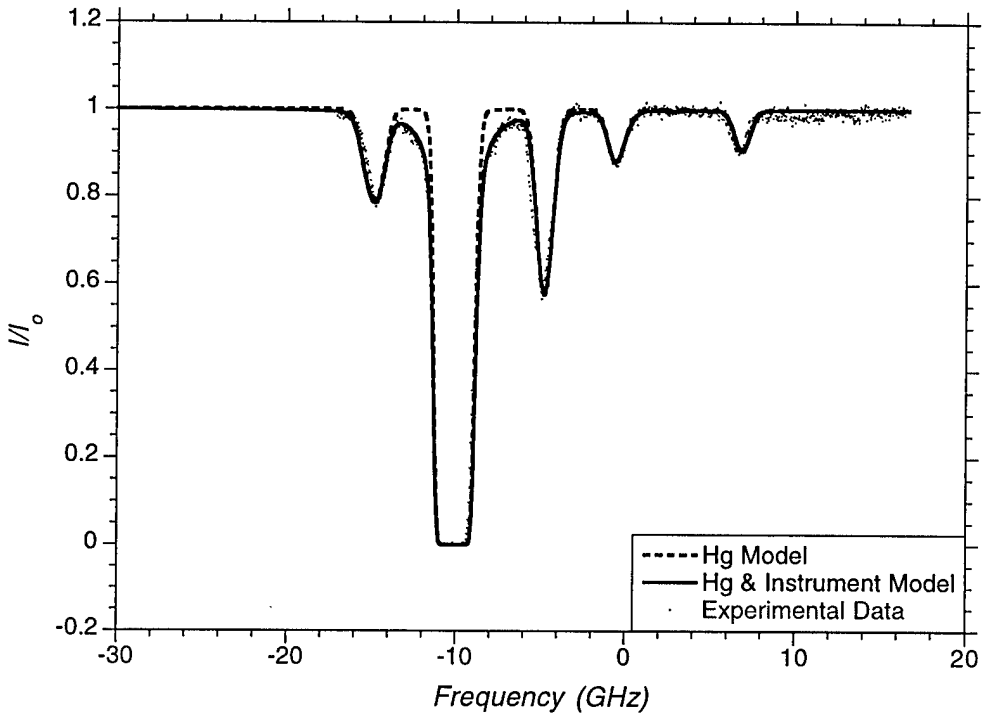

Figures 9: Isotopically enhanced mercury transmission profile (0.002 Torr). Experimental measurements, model, and predictions with instrument function.

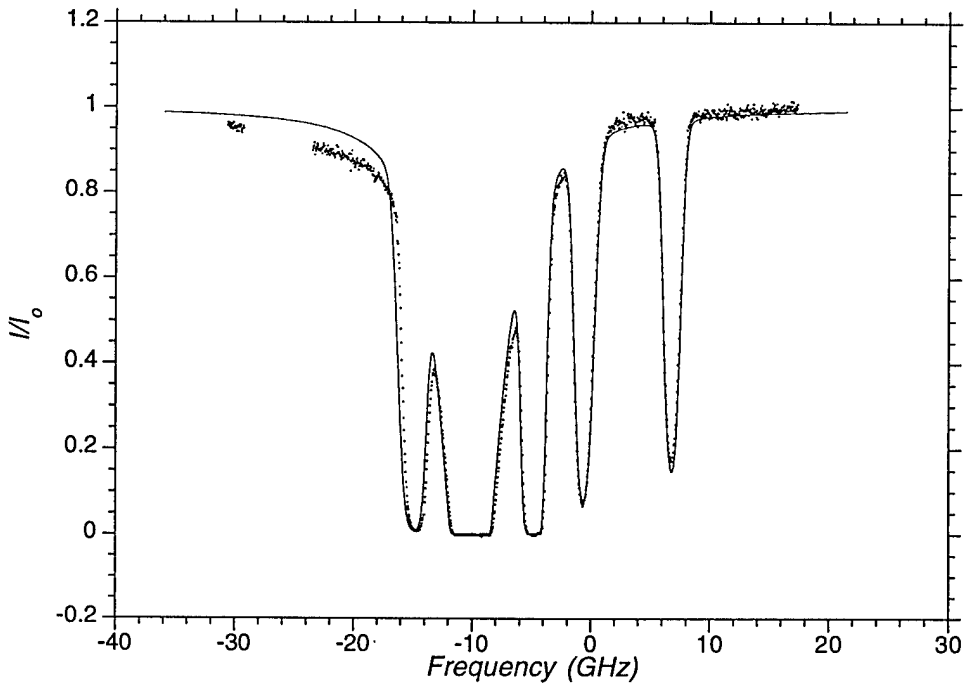

Figures 10: Isotopically enhanced mercury transmission profile (0.049 Torr). Experimental measurements, and model predictions which include instrument function

Fitting data sets & parameter extraction

As described above, often it is necessary or advantageous to fit the model to experimental data, allowing one or more of the model parameters to vary. This simultaneously gives greater confidence in the model, and allows for extraction of difficult or un-measurable model parameters. A fitting routine was developed based on minimizing the figure of merit, χ^2:

$$\chi^2 \equiv \sum_{i=1}^{N} \left(\frac{y_i - y(v_i; a_1, \ldots, a_m)}{\sigma_i} \right)^2 \qquad \text{III.8}$$

which arises from a maximum-likelihood estimation of a data set matching a given model, and assuming a normal distribution of statistical errors, with standard deviation of the data σ_i at each frequency.[Bevington, Press]. y_i is the experimental data point, $y(v_i;a_1, \ldots, a_m)$ is the model at frequency v_i with fit parameters $a_1 .. a_m$. χ^2 gives a weighted average fitting the experimental data to model predictions, with the expectation that $\chi^2 \approx$ N-m (the degrees of freedom) is a good fit, given a good understanding of the experimental deviation.[Bevington pg 69]

Given the figure of merit, a multidimensional minimization routine is desired to produce a best fit model, and give measure of parameter uncertainties. To avoid taking repeated numerical derivatives, a direction-set method minimization scheme is used.[Press, pg 413] Powell's method follows a set of input unit vectors, and minimizes the cost function (χ^2) along a particular direction, and iterates through the parameter space. Subsequently, the directional vectors are re-optimized, and the cost-function again minimized. This procedure is repeated until adequate convergence is achieved. The advantage of this scheme is that it is robust, and requires no directional derivative

information. The order of m^2 storage of this algorithm is not significant, due to the few fit parameters, and relative speed of personal computers. The complete fitting routine (which includes the Hg model) is listed in Appendix B.

In order to determine the uncertainty in a fit parameter, it is necessary to examine how the cost function varies with the change in parameter. From the formal definition of χ^2 it may be derived that an increase in a fit parameter, a_i, by one standard deviation σ_{ai} will increase χ^2 by 1 near its minimum. [Bevington pg. 145; Arndt]. Noting the first partial derivatives of χ^2 are zero at its minimum, the uncertainty in a fit parameter may be obtained from the curvature of χ^2:

$$\frac{\partial^2 \chi^2}{\partial a_j^{\,2}} = \frac{2}{\sigma_j^2} \qquad \text{III.9}$$

substituting a second difference function for the derivative and inverting the equation yields:

$$\sigma_j = \Delta a_j \sqrt{2(\chi_{-1}^2 - 2\chi_0^2 + \chi_1^2)} \qquad \text{III.10}$$

where σ_j is the standard deviation in the parameter a_j; Δa_j is a small variation in the parameter a_j; $\chi^2_{\pm 1}$ is the value of χ^2 evaluated at the point $a_j \pm \Delta a_j$.

Revisiting the data set of Figure 5, it is possible to perform a least-squares fit to determine the vapor pressure of the mercury. The fit to data gives a vapor pressure of $0.001979 \pm 2.75e^{-5}$ Torr, where the uncertainty is a two sigma deviation. The plot of the new data is indistinguishable from the plot shown earlier. Fits to other parameters are possible, depending upon the confidence one has in the measured parameters. For example the effective of the instrument linewidth for the isotopically enhanced mercury scans was

unknown and determined via line fitting.

The effect of mercury self-pressure broadening is of particular interest. Little if any data is given on pure mercury pressure broadening coefficients.[Matveev] Because the self-broadening co-efficient is small, it is difficult to observe in the low pressure cases heretofore described. To determine the effect of number density on homogeneous linewidth, another vapor cell which is more fully described in Chapter 7 and featured higher operating temperatures was used. The pulsed laser was used as an interrogation source, and the original 5cm cell used as a frequency reference. Figure 11 gives a simultaneous plot of pulsed laser interrogation of the reference (cold) cell, and the higher vapor pressure (heated) cell, with models simulating the two operating conditions. The reference cell was held at room temperature (23C, 0.0015 Torr) and the heated cell at (409K, 1.50 Torr), as the incident laser was scanned over marginally more than 2 cm^{-1} at 253 nm. While the data is somewhat noisy due to laser power fluctuations, it is good enough to extract a pressure broadening co-efficient of about 10MHz/Torr at 409K. Model plots are given for pressure broadening coefficients of 4 MHz/Torr, 10MHz/Torr and 20MHz/Torr. The model fitting routine yielded 9.8 (±.03) MHz/Torr broadening at 409K.

In summary, experiment and modeling of mercury vapor absorption at 253.7 nm has been conducted. Modeling of the mercury absorption profile includes the effects of isotopic variation and hyperfine splitting. An approximation to the Voigt absorption profile includes both homogeneous and inhomogeneous broadening effects. Experimental characterization of the absorption profile of mercury vapor at a variety of vapor pressures and isotopic abundances was used to verify the model, and produce a measure of mercury self-broadening. A least-squares fitting routine was developed to fit the model to experimental data to extract operational parameters

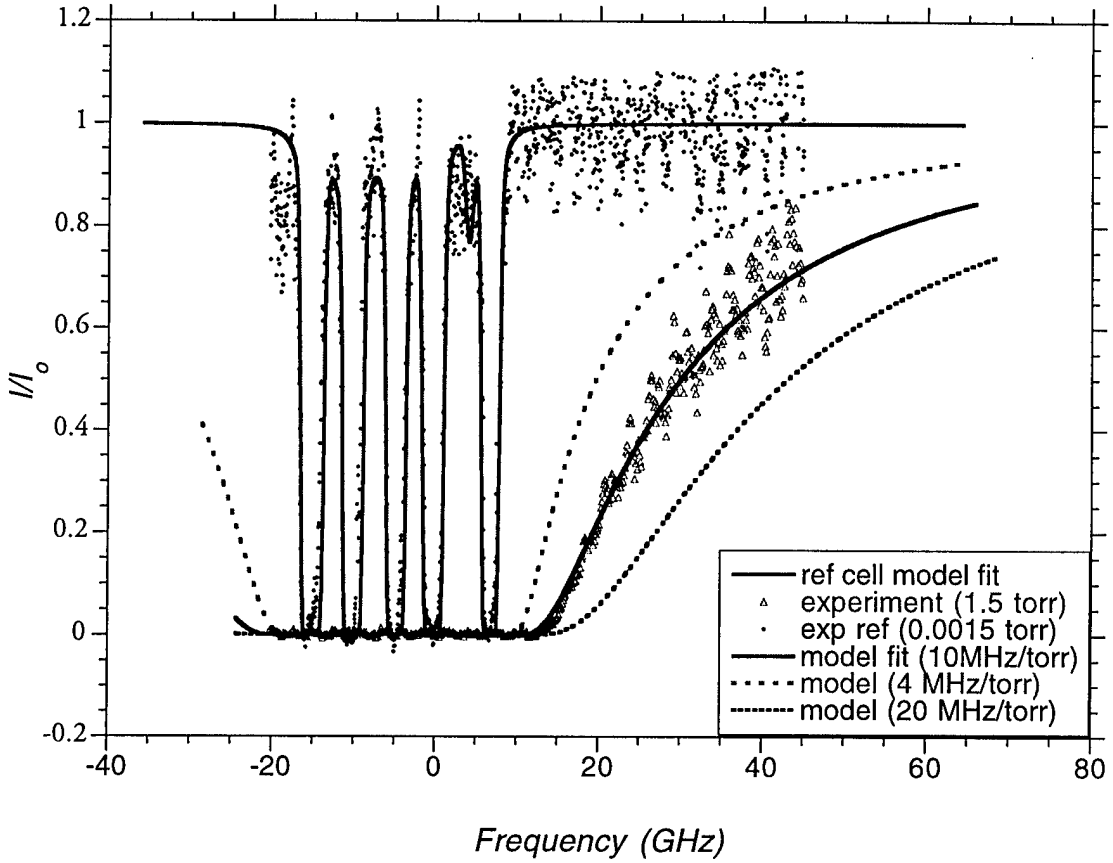

Figures 11: Measure of mercury self-broadening co-efficient. Simultaneous scan of cold 5 cm path cell (ref cell) and 1.5 Torr cell, with model predictions for various broadening parameters. The fitting routine extracted a broadening parameter of 9.8 MHz/Torr.

References

Arndt, R.A. and MH MacGregor, "Nucleon-Nucleon Phase Shift Analysis by Chi-Squared Minimization," Methods in Computational Physics, Vol 6, Academic Press, NY, 253-96, (1966).

Bevington, P.R. and Rominson D.K, Data Reduction and Error Analysis for the Physical Sciences, 2nd Edition, McGraw Hill, NY (1992).

Bitter, F.,"Magnetic resonance in radiating or absorbing atoms," *Applied Optics*, **1**(1), 1-10.(1962).

CRC Handbook of Chemistry and Physics, A ready-reference book of chemical and physical data, 78th edition, CRC Press, Inc., Boca Raton, (1997).

Edner, H., Faris, G.W., Sunesson, A., and Svanberg, S.,"Atmospheric atomic mercury monitoring using differential absorption lidar techniques," *Applied Optics*, **28**(5), 921-930, (1989).

Forkey, J.N., "Development and Demonstration of Filtered Rayleigh Scattering - A laser based Flow Diagnostic for Planar Measurement of Velocity, Temperature and Pressure," doctoral thesis #2067-T, Princeton University, Princeton NJ, pg.80, (1996).

Herzberg, G., Atomic Spectra and Atomic Structure, Dover Publications, NY, (1944).

Kuhn, H.G., Atomic Spectra, Academic Press, NY, (1962).

Migdalek, J, and Baylis, W.E., "Relativistic oscillator strengths for the $6s^2\ {}^1S_0$-$6s6p\ {}^3P_1$, ${}^1P_1$ transitions in neutral mercury. A new approach to the correlation problem," *Journal of Physics B: Atomic and Molecular Physics*, **17**, L459-L464, (1984).

Matveev, O., University of Florida, FL, personal communication, (1997).

Nishimura, Y. and Fujimoto, T., "λ =2537 Å line from a low pressure mercury discharge

lamp emission profile and line absorption by a gas containing a mercury vapor," *Applied Physics B*, **38**, 91-98, (1985).

Press, W.H., Flannery, B.P., Tevkolksy, S.A., Vetterling, and W.T., Numerical Recipes in C, The Art of Scientific Computing, Cambridge University Press, NY, (1990).

Radzig, A.A., and Smirinov, B.M., Reference Data on Atoms, Molecules and Ions, Springer Verlag, Berlin, pg 229 (1984).

Rasetti, F. *Nuovo Cimento*, **7**, 261 (1930) and Rassetti,F. *Nature* **127**, 626 (1931). referenced in Pelletier, M.J., "Ultraviolet Raman Spectroscopy Using and Atomic Vapor Filter and Incoherent Excitation," *Applied Spectroscopy* **46**(3), 395, (1992).

Reader, J., Corliss, C.H., Wiese, W.L., and Martin, G.A., Wavelengths and Transition Probabilities for Atoms and Atomic Ions, NSRDS, National Standard Reference Data System, U.S. Department of Commerce, National Bureau of Standards, 87, (1980).

Steinfeld, J.I., Molecules and Radiation: an Introduction to Modern Molecular Spectroscopy, The MIT press, Cambridge, MA (1981).

Whiting, E.E., "An Empirical Approximation to the Voigt Profile," J*ournal of Quantum Spectroscopy and Radiative Transfer,* **8**, 1379-84 (1968).

Chapter 4: A Notch Absorption Filter and UltraViolet Filtered Rayleigh Scattering

Introduction

Over the past several years, Filtered Rayleigh Scattering (FRS) has been employed as a diagnostic in a variety of fluid environments for non-intrusive flow visualization and quantitative study of velocity, temperature, and density fields. By looking at Rayleigh scattering from naturally occurring species or particulates in a flow, unseeded flowfield measurements are achievable given optical access to the test environment, a high power narrow linewidth light source, and appropriate optical filtering. In the development and characterization of this technique, Forkey highlights the benefits of FRS over conventional intrusive techniques, as well as a few optically based non-intrusive techniques.[Forkey, pg1]. The benefit of direct two-dimensional measurement of flow parameters (T,P,v) and planar (not volume integrated) imaging capabilities are key aspects of this technique. Seasholtz further highlights the benefit of filtering the Rayleigh signal rather than normalizing or subtracting out the background, both of which are susceptible to and amplify noise.[Seasholtz]. Filtered Rayleigh Scattering measurements have been demonstrated in a host of environments including: sonic flows,[Forkey, pg.157] supersonic flows,[Forkey, pg.182; Elliot(1994)] hypersonic flows,[Miles] boundary layer studies,[Erbland] atmospheric studies,[Shimizu] and flame environements.[Hoffman]

To date the work on Filtered Rayleigh has occurred in the visible, with doubled Nd: YAG paired with I_2 (at 532). Similar techniques in the LIDAR and other communities have paired narrow linewidth lasers and filters, but again from the visible to infra-red

region: an argon ion laser and I_2 (at 514 nm) [Devlin, Wall]; an alexandrite laser and potassium filter (at 770 nm)[Bloom]; a dye laser and Barium filter (at 554 nm) [Shimizu(1983)]; a dye laser and cesium filter at (389 nm).[Shimizu(1986)] Because of the strong frequency to the fourth power dependence of the Rayleigh scattering cross-section, it is desirable to work at high frequencies. Further, as will be demonstrated, mercury vapor provides nearly ideal filtering characteristics for Rayleigh based scattering techniques. By pairing the narrow linewidth tunable ultraviolet laser source described in Chapter 2 with the mercury vapor cell of Chapter 3, it is now possible to make measurements via ultraviolet Filtered Rayleigh Scattering.

This chapter will detail the concept of Filtered Rayleigh Scattering, the appropriate aspects of the ultraviolet laser source, and the mercury vapor filter. Experiments demonstrate both flow visualization with background suppression and velocity measurement capabilities of the system. Finally, some comparisons of the visible and ultraviolet implementations of this technique are given.

FRS concept

The Filtered Rayleigh Scattering diagnostic technique has been described in detail in earlier work,[Forkey] so that only a brief summary is presented here. A narrow linewidth laser is used to illuminate a flow, as shown in Figure 1. Scattering from the flow, as well as scattering from any background surfaces, is imaged through a narrow band absorption filter onto a camera. The narrow band absorption filter is used to discriminate the various frequency components of the scattered light. Two main spectral features exist: one component at the laser frequency (from background wall and window scattering), and one component Doppler shifted from the laser frequency (from the moving flow). In its

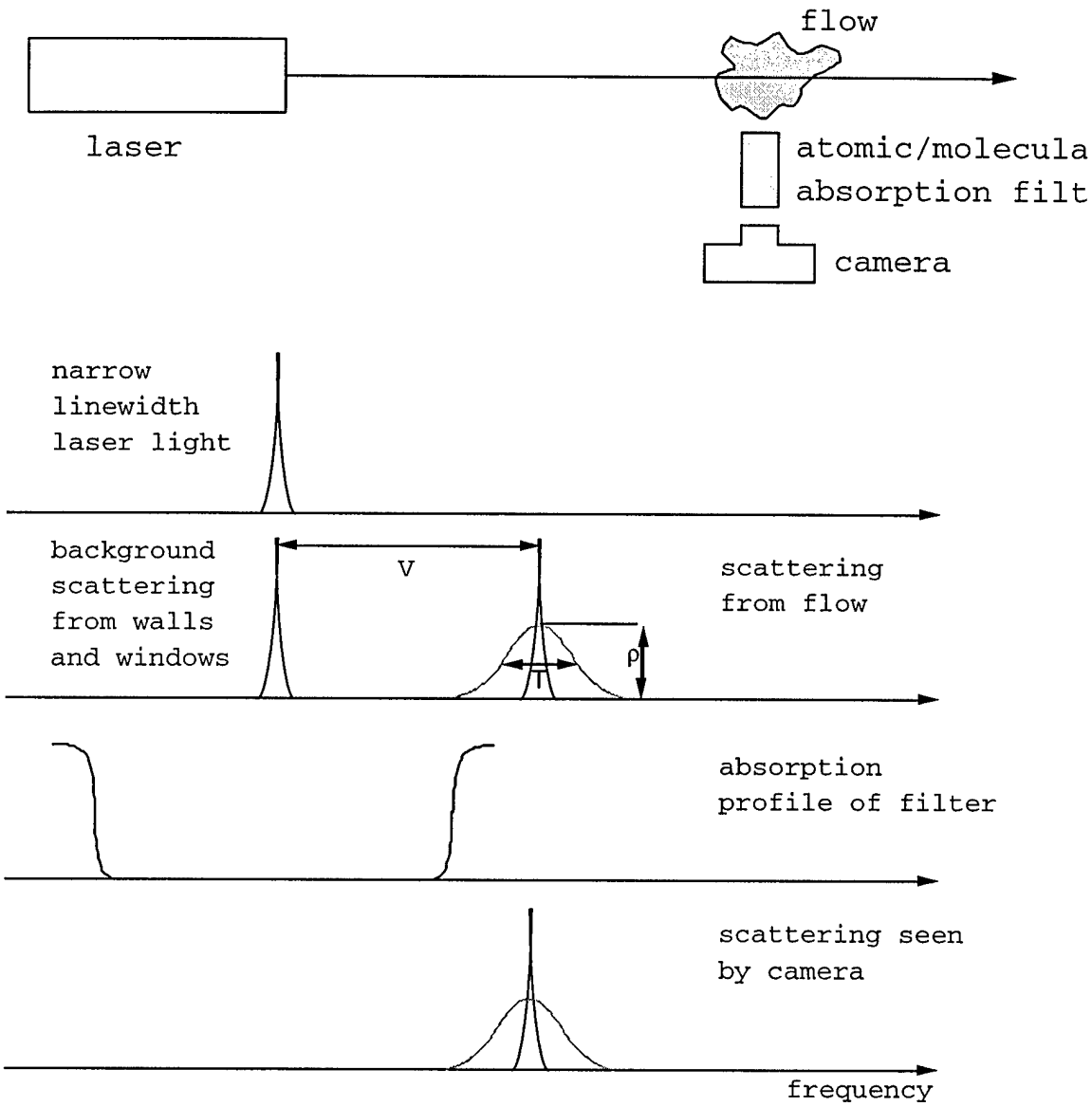

Figure 1: Filtered Rayleigh Scattering concept. Narrow linewidth light interrogates the flow. Scattering from the flow is observed through a notch absorption filter on an intensified camera. The technique is capable of planar measurements of T,p **v**.

simplest incarnation, Filtered Rayleigh Scattering may be used for flow visualization by blocking out unwanted background scattering. The laser frequency is set to coincide with the absorption band of the filter, while the flow scattering is Doppler shifted outside the band and imaged onto the camera. To quantitatively capture the velocity, temperature and density fields, the spectral profile of scattering from the flow is measured. The scattering

from the flow is spectrally shifted due to a mean velocity component; its spectral width is due to a mean temperature of the flow; its integrated intensity reflects the density of the flow. The intensity on each pixel of the CCD camera is a function of these three parameters, the absorption filter profile, the laser frequency and geometry. By varying the incident laser frequency, or the absorption profile of the filter, measurement of the spectral profile of light scattering from the flow may be made. At least four distinct measurement configurations must be made in order to determine velocity, temperature, pressure, and statistical uncertainty estimates. Rather than angularly resolving the scattering, or having different vapor cell configurations, which would vary the absorption profile of the spectral filter, the incident laser is tuned in frequency to resolve the spectral characteristics of the scattering. As the laser is scanned through the absorption band of the narrow linewidth filter, a varying intensity profile for each pixel is recorded. A computer model may used to extract measurements of velocity, temperature and density.

The Laser

To capture instantaneous flow structure, a high power laser pulse is necessary, and for strong Rayleigh or Raman scattering signals, that pulse must be in the ultraviolet. Because desired flow property information is imbedded in the spectral profile of the scattered light, it is essential that the laser be well controlled and narrow linewidth. Pulsed lasers, even when frequency-narrowed, do not operate single frequency and are not precisely frequency controllable. Such frequency selection and control is usually accomplished by injecting a cw laser into the pulsed laser cavity and locking one to the other. As described in Chapter Two, the traditional locking mechanism uses a feedback loop and minimizes the delay between Q-switch firing and laser pulse output. Such a

locking scheme is not ideal for Filtered Rayleigh Scattering, since many pulses are required before the laser cavity is locked. Furthermore, if the laser is tuned in frequency, the tuning rate must be very slow in order to maintain lock. Lastly, the Q-switch delay locking technique places a sinusoidal dither on one of the pulsed cavity end mirrors. The small variation in cavity length causes fluctuations in laser output frequency, despite the injection seed stability due to frequency pulling.[Park] For time-averaged measurements this small (10 MHz) oscillation in frequency is averaged out. For instantaneous measurements, the cavity locking scheme represents a fundamental limit in frequency measurement, and hence limits quantitative accuracy. The Ramp and Lock cavity-locking of the injection-seeded pulsed Ti: sapphire overcomes these difficulties by rapidly locking the cavity to the seed source before each pulse. Cavity lock requires only a few milliseconds, allowing for rapid and discontinuous change of the frequency of the seed beam. The rapid tuning feature is essential for implementation of FRS in facilities with limited run-time.

For realistic implementation of UV Filtered Rayleigh Scattering, the laser must also be stable in the harsh acoustic environments of wind tunnel operation. Again, the Ramp and Lock cavity locking accommodates such environments by using high bandwidth feedback. As demonstrated below, the laser remains stable in UV FRS measurements of a Mach 2 free jet issuing into the ambient laboratory, with an estimated acoustic noise level exceeding 100 dB.

The Filter

In Filtered Rayleigh Scattering, the optical filter is an essential component which provides the dual function of suppressing background scattering, and converting spectral

content to intensity variation which allows for quantitative measurement. Five features of the optical filter will characterize its performance as tool for Filtered Rayleigh Scattering: 1) in-band transmission; 2) out-of-band transmission; 3) edge discrimination between these bands; 4) width and control of the in-band notch; 5) ability to preserve planar images. Figure 2 summarizes these features. An ideal description of an optical notch filter for FRS will be presented followed by an examination of the mercury vapor filter.

Ideally, the in-band transmission of an optical notch filter will be zero. For the back-ground suppression application of FRS, it is clearly desirable to remove all unwanted scattering. For quantitative measurement of flow parameters, while this feature is not critical and depends upon precise implementation, a minimal in-band transmission gives a higher contrast between in-band and out-of-band transmission which results in a reduction of absolute errors.[Forkey, pg 60] Accordingly, the out-of-band transmission ideally

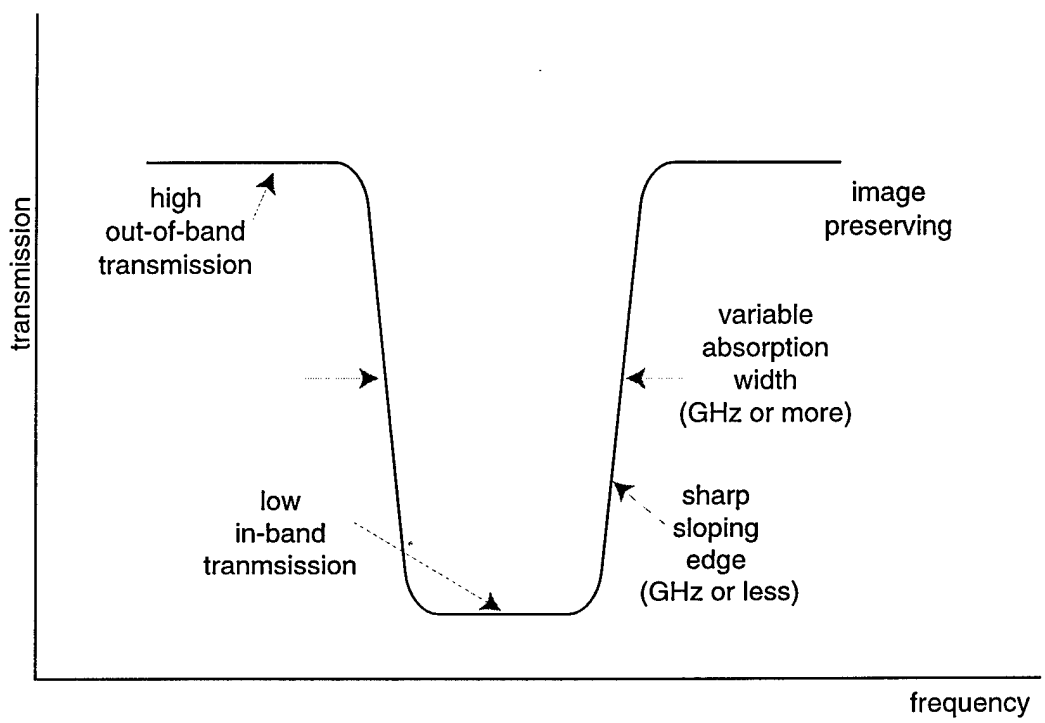

Figure 2: Characteristics of an ideal filter for filtered Rayleigh scattering.

would be 100%. High transmission assure collection of all desired light (Doppler shifted by flow velocity), and high contrast for quantitative analysis. The edge discrimination ideally should be sharp. Again, there is some dependence upon precise implementation as to how sharp the edge discrimination should be. For background suppression, the discriminating edge should have an infinite slope. This gives the greatest sensitivity to velocity, and allows for suppressing background scattering from slow moving flows. For Rayleigh scattering measurements where the incident laser is scanned in frequency, a sharp-sloping filter gives the most accurate means of determining the spectral profile of the flow scattering. However, there are cases where a finite sloping edge profile is desirable. In cases where instantaneous flow velocity is determined by placing the incident laser frequency on the sloping edge of the filter profile, the velocity is measured as a change in flow scattering intensity (spectrally moving up or down the edge of the optical filter due to a Doppler shift).[Meyers; Elliot] This technique is dubbed Doppler Global Velocimetry (DGV) or Planar Doppler Velocimetry (PDV).

For FRS, the spectral width of the notch absorption band needs to be broad enough to reject unwanted light, and to offer significant contrast for quantitative measurement. That is, in rejecting stray elastic scattering (from walls and windows in a flow facility), the absorption bandwidth need be on the order of several hundred MHz (many times the linewidth of the illuminating laser). For quantitative measure of Rayleigh (thermally) broadened scattering, the absorption bandwidth needs to be several GHz, to insure that a high signal contrast is achieved when the flow scattering frequency coincides with the absorption band. By having control of the absorption linewidth, an optical filter may be optimized for a particular experimental application. The profile of a filter for DGV will

look different from a filter used for background suppression. Further, if one works with a fixed frequency illuminating source, tunable filters allow for Filtered Rayleigh Scattering measurements. That is, instead of tuning the laser through an absorption band, it is possible to use several differing filter profiles (appropriately tuned) so that FRS scattering measurements may be made on a shot by shot basis. This sort of variation of FRS has been demonstrated with 1-D angularly resolved PDV.[Shirley; Elliot(1996)]. Finally, it is worthy to highlight the desire for imaging capability. It is this last criterion which motivates the development of atomic and molecular vapor based filters. While other technologies exist for narrow band notch filters, none simultaneously offer a narrow absorption band, sharp edge discrimination, and wide field of view / acceptance angle. [Forkey, pg 64] Thin film filters exist with high discrimination, and sharp cut-off, however, they are still broadband by comparison to atomic/molecular transitions. Further, they are angularly sensitive, and have limited out of band transmission.

Mercury vapor naturally fits the aforementioned criteria, making an excellent narrow band notch absorption filter. The transmission profile of mercury vapor is described and modeled in previous chapter. Here, briefly, will be described the attributes that make the previously described cell a desirable optical filter for ultraviolet Filtered Rayleigh Scattering. Figure 5 in Chapter 3 shows a plot of the transmission profile for one of the typical operating conditions of the mercury vapor cell. Highlighting a single absorption band, as in Figure 3, the plot begins to resemble the cartoon depicting the ideal features of an optical filter. While the mercury vapor pressure is only 0.002 torr, $4.5 * 10^{13}$ atoms per cc, the optical depth is quite high, yielding a transmission of e^{-48}, or 21 orders of magnitude suppression on line center. Out-of-band transmission is limited only by the

four uncoated surfaces of the filter windows. As appropriate, Brewster angle windows, or anti-reflection coated windows could eliminate reflection loss. Notably, as discussed in Chapter 3, there is no competing absorption mechanism that interferes with the out-of-band transmission. The spectral width of the absorption band is 2.8 GHz. As shown below, this gives an effective means of suppressing elastic background scattering, and even Doppler shifted particulate scattering both of which exhibit linewidths on the order of 100 MHz. The discriminating edge of the absorption band is sharp, 10% to 90% transmission occurring over 0.55 GHz. Realistically there is no way to achieve an infinite slope. Practically, a rising edge narrower than the Rayleigh broadened lineshape is the desired goal. This allows for background suppression, high contrast, and spectral

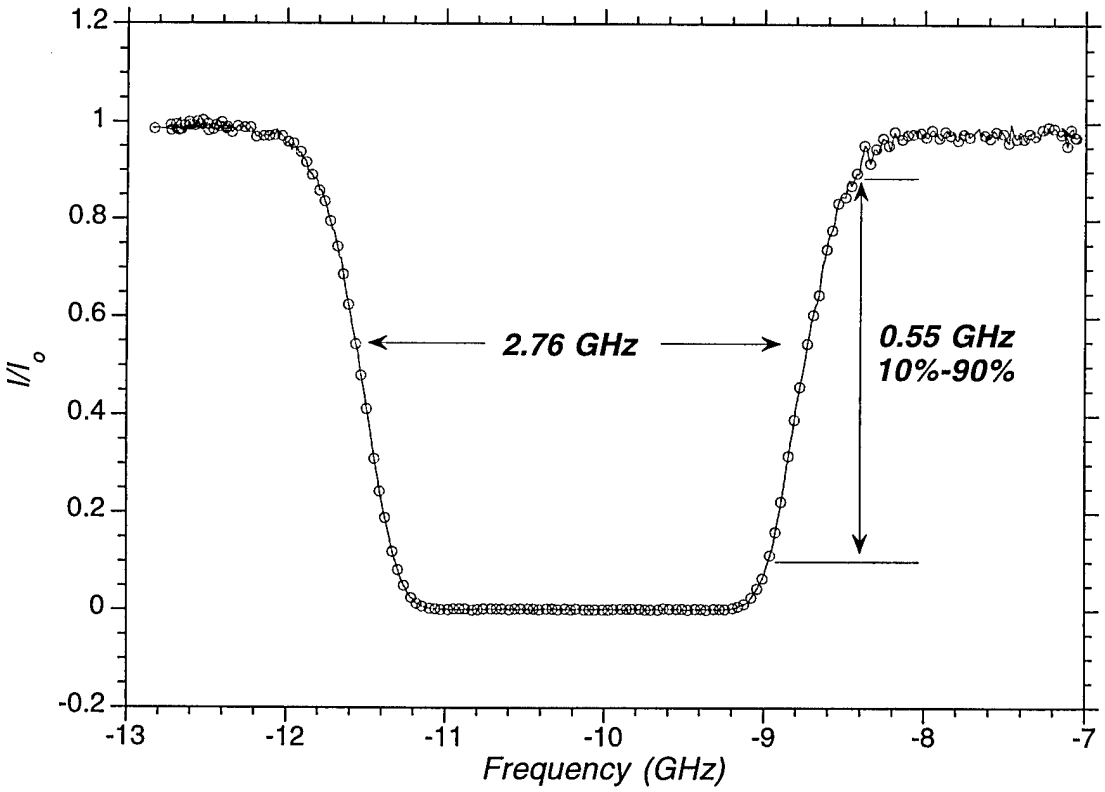

Figure 3: Detail of mercury 202 absorption band. Features of this mercury filter may be compared with the ideal filter characteristics for Filtered Rayleigh Scattering (Figure 2).

resolution of the Rayleigh broadened lineshape. The slope of the discriminating edge is limited by the homogeneous (Lorentzian) linewidth, which is minimal (0.001 GHz) at these vapor pressures. By increasing the vapor pressure of the cell, the absorption profile of the filter may be significantly varied. Increasing the vapor pressure yields increased optical depth, so the absorption bandwidth and centerline attenuation are both magnified. As shown in Chapter 3, at 0.05 torr, the absorption bands increases (4.4 GHz fwhm for Hg202), but also each isotopic absorption band is no longer independently resolved. Further the minimal Lorentz component becomes observable in the wings, limiting the rising edge slope (10%-90% transmission occurs over roughly 1.5 GHz). At yet higher vapor pressures, Figure 2(b) Chapter 3, the individual isotopes blend and further reduces the rising edge slope. Lastly, the imaging capabilities of the mercury vapor filter are clearly demonstrated below. Because the atomic absorption is insensitive to photon incidence angle, the filter will operate independently of viewing angle (within construction limits of the cell). There is a minor effect that the pathlength through the vapor cell changes with incident angle. For a beam propagating through the cell at an angle θ, the length scales with $(\cos\theta)^{-1}$. Angular deviation may be accounted for when the input angle changes by more than 8 degrees from normal, which induces a 1 percent change in pathlength (and hence optical depth). However, as described by Forkey, collection f/# (focal length/ lens diameter) plays a critical role in FRS analysis. For large enough f/#, the collection angle may be construed as constant. While for fast collection optics, it is important to account for angle variation across the collection lens.[Forkey, pg46] With the f/4.5 lens collection experiments below, we are assured 1% accuracy by assuming constant angle.

FRS theory

The Filtered Rayleigh Scattering signal depends upon the flow parameters (T,P,v), experimental configuration angles (θ,δ), and laser frequency (ν_c):[Forkey, pg27]

$$N_{PE} = \frac{E_L}{Ah\left(\frac{c}{\lambda}\right)}\eta\frac{PV}{kT}\frac{d\sigma}{d\Omega}\Omega\left[\int_{-\infty}^{\infty} t(\theta,\nu)\left(\int_{-\infty}^{\infty} l(\nu-(\nu_c+\Delta\nu_D(\theta,\delta,v)-\nu')g(\theta,T,P,\nu'))d\nu'\right)d\nu\right] \qquad \text{IV.1}$$

Here the signal is given by the number of photo-electrons ejected by the camera's intensified photocathode, per interrogation volume, N_{PE}. E_L is the incident laser energy (mJ/pulse); A is the cross-section of the laser interrogation volume; h is Plank's constant; c/λ is the absolute laser frequency; η is the quantum efficiency of both the camera lens and photocathode; k is Boltzmann's constant; $\frac{d\sigma}{d\Omega}$ is the differential Rayleigh scattering cross section; Ω is the solid collection angle. The normalized integrals represent a convolution of the laser linewidth $l(\nu - \nu_c)$ with the Rayleigh scattering profile $g(\theta,T,P,\nu)$. This scattering signal is attenuated at some frequencies by passing through the spectral filter with transmission profile $t(\theta,\nu)$. The spectral profile of the laser about central frequency ν_c is spectrally shifted to reflect bulk flow velocity, v. The velocity induced spectral shift, due to the Doppler effect, shifts the scattering profile given by:[Forkey, pg 29]

$$\Delta\nu_D(\theta,\hat{v}) = \frac{1}{\lambda}\bar{v}\bullet(\hat{O}-\hat{L}) \qquad \text{IV.2}$$

The spectral shift is given in cyclic frequency (Hz). It may be considered as a simultaneous two step process: first, a shift induced from the flow velocity relative to the laser, and second a shift induced from the flow velocity relative to the detector. As shown

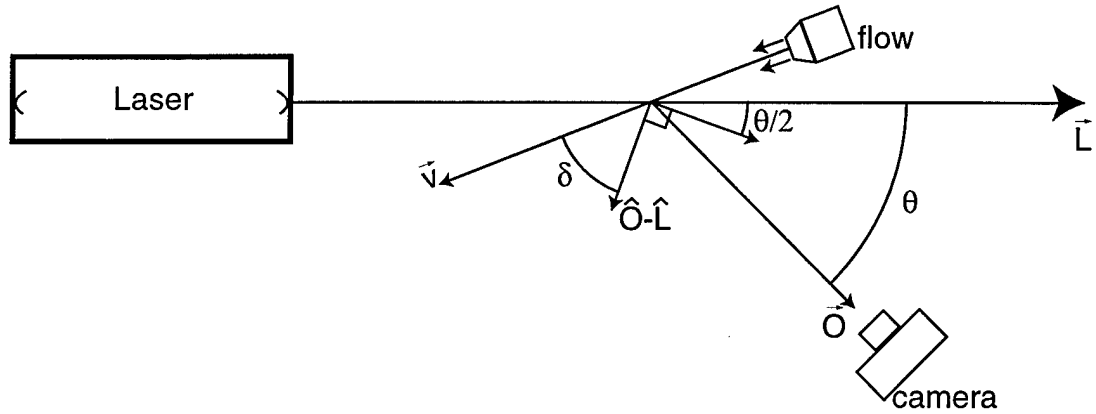

Figure 4: Filtered Rayleigh Scattering angle geometry. The technique is sensitive to velocity components in the (Ô-L) direction

in Figure 4, the laser propagates in the direction $\hat{L}$, scattering from a particle or molecule with velocity, $\bar{v}$ is observed in direction $\hat{O}$. λ is the wavelength of the incident light. This expression may be re-written in terms of δ, shown in figure 4, which relates the flow direction to the laser propagation and viewing angle:

$$\Delta\nu_D(\theta, \delta, v) = \frac{2v}{\lambda}\cos(\delta)\sin\left(\frac{\theta}{2}\right) \qquad \text{IV.3}$$

The spectral signature of the flow scattering, $g(\theta,T,P,\nu)$ is given by the Rayleigh-Brillouin scattering profile. A detailed analysis of this scattering signal is given by Forkey. [Forkey pg. 27] In summary, there are two regimes governing the scattering profile. The Knudsen regime is the limit of low pressure where molecular motion is considered uncorrelated, and thermal motion determines the scattering profile. As a result, a Maxwellian velocity distribution gives rise to a purely Gaussian scattering profile (known as the thermally broadened Rayleigh line):.

$$g(\theta, T, \nu) = \frac{2}{\Delta\nu_T(\theta, T)}\sqrt{\frac{\ln 2}{\pi}}\exp\left[-4\ln 2\left(\frac{\nu}{\Delta\nu_T(\theta, T)}\right)^2\right] \qquad \text{IV.4}$$

The linewidth, or thermal broadening is given by:

$$\Delta\nu_T(\theta, T) = \frac{2}{\lambda}\sin\left(\frac{\theta}{2}\right)\sqrt{\frac{8kT\ln 2}{m}} \qquad \text{IV.5}$$

where m is the mass of the scattering source. It is worthy of note that air has a Rayleigh linewidth of approximately 4 GHz (at 20°C, θ=90°, λ=254 nm). In the hydrodynamic regime, nearly all molecular motion is correlated (at high pressure), and three Lorentzian profiles (broadened by diffusion) are centered at the incident frequency ν_c and two side frequencies shifted by roughly the Doppler shift corresponding to the speed of sound in such a medium. Practically, Rayleigh-Brillouin scattering will often fall in an intermediary regime, the kinetic regime, which lies between the Knudsen and hydrodynamic limits. Forkey describes and employs a useful model developed by Tenti with operating parameter, Y which quantifies the relative contributions of random and correlated motion.[Forkey, pg 30]

Experimental setup

The narrow band ultraviolet laser and absorption filter have been used to image the shear layer of a supersonic free jet seeded with CO_2. The purpose of the CO_2 was to enhance the scattering signal due to condensation. The heavier clusters preclude the aforementioned temperature measurement (from spectral broadening), and signal levels do not necessarily indicate flow density. An interpretation of CO_2 scattering is currently being investigated.[Erbland] However, the small size of the CO_2 clusters indicate the scattering is still within the Rayleigh regime ($d_{scatt} \ll \lambda$), and follow the mean flow. As a result, the CO_2 scattering signal can be used for both flow visualization and velocity measurements. The exit diameter of the nozzle was 4.4 mm, while the throat was 3.0 mm.

The area ratio was 0.465 ± .05. The supply pressure of the jet was approximately 200 psi, and the exit pressure was matched to ambient atmospheric conditions. 30 mJ/pulse output of the Ti: Sapphire was frequency tripled to produce approximately 1 mJ/pulse in the ultraviolet. The UV light was formed into a sheet and intersected the flow at angle of 26.5° ± 1°. Figure 5 depicts the experimental configuration. The scattering normal to both the flow and the laser sheet was imaged through the mercury absorption filter onto a microchannel plate intensified CID video camera, using a Nikon 105mm f/4.5 lens. The vapor pressure of the mercury in the absorption cell was 0.002 torr, the same conditions as those used to obtain Figure 5 in Chapter 3. The field of view is shown in Figure 6. The camera view includes: the laser sheet propagating from top left to bottom right; the flow and shear layer propagating right to left; and the nozzle exit seen on the right of the field of view. Images were captured at 10 Hz on video tape as the laser continuously scanned approximately 40 GHz in the ultraviolet.

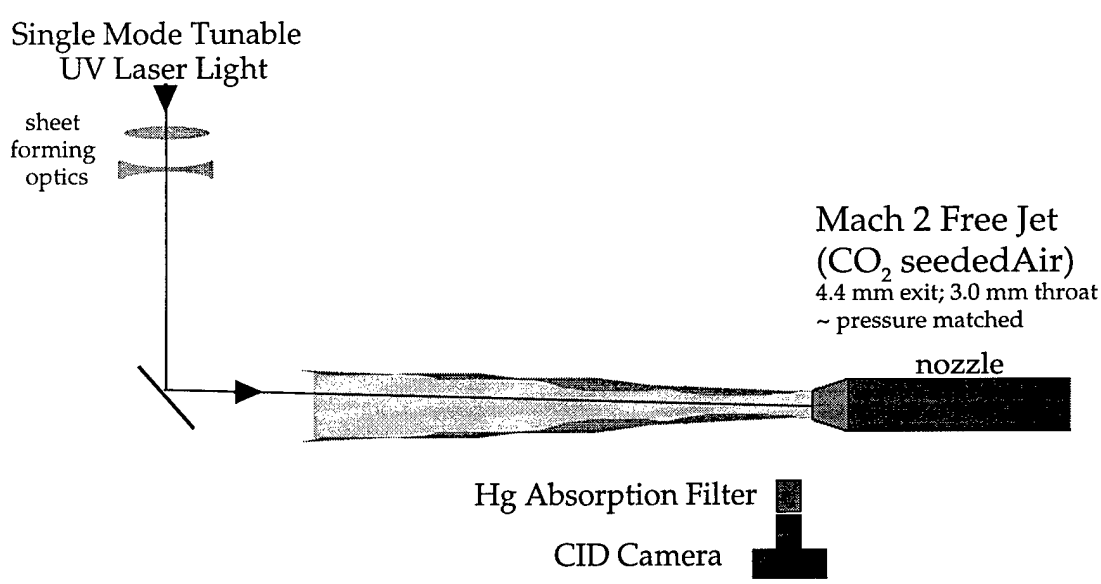

Figure 5: UltraViolet Filtered Rayleigh Scattering measurements: experimental set-up.

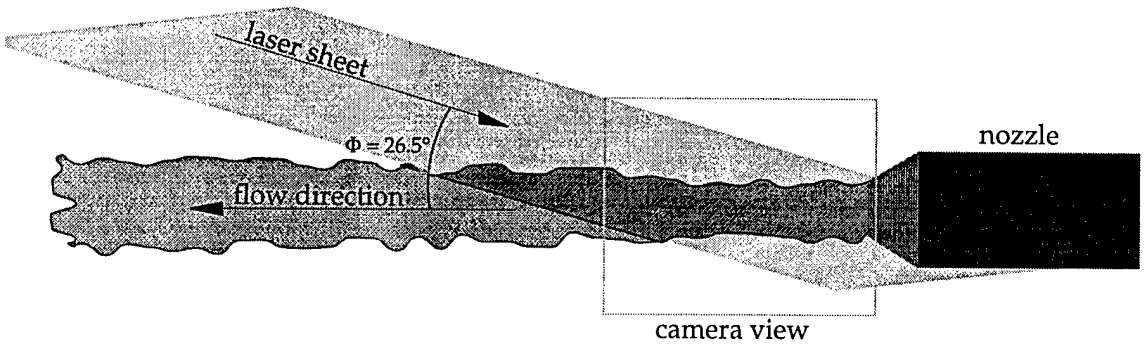

Figure 6: UltraViolet Filtered Rayleigh Scattering measurements: field of view.

Background Suppression

Figure 7 shows a collage of three single shot images of the Mach 2 free jet illuminated by three different ultraviolet frequencies. The laser was purposefully aligned to illuminate both the flow and the nozzle. A cartoon next to each picture gives the relative position of the laser frequency (ν) and the central frequency of the Doppler shifted flow scattering ($\nu + \nu_D$) relative to the filter absorption profile. In Figure 7a, both the laser and flow scattering occur outside the absorption band of the filter, at a spectrally higher frequency. As a result, both the Doppler shifted flow scattering and the unshifted scattering from the nozzle are imaged. In Figure 7b, the laser is tuned such that the flow scattering is Doppler shifted outside the absorption band of the filter, while the elastic scattering from the nozzle is absorbed. In Figure 7c, the laser is tuned such that the flow scattering is Doppler shifted into the absorption band, while the nozzle scattering at the laser frequency is imaged. Data was collected as the laser scanned continuously through the 5 strong absorption lines of mercury. It is interesting to note the increased scattering in the shear layer relative to the free stream. This is not completely understood, although a

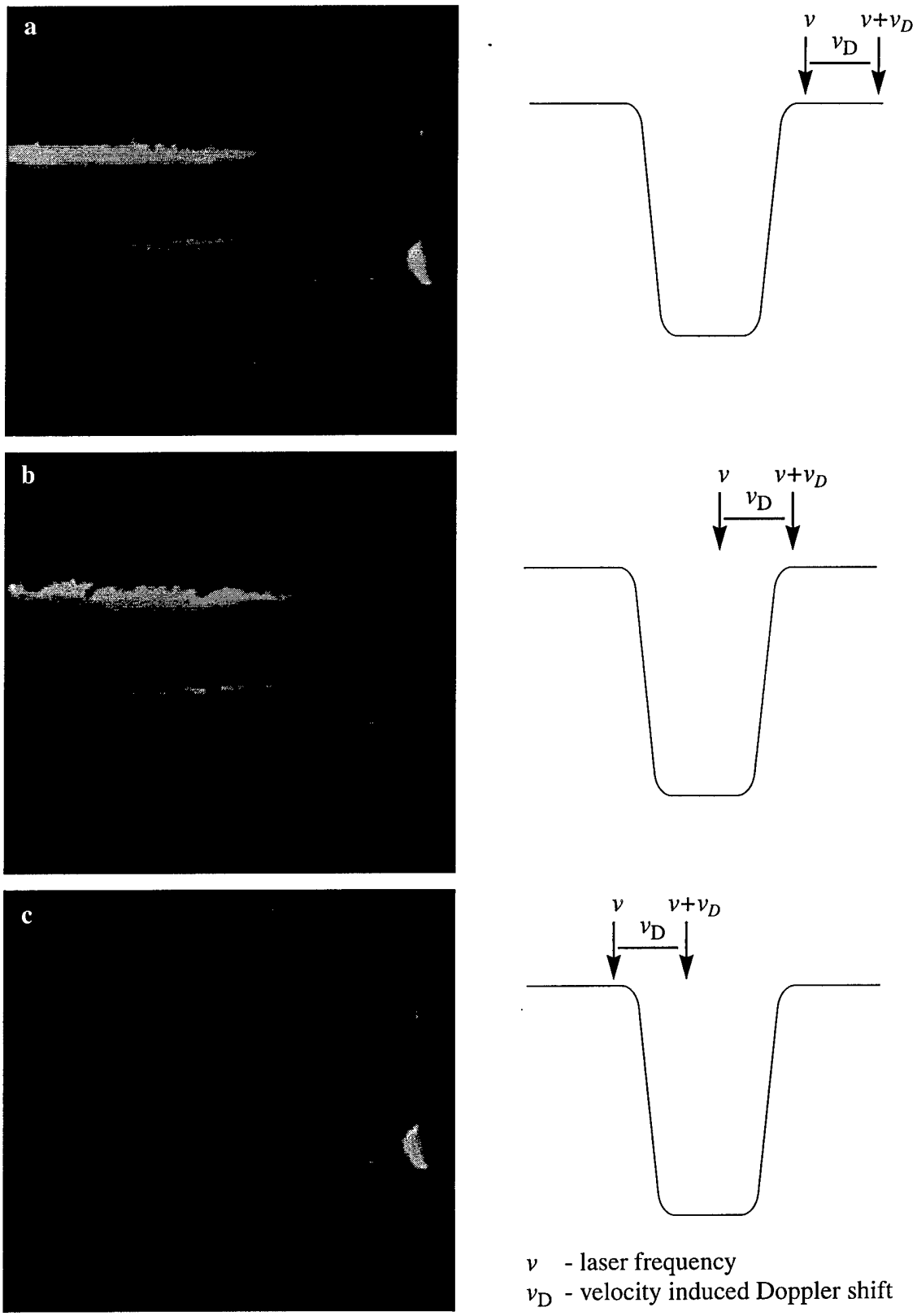

Figure 7: UltraViolet Filtered Rayleigh Scattering: images left, spectral location right

plausible explanation is that the CO_2 is condensed preferentially on the inner walls of the nozzle, or the signal reflects the entrainment of ambient water vapor.

Images similar to Figure 7 were collected with the laser discontinuously tuned in large frequency jumps (~ 4 GHz/shot). Resultant images similar to 7a, 7b, and 7c were captured; however, the images did not 'blend' from one to the next, but rather jumped—following the laser jumps into and out-of the absorption band. This experiment yields data similar to that presented in Figure 12, Chapter 2, except that it is two dimensional. This feature is significant for a variety of applications where rapid frequency change is useful, including shot-by-shot background normalization, and two line measurement up to 30 Hz.

Velocity Measurements

Because the frequency of the laser was varied as the free-jet was imaged, an average velocity measurement of the flow may be made. The spectral shift between the incident laser frequency (represented by the scattering from the nozzle) and the flow scattering is due to the Doppler effect, and hence contains velocity information, as described above. The images originally collected on video were digitized and analyzed. A series of 600 frames collected at 3 Hz, represented a scan of approximately 30 GHz. Grayscale values of representative segments of the flow and the nozzle were separately captured. A sample plot of the mean signal level (of scattering from the nozzle) versus video frame is shown in Figure 8. The representative collection areas are shown as grey boxes in the inset of the figure. Note that the laser is scanning down in frequency, so that the independent axis (frame) is reversed from spectral data presented earlier. As described above, the scattering signal is observed when the incident laser frequency is outside the absorption band of the mercury vapor cell. As described by Equation IV.1, the signal

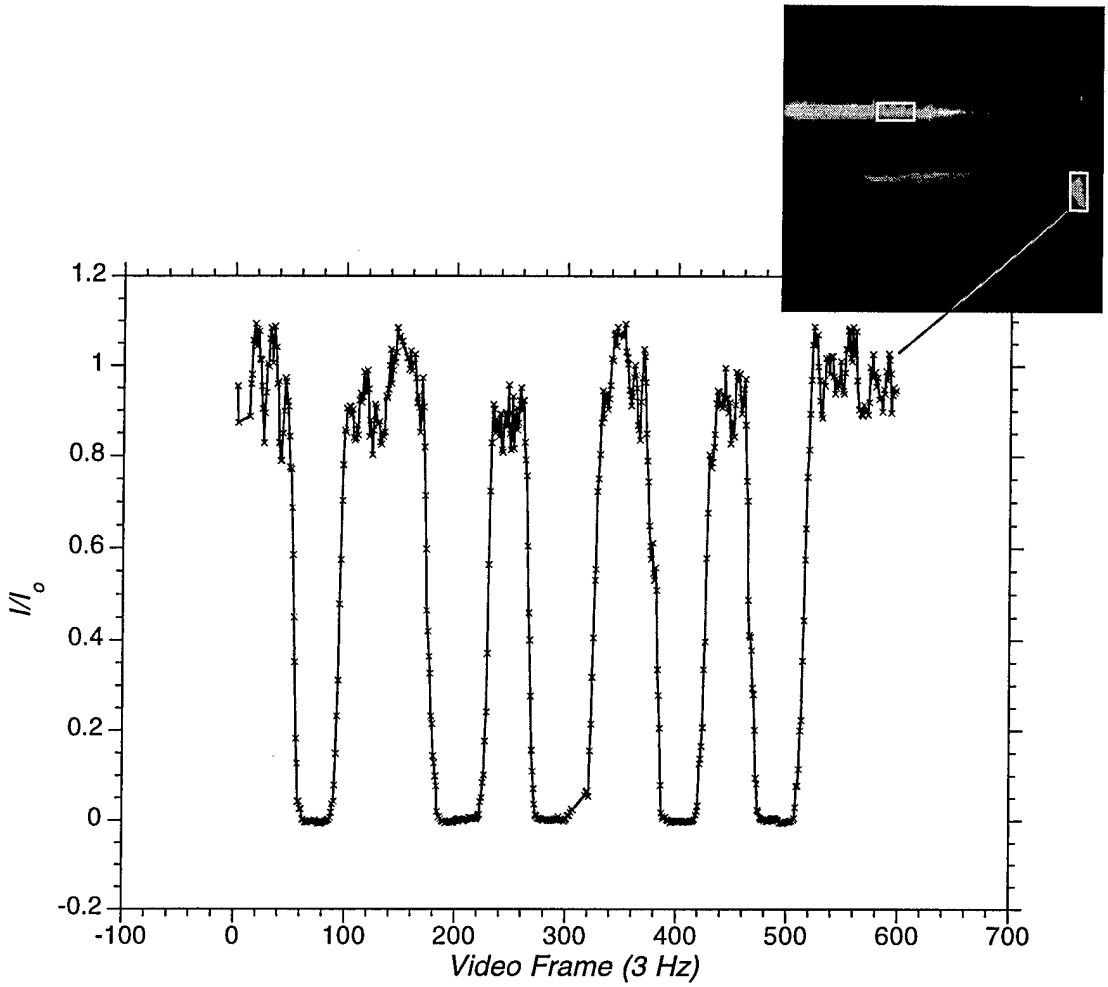

Figure 8: UltraViolet Filtered Rayleigh Scattering: intensity vs. video frame (frequency) imaging elastic (unshifted) light scattering from nozzle of Mach 2 free jet.

recorded by the camera is a convolution of the scattering profile with the transmission profile of the filter. The scattering profile, in turn, is a convolution of the laser spectral profile with the scattering linewidth. Because both the laser linewidth and the scattering linewidth are narrow, the observed camera signal closely mimics the transmission profile of the mercury vapor filter — 5 strong absorption lines are observed. Because this data is not normalized by incident laser intensity, the out-of-band transmission reflects shot-to-shot fluctuation of incident laser power. A similar plot of pixel value versus video frame is collected from the flow.

In order to determine the spectral shift between the two plots (of signal level versus video frame), it is necessary to know the rate of laser scan. Ideally, this is achieved by an external stabilized means, as described above and earlier.[Forkey, pg 127] A stabilized etalon, or fixed absorption line gives an excellent, reliable reference that may be used in comparing relative (or absolute) frequency shift by means of heterodyne or other techniques. In this experimental arrangement, lack of equipment prevented a stabilized spectral reference source. While an approximate laser scan rate may be set by computer control of the cw seed source, there was no means to lock the seed laser to account for thermal drift of the cw cavity. In this case, knowledge of the spectral profile of the mercury filter gave a spectral reference. While the laser and scattering profiles influence the shape of the plot, their effects are secondary. The centers of the absorption bands will remain fixed, while their widths and absorption edges may vary. This is tantamount to saying the spectral profiles of the laser and scattering source are symmetric. Comparing the model with the data yields a frequency step of 52.9 MHz/ digitized video frame.

The expected Mach number of the pressure matched free jet with an area ratio of 0.465 is 2.278 assuming isentropic expansion, and quasi-1-D flow[Liepmann pg 405]. Combining the definition of the speed of sound with the temperature relations for an adiabatic flow yields:[Liepmann pg. 53]

$$v = M\sqrt{\gamma R\left(\frac{T_o}{1+\left(\frac{\gamma-1}{2}\right)M^2}\right)} \qquad \text{IV.6}$$

where M is the Mach number, γ the ratio of specific heats, R the universal gas constant, and T_0 the stagnation temperature. Combining these quantities gives a flow velocity of 545 m/s. The greatest source of uncertainty in this estimation is calculating the area ratio

of the jet. A 100 μm uncertainty in diameter propagates into an error bar of ±15 m/s. An additional assumption, not accounted for are the effects of the CO_2 seeding. Work is underway to verify the effects of seeding CO_2; however, for this work minimal amounts of CO_2 seeding were assumed not to effect the dynamics of the flow.

Figure 9 gives a simultaneous plot of camera signal versus incident relative laser frequency for both the scattering from the nozzle (elastic/background) and the flow (Doppler shifted). The frequency axis of the flow scattering is not shown, but been shifted to overlap the nozzle scattering. The amount of spectral shift to achieve a best overlap of spectral signatures was determined by overlapping the edge transitions of the absorption

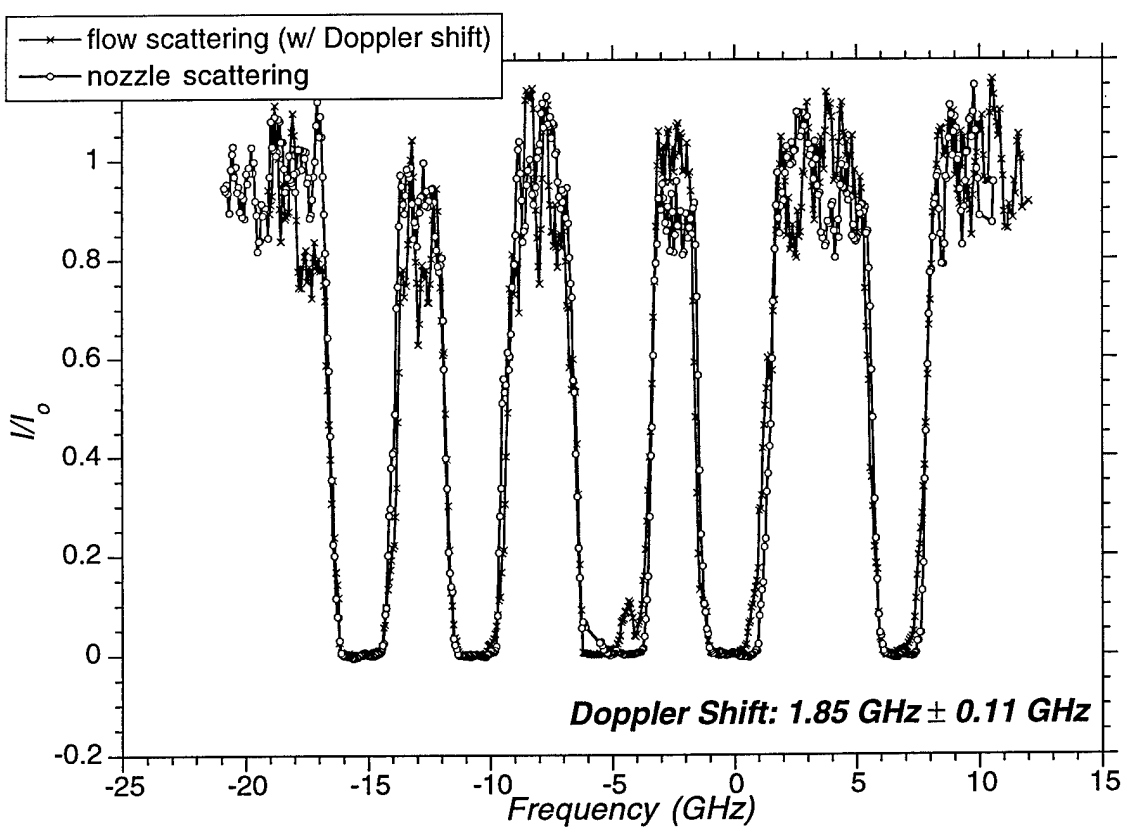

Figure 9: UltraViolet Filtered Rayleigh Scattering: velocity measurement. Simultaneous plot of the spectral signature of scattering from the nozzle (elastic/ unshifted) and flow scattering (with Doppler shift added to align frequency axes).

Seasholtz, R.G., and Bruggele, A.E., "Improvement in suppression of pulsed Nd: YAG laser light with iodine absorption cells for filtered Rayleigh scattering measurements," SPIE paper 3172-63, International Symposium on Optical Science, Engineering, and Instrumentation, SPIE 42nd Annual Meeting, San Diego CA, July 27-Aug 1, (1997).

Shimizu, H., Lee, S.A., and She, C.Y., "High spectral resolution lidar system with atomic blocking filters for measuring atmospheric parameters," *Applied Optics*, **22**, 1373, (1983).

Shimizu, H., Noguchi, K., and She, C.Y., "Atmospheric temperature measurement by a high spectral resolution lidar," *Applied Optics,* **25**,1460, (1986)

Shirley, J.A., and Winter, M., "Air mass flux measurement system using Doppler shifted filtered Rayleigh scattering," 31st Aerospace Sciences Meeting, AIAA paper #93-0513, Reno NV (1993)

Wall, K.F., and Chang, R.K., "I_2-vapor notch filter with optical multichannel detection of low frequency-shift inelastic scattering from surface-enhanced Raman-scattering active electrodes," *Optics Letters*, **11**,493,(1986).

Chapter 5: a word on Raman scattering

The understanding of a variety of engineering and scientific processes (from combustion, to reactive flow studies, to remote sensing) requires or is enhanced by species specific information. The quantities of particular importance include species mole fraction, and temperature. Additionally, high spatial and temporal resolution are desirable for studying small scale, turbulent and transient events. While Rayleigh scattering is particularly effective for temperature, density and velocity measurements, it does not distinguish between different constituent species. Further, it requires independent knowledge of species mole fraction, before data may be quantified, which makes measurements difficult or impossible in reactive environments. Raman scattering allows for such measurements of species and temperature with high spatial and temporal resolution.

Raman scattering is an inelastic scattering process, where incident radiation at frequency ν_o is scattered at a frequency shifted by one of the internal energy modes of the scattering molecule $\nu_s = \nu_o \pm \nu_{em}$. The frequency shift of the scattered light is determined by the internal energy modes of the scattering source, which are specific to a given molecule. Figure 1 depicts this process, where incident radiation may impart energy to the molecule (Stokes shifted), or remove energy from the molecule (anti-Stokes shifted). Classically, this is shown as incident radiation energizing the molecule to a virtual level, and the molecule instantaneously relaxing to an energy level differing from its original state. The energy level difference between the initial and final states must be less than the

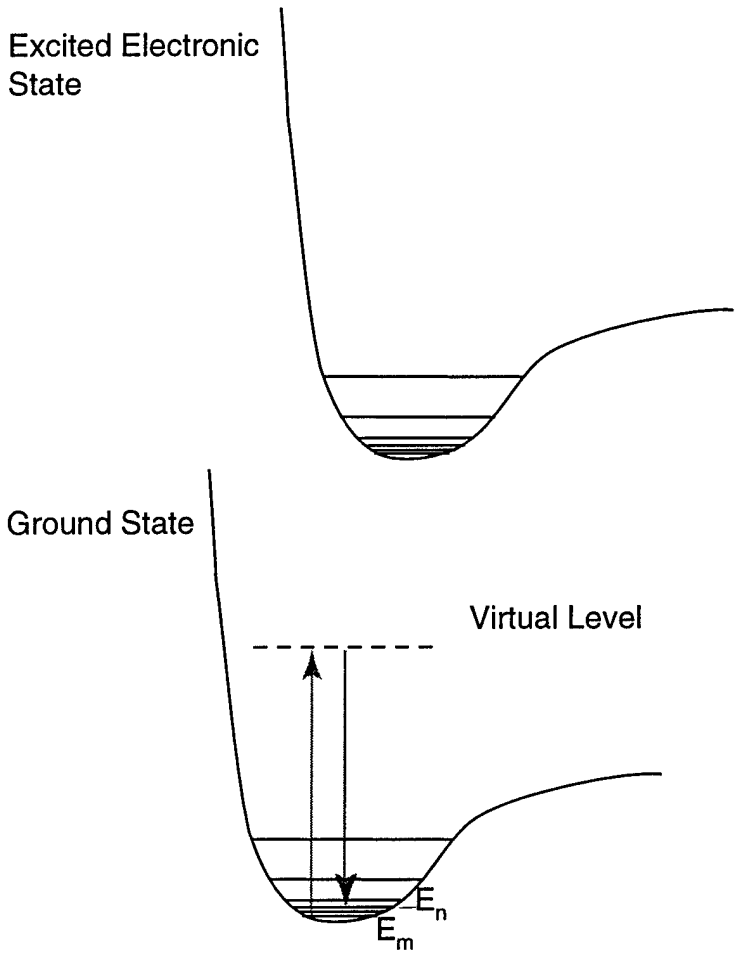

Figure 1: Raman scattering concept. Incident radiation scatters inelastically, with energy level shift corresponding to an internal energy mode (e.g. rotational) of the scattering source.

energy of the incident radiation ($h\nu_0$). The separation between initial and final energy levels distinguishes between vibrational and rotational Raman scattering. The separation of rotational energy levels is 100-1000 times less than that of vibrational, and hence the frequency shift of incident light is correspondingly smaller.[Eckbreth, pg 175]. Non-linear applications of Raman scattering will not be discussed here; Raman scattering in this instance refers solely to spontaneous Raman scattering, and the interested reader is referred to Eckbreth for discussion and application of other Raman based techniques.

Because Raman scattering depends upon the internal energy modes of the

scattering source, the spectral scattering signature for each scatterer differs, and hence provides a means of species selective measurement. Thus, in a reactive environment where species concentrations may be changing, direct measurements may be made. Further, because of its instantaneous nature, temporal effects such as signal quenching (reduction of signal due to competing effects) are not an issue. The scattering signal intensity is linearly proportional to the input signal intensity. These features make Raman scattering based diagnostics particularly attractive for major species measurement, and high pressure environments. Linearity in scattering signal has been demonstrated to approximately 50 atm.[Rothe]. The correlation of signal with density and temperature makes for relatively direct measurements and minimal data analysis. In imaging cases, the raw data can reflect relative number density of a given species. Moreover, quantitative information can be obtained for individual laser shots, both by normalization measurements and by relative signal strengths. Thus, high temporal resolution may be achieved with appropriate illumination and collection sources. Finally, like Rayleigh scattering, the Raman process is non-resonant, so the interrogation wavelength need not be at any fixed frequency. A recent review paper summarizes the application of Raman scattering diagnostics in combustion by reporting, "The Raman method can yield spatially resolved mole fraction for the major constituents like H_2, O_2, N_2, H_2O, CO, CO_2, CH_4 and T which are excellent tools for studying turbulence-chemistry interaction in combustive environments." [Rothe]

Because of its appeal, laser based Raman scattering has become a standard spectroscopic tool over the last three decades. However, its challenges have thwarted much of the effort to implement Raman based flow and combustion diagnostics. Most

significantly, the Raman scattering process is very weak. The small scattering cross-section leads to inherently low signals. The vibrational Raman scattering cross-section for N_2 at 488 nm is 6.8 10^{-31} cm^2/sr, while the comparable Rayleigh scattering cross-section is 8.4 10^{-28} cm^2/sr.[Eckbreth, pg 211] Often, Rayleigh scattering signals are difficult to detect; Raman scattering signals are typically three orders of magnitude weaker. In low density environments, there are simply too few scattering sources to detect. Further, because it is a weak scattering process, interference from background sources plague measurements. The background may come from broadband luminescence (as with soot incandescence), [Eckbreth, p202] or spectral overlap with other sources of laser induced emission (such as laser induced fluorescence).[Rothe] Background scattering and relative Raman scattering signal strengths largely depend upon the environment and means of interrogation.

The above features of Raman scattering have applied to both its vibrational and rotational variants. Focussing on rotational Raman scattering for diagnostics alleviates some of the aforementioned problems, while simultaneously presenting others. Rotational Raman scattering cross-sections are typically an order of magnitude larger than their vibrational counterparts; however, depending upon the detection system used, distribution of the signal over the manifold of discrete transitions often counteracts this gain. A quantitative description of the signal and population distribution is given below. Temperature measurements using rotational Raman scattering rely upon the relative strength of signals from different rotational levels. These signal strengths, assuming equilibrium, give a Boltzmann distribution of energy level population and hence rotational temperature. In contrast, vibrational measurements of temperature ratio the signal

strength of the vibrational Stokes to anti-Stokes bands which relies upon vibrational equilibrium. In transient environments such as shocks, flame fronts, or hypersonic nozzles, rotational equilibrium is achieved much more rapidly than vibrational equilibrium.[Vincenti].

Because the energy spacing of the rotational levels is small, and the population may be distributed among many of these levels, the rotational Raman scattering spectrum is complex and lies very near a significantly stronger signal, the unshifted Rayleigh line. The lack of ability to distinguish between various rotational levels, while simultaneously suppressing an overwhelming Rayleigh signal has lead most Raman work to focus on vibrational Raman scattering. Because the vibrational energy separation is greater, conventional filtering devices (spectral bandpass thin film filters, long or short wavelength pass filters, and spectrometers) can be employed. A system that is capable of rotational Raman scattering measurements will require both spectral sensitivity and high background suppression. While a demanding task, the requirement of spectral sensitivity effectively removes the difficulty of background laser induced emission which has posed difficulties for vibrational Raman scattering based techniques. The next two chapters detail the development of novel filtering devices for rotational Raman scattering measurements which feature the necessary spectral resolution and background suppression.

Recent reviews detail the application of spontaneous Raman scattering to diagnostics. Rothe and Andresen catalog the advances of excimer lasers and the impact of their high spectral brightness to combustion diagnostics.[Rothe]. A recent review of two dimensional spontaneous Raman scattering covers the history of Raman imaging and its application to the internal combustion engine.[Kyritsis] Other review papers abound

detailing the benefits and history of Raman spectroscopy, diagnostics, and applications.[McKenzie(1993); Eckbreth; Weber(1973); McKenzie(1992)] The majority of these reviews concentrate on vibrational Raman scattering. Indeed, several neglect to distinguish between rotational and vibrational scattering, which reflects the dominant theme of vibrational Raman scattering in the literature. Despite the difficulties with the Rayleigh background and requirements for high spectral sensitivity, rotational Raman scattering based diagnostics have been demonstrated for roughly three decades. Earlier work generally utilized an argon ion laser running narrow band (often at 488 nm) paired with a large (1m-8m) spectrometer. Exposure times were invariably long in order to collect enough light (as much as 30 hrs).[Weber(1979)] Rotational Raman measurements of flame temperatures were reported for point measurements in 1976, and 1978 by and Stricker and Drake, respectively.[Stricker; Drake] Each made a point measurement with time averaged measurement of a volume illuminated by an Ar^{++} laser, by filtering the scattering with a double monochrometer and capturing scattering on a photomultiplier tube. Scan times were on the order of an hour, resolution was sufficient to measure individual nitrogen lines for temperature measurements. A variety of other point measurements have been made, including the development of a rotational Raman scattering lidar system for atmospheric temperature measurements. It was proposed in 1972, [Cooney] demonstrated in 1976 [Cohen] and extended to temperature measurements in the lower stratosphere in 1993.[Vaughn] Vaughn uses a frequency doubled Nd: YAG and specialized nanometer bandwidth filters (which only resolved groupings of rotational lines). 10,000 shot (17 min) averages of data were collected to make the temperature measurement. Recently, 1-D rotational Raman scattering

measurements have been reported by using a high power, narrow band excimer laser, in combination with an imaging spectrometer.[Gu]. H_2 densities and temperatures were measured in an H_2-air flame. A relatively short spectrometer (.25m) is used in combination with polarization suppression based on the large difference between the depolarization ratio of Raman and Rayleigh signals. For hydrogen the Raman signal is slightly attenuated with a depolarization ratio of 3/4 (see below), while the Rayleigh depolarization ratio is only a few percent. A 1-D spatial resolution of 600 μm is reported (due to binning pixels to increase the S/N), with 200 shot averages. No estimates of spectral resolution are given, though difficulties with residual Rayleigh scattering plagued measurement of other species due to a smaller spectral shift of rotational Raman lines.

The devices used for rotational Raman scattering measurements presented in this thesis are the narrow band tunable ultraviolet laser source (discussed in Chapter 2), and two narrow bandpass filters (discussed in Chapters 6 and 7). Because of the small spectral separation of rotational bands, the interrogation and filtering mechanisms must be at least as narrow. The injection-seeded, cavity-locked, frequency-tripled titanium: sapphire source is an excellent narrow band tool for high resolution measurements of individual rotational lines. Further, because of the Raman scattering cross-section's strong frequency dependence (ν_o^4, see below) the laser's ultraviolet output is a desirable. Because the light source is paired with fixed frequency filters, it is necessary that the source be tunable, to obtain spectral signatures and maximize filter throughput. The novel spectral filters will be more thoroughly discussed in subsequent sections; however, it is informative to outline the goals of the spectral filters. As mentioned, high spectral resolution and background suppression are foremost. Each device acts as a narrow bandpass filter, rejecting out-of-

band light, while simultaneously capturing a spectrally narrow in-band component. High discrimination between in-band and out-of-band light is necessary, as is high throughput (efficiency). Finally, for diagnostics applications imaging is desirable. The two differing filter designs preserve 2-D and 1-D images respectively. Their relative merits and capabilities are discussed in the following chapters.

Raman scattering (theory)

In order to model the spectral signature and intensity of rotational Raman scattering of particular molecules it is necessary to explore some theory behind the scattering process. Volumes have been written detailing this theory. Notable sources listed in the references at the end of the chapter and include: Raman's original paper, Long's theoretical discussion, and theoretical and experimental descriptions given by Eckbreth and Weber. Here the governing equations are presented and implications discussed. The number of collected photons per camera pixel (which images an area l^2) is given by:[Penney]

$$S = N(\Delta N)_J l^2 \delta \frac{E_L}{h\nu A}\left(\frac{d\sigma}{d\Omega}\right)_{JJ'} \Delta\Omega \qquad \text{V.1}$$

where N is the number density of a given species; ΔN_J is the fraction of the population in rotational state J; E_L is the energy per pulse of the incident laser; A is area or cross-section of the laser sheet with thickness δ; $h\nu$ is the energy per photon; $\left(\frac{d\sigma}{d\Omega}\right)_{JJ'}$ is the differential cross-section (discussed below); $\Delta\Omega$ is the solid collection angle. Because even at modest temperatures, the population, N, is distributed among several rotational energy levels, the overall number density is multiplied by the Boltzmann faction of a particular level, $(\Delta N)_J$.

In thermal equilibrium, the Boltzmann distribution is given by the following relation:[Steinfield]

$$(\Delta N)_J = \frac{N_J}{N} = \frac{g_J(2J+1)\exp\left[-\frac{E_J}{kT}\right]}{\sum_J g_J(2J+1)\exp\left[-\frac{E_J}{kT}\right]} \qquad \text{V.2}$$

where g_J is the statistical weighting of the Jth rotational level; k is Boltzmann's constant; E_J is the energy level; T is the temperature. The denominator on the Boltzmann distribution, often call the rotational partition function, may be approximated for homonuclear molecules in the Σ state by:[Herzberg]

$$Z = (2I+1)^2 k\frac{T}{2hcB_o} \qquad \text{V.3}$$

where I is the nuclear spin quantum number; h is Plank's constant; c the speed of light; B_o is the rotational constant for the lowest vibrational level. The energy levels, E_J, are given approximately by:[Weber(1979)]:

$$E_J = hc\{B_o J(J+1) - D_o[J(J+1)]^2 + \ldots\} \qquad \text{V.4}$$

where the first term B_o is the solution to a rigid rotor, and the second term includes centrifugal distortion, D_o. Strictly speaking, these are the rotational energy levels represented by the lowest vibrational state v=0. To include rotational-vibrational coupling, the constants B_o and D_o are replaced by:[Weber(1979)]

$$B_v = B_e - \alpha_e\left(v + \frac{1}{2}\right) \text{ and } D_v = D_e + \beta_e\left(v + \frac{1}{2}\right) \qquad \text{V.5}$$

The spectral signature of rotational Raman scattering is determined from the constants B, D, J and the allowed transitions. For homonuclear molecules, $\Delta J = J' - J = \pm 2$,

representing the S- and O- branches respectively. Intuitively, a homonuclear molecule rotates about its axis reaching an identical position every half revolution, or twice the rotational frequency. Subtracting two energy levels (Equation V.4) gives:

$$\Delta\bar{\nu} = (4J+6)B_o - D_o[6J+9+(2J+3)^3] \qquad \text{V.6}$$

Note that for the O- branch, J → J'=J-2, but the above equation uses the lower, final state J' to calculate Raman shift (intensity will still depend upon upper state population). For the S branch, the lower J level is used, as would be expected. Figure 2 gives a simplified model plot of nitrogen rotational Raman scattering, where the even: odd degeneracy, relative population distribution, and energy separation are shown, but the scattering cross-

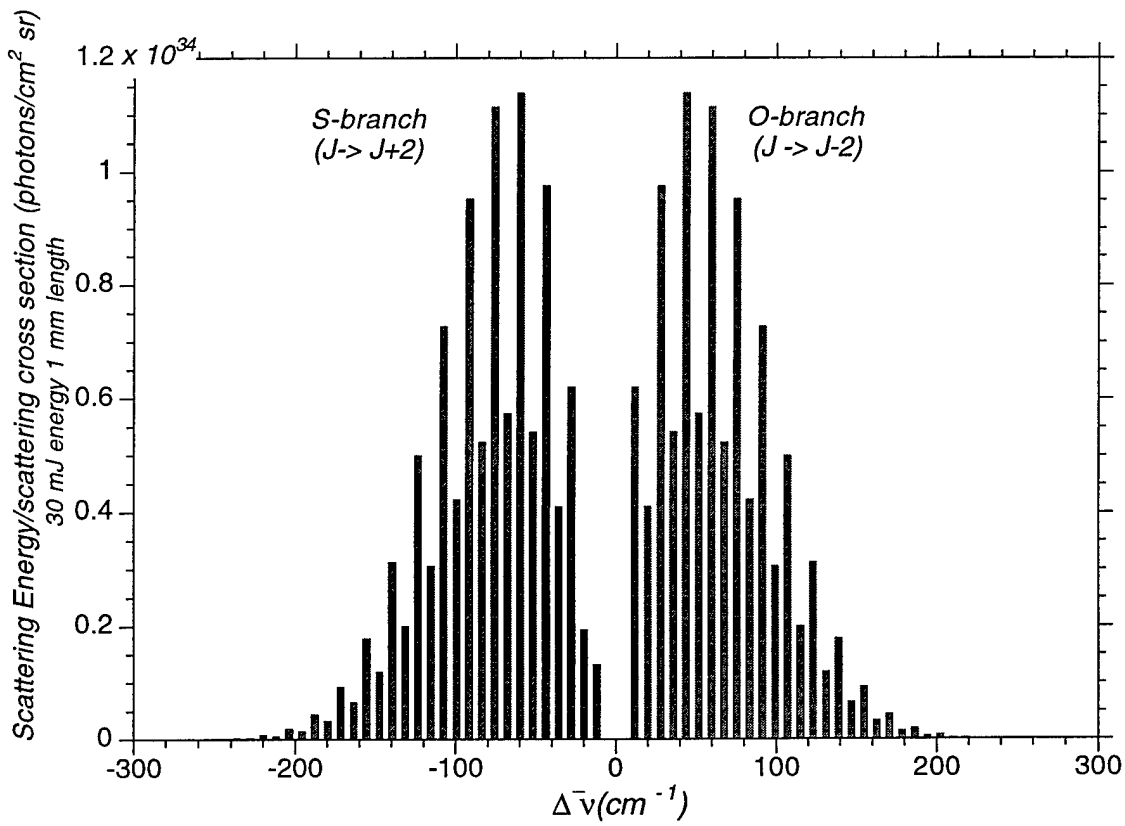

Figure 2: Rotational Raman scattering for N_2 at STP. The normalized signal does not include the scattering cross-section to highlight the Boltzmann population distribution

section (with J-level dependence) is not included. The signal levels reflect the relative number of photons scattered from a 30mJ/pulse laser across 1mm sample at STP.

To quantitatively describe rotational Raman scattering requires knowledge of the differential cross-section incorporated in Equation V.1. The differential rotational Raman scattering cross-section, including direction and polarization dependence is given by:[Penney]

$$\left(\frac{d\sigma}{d\Omega}\right)_{JJ'} = \left(\frac{d\sigma}{d\Omega_{zz}}\right)_{JJ'}\left[(1-\rho)\cos^2\psi + \rho\right] \qquad \text{V.7}$$

where ψ is the angle between the polarizations of the incident electric field (laser) and the scattered electric field. As may be deduced, $\left(\frac{d\sigma}{d\Omega_{zz}}\right)_{JJ'}$ is the scattering cross-section for light scattering polarization parallel to that of the incident beam. Here, the z direction is denoted as the polarization direction. The depolarization ρ indicates the ratio of perpendicularly polarized component to the parallel polarized scattering. Theory gives the depolarization ratio of 3/4 for rotational Raman scattering.[Long, pg 104] Notably, this is quite different for Rayleigh scattering where the depolarization ratio is on the order of a few percent.[Rothe]

The differential cross-section for scattered light polarized in the same direction as the incident beam polarization is:[Penney]

$$\left(\frac{d\sigma}{d\Omega_{zz}}\right)_{JJ'} = (2\pi)^4 \frac{4}{45} b_{JJ'}(\bar{\nu}_o + \Delta\bar{\nu})^4 \gamma^2 \qquad \text{V.8}$$

where $\bar{\nu}_0$ is the incident light frequency (in wavenumbers), γ is the anisotropy of the molecular-polarizability tensor, and $b_{JJ'}$ is one of the Placzek-Teller coefficients. For linear atomic molecules the Placzek-Teller coefficients for the S- and O-branches

are:[Eckbreth, pg 170]

$$b_{J,J+2} = \frac{3(J+1)(J+2)}{2(2J+1)(2J+3)}$$

$$b_{J,J-2} = \frac{3J(J-1)}{2(2J+1)(2J-1)} \qquad \text{V.9}$$

The anisotropy γ arrives from the interaction of the diagonal and off-diagonal elements of the polarizabilty tensor. While theory has been developed to calculate values for given molecules, experimental measurements are taken in this work. The above theory is used to scale the previously measured cross-sections for interrogation wavelength, and rotational level. Table 5.1 lists the relevant parameters (and references) for the molecules discussed here.

Rotational Raman Scattering Constants

Gas	g_{odd}	g_{even}	I	B_o[cm^{-1}]	D_o[cm^{-1}]	$\left(\frac{d\sigma}{d\Omega_{zz}}\right)_{JJ'}$ (10^{-29}/cm^2 sr)
N_2	3	6	1	1.990	$5.7\ 10^{-6}$	7.4 (J=6 → J=8)
O_2	1	0	0	1.438	$4.8\ 10^{-6}$	19.3 (J=7 → J=9)
H_2	3	1	1/2	60.8	0.046	1.7 (J=2 → J=4)
CO_2 (00^{0}0)	0	1	0	0.390	$1.3\ 10^{-7}$	73 (J=16 → J=18)

Table 5.1: Rotational Raman scattering parameters for N_2, O_2, CO_2, and H_2.
N_2,O_2, CO_2 cross-sections from Penney (scaled from 488 nm), H_2 cross-section from theoretical calculations by references Victor; Bridge. Rotational constants B_o, D_o from Weber; Eckbreth

Figure 3 plots the relative rotational Raman scattering signals for nitrogen and oxygen (each at 296K, 1 atm for a 30mJ laser pulse along 1mm). Specifically, the plot is of the parallel polarized scattering cross-section multiplied by the Boltzmann fraction for a given rotational level at 296K, and thereby includes all the J-level dependent terms. Additionally, the relative scale (and location) of the Rayleigh line is plotted in the same units on the right-hand axis. This figure demonstrates a few of the aforementioned salient features of Raman scattering. Notably, another axis had to be employed to simultaneously plot the relative strength of the Rayleigh line to any given rotational Raman line. While

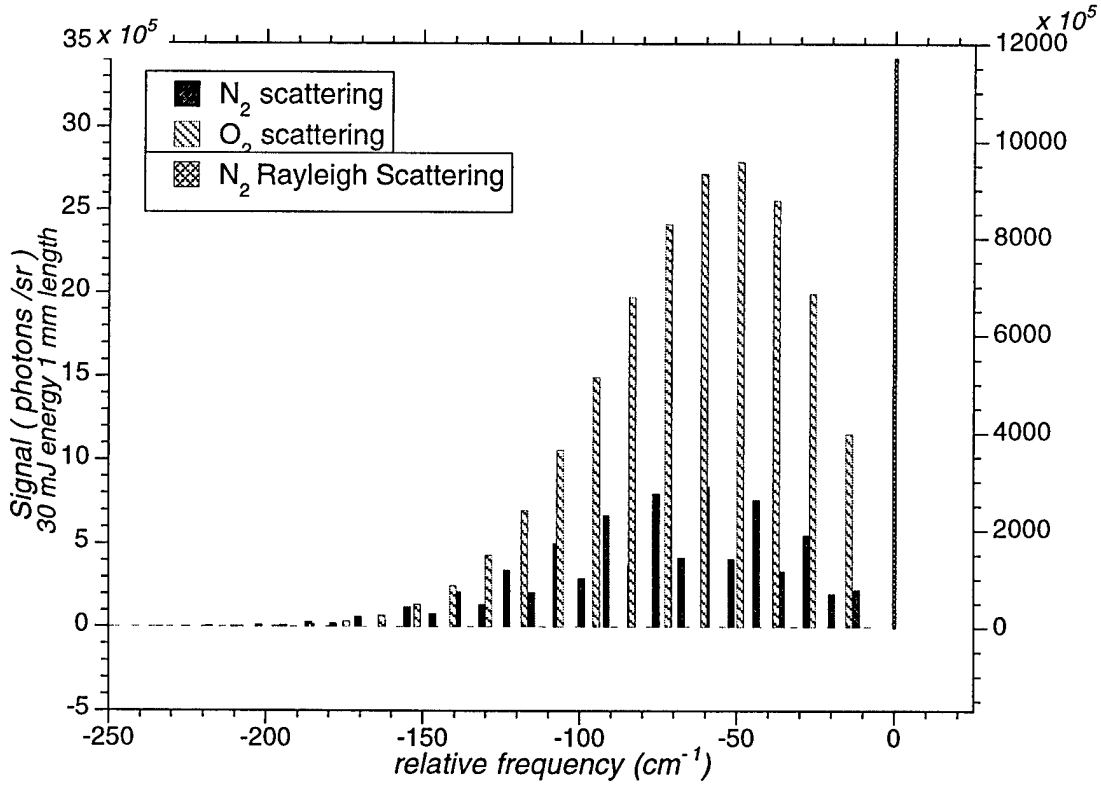

Figure 3: Rotational Raman scattering signal for N_2 and O_2 each at STP (left axis) compared with N_2 Rayleigh scattering signal (right axis)

the N_2 Rayleigh cross-section of 1.1 10^{-26} cm^2/sr,[Eckbreth, pg 175] is roughly 150 times the rotational Raman scattering cross-section, the Boltzmann fraction in any given rotational level reduces the fractional signal (Raman/Rayleigh) to roughly 1: 1500. At higher temperatures, as the Boltzmann distribution spreads out (populating higher rotational energy levels), this effect is accentuated. The relatively larger scattering cross-section of oxygen is evident in the higher peaked lines. While oxygen has a smaller B_o coefficient which leads to more closely spaced lines, the even: odd statistical weighting of O_2 (0:1) reflects the absence of every other line. The even: odd weighting of N_2 (2:1) varies the signal strength of the alternate nitrogen lines. The challenge for spectral filtering technology is to resolve rotational Raman lines separated by wavenumbers, while suppressing more than three orders of magnitude of Rayleigh scattering which is spectrally shifted on the order of 10 cm^{-1}. Further, for diagnostics applications, it is desirable to maintain imaging (2-D spatial resolution) while meeting these spectral filtering demands.

References

Bridge, N.J., and Buckingham, A.D., *Proceedings of the Royal Society A*, 295, 334 (1966).

Cohen, A., Cooney, J.A., and Geller, K.N., "Atmospheric temperature profiles for lidar measurements of rotational Raman and elastic scattering," *Applied Optics*, **15**, 2896-2901, (1976).

Cooney, J.A., "Measurement of atmospheric temperature profiles by Raman backscatter," *Journal of Applied Meteorology*, **11**, 108-112, (1972).

Drake, M.C., and Rosenblatt, G.M., "Rotational Raman Scattering from Premixed and Diffusion Flames," *Combustion and Flame*, **33**, 179-196, (1978).

Eckbreth, A.C., Laser Diagnostics for Combustion Temperature and Species, Abacus Press, Cambridge, MA (1988).

Gu, Y., Rothe, E.W., Reck, G.P., "One-Dimensional Imaging of H_2 Densities and of Temperatures via Rotational Raman Scattering of Narrow-Band, 248nm, Laser Light," *Journal of Raman Spectroscopy*, **28**, in press (1997).

Herzberg, G., Molecular Spectra and Molecular Structure, II: Spectra of Diatomic Molecules, Van Norstrand Reinhold Co, New York, NY, (1950).

Kyritsis, D.C, "Investigation of two dimensional spontaneous Raman imaging for fluid mechanics and engine applications," Doctoral Thesis, Department of Mechanical and Aerospace Engineering, (1997)

Long, D.A., Raman Spectroscopy, McGraw Hill, New York, (1977).

McKenzie, R.L., Hanson, R.K., and Eckbreth, A.C, "Shedding new light on gas dynamics," *Aerospace America*, **30**(11), 20-29, (1992).

McKenzie, R.L., "Progress in Laser Spectroscopic Techniques for Aerodynamic Measurements: An Overview," *AIAA Journal*, **31**(3) 465-477, (1993).

Penney, C.M., St.Peters, R.L., and Lapp, M., "Absolute rotational Raman cross sections for N2, O2, and CO2," *Journal of the Optical Society of America*, **64**(5), 712-716, (1974).

Raman, C.V., and Krishnana, K.S., "A new type of secondary radiation," Nature, **121**, 501 (1928).

Rothe, E.W., and Andresen, P., "Application of tunable excimer lasers to combustion

diagnostics: a review," *Applied Optics*, **36**(18), 3971-4033, (1997).

Steinfeld, J.I, Molecules and Radiation: An Introduction to Modern Molecular Spectroscopy, MIT Press, Cambridge, MA, 261, (1978).

Stricker, W., "Local Temperature Measurements in Flames by Laser Raman Spectroscopy," *Combustion and Flame*, **27**, 133-136, (1976).

Vaughn, G., Wareing, S.P., Pepler, S.J., Thomas, L., and Mitev, V., "Atmospheric temperature measurements made by rotational Raman scattering," *Applied Optics*, **32**(15), 2758-2764, (1993).

Victor, G.A. and Dalgarno, A., "Dipole Properties of Molecular Hydrogen," *Journal of Chemical Physics*, **50**(6), 2535-2539, (1969).

Vincenti, W.G., and Kurger, C.H., Introduction to Physical Gas Dynamics, Wiley and Sons, Inc., New York, Chapter 7, Section 2, (1965).

Weber, A., "High Resolution Raman Studies of Gases," in The Raman Effect, ed. A.Anderson, Vol 2, Marchel Decker, New York, 543-757, (1973).

Weber, A, "High-Resolution Rotational Raman Spectra of Gases," in Raman Spectroscopy of Gases and Liquids, ed. A.Weber, Springer Verlag, Berlin (1979).

Chapter 6: A Narrow Passband Imaging Filter Applied to Rotational Raman Scattering

Filter description and background

Many diagnostic techniques require, or are enhanced by, ultra-narrow linewidth spectral filters. In their simplest incarnation, narrow bandwidth notch filters may be used to suppress elastic background scattering, while simultaneously imaging Doppler shifted, or thermally broadened Rayleigh or Mie scattering.[Lempert] As detailed in Chapter 4, spectral filters utilizing atomic or molecular transitions can provide high attenuation, sharp spectral cut-off, and spectral absorption bands on the order of GHz. Such a filter has been used in combination with a monochrometer to suppress one strong feature, as with the Rayleigh/elastic scattering, while the monochrometer spectrally resolve other scattering (Raman scattering or molecular fluorescenece).[Rasetti; Indralingam; Guenard] However, such notch filters absorb only over a small spectral band and transmit light everywhere else. In many cases, a filter with a narrow passband is preferable. Rather than attenuate light at one given frequency (as a notch absorption filter does), a passband filter attenuates all light, except at a given frequency. Diagnostic techniques in which background scattering at multiple frequencies must be suppressed or where weakly scattered spectral lines are to be observed require the use of a narrow passband filter.

While ultra-narrow spectral passband filters exist, they typically suffer from difficulties with background suppression, center line transmission, collection efficiency, or lack imaging capability. For example, conventional thin-film coated spectral filters are limited by a constrained acceptance angle, a few orders-of-magnitude attenuation

out-of-band, poor edge discrimination (shallow sloping spectral profile), and spectral widths on the order of wavenumbers. Gelbwachs reviews an alternative — atomic resonance filters (ARF), which provide an ultranarrow passband.[Gelbwachs] A narrow band of incident radiation is absorbed by an atomic vapor and subsequently fluoresced at a different frequency. This frequency shift allows for conventional filters to provide out-of-band extinction by placing appropriate filters on the entrance and exit of the vapor cell. Conversion efficiency, the signal-to-noise ratio, and background suppression can be quite high. However, since the absorption and fluorescence process takes place through the volume of the vapor cell, it is not appropriate for spatially resolved measurements. In a similar vein, Faraday filters provide desirable spectral profiles by using the index-of-refraction dependence and Zeeman splitting of resonance levels.[Menders] Cross-polarizers replace the conventional broad spectral filters of the ARF, and provide out-of-band attenuation. When a strong magnetic field is applied to a vapor, light near resonance undergoes a polarization rotation and passes through the polarizers. Ultra-narrow band operation has been demonstrated in the infra-red, and visible. However, difficulties with ultraviolet polarizers make for poor extinction ratios in the UV. Furthermore, the acceptance angle is limited to large f/# collection by the geometry of the cells and the strong angle dependence of polarizers.

Atomic resonance radiation as spectral filtering tool has been in use for many decades, especially in the field of spectroscopy.[Sullivan]. Dubbed atomic resonance spectrometers, early use focussed on isolating resonance lines in high resolution atomic absorption spectroscopy. Matveev reviews the development of such filters, categorizing the variations of the atomic spectrometer.[Matveev (1987)] While many of the filters offer appropriate filtering properties, none maintain imaging capabilities. More recently,

Matveev and co-workers have demonstrated a narrow spectral band imaging filter utilizing mercury vapor and laser pumping.[Matveev (1997)] Two alternate schemes are presented: fluorescence imaging and resonance ionization imaging. Because there is a fluorescence channel from the 7^3S_1 state to the 6^3P_2 at 546.1 nm, laser pumping at 435.8nm allows for narrow band detection at 253.7 nm, see Figure 1 Chapter 3. As a compliment, laser pumping at 253.7nm allows for detection at 435.8 nm. Spatial resolution achieved an estimated 300 μm, while the spectral sensitivity was roughly 1 cm^{-1}. Aside from the active nature of the filter (laser pumping), the efficiency of the system collecting fluorescence at f/1 is approximated to be 1.25%. Alternatively, resonant ionization imaging is anticipated to yield higher efficiencies. With the presence of a neon buffer gas and adding a high voltage across the vapor, excited state mercury atoms (7^3S_1) are ionized before they fluoresce. A high frequency (rf) power supply is required to localize ionized charge pairs, and subsequent neon emission is observed. 1-D images are presented with no resolution, or efficiency measurements.

The filter presented in this chapter is based on the absorption and subsequent fluorescence of light by atomic mercury vapor, and most similar in design to Langberg's "image forming resonance scatter filter."[Langberg] The strong, and spectrally sharp absorption features of mercury (at 253.7 nm) provide the desired spectral discrimination. The fluorescence process and the long relative lifetime (120ns) of the excited mercury state allow for temporal gating which further eliminates background scattering from relatively short interrogation laser pulses. Due to the large transition strength of mercury, absorption can be made to occur over a short distance through the vapor, and fluorescence is effectively from a planar sheet. Thus, images may be preserved, despite the absorption and fluorescence processes.

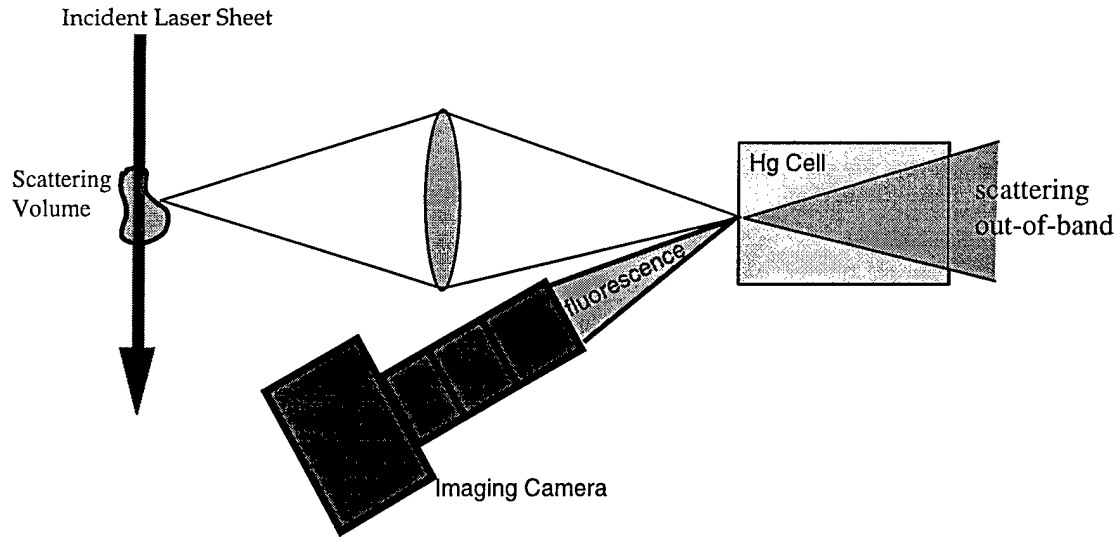

Figure 1: Narrow passband imaging filter: concept. Scattering from an interrogation volume is imaged onto the inside surface of a mercury vapor cell. Light co-incident with the ground state transition at 253.7nm is fluoresced, and imaged onto a camera.

The ultra-narrow mercury vapor passband filter is based on absorption of incident light at 253.7 nm, and it subsequent resonant fluorescence. Figure 1 illustrates a typical implementation of the filter. A laser or light source is used to illuminate a target volume. Scattering from the volume is imaged onto the front surface of a cell containing mercury vapor. If the incident light on the cell surface is spectrally outside the mercury vapor absorption band, the light passes through the vapor cell. Light passing though the vapor cell is considered rejected. If the light scattering frequency is coincident with the mercury absorption band, the scattering is absorbed. Even with a modest amount of mercury vapor present, incident light coincident with the ^3P-^1S transition is absorbed close to the front surface of the cell. Thus, for two dimensional resolution, the scattering source is imaged onto a sheet near the front of the mercury vapor cell. Because the absorption is a ground state transition and the vapor pressure is low, the fluorescence efficiency is quite high.

Almost all of the light incident on the cell surface, coincident with the mercury absorption band, is re-radiated out the front surface of the cell. This re-radiation is then imaged onto an intensified camera. Thus, the only light reaching the camera is that scattered light coincident with the mercury absorption band.

The cell used for characterization of the filter concept and experimental application was the same cell used earlier, Figure 3 in Chapter 3. The spectral profile of the filter, in the simplest approximation, is just the inverse of the absorption profile at low vapor pressure. Modeling gives a prediction for the spectral profile as well as the limiting out-of-band rejection. The temporal fluorescence characteristics of the narrow passband filter provide a means of further filtering background scattering, and give insight into the dynamics of the filter fluorescence process. By using a pulsed laser, with a typical pulse duration of approximately 10 ns, unwanted background scattering may be temporally gated out. Because mercury vapor has a natural lifetime of 120 ns, the fluorescence is much longer lived than the initial laser pulse. Stray reflections and other out-of-band noise may be gated out by operating a high speed micro-channel plate intensifier to collect light after the laser pulse illuminates the scattering source. Experimental characterization of the spatial resolution of the filter has been performed, along with analysis of efficiency of the dual collection imaging system inherent to this filter design. Saturation limits of the filter were explored, detailing its utility for quantitative imaging. Finally experimental measurements of both Rayleigh and Raman scattering were performed, illustrating the filter's features.

Filter characterization

spectral characteristics and rejection

Scans of the spectral transmission of the narrow passband filter were collected by illuminating the Hg cell with the ultraviolet laser source. The experimental set-up was similar to the concept Figure 1; however, the initial imaging/ collection step was replaced by directly illuminating the Hg cell with the laser. The incident laser power was attenuated to approximately 100 pico-Joules with a combination of several front surface reflections, neutral density filters, and finally a polarizer as a variable attenuator. The beam was attenuated until the data collected varied linearly with incident laser power. Fluorescence from the mercury vapor was imaged with a 50mm f/1 lens through a mercury line interference filter, onto a photomultiplier tube. Simultaneously, the transmission through the 5 cm cell was monitored with a second photomultiplier tube and an identical mercury line interference filter. In this way, measurements of the mercury vapor cell acting as a narrow passband, and a narrow absorption band filter were made simultaneously. Ten pulse averages, with a variety of collection gate times, were collected with a Stanford Research Systems boxcar integrator, digitized, and stored on a personal computer. Laser power was simultaneously tracked with a photodiode and a boxcar integrator.

Figure 2 is a measure of intensity versus laser frequency for both the absorption and fluorescence filtering modes of the mercury vapor cell. The sidearm is held at 27.5C (corresponding to 0.0023 Torr). The body temperature is 67 C. The laser is scanned continuously over approximately 1 cm^{-1} in 12 MHz steps. The upper trace is the fluorescence signal with relative signals levels plotted 0 to 1. The integrator gate time for

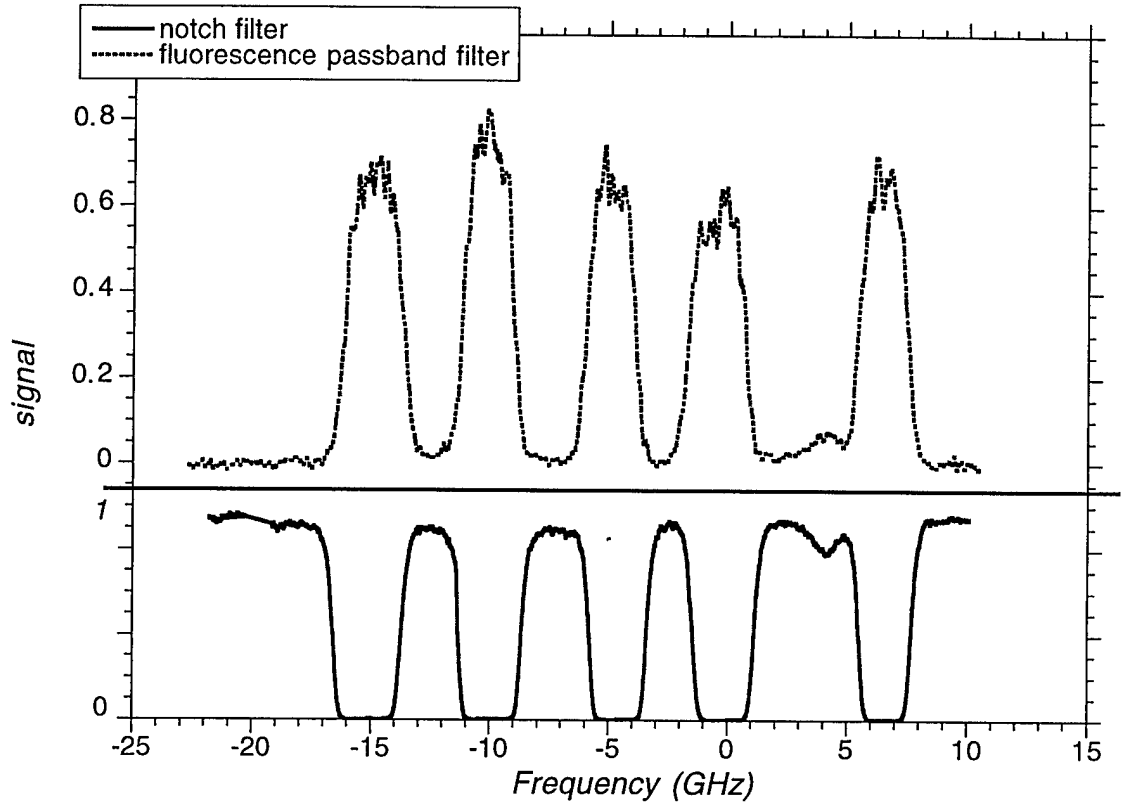

Figure 2: Narrow passband filter and notch absorption filter: spectral profiles. Simultaneous spectral scans of the Hg cell operating in two modes. Above narrow passband; below notch absorption. The bands arise from naturally occurring isotopes.

the fluorescence channel was 4 microseconds and began 60 ns after the laser pulse. The lower trace is the absorption notch filter profile, similar to those seen in Chapters 3 and 4. The integrator gate time is roughly 50ns, centered on the laser pulse. Six absorption and fluorescence lines can be identified, corresponding to the naturally occurring isotopes of mercury. Note that the Hg 196 line is optically thin (due to its low natural occurrence), whereas all other isotopes are optically thick. To a first approximation, the absorption and fluorescence spectra are inverses of one another. They both exhibit sharp walls, narrow bandwidth, and relatively flat in-band profiles.

model

A Monte Carlo model was developed to describe the temporal and spectral behavior of the narrow bandpass filter. Resonance radiation has been examined in a variety of contexts, both integral-differential and Monte Carlo treatments of the problem have been published.[Holstein; Anderson; Sommerer] Generally, at issue is tracking of photons initiated *inside* a volume, and observing radiation exiting (e.g. fluorescent lamps). In this application, photons *enter* the volume, excite atoms, and subsequent fluorescence is observed. Figure 3 gives a flow-chart of the model which is listed in Appendix C. The model is a two dimensional simplification of the problem, and yields fluorescence signal as a function of input frequency, and temporal response to instantaneous (delta-function) input radiation. A photon with frequency ν_i enters the cell of mercury vapor at pressure P, and temperature T. A penetration depth is calculated based on the absorption co-efficient, $\Gamma_i(\nu,T,P)$ given in Chapter 3, and yields a weighted exponential distribution (according to Beer's law):

$$distance = -\frac{1}{\Gamma(\nu, P, T)}\ln(\chi) \qquad \text{VI.1}$$

where χ is a random number between 0 and 1. After an similarly distributed exponential amount of time, t, the photon is emitted.

$$t = -\tau\ln(\chi) \qquad \text{VI.2}$$

where τ is the lifetime of the excited atom; χ is another random number between 0 and 1. The photon exits the atom with a random angle θ, and new frequency ν_f. The fluorescence frequency has been treated in two fashions, which yield results within a few percent of one-another. As described by Holstein, and Anderson, the probability of emission at a

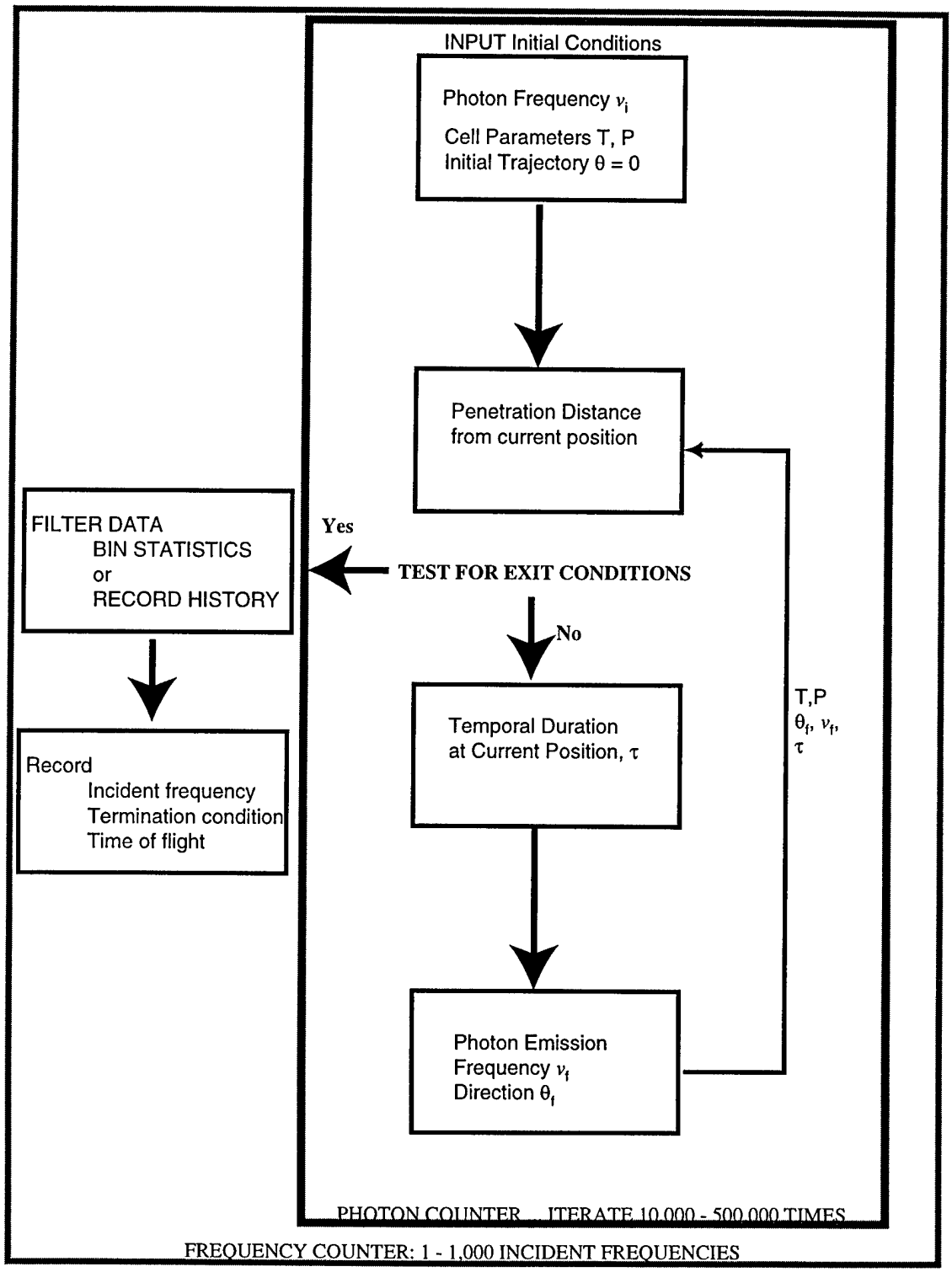

Figure 3: Flow chart for Monte Carlo model of narrow passband filter. Input parameters are cell conditions (temperature, pressure), incident light frequency, and trajectory. Output is either a photon flight history, or catalog of incident frequency versus cell response.

frequency is proportional to the absorption co-efficient for that frequency.[Holstein; Anderson] In this case a Gaussian distribution about the atomic resonance center is sufficient (pressure broadening effects are essentially absent). The second means of ascertaining fluorescence frequency is to track both the photon direction, and atom direction. In the atom's frame of reference, fluorescence will be at the resonant frequency (with narrow Lorentz distribution). Knowing the atomic direction and photon fluorescence direction, a Doppler shifted frequency may be calculated yielding the lab frame frequency of the photon, ν_f. This process assumes that the atomic path doesn't change during its excited state. Such an assumption is valid with the large mean free path of a low density vapor; it is tantamount to using the Gaussian profile above without the pressure broadening Lorentz component. The new photon frequency and direction are used as inputs to calculate a new distance travelled by the photon, as per Equation VI.1. The process is iterated until an end condition is met. One temporal and three physical boundaries terminate the photon's travel: the photon exits the front surface (signal); the photon passes through the length of mercury vapor (notch filter); the photon reaches a side-wall (quenching); or the photon doesn't exit after a prescribed about of time (quenching or trapping). This entire process is repeated until the results are statistically meaningful. Typically 10-500 thousand photons are run for a given incident frequency. On an Silicon Graphics R10000 processor a run of 10^4 photons takes roughly 10 seconds.

For the purposes of verifying the spectral component of this model, it was compared with the experimental spectral scans of Figure 2. The model input (incident) frequency ν_i was varied between -25 GHz and 15 GHz in 0.04 GHz steps. The model outputs a table of incident frequency, and photon counts out the front, back, side-wall, and

held by the cell. The vapor pressure and temperature of the modeled filter matched those listed above. Plotting the number of photons ejected photons from the front surface (out of 10,000 incident) as a function of input frequency results in Figure 4. For comparison, experimental measurements are simultaneously plotted. Good agreement between the model and experiment is observed. While the data is somewhat noisy, the model accurately captures the modest change in transmission* peak heights at this vapor pressure. The bandwidth of individual isotopic passbands is generally captured, and deviation of line locations is within the experimental uncertainty and control of the laser. At higher vapor pressures, the model predictions are given in Figure 5. While the in-band transmission increases from 0.002 Torr, the maximum transmission is reached by 0.1 Torr. Increasing the vapor pressure beyond this point has marginal effects on the spectral response of the filter, as demonstrated by the excessively high vapor pressure of 1 Torr. At peak transmission, only 80% of the incident radiation is passed. The remainder of the incident light is radiatively trapped, or quenched. The most demonstrative effect is seen in the Hg 196 line where increasing vapor pressure increases transmission, to the approximately the peak levels of the other isotopes. This strongly suggests that beyond a given optical depth (approximately 100/cm), no gain is observed in fluorescence yield. It is also worthy of note that given appropriate parameters, the model follows the fluorescence trends of mercury pen lamps, which reach the highest intensity not a line center, but in the edges of the absorption band.[Anderson] Similar behavior has been observed in particular operating regimes of the optically thick vapor cell.

---

* It is important to not the distinction between *transmission* peaks or *transmission* filter (that light which is absorbed and subsequently fluoresced by mercury) and *transmission* through the vapor cell (where the cell acts as a notch absorption filter described in Chapter 4).

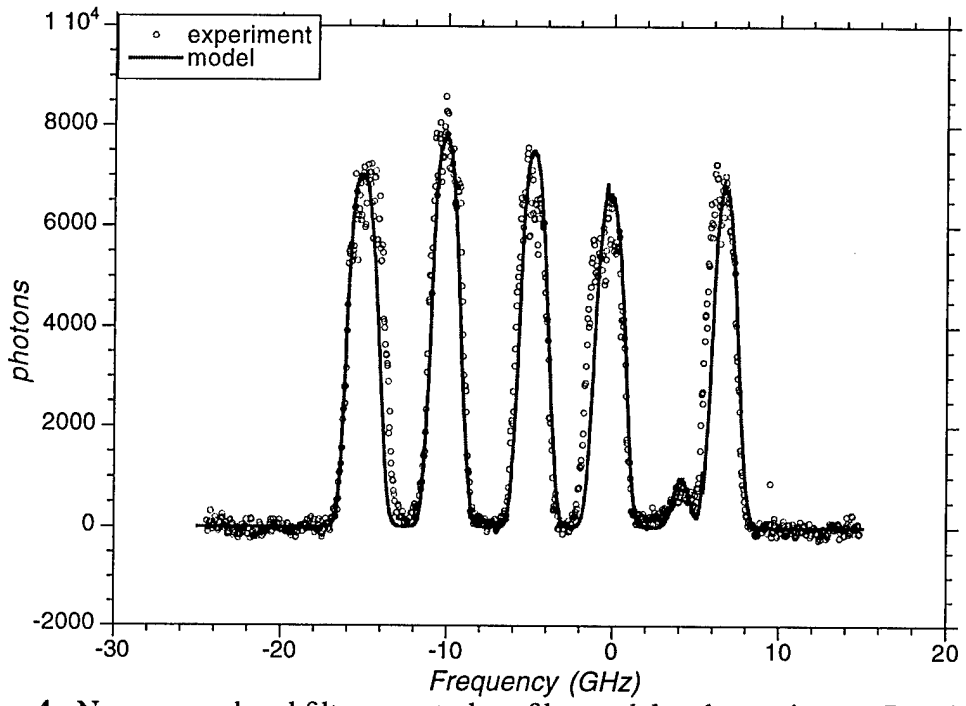

Figure 4: Narrow passband filter: spectral profile, model and experiment. Results from the Monte Carlo simulation are plotted with data off Figure 3.

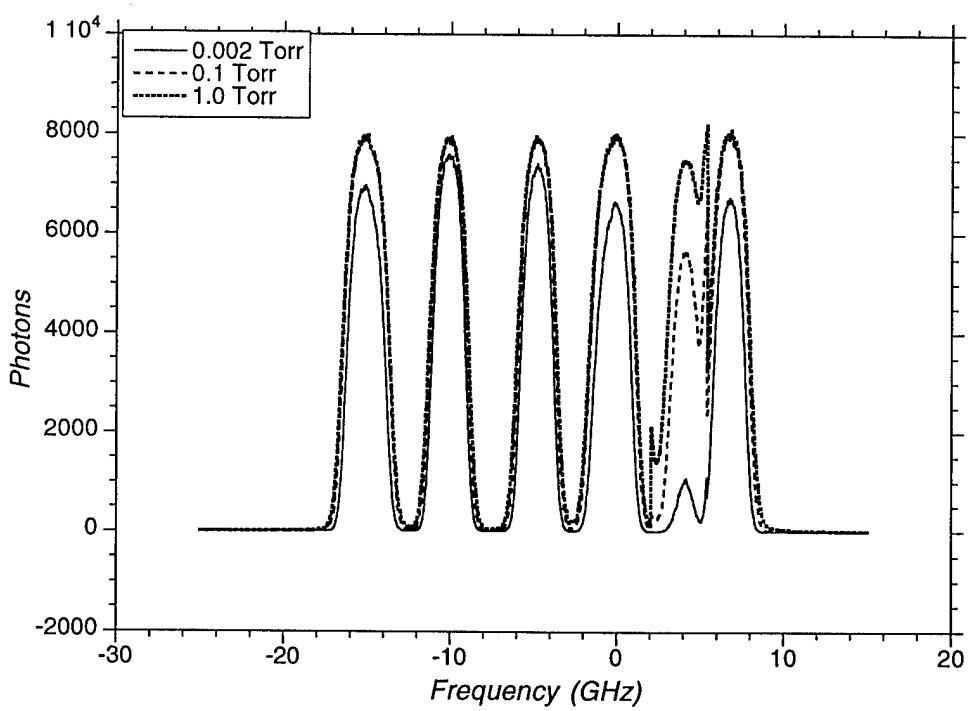

Figure 5: Narrow passband filter: model response at varying mercury cell vapor pressures. 10,000 photons incident on the cell yield signal levels shown.

By assuming a more simplistic model, where the fluorescence signal is the inverted absorption profile, we may calculate an upper bound to the out-of-band extinction of the filter. The absorption spectrum is modeled as an optically thick (center line attenuation >> e^{-1}) Voigt profile. Since the Lorentzian component in the wings of the absorption dominates out-of-band it will be this homogeneous component of the broadening which determines the extinction. In all of the cases considered, the vapor pressure is well below 1 Torr, and thus, the dominant homogeneous broadening mechanism is the natural 120ns lifetime of the mercury transition. The predicted out of band transmission 0.5 cm^{-1} away from line center is: 1 10^{-4}, 1.8 10^{-3}, and 3.7 10^{-3} for cell pressures of 0.002 Torr, 0.02 Torr, and 0.04 Torr respectively. At 3 cm^{-1} from linecenter, the corresponding transmission drops to 4 10^{-6}, 6 10^{-5}, and 1.2 10^{-4}, respectively. It is interesting to note that the predicted out-of-band extinction is highest at the lowest vapor pressure.

temporal characteristics

The extended temporal lifetime of fluorescence from the narrow passband filter gives an effective means of suppressing background noise induced by and coincident with a short pulse interrogation source. For applications where a short lived, spectrally close/ coincident and large background signal exists (due to elastic scatter for instance), the temporal features of this filter provide an excellent means of capturing desired signals. Because the filter relies on the fluorescence of excited state mercury vapor, a filtered signal that is 'passed' by this filter exists for an extended time, even if it is produced by a short-lived event. While the excited state natural lifetime of mercury vapor is 120 ns,

optical trapping of radiation stretches signals to the microsecond time scale. Because the absorption band used to excite the mercury vapor is a ground state transition, fluorescence is resonant with the excitation source. Thus, as a photon is fluoresced by an atom, it likely encounters another atom which absorbs the photon before it exits the cell. This radiative trapping insures high signal yields (high quantum efficiency), and causes the temporal profile of incident radiation to be stretched. Interfering background light does not experience this temporal stretch (unless it too is imaged onto the cell, and co-incident spectrally), and thus disappears when the source laser pulse terminates. By gating the imaging camera to capture signal after the laser pulse, this background signal is suppressed. The amount of signal lost is proportional to the gating delay, but may be minimized due to the relative durations of the laser pulse and fluorescence signal.

The temporal profile of the passband filter was characterized by capturing fluorescence from the mercury after it is excited by a short (10 ns) interrogation pulse. The experimental setup was the same as for the above described spectral scans, except that the fluorescence signal was captured with a digital oscilloscope (Tektronix TDS 350) instead of the boxcar integrator. Simultaneously, a reference signal was captured on the scope to normalize signals and remove rf pickup from the flashlamp driver discharge. The temporal decay of the fluorescence intensity was recorded for a variety of different incident laser frequencies and cell vapor pressures.

Figure 6 shows the fluorescence signal from incident radiation (10ns) coincident with the peak of the Hg 202 absorption at a cell vapor pressure of 0.045 Torr. The temporally elongated decay demonstrates the effects of fluorescence and radiative trapping. The signal decays to 1/e of its initial value after about 450 ns, or almost four

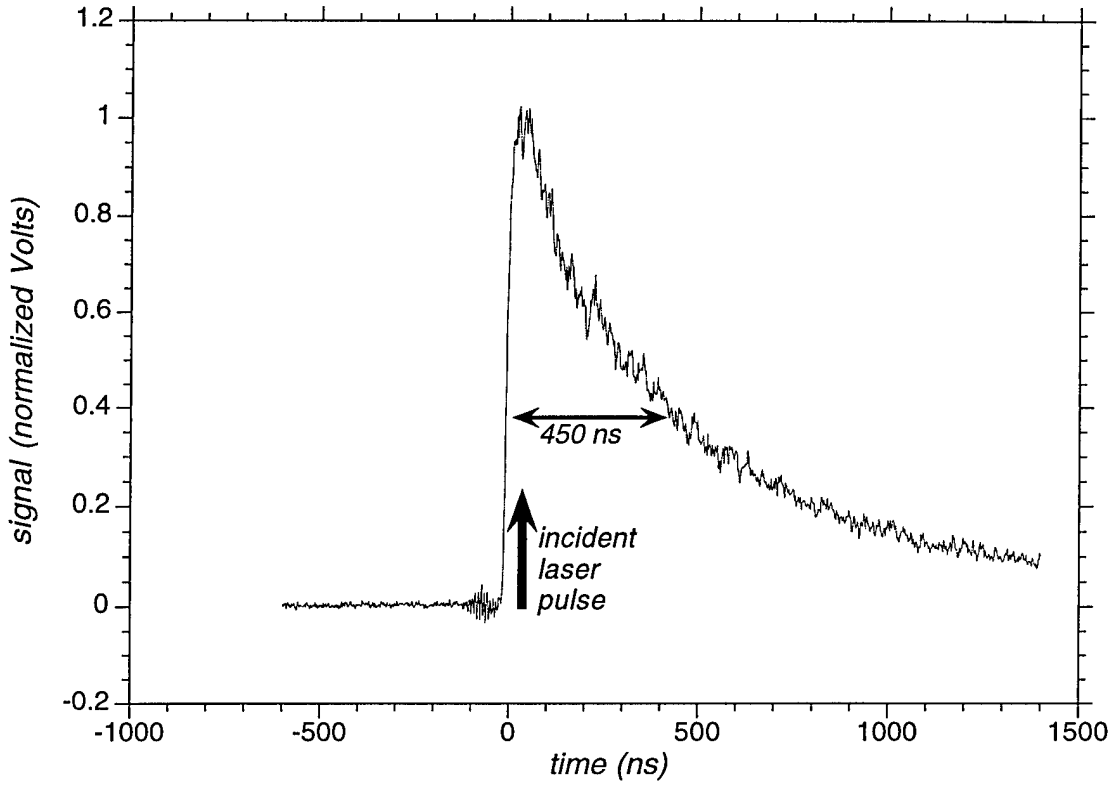

Figure 6: Narrow passband filter: temporal response. The long lived fluorescence decay of the narrow passband filter in response to a short (10ns) incident pulse.

natural lifetimes. Two temporal models describing this profile are discussed below. A further examination of the data presents the salient temporal characteristics. The extent of the profile is well beyond the 1/e point, extending beyond the collection gate of the oscilloscope (1.4 μs) Furthermore, the fluorescence which is temporally coincident with the incident laser pulse represents a minimal amount of the total yield. Conservatively, gating out the first 50ns of light reduces the overall signal by less than ten percent. As discussed in the resolution section below, however, temporal gating does have an effect on the overall resolution of the filter — inherently there are a trade-offs among light collection, resolution and temporal gating.

It is not altogether intuitive as to the effects of optical depth on the temporal profile

of the filter. For incident radiation on line center of an absorption band, it would seem appropriate that a photon will statistically pass a fixed number of atoms before being absorbed. Thus, at lower optical depth light penetrates farther into the cell than it would for a cell at higher optical depth. For given situations (peak of the absorption profile), the same is true to exit the cell. Hence, as depicted by the plots in Figure 7, the effects of vapor pressure and relative number density play a negligible role on fluorescence decay time. Each of the normalized decay profiles follows approximately the same curve. These data represent experimental conditions that vary in number density for a given isotope (Hg 202) by a factor of more than twenty, and relative isotope abundance variation of greater than two.

While the temporal profile appears insensitive to number density, it is not wholly independent of optical depth. More precisely, the temporal profile of fluorescence changes with incident frequency. Figure 8 demonstrates the changing temporal profile of fluorescence from the filter as the incident light source was scanned in frequency. As the incident light source was scanned into the passband of the filter, it was paused at approximately 30%, 50%, and 100% of peak transmission by the Hg 202 band. The 100% transmission plot is the same data as presented in both previous plots (full transmission of the Hg 202 band at a vapor pressure of 0.045 Torr). The signal levels are normalized to highlight the markedly different fluorescence decay profiles. Exponential decay fits to the long lived portion of the graph (to the right of the vertical bar) yield successively longer lived fluorescence for lower optical depth, as shown by the time constants given in the legend of the plot. This increased lifetime is consistent with optical trapping. Given a fixed number density, at frequencies off resonance (and hence lower

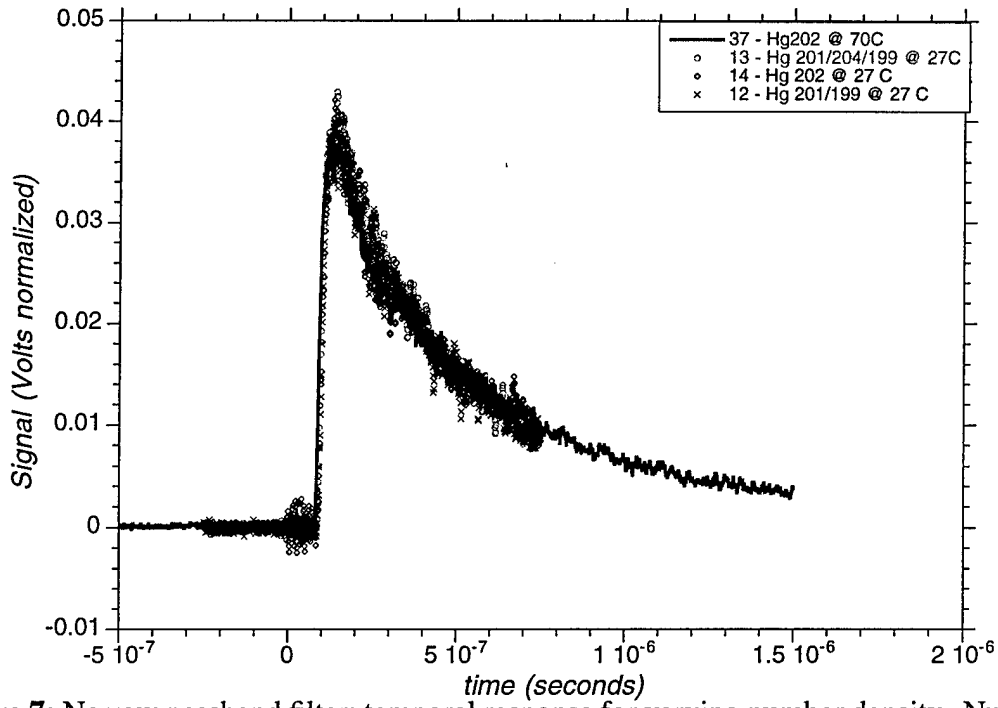

Figure 7: Narrow passband filter: temporal response for varying number density. Number density varies by a factor of 20 for Hg 202 and a factor of two between isotopes.

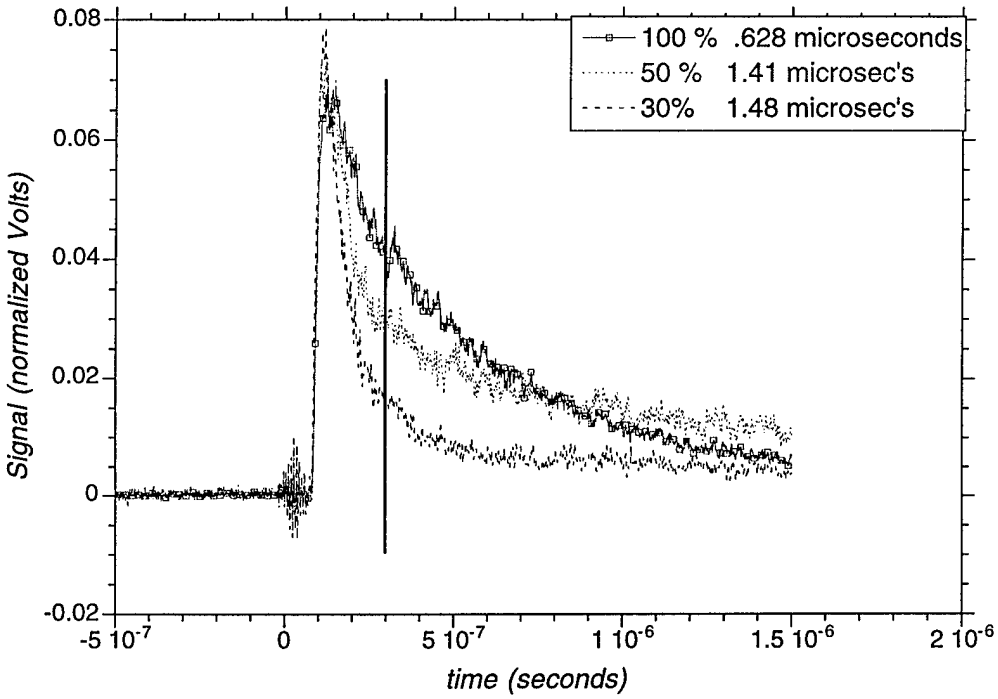

Figure 8: Narrow passband filter: temporal response, varying incident laser frequency. Exponential decay fits to data (right of bar) yield 1/e times listed in legend.

optical depth), photons penetrate further into the cell and are more susceptible to being trapped upon fluorescence.

Examining the temporal decay of each plot demonstrates that the fluorescence is not a simple single exponential decay with extended lifetime. The multiple absorption and fluorescence processes indicate that the decay profile is a sum of independent exponential decay processes, which may be represented as:

$$S(t) = \sum_n \alpha_n(v) e^{-\frac{t}{n\tau}} \qquad \text{VI.3}$$

where S(t) is the time dependent signal; n is the nth decay mode (or the escape of a photon after an average of n absorptions); $\alpha_n(v)$ is a weighting parameter dependent upon both decay mode and incident light frequency; τ is the natural lifetime, or the average 1/e decay time of an excited state atom. Thus in various time regimes, a particular decay mode will dominate, initially the prompt fluorescence, and ultimately the longer lived radiatively trapped light. Figure 9 re-plots the data from Figure 6 with three modeled fits: a single exponential decay fit to the prompt fluorescence (first 200 ns), an exponential decay of the long lived fluorescence (last 600 ns), and a fit of the form in Equation VI.3. Clearly a simple exponential decay captures a portion of, but not the entirety of the fluorescence signal. As may be observed from the fit of summed exponentials, there is contribution from light emanating after even ten or twelve natural lifetimes.

The earlier described Monte Carlo model also gives model predictions for the temporal response of the filter. For each photon at a given incident frequency, the model tracks the duration of the photon-mercury interaction. For incident photons at the peak of a transmission band (-10.106 GHz), a sample of 100,000 photon flight-times were collected. Figure 10 is a histogram of the number of photons exiting per 12.5 ns window.

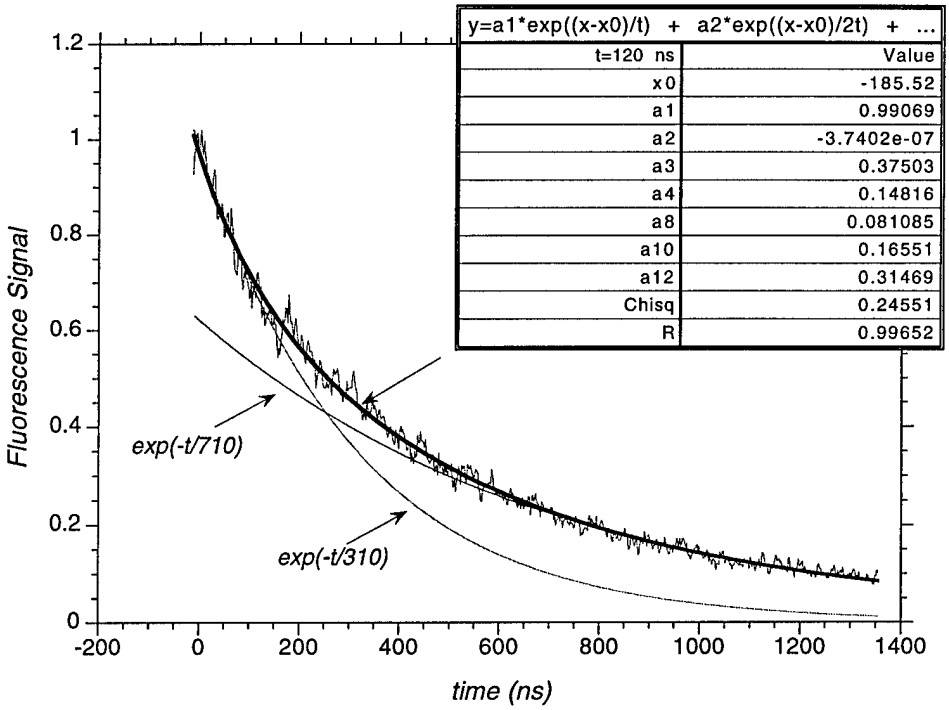

Figure 9: Narrow passband filter: temporal response with fit of summed exponentials. Three fits: two individual exponential decays, and a third which sums eight exponentials.

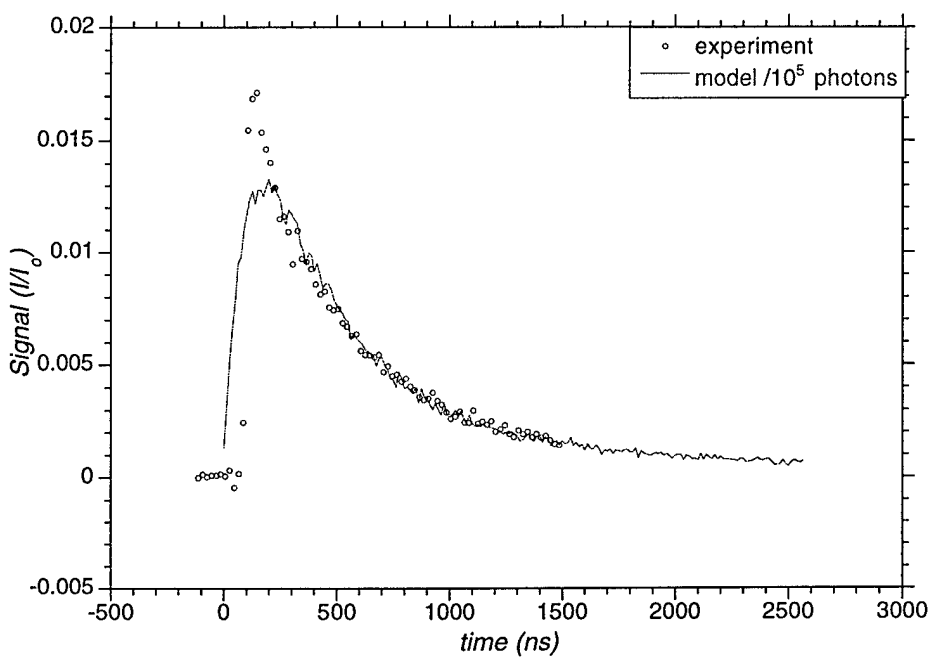

Figure10: Narrow passband filter: temporal response and Monte Carlo model.

The earlier plotted experimental temporal profile is simultaneously shown. Good agreement of the decay profile is observed, especially at longer time scales. The initial mismatch between experiment and model (the first 120 ns), is believed to be due to a convolution of temporal response of the photomultiplier tube and initial ambient radiation/ scattering from the laser pulse. The jagged nature of the model data is due to photon statistics. Though 100,000 photons were modeled, the binning window of 12.5 ns, dramatically reduces the count of photons per bin. The model also captures the variations in optical depth. For variations in isotope and vapor pressure, identical temporal response is observed, in agreement with the plot in Figure 7. Similarly, the model predicts that changes in optical depth due to incident frequency do have an effect, as shown in Figure 11. Two Monte Carlo model predictions along with the data of Figure 8 show the same trends discussed above.

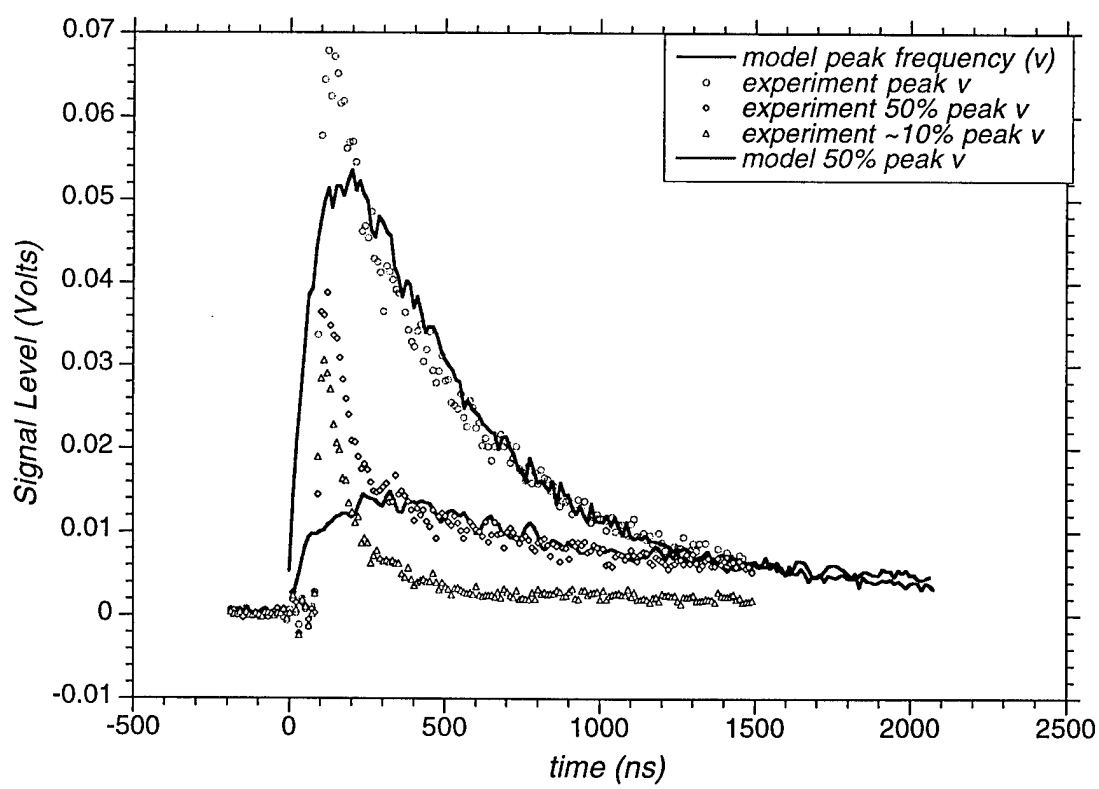

Figure 11: Temporal response of filter and Monte Carlo models with data of Figure 8.

spatial resolution

The narrow passband fluorescence filter is capable of preserving images. Because the mercury vapor absorption may be made optically thick, light imaged on the cell will be absorbed close to the cell surface. For modest cell vapor pressures, 0.05 Torr, the 1/e intensity penetration depth is modeled to be 35 microns. Therefore, subsequent fluorescence will arrive from a well defined plane of minimal thickness, and allow for image preservation. Figure 12 demonstrates this imaging capability. The experimental setup is as described in Figure 1; however, the scattering source is a business card. An f/1 lens is used to image scattering from the card onto the front surface of the mercury vapor cell. An f/4.5 imaging system is then used to re-image the fluorescence onto an intensified CID camera. A mercury line interference filter is placed in front of the camera imaging

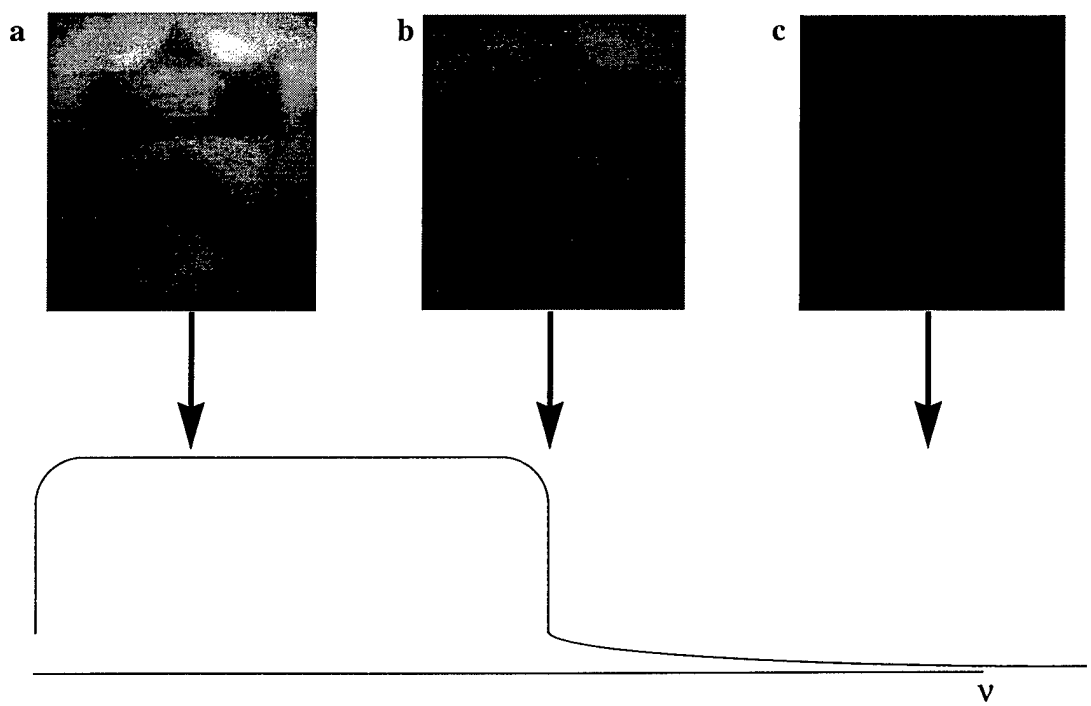

Figure 12: Narrow passband filter: imaging capability. Business card illuminated by laser, imaged through filter. The spectral location of the illumination source is varied. The laser frequency is indicated by arrows above the cartoon of the spectral passband of the filter.

lens to eliminate background scattering. The three images correspond to three differing spectral locations of the illuminating laser source. With the scattering frequency coincident with the filter passband, light is transmitted and the image preserved. As the narrow linewidth laser is scanned in frequency the image scattering is attenuated until the illuminating source is no longer in the passband of the fluorescence filter. Partial detuning of the laser frequency from the center of the filter passband decreases the resolution of the system (Figure 12b). This behavior is consistent with the imaged scattering penetrating farther into the mercury vapor cell, as the optical depth of the filter is lower at this detuned frequency. Finally, out-of-band (Figure12c), no image is radiated by the fluorescence filter.

As anticipated, increasing the optical depth (vapor density) of the cell decreases the penetration depth of incident light, and increases resolution. Figure 13, gives a model

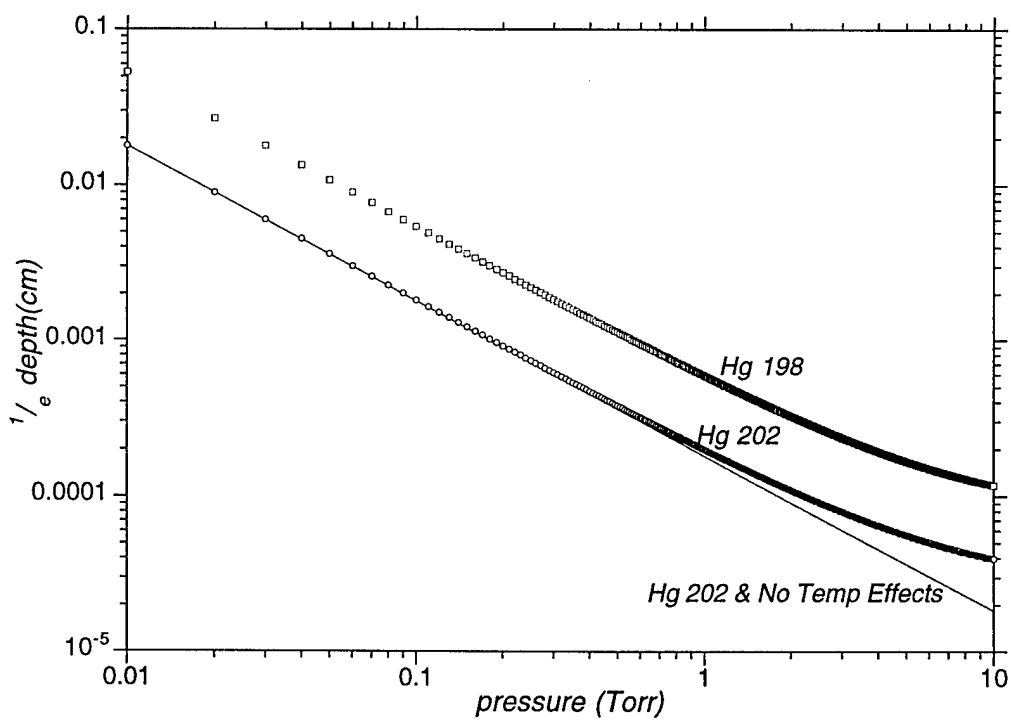

Figure 13: Narrow passband filter: penetration depth as a function of vapor pressure. Plots for two isotopic abundances which include effects of temperature.

of penetration depth (1/e attenuation) into the vapor cell as a function of vapor pressure. Plotted on a log-log scale a linear relation between vapor pressure and penetration depth is observed. This comes directly from the linear relation of number density and absorption co-efficient given by Equation III.6. As shown in the plot, when the increased cell temperatures for elevated vapor pressures is accounted for, the penetration depth falls away from its linear dependence. This result arises from applying the perfect gas law, where the number density will decrease with increased temperatures. The effect of isotopic abundance is also shown where the Hg 198 line is shifted up from the Hg202 (the strongest absorption line).

Initial measurements of spatial resolution were made by imaging laser scattering from a pin. The pin scattering was imaged 1:1 via an f/3 lens onto a diffuse reflector (a sand blasted metal plate). The scattering from the diffuse reflector was then imaged via an f/4.5 lens onto the intensified CID camera. In the object plane of the camera, the spot size was measured to be 540 microns (fwhm), shown in Figure 14. The camera intensifier resolution was measured to be 12 lines/mm.[Grinstead] These measurements gave a measure of the resolution of the imaging system. Next the diffuse scattering source was replaced by the fluorescence filter operating with a mercury vapor pressure of 0.022 Torr (approximately half the vapor pressure of typical operation). The imaged spot size was measured to be 800 microns in the object plane. This measurement is a convolution between the imaging system resolution and the filter resolution at this vapor pressure. Deconvolving the linewidths, assuming Gaussian profiles, yields 3.4 lines/mm (based on half-width-half-maximum resolution) filter resolution.

By imaging scattering from a ruled grating, further measurements of the spatial

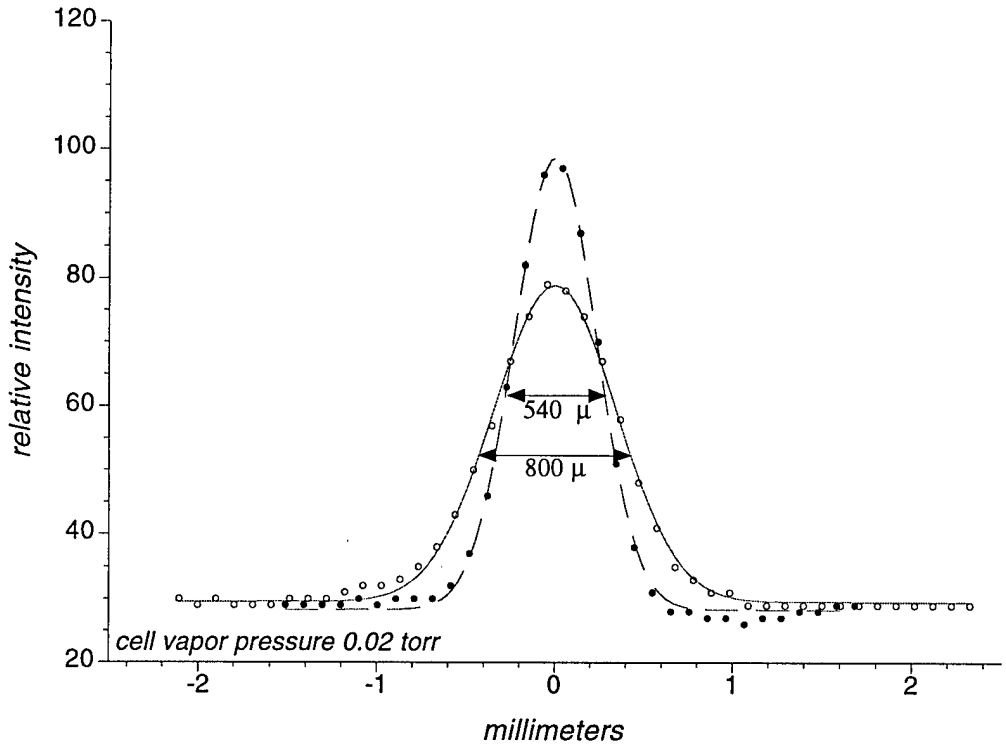

Figure 14: Narrow passband filter: spatial resolution. Intensity of pin scattering as imaged with diffuse reflector and with vapor filter.

resolution of the narrow passband filter were made. In a similar geometry to other experiments, the tunable, UV laser source illuminated a variable ruled grating (5 lines/mm to 200 lines/mm). Scattering from the grating was imaged and magnified two times onto the inside surface of the vapor cell. Fluorescence from the mercury vapor was re-imaged (f/4.5 magnified 1:1.5) onto an intensified CCD Stanford Quick 04 camera. Images were captured for a variety of gate times (50 ns, 500ns, 1μs) as the laser was scanned through the mercury absorption band.

Figure 15 plots images of the ruled target as imaged with the narrow passband filter (at the peak of the Hg 202 line held at 150 mTorr, 400K cell), and with a diffuse scattering source replacing the filter. The images are averages of mercury vapor

fluorescence from 10 laser shots, collected with gate times of 500 ns and 1 μs. The diffuse scattering (15a) gives a measure of the spatial resolution of the imaging system independent of the filter. The system resolution, as defined by the half-width-half-maximum Rayleigh criterion, exceeds 7.5 lines/mm in the image plane. Imaging with the narrow passband filter at the shortest gate time 50 ns (not plotted), and the 500 ns gate (15b) the images are not limited by filter resolution, but rather the collection system. As the temporal gate is extended, a degradation of image resolution is observed. With a 1 μs gate (15c), the resolution exceeds 5 lp/mm, but 7.5 lp/mm are no longer fully resolved. This decrement in resolution is due to the extended temporal gate, collecting light that has been optically trapped by the filter. Light emanating from the filter after multiple absorptions is less likely to preserve images.

The absorption depth of incident radiation is due to both the number density of mercury atoms (Figure 13) and the incident frequency. As the laser is scanned into the transmission band of the filter, the resolution and transmission intensity are seen to increase. Figure 16 characterizes this feature. Single shot images (500 ns gating time) of the variable ruled grating for varying incident laser frequencies are shown. At the bottom of the picture, a plot of the absorption profile (the transmitted light through the vapor cell) is given with arrows highlighting the spectral location of the laser when the images were captured. Operating at an optical depth of approximately 15/cm, the 2.5 lines/mm are just discernible, but not fully resolved. Tuning further into the absorption band of mercury increases the optical depth, and hence resolution: approximately 5 lp/mm at an optical depth of 30/cm, and 7.5-10 lp/mm at a depth of 55/cm.

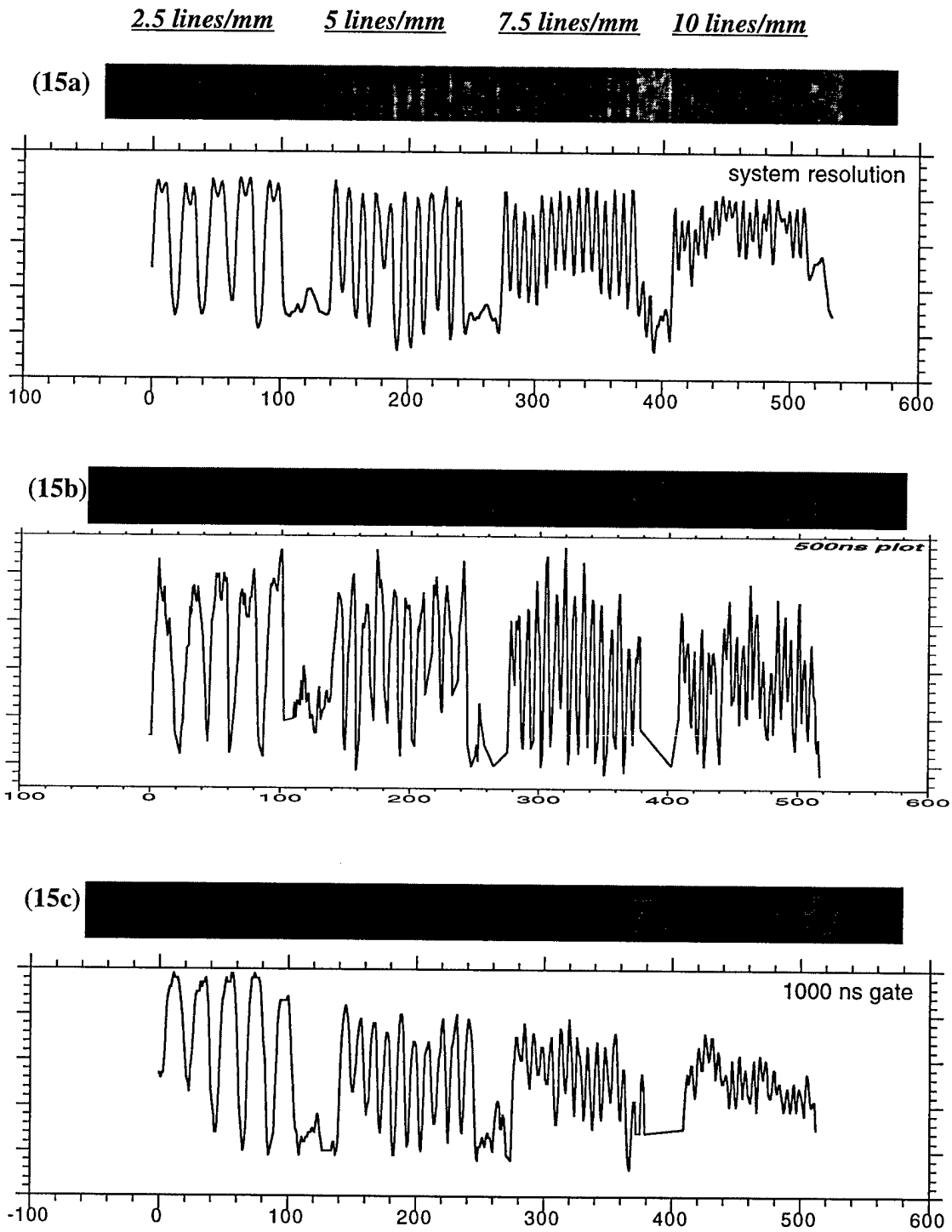

Figure 15: Narrow passband filter: spatial resolution. Imaging variable ruled grating. Images and pixel values for (a) system resolution, (b) filter with 500 ns gate (c) filter with 1000 ns gate

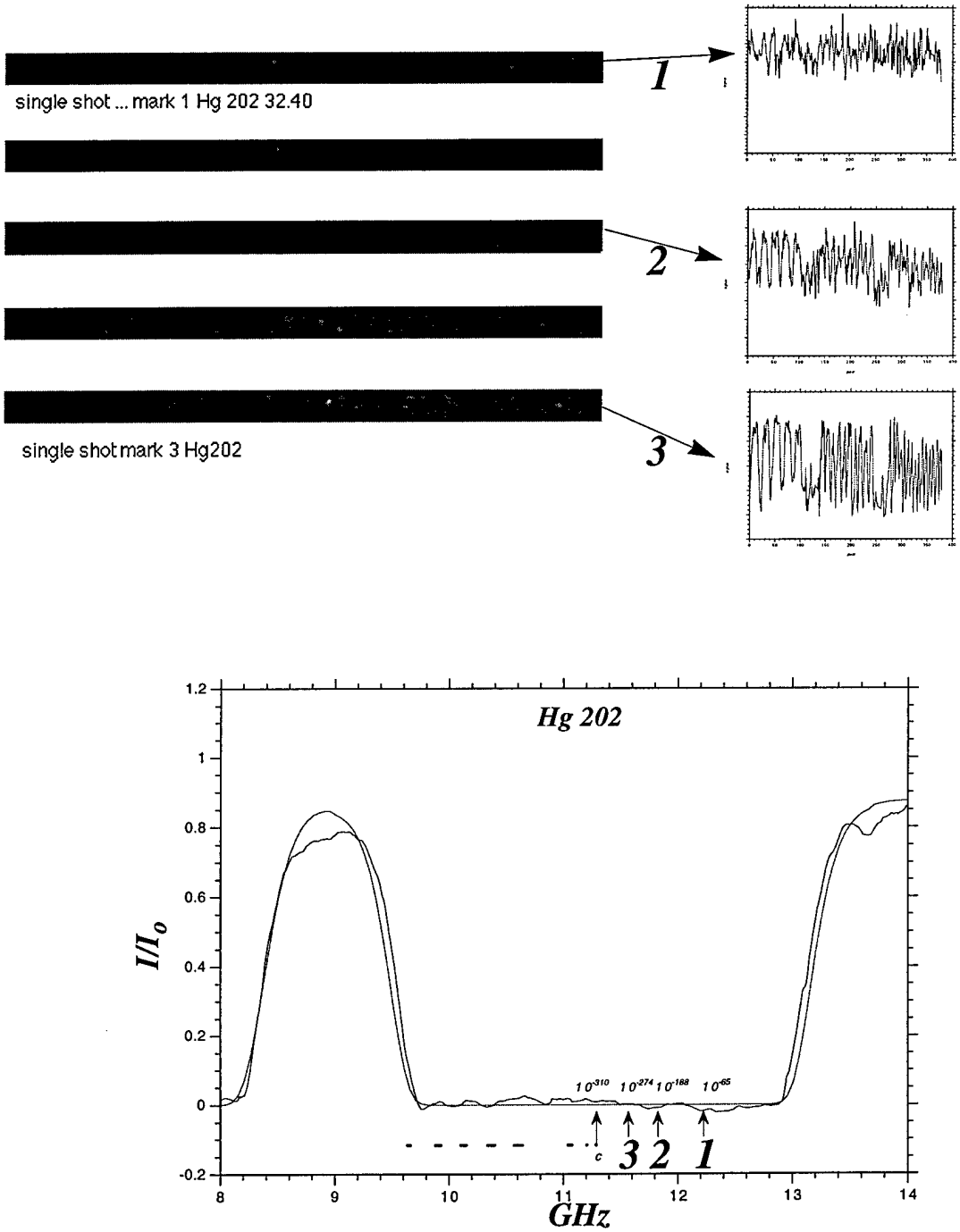

Figure 16: Narrow passband filter: spatial resolution. Imaging variable ruled grating with three different incident laser frequencies. Images and pixel values (above) corresponding to three different spectral locations (below). Optical depth of the filter is determined by observing spectral location versus cell transmission (lower plot).

Clearly, resolution is related to optical depth of the absorption. In a simplistic evaluation the resolution is related to the penetration depth by the incident angle formed by an imaging system. A perfectly imaged spot will become a disc of diameter:

$$D = \frac{d}{f^{\#}} \qquad \text{VI.4}$$

where d is the (1/e) penetration depth and $f^{\#}$ is the imaging f-number of the system. For the images presented above, multiple fluorescence must be accounted for as well. In fact, unless the shortest gate times are used, this presents the resolution limiting behavior of the filter. Whereas as slow collection lens affords higher resolution for the first absorption process, the absorption and fluorescence by subsequent atoms is not directed. Thus, the ultimate resolution limit will be proportional to the penetration depth d, and the number of atomic absorptions minus the initial absorption, n-1. The constant of proportionality, $\alpha(\theta)$, reflects the angular distribution of the fluorescence process:

$$resol = \frac{d}{f^{\#}} + d(n-1)\alpha(\theta) \qquad \text{VI.5}$$

While the average angle of fluorescence may be considered the integrated mean angular value, the $2/\pi$ overestimates the angular component, again because it fails to include subsequent fluorescence. The experimental data with varying optical depth (Figure 16) are consistent with $\alpha(\theta) \approx 0.5$. The penetration depth shown in Figure 16 (mark 2), and 16 (mark 3) was modeled to be 120 μm, and 80 μm respectively. Imaging f/13, and gating for 500ns (4.2 fluorescence lifetimes), gives a predicted resolution of 200 μm (5 lp/mm) and 134 μm (7.5 lp/mm), consistent with the resolution plots of Figure 16.

The above analysis neglects atomic motion, which must begin to be accounted for, once the vapor pressure exceeds a few hundred milli-Torr. The velocity distribution of

mercury atoms follows the well known Maxwellian distribution, where the average velocity $\bar{v}$ is given by:[Vincenti]

$$\bar{v} = \sqrt{\frac{8kT}{\pi m}} \qquad \text{VI.5}$$

where k is Boltzmann's constant; T is the temperature; m is the mass. At an operating temperature of 373 K, average velocity is roughly 200 m/s. At low vapor pressures and short time scales, collisions may be neglected. The propagation distance of an atom is bounded by the average velocity multiplied by the time of travel. Figure 17 gives a plot of the distance travelled by an atom versus cell temperature for three appropriate time scales

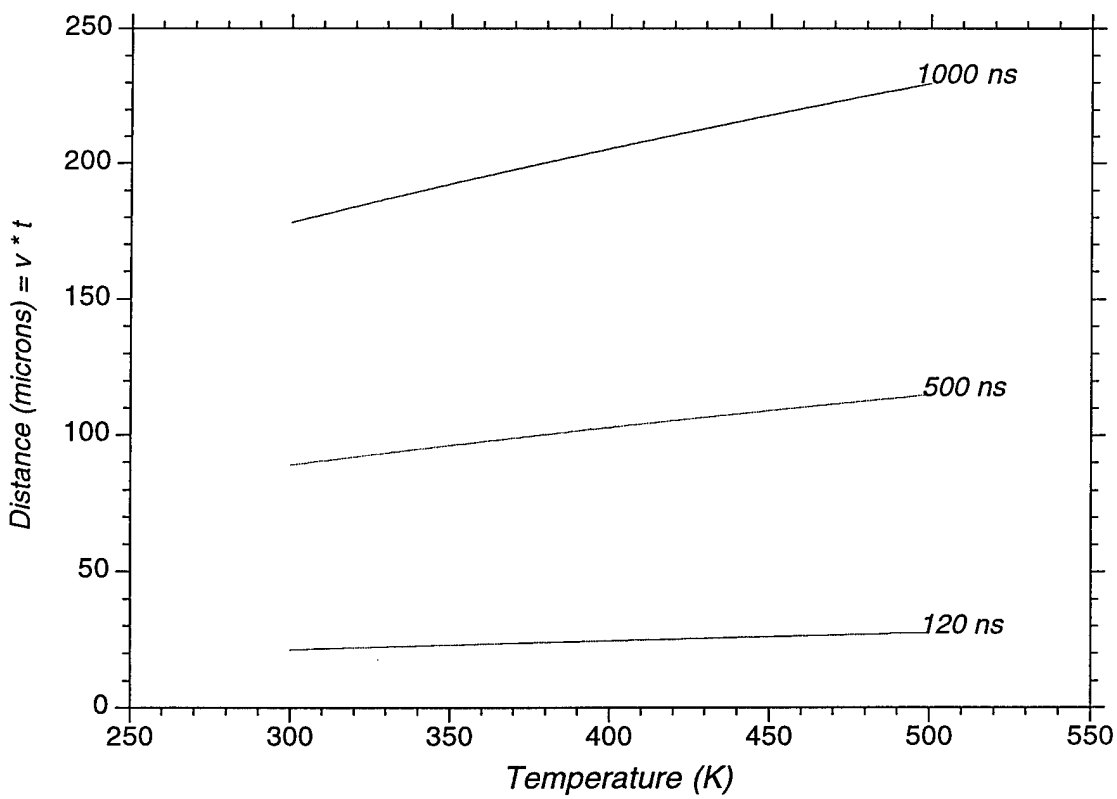

Figure 17: Atomic transport as a function of temperature. Distance travelled for varying time-scales.

(120 ns, 500 ns, 1 μs). This conservative estimate gives a bound on the effect of atomic transport That is, given no collisional effects, an atom on average will translate the marked distance in the given temporal window. In the worst case, assuming that the multiple atoms involved in the subsequent fluorescence processes act as a single atom over the same time frame (i.e. all moving the same direction), the temporal gate of the imaging system determines the resolution. For a 500 ns gate, an atom at 400K will travel about 100 microns. At best case, the natural lifetime (120 ns) gives the temporal window of the transport, yielding 25 micron resolution.

At elevated pressures, collisional effects will lead to reduced translation of the atoms, and a diffusion model is more informative to examine the length and time scales. The mean free path is the average distance an atom travels between collisions:[Vincenti]

$$\lambda_m = \frac{1}{\sqrt{2}\pi d^2 n} \qquad \text{VI.6}$$

the denominator is an effective collision cross-section multiplied by the number density, n. Taking a large collision cross-section (d = 10Å) still leads to a relatively large mean free path. It is not until the vapor pressure reaches 0.1 Torr that the collision time ($\lambda/\bar{v}$) reaches 500 ns (the relevant time scale). The self-diffusion constant, D_{AA} is given by:[Vincenti]

$$D_{AA} = \beta_D \bar{v} \lambda_m \qquad \text{VI.7}$$

where β_D is a constant of proportionality of order 1, taken in this case to be 0.5 (averaging atomic direction); v is given above; λ_m is the mean free path above. Solving the governing differential equation for mass diffusion yields a solution in the form of the error function,

which may be approximated yielding:[Hirschfelder]

$$L \approx \sqrt{D_{AA} t} \qquad \text{VI.8}$$

which simply relates the length scale, L to the time scale t, via the diffusion constant D_{AA}. Figure 18 gives a plot of the diffusion length as a function of cell vapor pressure (and fixed 400 K temperature), for given time scales. Increased pressure decreases propagation distance, because of collisions. The gating time constrains diffusion distance which is negligible except perhaps with the longest temporal window at lowest density.

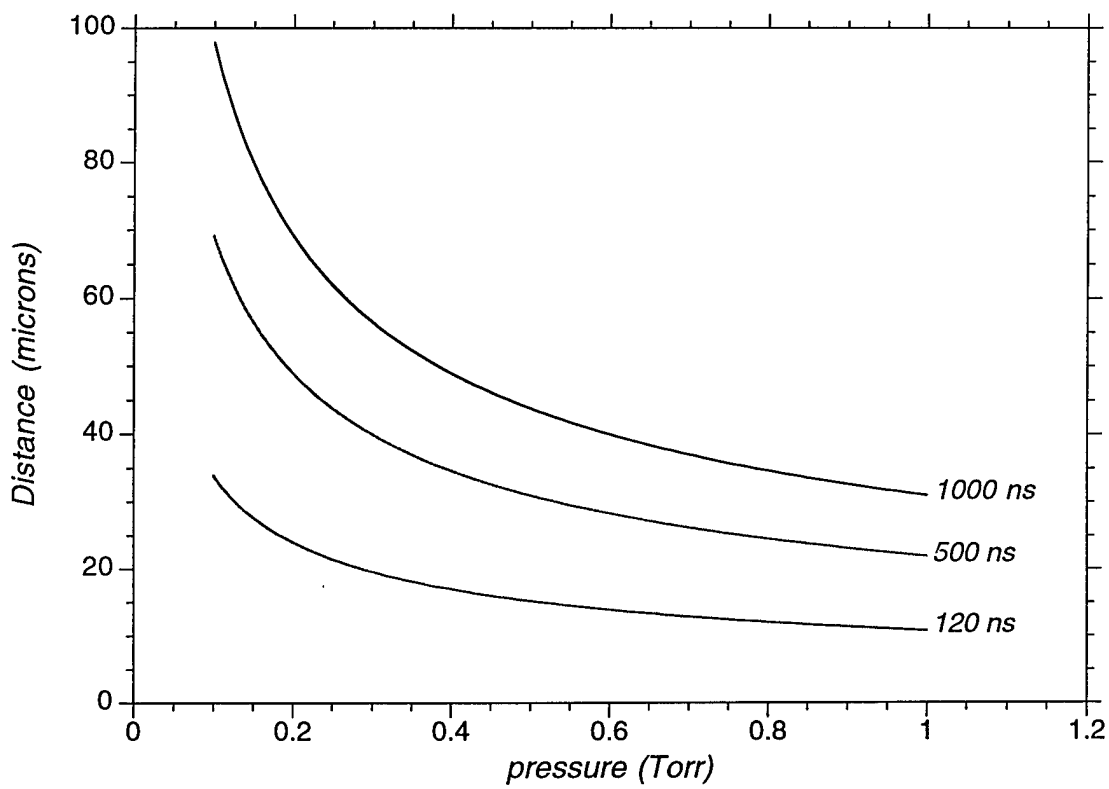

Figure 18: Atomic diffusion. Diffusion distance of atoms in vapor filter as a function of cell vapor pressure for varying time scales.

efficiency

The efficiency of the narrow bandpass filter is composed of two elements: fluorescence yield, and geometrical collection efficiency. The fluorescence efficiency addresses how effective the filter is at re-radiating incident light. The collection efficiency addresses the geometrical limitations of imaging. Because of the low vapor pressure, collisional effects are minimal, and the efficiency of the passband filter is limited by its the dual collection process. As shown above, very conservative estimates on the collision frequency, demonstrate that even at the high end of operation (400 K, 0.15 Torr) the collision frequency is still only on the order of MHz. At most there are a few collisions per collection period, and fractional amounts of those are de-activating collisions. More significant is the effect of wall collisions with the front window of the cell. Taking the velocity component in one direction (exiting the cell), yields $\bar{v}/4$. The 1/e penetration depth divided by the atomic velocity in this direction gives a characteristic time for an atom to collide with the wall. At 400 K and 0.1 Torr the penetration depth is roughly 20 microns, $\bar{v}/4$ is 50 m/s yielding a characteristic time of 400 ns. Under such conditions, desirable for high resolution measurements, wall quenching begins to become a factor.

Experimental measurements confirm the high fluorescence yield of the mercury vapor filter. For both resolution experiments, pin scattering and reticle scattering, comparative measurements of fluorescence signal and diffuse scattering signal of known efficiency were made. In the case of the pin scattering, a sand blasted piece of aluminum was used to replace the narrow passband filter. Signal levels were comparable with the fluorescence signal marginally greater than aluminum scatterer. Earlier measurements of a sand blasted aluminum plate give a spectral reflectance of 0.5, at 254 nm.[Touloukian]

The second experiment replaced the fluorescence filter with a specialized diffuse UV scattering source to image the variable ruled grating. The fluorescence signal of the mercury filter was 67% of the scattering source. Allowing for two surface reflections of the front quartz window (~6-8% / surface, which may be minimize by anti-reflection coatings), the fluorescence efficiency was experimentally verified to be in the range of 60% to 80%. As observed independently in the Monte Carlo model, Figure 5, a maximal fluorescence yield of approximately 80% is achieved, due to quenching and optical trapping.

The geometrical efficiency of a single imaging collection system may be approximated by:

$$\frac{\Delta\Omega}{4\pi} = \frac{1}{16F^2}\left[\frac{1}{1+\frac{1}{m}}\right]^2 \qquad \text{VI.9}$$

Light emitted into 4π steradians, is collected in a solid angle, $\Delta\Omega$, via optics with an f/number, F, and magnification, m. Initial scattering is assumed to radiate into 4π steradians. The fluorescence is assumed to be emitted into 2π, because the absorbed light will radiate out the front cell surface. Multiplying the efficiencies of each step yields an overall geometrical collection efficiency. For a magnification of 1:2:1 and an f/1 followed by f/2 collection yields: 10^{-4}. Using a magnification ratio of 1:1:1 is optimal. A faster collection f/1 followed by f/1, yields 5 10^{-4} efficiency, which is equivalent to a single f/5 collection step. Perhaps more informative is to examine just the second step, since imaging inherently requires the first collection step. Thus, included in the cell efficiency is simply the required second imaging step. A single f/1 (1:1) collection from the cell collects 6% of the scattered light. For the 1:1.5 (f/4.5) imaging experiments above, 0.2 percent of incident light on the imaging filter is captured.

Imaging constraints

To increase resolution, it is desirable to run at higher vapor pressures, which increases the centerline attenuation, and decreases the penetration depth into the vapor cell. However, there is an inherent trade-off between increased resolution, and cell performance due to extinction ratio and fluorescence efficiency. As noted previously, at higher densities the wings of the Voigt modeled absorption profile become significant. As a result, the out-of-band extinction ratio is decreased. Additionally, increasing vapor pressure increases both the mercury-mercury collision frequency and the mercury-wall collision frequency. Each leads to decreased fluorescence efficiency. Alternative cell designs may allow for simultaneously achieving high resolution and high out-of-band extinction. For example, a 50 micron thick vapor cell would achieve high resolution, and still allow for low enough vapor pressures to achieve desirable background suppression. Of course, there is a loss of efficiency in such a design. Some of the in-band light would be lost because it would pass through the short cell, and wall collision effects arise at both entrance and exit of the cell.

For imaging applications, a limiting constraint of the narrow bandpass filter is insuring its linearity as a detector. Because the dual imaging step limits efficiency, significant incident light levels are desirable. However, the low saturation intensity of mercury constrains ultimate light levels. For a steady-state two level system, population of energy levels is given by:[Miles; Yariv]

$$N_1 - N_2 = \frac{\Delta N^e}{\left(1 + \frac{I}{I_{sat}}\right)} \qquad \text{VI.10}$$

where $N_1 - N_2 = \Delta N$ is the population difference between the two levels, ΔN^e is the

equilibrium state, and I_{sat} is defined as.

$$I_{sat} = \frac{h\nu}{2\sigma\tau} \qquad \text{VI.11}$$

$h\nu$ is the energy per incident photon; σ is the absorption cross section; τ is the natural lifetime of the state. For $I > I_{sat}$, light is not absorbed in the exponential fashion described in Chapter 3. A smaller percentage of light is absorbed than in the linear regime, where the response of the filter will vary linearly with incident light levels. Particularly interesting is that I_{sat} is independent of number density and reflects an individual atom's propensity to absorb light. For mercury vapor absorption at 253.7 nm, experimental data and modeling (as from Figure 5 in Chapter 3, and recognizing that in Equation III.6, $\Gamma(\nu)=N\sigma$) yields an absorption cross-section of $\sigma = 5.2\ 10^{-13}$ cm^2. Thus, as may be expected with a relatively strong absorber, I_{sat} is 6.3 W/cm^2.

For 10 ns of incident ultraviolet light, this corresponds to 80 billion photons per square centimeter. Unfortunately, this large number quickly dwindles, as one accounts for collection efficiency of the optical system, and quantum efficiency of the detector. For typical experiments, imaging f/4.5, with no magnification yields 7.7 10^{-4} collection efficiency. Assuming a highly efficient detector, 0.2 photo-electrons per incident photon, 1.2 10^7 photo-electrons per cm^2 are collected. Typical cameras have 500x500 pixel resolution or better per cm^2, yielding roughly 50 photo-e$^-$ per resolution element -- or, a signal to noise ratio of 7 for shot-noise limited experiments. However, assuming 100 μm x 100 μm resolution limit of photocathodes, i.e. binning camera resolution elements, increases signal counts to 1,200 photo-e$^-$ per resolution element per laser shot (or a S/N ratio of about 35). This discussion has neglected the quantum efficiency of re-radiation of

light by the mercury itself. While one must be wary not to saturate the detector (filter), a variety of solutions exist, which include binning resolution elements, averaging frames (shots), stretching out the interrogation pulse, faster collection optics, magnification of the scattered light. Each of these options presents its own experimental trade-offs.

Finally it is worthy of note that the filter is still useful for persevering images, or spectral filtering if one forgives or loosens the other constraint. It is possible to maintain imaging capabilities even in the saturated regime. In such instances, however, images represent both scattering signal intensity and mercury number density. In the other case, where spectral profiles are of interest, it is clearly possible to operate unsaturated if one forgives the imaging constraint. Following are two experiments demonstrating the spectral filtering capabilities of the filter.

Diagnostic applications

Rayleigh

Experiments, designed to demonstrate the unique features of the laser and filter pair, independently captured Rayleigh scattering and pure rotational Raman scattering from room air. Figure 19, illustrates the experimental set-up. Light scattering from a 2

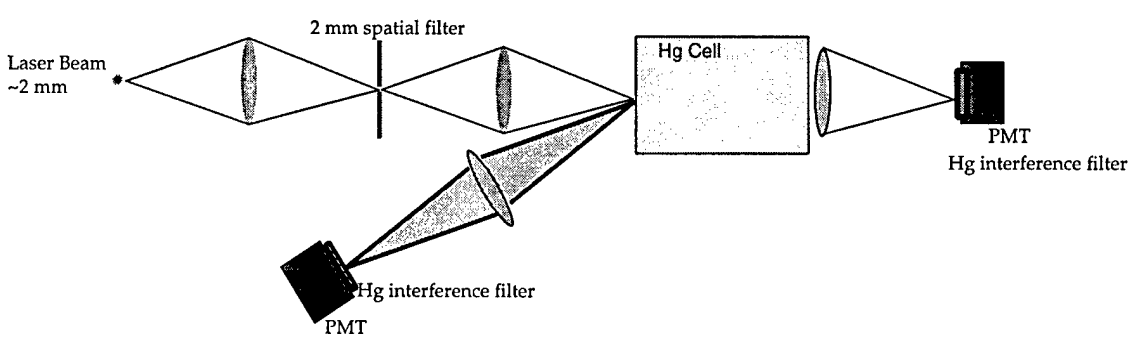

Figure 19: Experimental setup: Rayleigh and Raman scattering measurements

cm length of ambient air was 1:1 imaged (f/1 lens) through a vertical slit onto the inside surface of the mercury vapor filter. The mercury vapor fluorescence was re-imaged (f/1) off axis through a mercury line interference filter onto a photomultiplier tube. A boxcar integrator gated the fluorescence signal, while another photodiode/ boxcar integrator simultaneously measured the laser power. A personal computer and A/D card recorded averages of the fluorescence signal, the laser power, and the laser frequency.

With the laser tuned to the resonance band of the mercury vapor cell, Rayleigh scattering was collected with the fluorescence filter. The laser was scanned continuously (in 12 MHz steps) over nominally 1 cm^{-1}. With the cell held a vapor pressure of 0.1 Torr, fluorescence was captured with 1.5 μs gate and 10 shot averages recorded. Model predictions are simultaneously plotted with the experimental data in Figure 20. The model

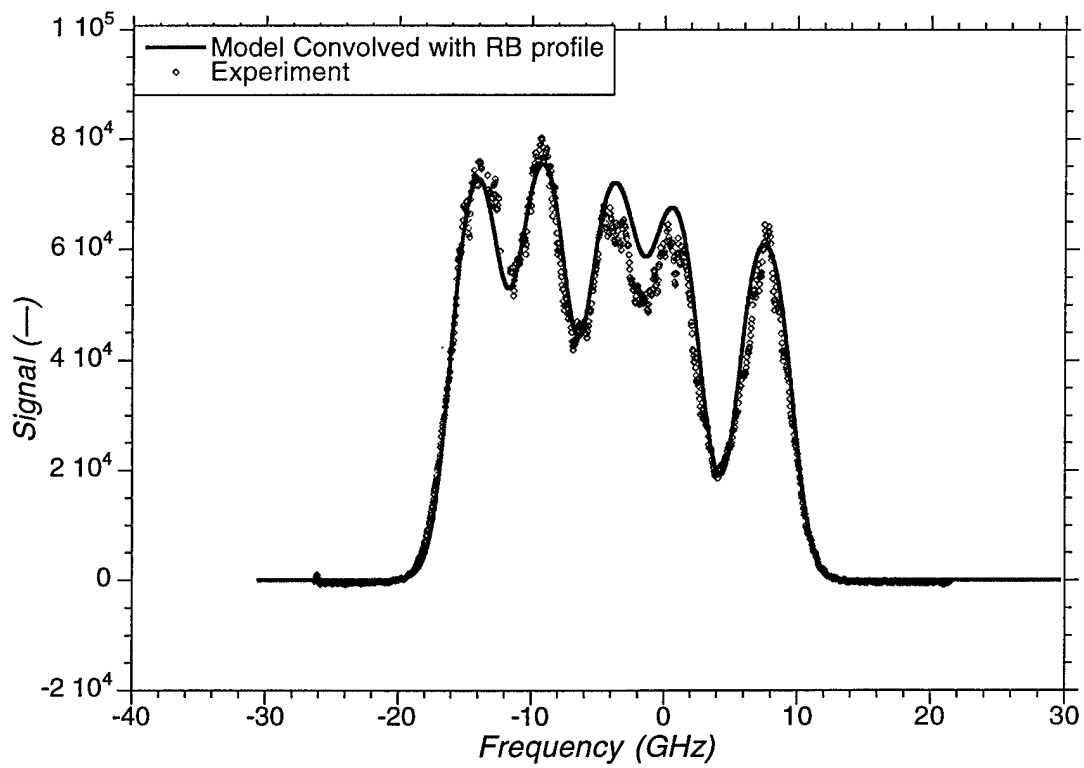

Figure 20: Rayleigh scattering from room air. Experiment and model predictions. Model includes Rayleigh-Brillouin lineshape convolved with Monte Carlo model for the passband filter.

prediction is a convolution of the Rayleigh scattering with the fluorescence filter model above. The Rayleigh-Brillouin profile is significantly Gaussian in this regime, but contains some collisional contribution leading to the Brillouin wings (Y parameter value of 0.376).[Forkey, pg 31]. The model predictions for the Rayleigh scattering profile are given by the Tenti model as described by Forkey. Good agreement is observed in the structure of the passband, and especially in the wings, where the broadening reflects a blending of spectral profiles.

Raman

By spectrally detuning the laser from the Hg resonance, pure rotational Raman shifted scattering was made spectrally coincident with the 253.7 nm transmission filter. Scattering at the detuned laser frequency was rejected by the filter. Three different data sets, each with the laser scanning over 2.5 cm^{-1}, captured four different Stokes shifted pure rotational Raman lines. Fluorescence signal was captured with a gate time of 1.5 μs, and 30 shot averages on the boxcar averager. Each data set was normalized by incident laser power, so the data sets could be weighted relative to each other. The spectral position of each data set was determined with a Burleigh wavemeter which measured the wavelength (± 0.1 cm^{-1}) of the cw seed laser in the infra-red.

The three data sets are plotted in Figure 21. Simultaneously, model predictions are plotted. The predicted absolute location of the rotational lines is given in Chapter 5, along with references to scattering signal cross-sections (including J-level dependence).[Penney; Weber] The modeled signal levels are scaled for natural abundance of nitrogen (78.1%) and oxygen (21.0%). The modeled spectral profile of the rotational Raman scattering is Lorentzian due to Dicke narrowing at pressures of 0.2 atm and above.[Rosasco] The

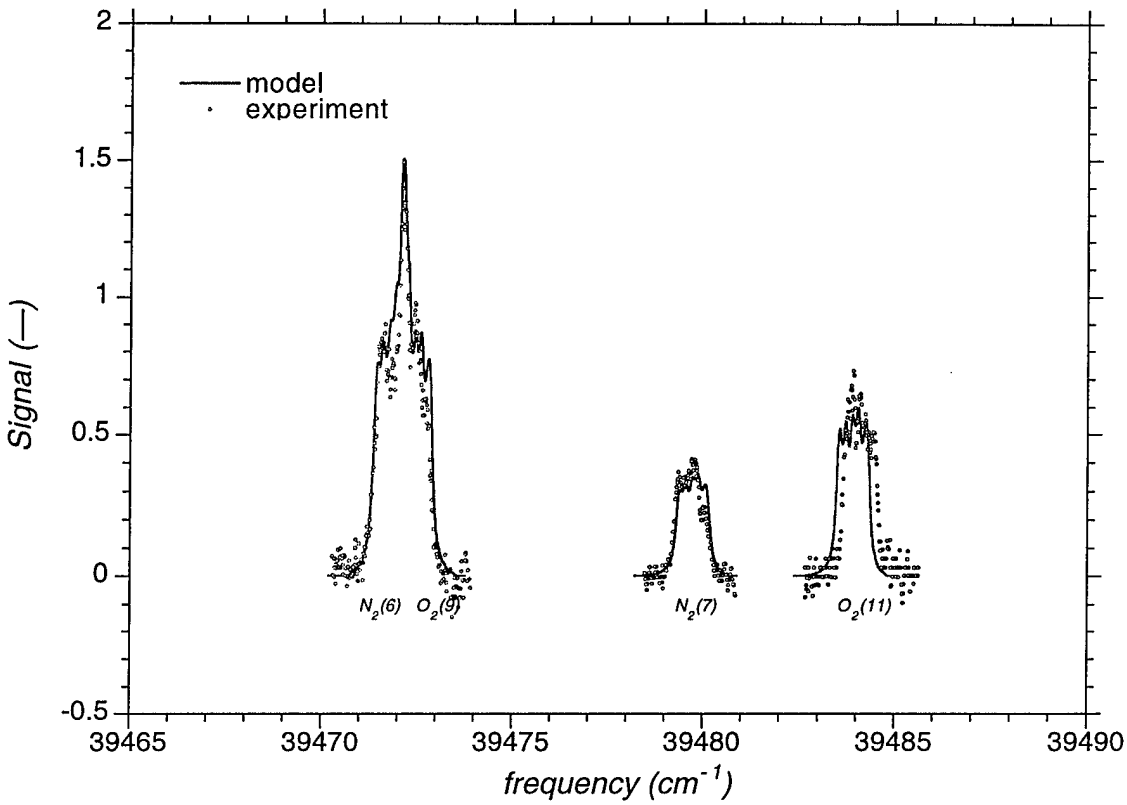

Figure 21: rotational Raman scattering from room air. Experiment and model predictions. Model includes rotational Raman broadened lineshape convolved with Monte Carlo model for the passband filter. Three different spectral scans cover four individual rotational Raman lines.

Lines	Shift (cm^{-1})	Rel. Strength (-)	Line Width (GHz)
N_2 (J=6)	-59.681	0.6433	2.76
N_2 (J=7)	-67.632	0.3184	2.70
O_2 (J=9)	-60.351	0.5583	2.26
O_2 (J=11)	-71.825	0.4954	2.20

Table 6.1: Rotational Raman scattering parameters, used for normalizing the signal strength and spectral width.

Lorentz linewidths are J-level dependent and extracted from earlier experimental and theoretical work.[Jammu] Table 6.1 gives a summary of the parameters used for the rotational Raman scattering signal predictions. The modeled relative strength, and absolute spectral widths and locations were convolved with the Monte Carlo model presented above. The resultant model predictions were scaled in absolute intensity (fixed relative to one another), to match the experimental data at 39472 cm^{-1}.

Figures 22 (a), (b), and (c) detail each of the spectral scans above. To emphasize the agreement between model and experiment, the spectral locations are shifted to precisely overlap the model. (This artificial shift is well less than the 0.3 cm^{-1} uncertainty of the wavemeter). Additionally, the frequency axis was scaled (equivalently on all three plots) to account for the unknown laser scan rate. (This linear scaling stretched the frequency axis by less than 10% of the computer controlled scan rate). The detailed

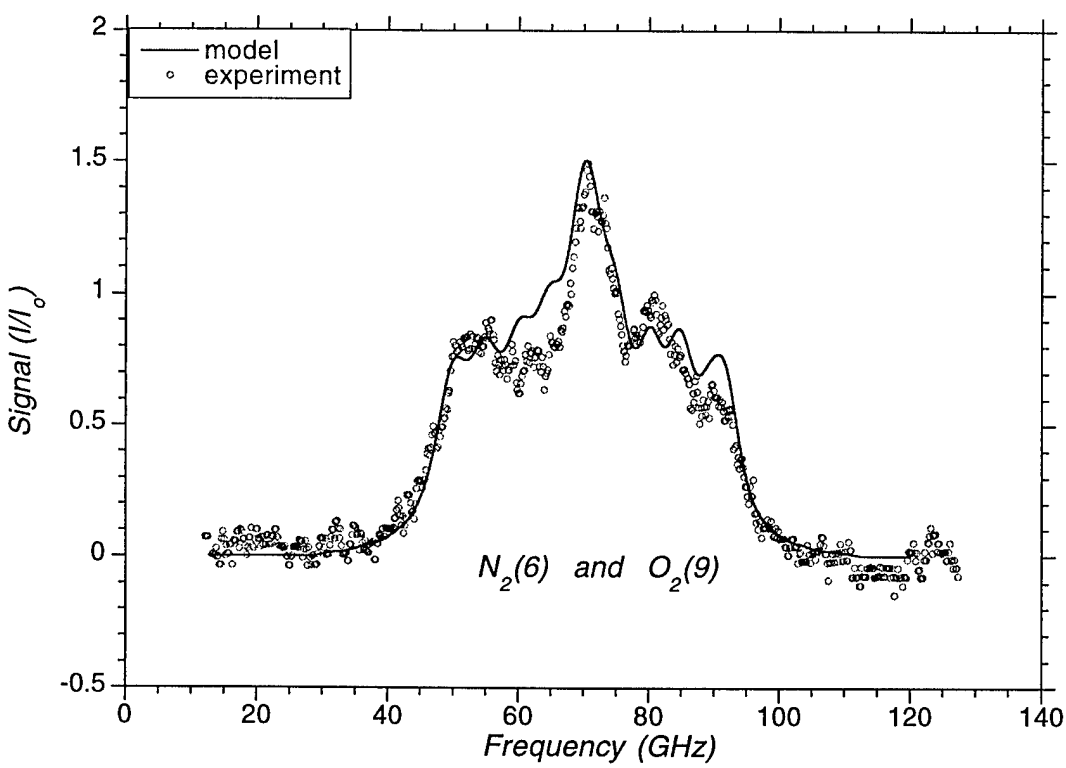

Figure 22a: Detail from Figure 22. Model and experiment of rotational Raman scattering from N_2 and O_2. Two rotational lines are convolved due to small shifts.

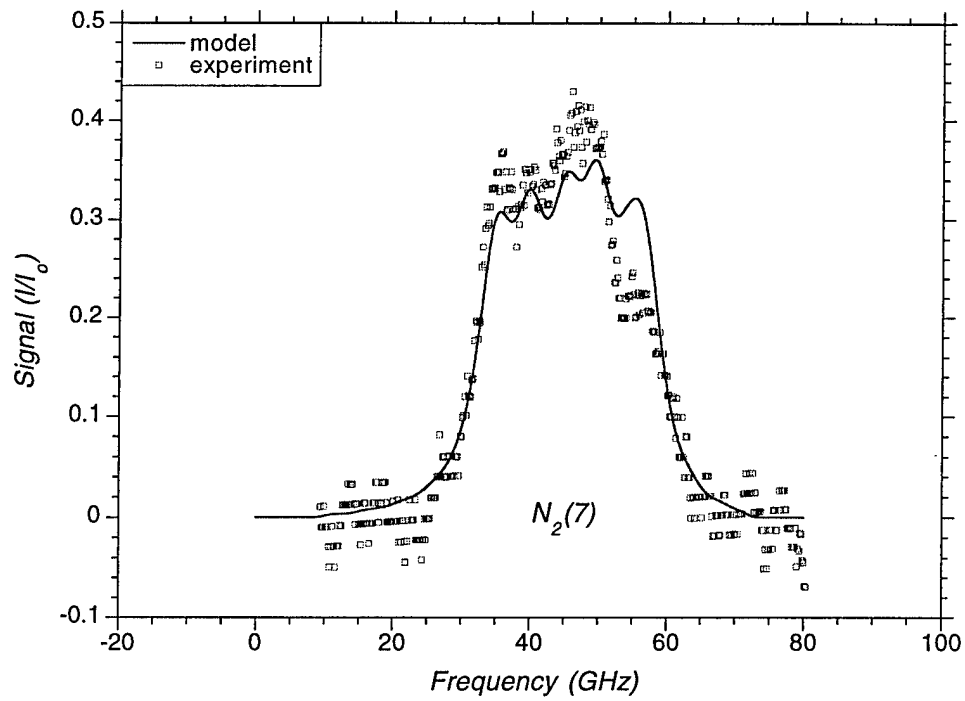

Figure 22b: Detail from Figure 22. Model and experiment of rotational Raman scattering from $N_2(7)$.

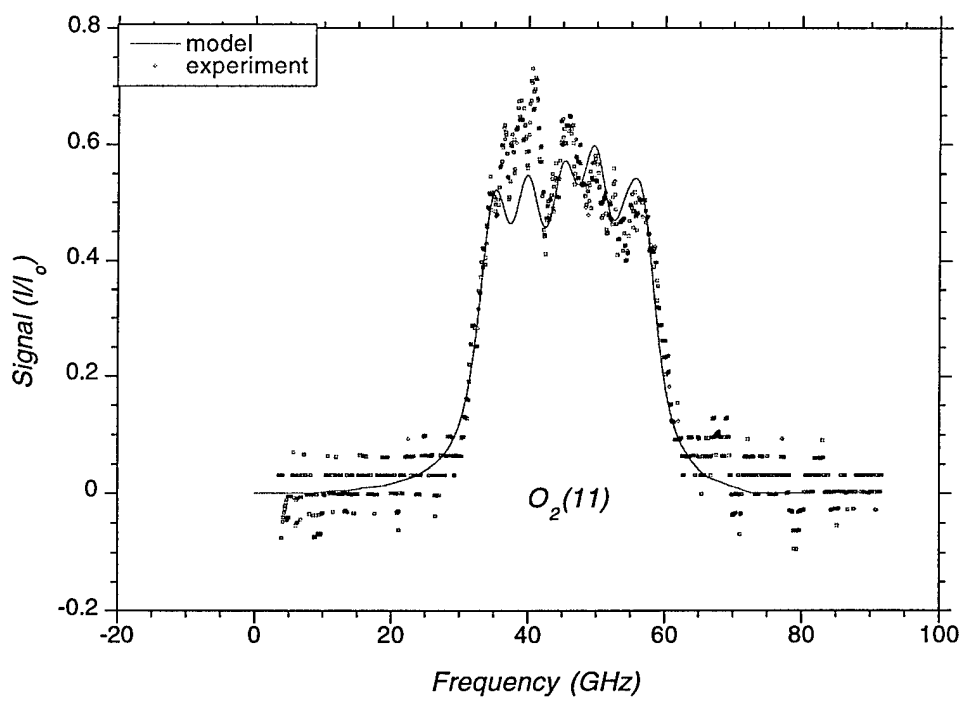

Figure 22c: Detail from Figure 22. Model and experiment of rotational Raman scattering from $O_2(11)$.

figures reveal expected structure in the experimental data. Figure 22(a), convolves the $N_2(6)$ and $O_2(9)$ rotational lines, because their peak separation of roughly 0.7 cm^{-1} is less than the passband of the filter. Figures 22(b) and (c) both capture the relative intensity of scattered light. Furthermore, the variational in-band peak height of the filter is observable in the data. The Lorentz broadening of the rotational lines is observed, in the good agreement between model and experiment in the edges of the spectral profile.

References

Anderson, J.B., Maya, J., Grossman, M.W., Lagushenko, R., and Waymouth, J.F., "Monte Carlo treatment of resonance radiation imprisonment in fluorescent lamps," *Physical Review A,* **31**(5), 2968, (1985).

Forkey, J.N., "Development and Demonstration of Filtered Rayleigh Scattering - A laser based Flow Diagnostic for Planar Measurement of Velocity, Temperature and Pressure," doctoral thesis #2067-T, Princeton University, Princeton NJ (1996).

Gelbwachs,J.A. "Atomic Resonance Filters," *IEEE Journal of Quantum Electronics*, **24**, 1266 (1988).

Grinstead, J.H., Lempert, W.R., Miles, R.B., and Lavid, M., "From Laboratory to Large-Scale Facility: Scaling of the RELIEF Velocimetry Technique," AIAA paper# 96-2223, 19th AIAA Advanced Measurement and Ground Testing Technology Conference, New Orleans, LA (1996).

Guenard,R.D., Lee,Y.H., Bolshov,M., Huebuer,D., Smith,B.W. and Winefordner,J.D. "Characteristics of a Rubidium Metal Vapor Filter for Laser Scatter Rejection in Single Molecule Detection," *Applied Spectroscopy*, **50**(2), 188 (1996).

Hirschfelder, J.O., Curtiss, C.F., and Bird, R.B., Molecular Theory of Gases and Liquids, John Wiley and Sons, U.S, 519, (1964).

Holstein, T., Alpert, D., and McCoubrey, A.O., "Isotope Effect in the Imprisonment of Resonant Radiation," *Physical Review*, **85**(6), 985, (1952).

Indralingam, R., Simeonsson, J.B., Petrucci, G.A., Smith, B.W., and Winefordener, J.D., "Raman Spectrometry with Metal Vapor Filters," *Analytical Chemistry*, **64**(8), 964-67, (1992).

Jammu, K.S., St.John, G.E., and Welsh, H.L., "Pressure Broadening of the rotational Raman lines of some simple Gases," *Canadian Journal of Physics*, **44**, 797, (1966).

Langberg, E.,Naylor,M. and Heckscher, H., "An Image-Forming, Resonance Scatter Filter," Conference on Optical Instruments and Techniques, Chapman and Hall, p. 229 (1962).

Lempert, W.R., Wu, P., Finkelstein, N., Erbland, P., and Miles, R.B., "Imaging fluid phenomena with atomic and molecular vapor filters," AIAA paper 97-2520, American Institute of Aeronautics and Astronautics, 32nd Thermophysics Conference, Atlanta, GA (1997).

Matveev, O.I., "Atomic Resonance Spectrometers and Filters (Review)," *Journal of Applied Spectroscopy*, translated from Russian, **46**(3) 217, (1987).

Matveev, O.I., Smith, B.W., and Winefordner, "Ultra-narrowband resonance ionization and fluorescence imaging ina a mercury atom vapor cell," *Optics Letters*, submitted August, (1997).

Menders,J., Benson,K., Bloom,S.H., Liu, C.S., and Korevaar, E., "Ultranarrow line filtering using a Cs Faraday filter at 852 nm," *Optics Letters*, **16**(11), 846 (1991).

Miles, R.B., Course Notes, Lasers and Optics MAE 547, Chapter IV, 85-86, (1992).

Sullivan, J.V. and Walsh, A., "Resonance radiation from atomic vapours," *Spectrochimica Acta*, **21**, 727-30, (1964).

Penney, C.M., St.Peters, R.L., and Lapp, M., "Absolute rotational Raman cross sections for N2, O2, and CO2," *Journal of the Optical Society of America*, **64**(5), 712-716, (1974).

Rasetti, F. *Nuovo Cimento*, **7**, 261 (1930) and Rassetti,F. *Nature* **127**, 626 (1931) referenced in

Rosasco, G.J., Lempert, W., Hurst, W.S., and Fein, A., "Line interference effects in the vibrational Q-branch spectra of N_2 and CO," *Chemical Physics Letters*, **97**(4,5), 435, (1983).

Pelletier, M.J., "Ultraviolet Raman Spectroscopy Using and Atomic Vapor Filter and Incoherent Excitation," *Applied Spectroscopy* **46**(3), 395, (1992).

Sommerer, T.J., "A Monte Carlo simulation of resonance radiation transport in rare-gas-mercury positive column," *Journal of Applied Physics*, **74**(3), 1579, (1993).

Touloukian, Y.S., and DeWitt, D.P., Thermal Radiative Properties Metallic Elements and Alloys in Thermophysical Properties of Matter, **7**, IFI/Plenum, New York, 25, (1970)

Vincenti, W.G., and Kurger, C.H., Introduction to Physical Gas Dynamics, Wiley and Sons, Inc., New York, Chapter 2, (1965).

Weber, A, "High-Resolution Rotational Raman Spectra of Gases," in *Raman Spectroscopy of Gases and Liquids*, ed. A.Weber, Springer Verlag, Berlin (1979).

Yariv, A., Optical Electronics, Holt, Rinehart and Winston, New York, 139, (1985).

Chapter 7: Dispersion Filter

The collection efficiency of the refluorescence filter is limited (to order percent) by the dual collection process inherent in its design. Furthermore, the imaging passband filter measures a single Raman line at a time — only time averaged temperature measurements may be made. For limited light applications, such as Raman imaging in complex time-evolving flowfields, an alternative concept based on resonance enhanced dispersion has been developed and characterized. The concept is based on the anomalous dispersion of an atom near resonance. As demonstrated by Robert Wood, near resonance, the strong variation in index-of-refraction may be used to refract light.[Wood] By employing a prism geometry, variation in frequency induces variation in angular deviation, and after some path length, spatial variation. Thus, by foregoing one dimension in spatial resolution, simultaneous 1-D measurements of multiple frequencies may be obtained. The concept is illustrated in Figure 1, which shows a plot of the index-of-refraction and conceptual use of the vapor prism. For incident light at a higher frequency than the resonance, the index is less than that of air (shown as a short dashed-line in 1a and 1b). As this scattered light is imaged through the vapor cell, it is deviated up (away from the input normal) on the detector. For light at a lower spectral frequency (the long dashed line), the index is greater than that of air, and the light is bent towards the input normal shifted down on the detector. For light far from resonance, the index of refraction is one, and the propagation path is undeviated (solid line). Light on resonance, of course, is suppressed due to the absorption. Notably, the light deviated

1a

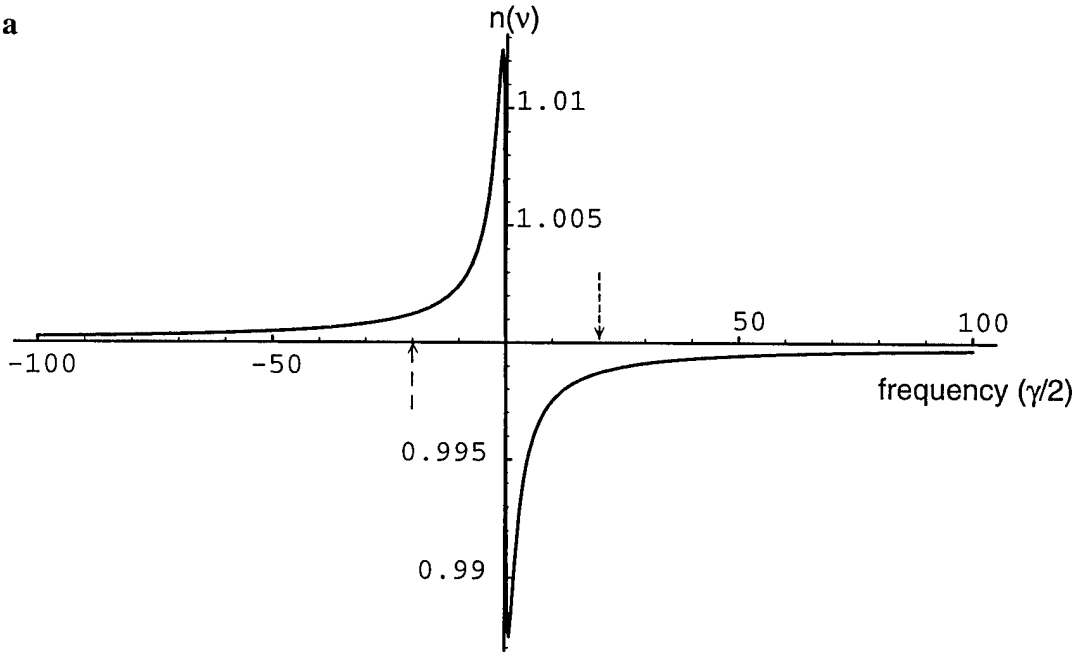

1b

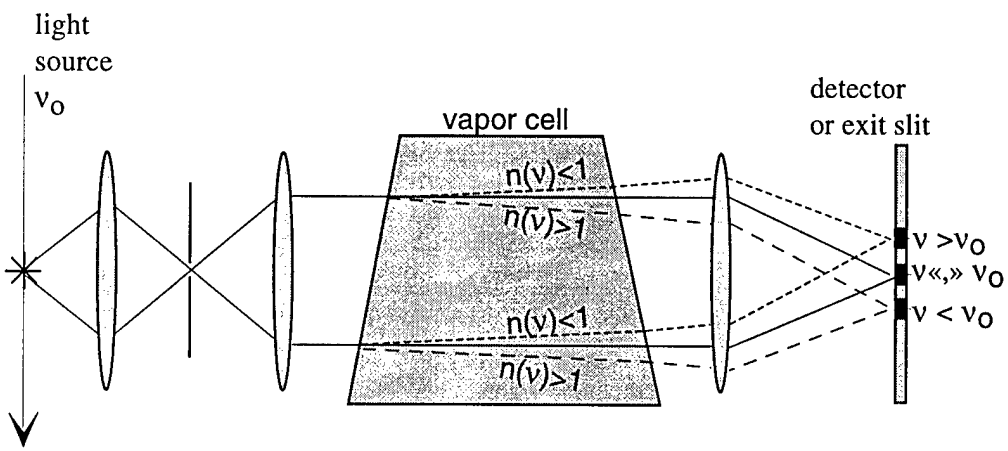

Figure 1: Anomalous dispersion vapor prism. Above (1a), plot of the change in index-of-refraction near resonance. The frequency axis is normalized by $\gamma/2$, the linewidth of the resonant transition. Below (1b), concept of filter. Light scattering is imaged through a spatial filter, through a vapor prism, onto a detector or exit slit. Light far from resonance is undeviated. Light on resonance is absorbed. Light spectrally higher than resonance is shifted up (due to an index of refraction less than one). Light at lower frequencies is shifted down.

most significantly is that which is closest to resonance, making this device particularly sensitive to small spectral shifts.

The anomalous dispersion prism is attractive for resolving rotational Raman scattering. It features the ability to suppress significant background radiation from the nearby Rayleigh line, while simultaneously resolving multiple rotational Raman lines. By placing an intensified digital camera in the image plane of the detection system, one dimension captures spectral information while spatial information is preserved in the other dimension. Furthermore, aside from imaging system losses, the system posses no other inherent inefficiencies, so the quantum efficiency of detection may be quite high. The high throughput near resonance, the high background suppression on resonance, and the spectral and spatial resolution of multiple rotational lines make this device uniquely attractive for Raman based diagnostics.

Background

The use of the index-of-refraction variation near resonance has long been exploited for spectroscopic measurements. A review of the hakenmethode (hook method or dispersion method) is given by Marlow.[Marlow] The basic implementation of the hook method is to use the phase delay induced by the changing index-of-refraction in an interferometer set-up. Collimated broadband light is passed through two separate legs, one containing an empty cell and the other a cell with some vapor under investigation. A beam splitter recombines the light which subsequently passes into a spectrometer. Depending upon pathlength difference of the two legs, fringes appear by constructive and destructive interference of the two light paths. Near resonance due to anomalous dispersion there is a variable phase delay which produces a 'hook' pattern in the

resulting spectrograph. By analyzing the hook separation, measurement of the *Nf* value (number density times oscillator strength, from Equation III.6) may be made. Traditionally, this method has been used for spectroscopic measurements such as highly accurate oscillator strengths; however, studies have also been performed to study shock waves.[Marlow] More closely related, Wood demonstrates the feasibility of using anomalous dispersion for deferentially refracting light of differing wavelength. By placing small pieces of sodium in the base of a meter length tube, and applying a flame to the base and wet cotton to the top, a temperature gradient was created across the diameter of the tube. The resulting gradient in sodium number density created a vapor prism— light at the top of the cell traverses a high number density, while light at the base of the cell traverses a low number density. Because the gradient could be severe, the angular deviation was significant. Wood used this method to measure the relative indices of refraction; however, absolute indices required the use of the hakenmethode because he could not determine the effective angle of his vapor prism.[Wood]

More recently, spectrometers have been employed for high sensitivity spectral measurements. The high spectral resolution combined with their 1-D imaging capability has allowed for Raman measurements in combustion environments. Not until relatively recently, however, have rapid measurements been made in a combustion environment. Pitz and co-workers report the first successful single-pulse concentration and temperature point measurement of all major species in an H_2-air flame, utilizing vibrational Raman scattering and laser induced fluorescence.[Wehrmeyer] A narrow band tunable KrF laser emits in the ultra-violet, and avoids background interference seen with broadband sources. A spectrometer and double pass monochrometer filter scattered

light, which is measured by photomultiplier tubes. The same group has made 1-D measurements averaging more laser shots (200-1000) utilizing a PMT array at the exit of the spectrometer,[Cheng] and ultimately ICCD cameras.[Skaggs] The weaker vibrational Raman scattering is used because its larger energy shift which simultaneously allows for discrimination from the strong Rayleigh line and broader spectral window on the spectrometer. In the last year, Rothe and co-workers report the first 1-D images of rotational Raman scattering with hydrogen.[Gu; Rothe] Using a modified KrF laser to produce narrow band highly polarized output, rotational raman scattering is observed through a 0.25m spectrometer (2400 lines/mm) onto an intensified CCD camera. Attenuation of the Rayleigh line is achieved by viewing depolarized scattering, and dispersion through the spectrometer. Nonetheless, the imaging detector is saturated for several hundred wavenumbers about the Rayleigh line. Rotational Raman scattering is viable because of hydrogen's large B_o coefficient (61 cm^{-1}).

Theory

The dispersion filter is based on the well known expression for the real part of the index-or-refraction given by:[Longhurst]

$$n' = 1 - \left(\frac{e^2}{2M_e}\right) Nf \frac{1}{\varepsilon_o} \left[\frac{(\omega^2 - \omega_o^2)}{(\omega^2 - \omega_o^2)^2 + \omega^2 \gamma^2} \right] \qquad \text{VII.1}$$

where:	e	is the electron mass	M_e	is the electron mass
	N	is the number density	f	is the oscillator strength
	ε_o	is the electric permittivity	γ	is the linewidth
	ω	is the radial frequency	ω_o	is the resonant frequency

Using the strong variation in index of refraction, a prism may be constructed from a vapor near resonance. In the simplest incarnation a controlled amount of vapor is contained between two angled windows. Incident light imaged through this cell is refracted according to its input frequency, Equation VII.1, and Snell's law. The resultant angular deviation is spectrally dependent and produces spatial deviation which may be imaged on a CCD array or camera. Small spectral shifts become significant deviations in space, given by

$$\Delta y(v, T, P, \theta_i) = d \bullet \tan(\delta\theta) \qquad \text{VII.2}$$

where Δy is the linear deviation after a path length d. Assuming end windows canted to make an isosceles triangle, the angular deviation, $\delta\theta$ is dependent upon the incident light frequency, input angle θ_i, and cell parameters temperature and pressure:

$$\delta\theta = sin^{-1}\left(\frac{n}{n_{air}} \cdot \sin\left(2\theta_i - sin^{-1}\left(\frac{n_{air}}{n} \cdot \sin\theta_i\right)\right)\right) - \theta_i \qquad \text{VII.3}$$

Figure 2 gives the relative geometry of the prism, and delineates these angles.

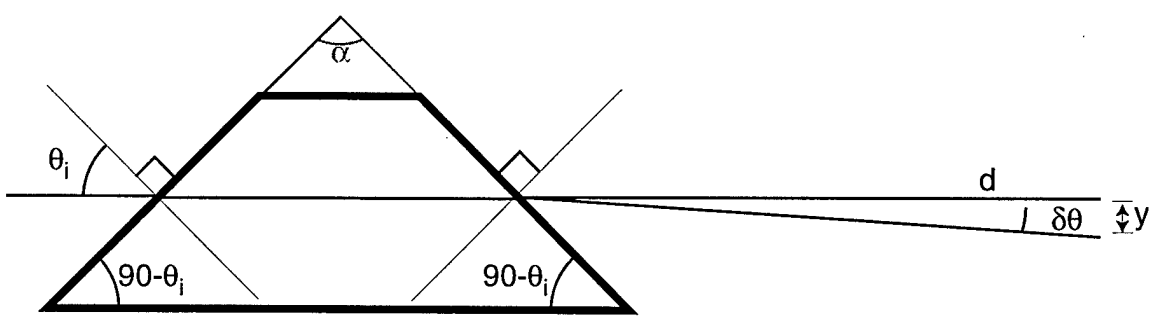

Figure 2: Geometry of vapor prism. Light entering at an angle θ_i from normal is deviated a distance y. Deviation distance depends upon incident angle, incident frequency, vapor number density, and distance (d) imaged.

For the case of mercury vapor, where hyperfine splitting and isotope variation split the energy level resonance slightly, the index of refraction is appropriately re-represented as:

$$n - 1 = \sum_i [n'(N_i, f_i, \omega_{oi}) - 1] \qquad \text{VII.4}$$

where n' is given in Equation VII.1, and N_i accounts for isotopic abundance, f_i accounts for hyperfine degeneracy, and ω_{oi} reflects the differing resonance frequencies for mercury isotopes, as discussed in Chapter 3. Figure 3 replots the index of refraction variation for the case of naturally abundant mercury at one Torr, 400K.

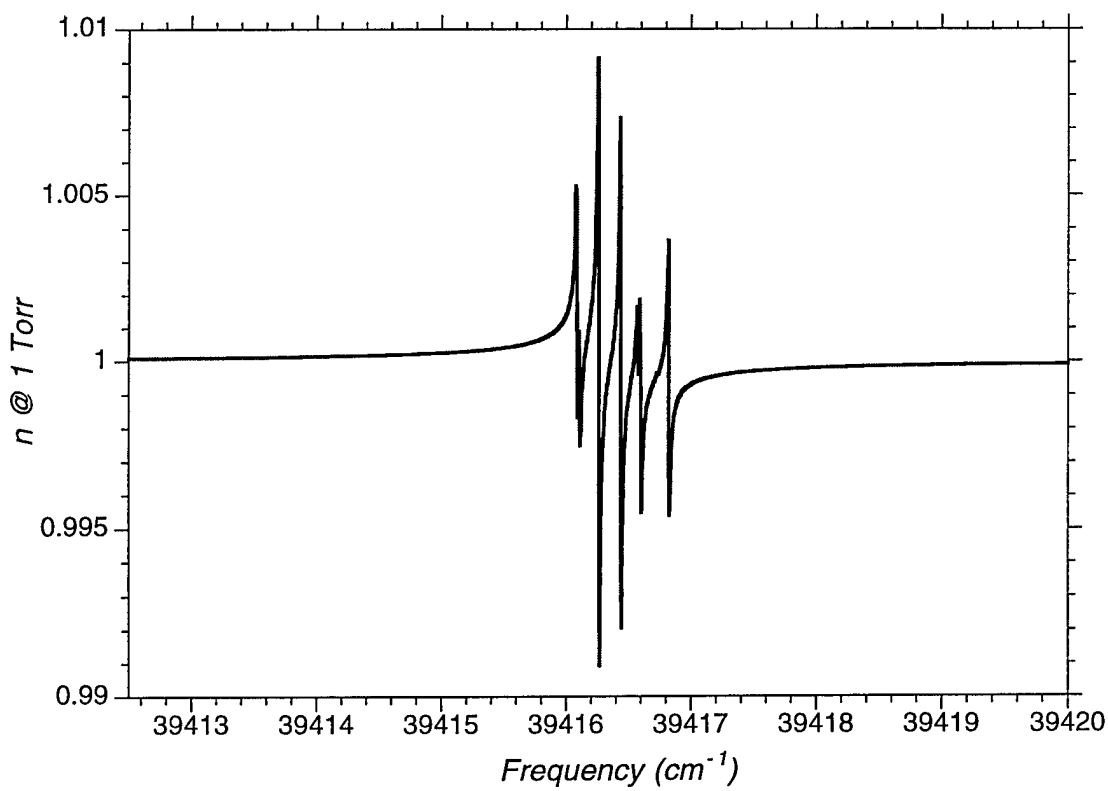

Figure 3: Index-of-refraction for multiple isotopes of mercury. The indices-of- refraction add according to Equation VII.4.

Examining Equation VII.3, or Snell's law, one may observe increased dispersion with increased angle of incidence. Figure 4 plots of angular deviation $\delta\theta$ at a single interface as a function of incidence angle θ_i and relative indices of refraction, n_{in}/n_{out}. As expected, the greater the ratio of the indices-of-refraction, the greater the angular dispersion. Similarly, the greater input angle (measured from normal), the greater the deviation. The index of refraction is constrained by the input frequency, and the number

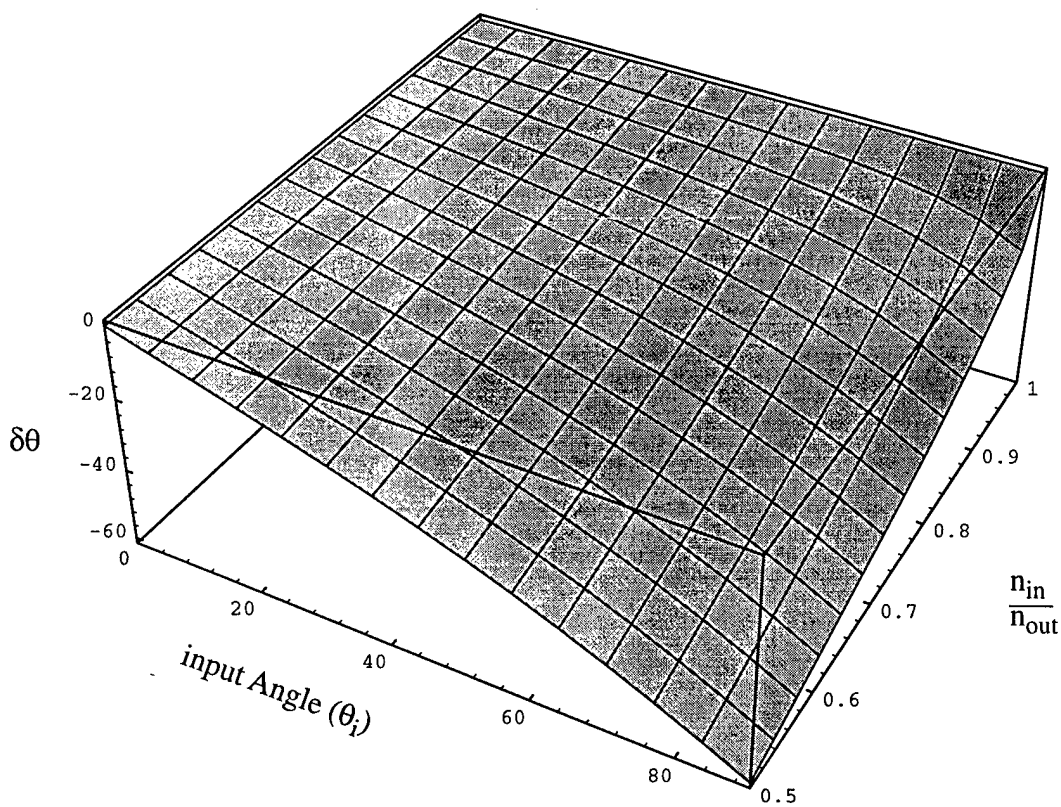

Figure 4: Angular deviation $\delta\theta$, at one interface, as a function of input angle θ_i, and relative indices of refraction.

density, suggesting the filter operates well close to resonance and at high vapor pressure. The limiting constraint on input angle is reflectance. As the angle deviates from normal, for appropriately p-polarized light, the reflection co-efficient passes though a minimum of zero at Brewster's angle, and rapidly increases, as given by:[Klien]:

$$R(n,\theta) = \left(\frac{tan\left(\theta - sin^{-1}\left(\frac{1}{n}sin(\theta)\right)\right)}{tan\left(\theta + sin^{-1}\left(\frac{1}{n}sin(\theta)\right)\right)}\right)^2 \qquad \text{VII.5}$$

For super-silica, the index of refraction at 250 nm is approximately 1.5 yielding a Brewster's angle of 58°. As plotted in Figure 5, the reflection co-efficient becomes significant at larger input angles, countering the benefit of the increased dispersion at larger angles.

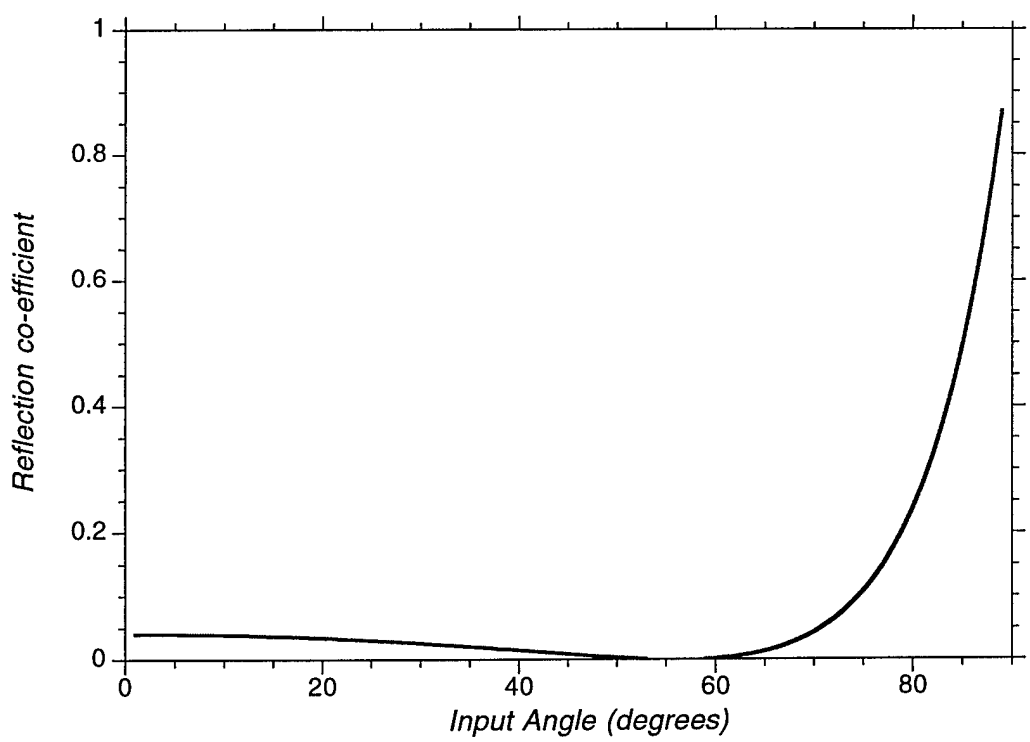

Figure 5: Reflection co-efficient for p-polarized light at a surface (quartz). Brewster's angle is 58°.

As mentioned above, another means of increasing angular deviation is by increasing the relative indices of refraction. In addition to the spectral dependence of the index of refraction there is a density dependence. By increasing the cell vapor pressure, the number density, angle deviation and spatial deviation all increase. Hence, for increased sensitivity, higher vapor pressure is desirable. With mercury vapor it is possible to produce vapor pressures in excess of 10 Torr. (At 500 K, the vapor pressure of mercury is 32 Torr). In addition to the increased deviation of nearby spectral lines, increased absorption on resonance results. As mentioned in earlier chapters, the strong absorption of mercury vapor is apparent at low vapor pressures (0.001 to 0.1 Torr). At such elevated vapor pressures, it is important to consider the effects of absorption on measured signal.

As shown in Figure 6, increased vapor pressure increases both the angle deviation and the absorption band-width. The figure simultaneously plots the transmission profile and deviation versus input frequency for two vapor pressures: 1 Torr and 10 Torr. The mercury vapor path length is roughly 12.5 cm. At 10 Torr, significant enhancement of spatial deviation is exhibited, but the absorption band is also increased. This operating condition is ideal for resolving scattering 4 cm^{-1} from line center. For an 895mm focal length imaging system, 1.7 mm deviation is predicted; whereas, for the 1 Torr cell, these conditions would produce less than 300 microns deviation. The benefit of the lower vapor pressure is that the nearly all light is transmitted through the cell versus 20% transmission at 10 Torr. Roughly 1 cm^{-1} from line center, the 10 Torr cell passes no light; whereas, the 1 Torr cell passes 90%, and deviates light by more than 700 microns. To emphasize the background suppression, the absorption co-efficient is

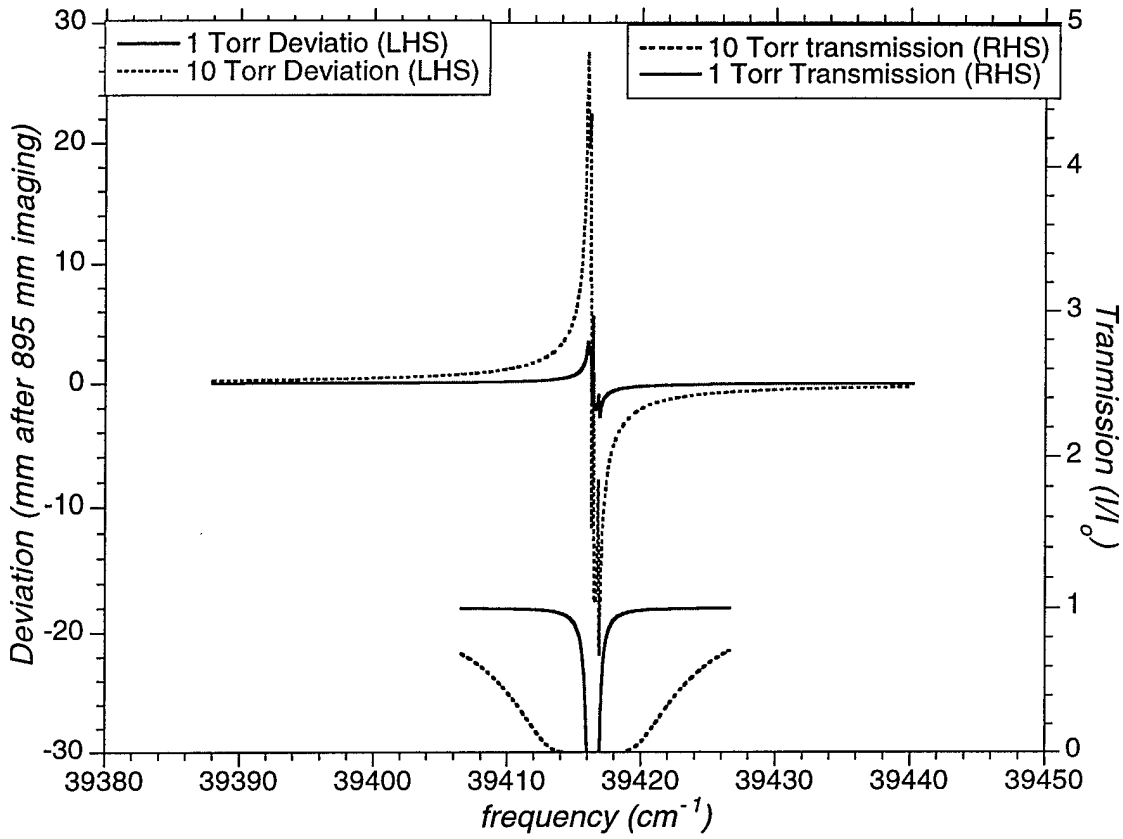

Figure 6: Deviation vs. frequency for two varying vapor pressures (left axis). Simultaneously plotted are transmission profiles vs. frequency (right axis).

modeled to peak at roughly 20,000/cm for 10 Torr. For given spectral features, the cell operating conditions may be optimized to yield high throughput, and large spatial deviation.

Ultimately, the spectral resolution of the dispersion filter is determined by the spatial deviation of spectral features and the resolving element of the detector. From Equation VII.2 it is evident that a long imaging distance is desirable. For fixed lens size, this means larger f/# (defined as the lens focal length divided by the diameter of the lens). However, for low light level collection, fast collection optics are desirable, i.e. small f/#. The resulting trade-off depends upon particular experimental set-up.

Generally, conditions of fast collection and large imaging distance can be achieved by a large aperture (large diameter) system. Practically, large scale optics and cells are limited to a few inches in diameter. As with spectrometers, if the collection and imaging f/#'s are not matched image magnification results. If the entrance slit or object width is smaller than the resolution element of the camera, it is desirable to magnify (decrease the collection optics f/# and increase the imaging distance d) until the image fills at least one resolution element of the detector. Finally, if the detection area is large, relative to the image deviation, magnification beyond one resolution elements in the detector will increase deviation distance, but not increase spectral resolution because the spatial shift-to-width ratio for a given spectral feature is fixed, as each component is independently magnified.

Design

A resonant dispersion prism filter has been fabricated recently in our laboratory. It consists of a pair of concentric all quartz cells, the outer of which is surrounded by a large aluminum sheath, depicted in Figure 7. The inner cell consists of a main body with 2" diameter clear aperture Brewster angle windows, and a side arm cold tip containing 5 gms of mercury. Brewster's angle was selected as the angle of incidence to minimize surface reflection and maintain significant angular deviation. The main body of the inner cell is jacketed with a copper heat conductor which is used to control the temperature and prevent condensation on the Brewster windows. The space between the inner and outer quartz shells is evacuated to allow for heating of the inner cell, while keeping the outermost windows at room temperature. The combination of inner and outer cells allows heating of the inner Brewster windows while simultaneously avoiding

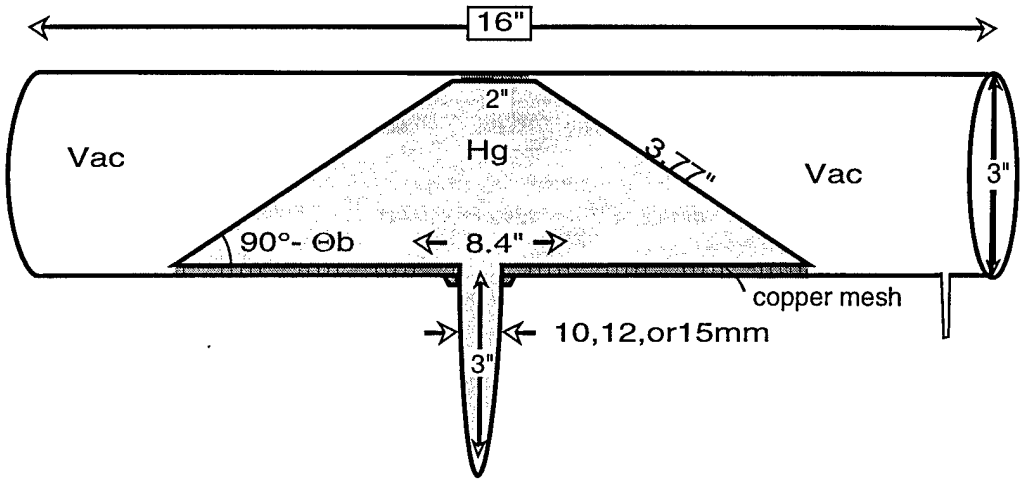

Figure 7a: Schematic of the Hg vapor prism. Concentric quartz cylinders allow for heating of the inner Brewster cut windows, while keeping the outer flat windows cool.

the creation of thermal room currents near the hot windows which would induce additional refraction. Separate heaters and temperature controllers are used to insure that the inner cell body is held at a constant temperature which is slightly warmer than the sidearm cold tip (which controls the vapor pressure). Four resistive cartridge heaters are used to heat the aluminum housing of the side arm cold-tip, while eight identical heaters (two sets of four in parallel), are used to heat the upper aluminum housing. Sea sand is used to increase coupling from the aluminum sheath to the side-arm. The temperature controllers are Omega 7600, rated to ±0.1C. RTD elements are used to assess and control the temperature at four locations on the cell, as listed in Figure 7. Notably, since two wire RTD is used, calibration of the RTD is at the temperature controller rather than the sensing device itself which may induce an offset in measured temperature. This offset reduces the accuracy and not precision of the instrument. The entire cell and housing unit is wrapped with one inch thick ceramic fiber blanket surrounded by Fibercon insulating tape. Operating conditions for the cell range from room temperature to roughly 500K, which is the upper limit of the RTD elements.

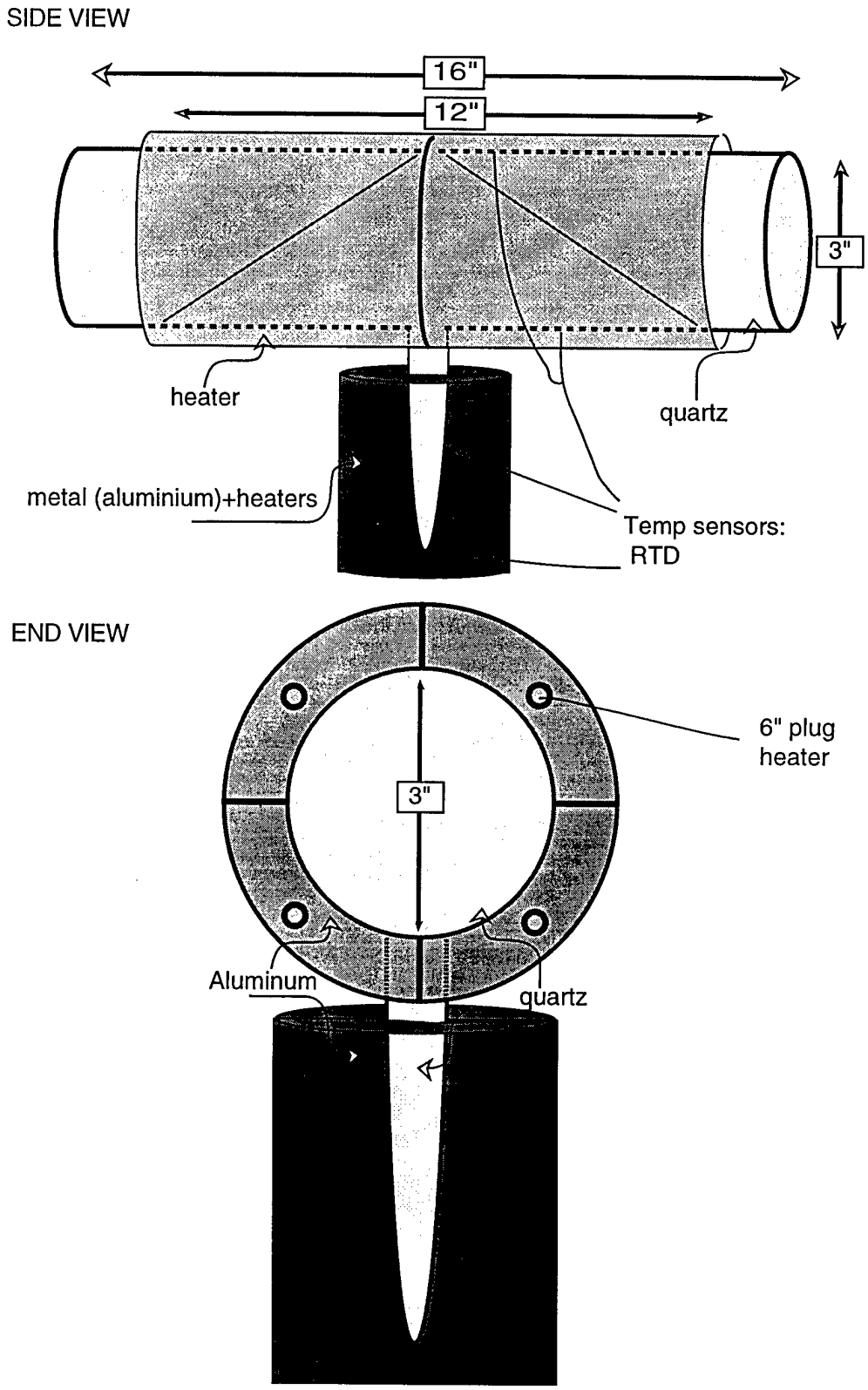

Figure 7b: Schematic of the Hg vapor prism and heater assembly.

Experimental verification

Operating conditions for these experiments were roughly 190C for the inner cell body temperature and 170C for the side arm. This corresponds to a mercury vapor pressure of 6.3 Torr and a thermally broadened absorption linewidth of 1.2 GHz. It is significant to point out that the line center attenuation for this cell is predicted to be in excess of 10^4/cm, due to the exceedingly high value of the imaginary (or absorptive) part of the index-of-refraction. The cell, therefore, simultaneously achieves high suppression on line center and high dispersion off line center.

In order to provide an experimental verification of the predicted dispersion, a target was illuminated with the third harmonic output of the Ti: sapphire laser. A 300 micron slit was illuminated by the diffuse scattering source, and scattering through the slit was collimated with an f/10 lens through the vapor prism. The refracted beam re-imaged (895mm) directly onto the microchannel plate of an intensified video camera which captured images to video. As the laser was tuned in wavelength a camera recorded the displaced image of the slit as a function of spectral detuning from line center of the mercury vapor resonance. The scattering wavelength was determined with the Burleigh wavemeter (± 0.3 cm^{-1}). Camera pixel displacement was calibrated to yield spatial deviation. The results are illustrated in Figure 8, along with model predictions. The agreement is to within the combined uncertainty in the imaging system calibration and the cell pressure. As seen, agreement between model and experiment is further improved by modeling a slightly lower cell temperature (168°C rather than 170°C), suggesting a roughly two degree offset in the measurement of the cell temperature.

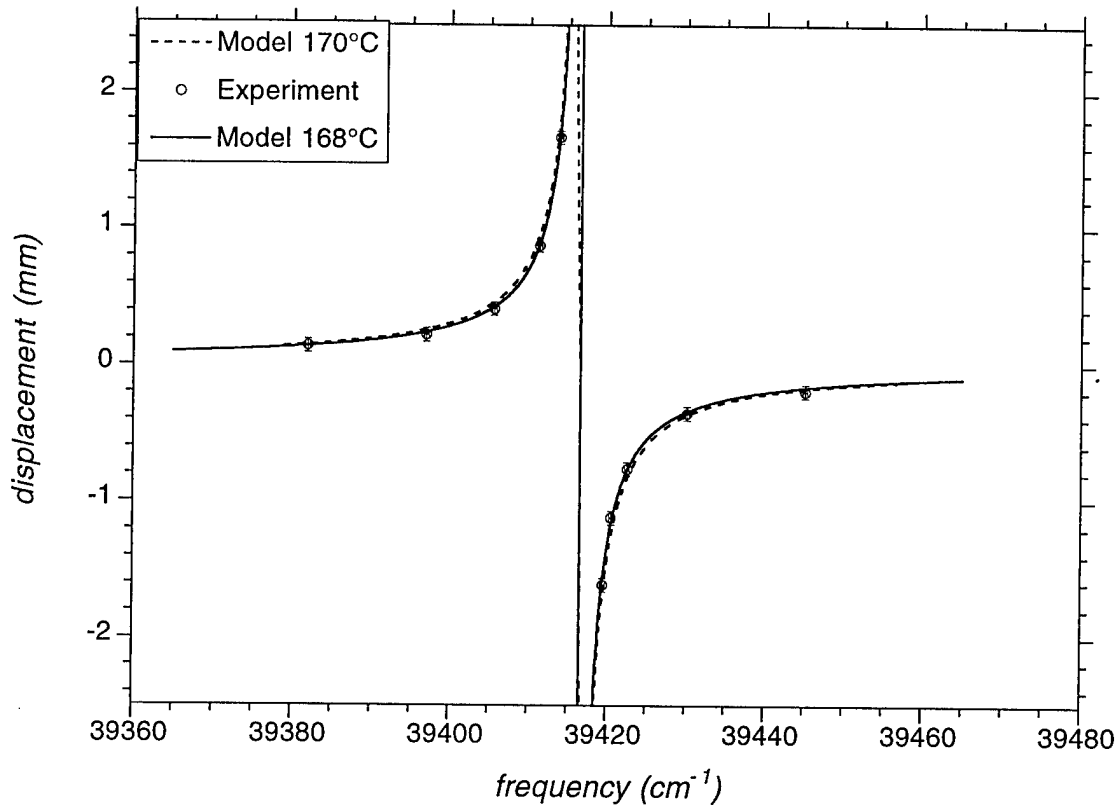

Figure 8: Vapor prism: measured and predicted deviation as a function of incident frequency.

Predictions

Applying this model gives predictions for imaging rotational Raman scattering from various species. Figure 9 models the deviation, and signal strength in a 200 micron pixel resolution element for N_2 and CO_2 scattering. The modeled laser intensity is 30 mJ/ pulse; the cell vapor pressure is 10 Torr; collection is f/10, with a 1 meter imaging length, 0.2 quantum efficiency. Plotted are the predicted Stokes shifted rotational Raman scattering lines for CO_2 and N_2 at STP. As observed, the different spectral signatures of the two species become different spatial signatures. The profiles give a means of measuring temperature (from the Boltzmann distribution), species identification and detection (from the spatial/spectral signature), and density (from the signal strength). For

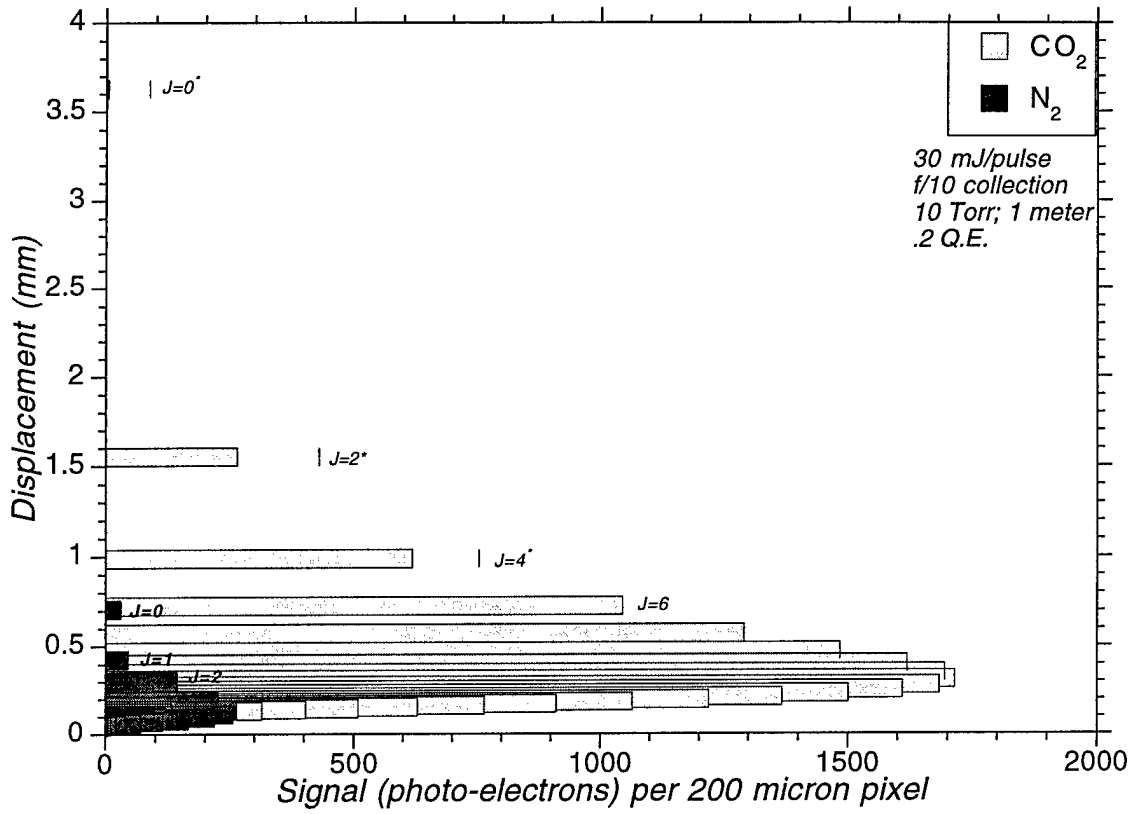

Figure 9: Model predictions for signal level and deviation of CO_2 and N_2 rotational Raman lines. The * indicates absorption of some fraction of incident radiation.

the first three CO_2 lines, there is some absorption by the mercury vapor. This is denoted with the asterisk, and the original, un-attenuated signal levels are plotted as vertical bars. To maximize these lines, a lower vapor pressure or shorter cell would be used. Because the Raman shifted nitrogen lines are further split, their observed dispersion is smaller. To increase the relative spatial deviation of these lines, a higher cell vapor pressure is required.

CO_2 demonstration

Experimental demonstration of rotational Raman scattering from carbon dioxide at STP are given in Figure 10. An incident laser energy of 30mJ/pulse was focused into a

200 μm line, and a 6 mm length of scattering collected with a 550mm lens (roughly f/20 collection) through the vapor prism. A 900 mm imaging lens focused light passing through the prism onto an intensified CCD camera (Princeton Instruments, Pentamax). The image captures roughly 6mm x 6mm in the object plane, with a 1.6x magnification. Two pixels are binned in the vertical dimension, to resolve spectrally induced deviation, while eight pixels are binned in the horizontal. The vapor prism was held at 12 Torr, 210° C. The ultraviolet laser was tuned to 39409 cm^{-1}, which corresponds to roughly a 3 cm^{-1} shift down from the center of the absorption band of the mercury cell. By shifting the incident laser frequency, Stokes shifted scattering is emphasized. Experimental limitations in focusing, and laser beam size (to avoid breakdown), constrained resolution to several hundred microns. Improved alignment, and appropriate beam focussing optics

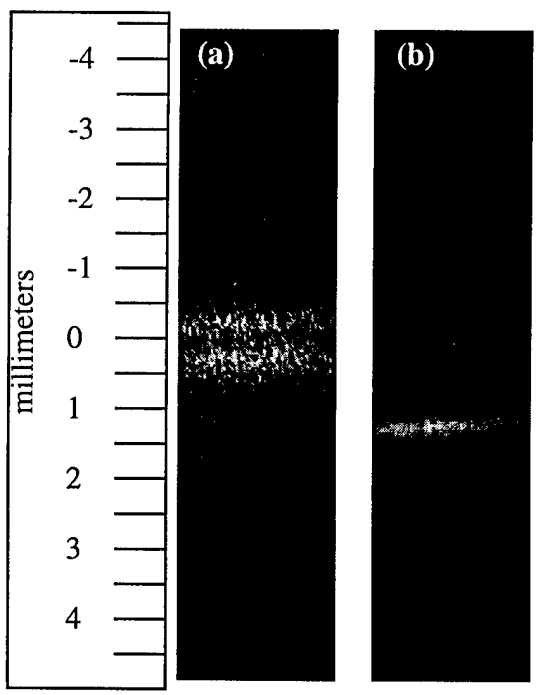

Figure 10: CO_2 rotational Raman scattering imaged with the Hg vapor prism. (a) Raman scattering images of CO_2, with the incident laser in the absorption band of Hg. Figure (b) Rayleigh scattering from CO_2 as the laser is detuned from the absorption band. Spatial deviation arises from the vapor prism and reflects the near resonance of the incident laser light

are expected to yield the camera resolution limit of 80μm depicted in the predictions of Figure 9. Ten shot averages are presented in the image, and while individual rotational Raman lines are not discernible, the Stokes and Anti-Stokes branches are clearly defined.

Comparison of dispersive prism with diffraction spectrometer

Because of their similarities in application and implementation, it is fruitful to compare the dispersion prism to a more conventional spectrometer. First, worthy of note is the similarity that in both cases angular dispersion results in a linear displacement after some imaging distance; the greater the distance the greater the deviation and hence resolution. Second, as discussed above, both feature identical trade-offs between fast collection and increased imaging distance for spectral resolution. Most notably different is the inverted deviation of the dispersive prism. As evident from the index-of-refraction, those spectral features closest to the resonant absorption are deviated the most. A spectrometer deviates linearly — the higher the frequency the greater the deviation. The dispersion prism deviates non-linearly (as seen with the non-linear behavior of the index of refraction), and only close to resonance; whereas the spectrometer/diffraction grating has a broadband dispersion.

The dispersive prism near resonance out performs the state-of-the-art commercial spectrometer both in spectral sensitivity (linear dispersion) and throughput efficiency. The model predictions of the dispersive prism were compared to the specifications of an Acton Research Corporation AM512 2-meter monochrometer with 3600 groves/mm grating.[ARC] At two meters, the linear dispersion of the spectrometer is 0.138 nm/mm. The dispersion of the vapor prism is non-linear with frequency and vapor pressure. Comparisons were made at two vapor pressures, at spectral locations close to

resonance (80% transmission through the cell), and further from resonance. The results are listed in Table 6.1. Close to resonance, the linear dispersion of the vapor prism exceeds the spectrometer from 5 to 25 times. Farther from resonance, the dispersion of the vapor prism matches and eventually drops below that of the diffraction grating. Aside from common imaging loss (collection f/#), the vapor prism throughput depends upon surface reflections and transmission through the mercury vapor. Surface reflection loss is minimal and neglected because it may be eliminated with surface coatings and Brewster angle windows. The trade-off between high vapor pressure (large dispersion) and reduced transmission depends upon precise operating conditions. However, 80% transmission was used as the 'near resonance' operating condition of Table 6.1. Furthermore, minimizing the vapor path length further increases transmission without affecting the deviation (as this arises at the mercury- air interface). In the case of

Hg Prism Modeled Dispersion

pressure (Torr)	v_o (cm^{-1})	v_1 (cm^{-1})	Δy (mm)	**linear dispersion** ($^{nm}/_{mm}$)
10	39424*	39430	1.0	**0.039**
10	39425*	39426	0.26	**0.025**
10	39440&	39441	0.03	**0.22**
1	39417.4*	39418.1	1.0	**0.0045**
1	39425&	39426	0.257	**.251**

Table 7.1: Comparison of spectrometer and dispersive vapor prism. Linear dispersion at two vapor pressures: near resonance * and far from resonance &, for a 2 meter image length. Compare with 0.138 nm/mm linear dispersion of an ARC 2m monochrometer. (The lower the number for linear dispersion, the higher spectral sensitivity).

spectrometers, the dispersive element itself is lossy due to higher orders of diffraction. Optimizing the grating for a particular wavelength region by blazing, efficiencies of 50-70% can be achieved for first order diffraction.[ARC]

Improvements

A variety of mechanisms may be used to increase the dispersion, and hence sensitivity of this filter. Because the filter relies upon the index variation at the Brewster window interface, and not the path length through the vapor, a multi-pass or series of vapor prisms additively improve the dispersion. Successive placement of vapor prisms, or multi-pass arrangements will only fail when the dispersion exceeds the given aperture. In such cases, the desired deviation has presumably been achieved. An alternative approach arises from creating a density gradient in the mercury vapor which is perpendicular to the input radiation (i.e. a vertical gradient in Figure 1b). This variation in the number density is analogous to the volume effects observed in schlieren or shadowgraph. Incident radiation is deviated by the variation in index-of-refraction, or number density. The longer the traversed path, the greater the angular deviation. In essence, the gradient in number density (which may be made quite dramatic with temperature variation) produces a very large effective incidence angle. Meanwhile the input window may be placed at any angle, including Brewster's angle to reduce reflection loss. This is just as Robert Wood demonstrated with sodium vapor in a cell placed over a flame.[Wood] The dramatic variation in number density, created significant dispersion, and resulted in measurable dispersion over nanometers. Appropriate temperature measurement and control, along with calibration could overcome Wood's difficulty in determining number density.

References

ARC, Acton Research Corporation, Monochrometers Systems and Accessories Catalog, Acton Mass, (1997)

Cheng, T.S., Wehrmeyer, J.A., and Pitz, R.W., "Simultaneous Temperature and Multispecies Measurement in a Lifted Hydrogen Diffusion Flame," *Combustion and Flame*, **91**, 323-345 (1992).

Gu, Y., Rothe, E.W., Reck, G.P., "One-Dimensional Imaging of H_2 Densities and of Temperatures via Rotational Raman Scattering of Narrow-Band, 248nm, Laser Light," *Journal of Raman Spectroscopy*, **28**, in press (1997).

Longhurst, Geometrical and Physical Optics, Longman Group, London, 458, (1967).

Klien, M.V., Optics, John Wiley & Sons, Inc., New York, 589-90, (1970).

Marlow, W.C., "Hakenmethode," *Applied Optics*, 6(10), 1715-1724, (1967).

Rothe, E.W., and Andresen, P., "Application of tunable excimer lasers to combustion diagnostics: a review," *Applied Optics*, **36**(18), 3971-4033, (1997).

Skaggs, P.A., Brown, T.M., Nandula, S.P., Pitz, R.W., and Hassel, E.P., "Multi-Species Measurements in CH4-Air Flames using a Narrowband KRF Excimer Laser by UV Raman Scattering," AIAA paper 94-0613, 32nd Aerospace Sciences Meeting & Exhibit, Reno NV (1994)

Wehrmeyer, J.A., Cheng, T-S, and Pitz, R.W., "Raman scattering measurements in flames using a tunable KrF excimer laser," *Applied Optics*, **31**(10), 1495-1504, (1992).

Wood, R.W., Physical Optics, Dover Publications, New York, 495, (1967).

Chapter 8: Concluding Remarks

This thesis has detailed the development, characterization and implementation of a new ultraviolet laser source and three new spectral filters for non-intrusive diagnostics. The significance of the laser is that is gives a precise and controllable probe for interrogating complex flowfield parameters. The unique characteristic of this light source is that it combines high power (50 mJ/pulse) with excellent spectral characteristics in the ultraviolet. Because the output is near transform limited spectrally, the spectral density (energy per bandwidth) is exceedingly high. Furthermore, the system is tunable, and frequency agile. It is capable of operating in a broad range of frequencies, limited practically to a 30 nm range in the ultraviolet (at 250 nm) by coatings and harmonic generating crystals. Within that operating range, because of a new cavity locking scheme, the laser is capable of tuning continuously (12 MHz discrete steps), discontinuously, and rapidly without loosing its narrow band operation. The the spectral purity, tuning capabilities, high energy, and ultraviolet operation of this laser system uniquely make it attractive for spectroscopic and diagnostic applications.

Each of the three optical filters presented advances spectral filtering capabilities for imaging. The notch absorption filter achieves very high contrast between in-band and out-of-band light by strongly absorbing light resonant with the ground state ^3P-^1S transition of mercury. This filter is used both qualitatively for flowfield imaging, and qualitatively for flowfield measurement of velocity in a demonstration of UltraViolet Filtered Rayleigh Scattering measurements of a Mach 2 free jet. For species specific

measurements, two filters capable of resolving rotational Raman scattering are developed, characterized and modeled. A notch passband filter based on the resonant fluorescence of the ground state mercury vapor simultaneously offers high spectral resolution and high spatial resolution. High resolution measurements of individual rotational Raman lines are made, and agree well with model predictions. Sacrificing one spatial dimension, measurements of multiple rotational lines may be achieved with one-dimensional spatial resolution. This final filter is realized by creating a mercury vapor prism and refracting nearby rotational Raman lines while suppressing the elastically scattered Rayleigh line.

Each of these tools may be further tailored to specific experimental application. For continued work in filtered Rayleigh scattering, higher accuracy measurements will be achieved with a more stable frequency reference. The pulsed laser is currently limited in spectral stability by its seed source; locking the seed source to a known reference will yield better measurements. In the infra-red at 760nm, the oxygen A band is a likely candidate for an absolutely stable reference for a heterodyne scheme. Alternatively, a stabilized etalon can provide relative frequency stability which is the minimum criteria for UVFRS measurements. An additional improvement in the laser system is laser diode injection seeding. Diodes offer the advantage of being compact, solid state, and rapidly and easily tunable. Diode seeding requires an additional optical isolator (for a minimum of 60dB attenuation of feedback), and the spectral range is constrained. However, for limited tuning range experiments such as filtered Rayleigh scattering, a diode seed source is an attractive alternative.

Alternate filter designs are discussed in the appropriate chapters. However, it is worthy to highlight the potential for the narrow passband imaging filters. The most

significant improvement for the fluorescence based imaging filter is to increase signal for low light level applications. Faster imaging optics present one alternative. For instance an f/1.2 ultraviolet imaging lens is newly available from Princeton Instruments, Inc. A second alternative is to operate the experiment at the front surface of the filter, which avoids the initial imaging step. For laser based experiments, the significant flare or elastic scattering coincident with the interrogation pulse is inconsequential, as the temporal extent of the fluorescence removes non-resonant scattering. Another design for the filter is to implement a short-cell, where the vapor cell extends for tens of microns in depth. While some signal is lost, a short cell design allows for imaging fluorescence *through* the cell. Imaging is maintained due to the short physical extent of the vapor. Such an implementation bears high potential for higher yield processes — as with fluorescence for mercury monitoring and detection. The current challenge with the dispersion vapor prism is to increase the dispersion without increasing the optical depth of the cell. As the optical depth increases, it occludes imaging the scattering which is spectrally close to the mercury resonance. In some cases, such scattering may be the most informative to the experimentalist. Ideally, the filter would allow for separate control of optical depth and refractive index. While inherently coupled (by number density), alternative designs provide for some leverage. Because the optical depth is a volume effect and the refraction is an interface effect, a short cell reduces attenuation without affecting dispersive properties. By passing through a single short cell more than once or passing through a series of short prisms, the dispersion adds linearly (with number of interfaces) while the optical depth adds exponentially (with the pathlength of vapor). Alternatively, a cell with a controlled vapor density gradient would allow for some separate control of optical depth

and refraction. Setting the minimum vapor density would determine the minimum optical depth, and the highest vapor density would determine the gradient and hence refractive properties. With either the multiple interface (series of cells) or the density gradient arrangement, significant potential exists for accentuating the dispersion, which in particular spectral regimes already offers linear dispersion far surpassing existing prism or grating technology.

This thesis concentrated on the application of these tools for non-intrusive aerodynamic flowfield measurements. Creative application of these filters and light source give rise to a host of alternative applications. The field of remote sensing in general offers generous opportunity for exploiting these pieces. Both fluorescence and differential absorption lidar based non-intrusive monitoring of atmospheric mercury have recently been demonstrated.[Bahns; Edner]

References

Bahns, J.T., Lynds, L., Stwalley, W.C., Simmons, V., Robinson, T., and Bililign, S., "Airborne-mercury detection by resonant UV laser pumping," *Optics Letters*, **22**(10), 727, (1997).

Edner, H., Faris, G.W., Sunesson, A., Svanberg, S., "Atmospheric atomic mercury monitoring using differential absorption lidar techniques," *Applied Optics*, **28**(5), 921, (1989).

Appendix A

Hg Absorption Lineshape Profile

Voigt profile (Whiting approximation) for the 3P-1S transition of Hg at 253.7 nm Includes the differening naturally occuring isotopes and their relative positions and oscillator strengths. It takes into account the hyperfine splitting of the odd isotopes. The output produces three columns: frquency, the normalized absoption lineshape, and the transmission through a fixed length cell (from Beer's Law). It includes the relative number density, and oscillator strengths...

FILE: MAIN.C

```
#include <stdio.h>
#include <math.h>
#include <stdlib.h>
#include "utility.h"

#define NUMLINES 10

double lineshape(double x, double x0, double g_width, double l_width);

/*          Hg Absorption Lineshape Profile

   this is a voigt profile (Whiting approximation) for the 3P-1S transition
   of Hg at 253.7 nm ... it includes the differening naturally occuring isotopes
   and their relative positions and oscillator strengths.  It takes into account
   the hyperfine splitting of the odd isotopes.
   The output is the _normalized_ absoption lineshape (which belongs in the exponent of
   transmission profile (Beer's Law)  exp[- constant * output lineshape)]  It includes the
    relative number density, and oscillator strengths...
    It is meant as an empical fit to absorption profile.  The leading constant will account
    of overall number density, etc.*/

double lineshape(double x, double x0, double g_width, double l_width)
{
        double wv, det, z, norm, p2, p225, val;

        wv = l_width/2 + sqrt(pow(l_width,2)/4 + pow(g_width,2));

        det = x - x0;
        z = l_width/wv;

        norm = wv * (1.065 + 0.447 * z + 0.058 * pow(z,2));
        norm = 1/norm;

        p2 = pow(det/wv,2);
        p225 = pow(fabs(det/wv),2.25);

        val = (1 - z) * exp(-2.772 * p2) + z/(1 + 4 * p2);
        val += 0.016 * (1 - z) * z * (exp(-0.4 * p225) - 10/(10 + p225));
        val *= norm;

        return val;
}


void main(void)
{
        int again = 1;
        double a[10],f[10], l_width, g_width, lorentz, temp, pres, z, os, mass, x0[10], x_min,
            x_max, freq, dx;
        int             steps, i, j;
        FILE *f_file;
        double val, trans;
```

```
while (again)
{

temp = GetFloat("Temperature (K): ", TRUE);
pres = GetFloat("Pressure (Torr): ", TRUE);
lorentz = GetFloat("Pressure Broadening (GHz/Torr): ", TRUE);
z = GetFloat("Cell length (cm)1,5,12.7: ", TRUE);

//x0 = GetFloat("Line center: ", FALSE);
//x_min = -100*(g_width + l_width);
//x_max = -x_min;

// cell length [cm]
//      z = 12.7;
//      z = 5.0;
//      z=1.0;

// oscillator strength
os = 0.0241364;

//calculate lorentz and gauss widths (GHz)
mass = 200.59;
l_width = 1/(2*3.14159*120) + lorentz*pres;
g_width = 0.846354*sqrt(temp/mass);

printf("lorentz (GHz)\tgauss (GHz)\ttemp. (K)\tpressure (Torr)\tlength (cm)\n");
printf("%7.6le\t%7.6le\t%7.6le\t%7.6le\t%4.3le\n", l_width, g_width, temp, pres, z);


l_width = GetFloat("Lorentz width (GHz): ", TRUE);
g_width = GetFloat("Gauss width (GHz): ", TRUE);

//GetFloatRange(&x_min, &x_max, "range for calculation ", NULL);
steps = (int) GetFloat("number of steps: ", TRUE);



// positions of the lines
x0[0]=-15.409; /* Hg 199 1/2 ***** corrected * 9/19 */
x0[1]=-15.313; /* Hg 204 */
x0[2]=-14.662; /* Hg 201 5/2 */
x0[3]=-10.106; /* Hg 202  */
x0[4]=-4.805;  /* Hg 200  */
x0[5]=-0.676;  /* Hg 201 3/2 */
x0[6]=0.0;     /* Hg 198  */
x0[7]=4.107;    /* Hg 196  */
x0[8]=6.728;   /* Hg 199 3/2 */
x0[9]=6.872;   /* Hg 201 1/2 */

// relative population density ... natural abundances //
a[0]=.1684;
a[1]=.0685;
a[2]=.1322;
a[3]=.298;
```

```
a[4]=.2313;
a[5]=.1322;
a[6]=.1002;
a[7]=.0016;
a[8]=.1684;
a[9]=.1322;

/*      // Hg 202 cell abundances //
a[0]=.0017;
a[1]=.0028;
a[2]=.01;
a[3]=.9650;
a[4]=.015;
a[5]=.01;
a[6]=.0006;
a[7]=.0000;
a[8]=.0017;
a[9]=.01;
*/
        // hyper fine degeneracy ... relative to no HF splitting //
f[0]=.3333;
f[1]=1;
f[2]=.5;
f[3]=1;
f[4]=1;
f[5]=.3333;
f[6]=1;
f[7]=1;
f[8]=.6667;
f[9]=.1667;

x_min=-300;
x_max=300;

dx = (x_max - x_min)/((double) (steps - 1));
freq = x_min;

f_file = AskAndOpen("file name: ", "w");
fprintf(f_file, "lorentz\tgauss\ttemp\tpres\tlength\n");
fprintf(f_file, "%7.6le\t%7.6le\t%7.6le\t%7.6le\t%4.3le\n", l_width, g_width, temp, pres,
    z);
fprintf(f_file, "freq\tvalue\ttrans\n");
for (i = 0; i < steps; i++)
{
//              val = lineshape(freq, x0, g_width, l_width);

                val=0.0;
                trans = 0.0;
                for(j=0;j<NUMLINES;j++) val += a[j]*f[j]*lineshape(freq, x0[j],
                        g_width, l_width);
                trans = exp(-2.65e-11*(pres/temp)*(9.657e+18)*os*z*val);

                fprintf(f_file, "%7.6le\t%9.9le\t%9.9le\n", freq, val, trans);
                freq += dx;
```

```
        }

        fclose(f_file);
        printf("again(0=no, 1=yes)? ");
        scanf("%d",&again);
```

FILE UTILITY.C:

contains utilities for file / i/o operations called by MAIN.C

```
#include        <stdio.h>
#include        <math.h>
#include        "utility.h"
#include        <string.h>

int GetFloatRange(float *inMin, float *inMax, char *message1, char *message2)
{
    float   low;
    float   high;
    int     ok;
    int     skip;

    ok = skip = FALSE;

    printf("\n%s\n", message1);
    printf("Range: Min = %9.2f; Max = %9.2f.  [0, 0] to skip.\n\n", *inMin, *inMax);

    while (!ok)
    {
        printf("%s [low, high]: ", message2);/* low, high are not the variables here */
        if (scanf("%f,%f", &low, &high) == 2)
        {
            if ((low == 0.0) && (high == 0.0))
                ok = skip = TRUE;
            else if ((low < high) && ((low <= *inMax) && (low >= *inMin) && (high <= *inMax) &&
      (high >= *inMin)))
                ok = TRUE;
            else
            {
                printf("Invalid range.  Min = %9.2f; Max = %9.2f.\n", *inMin, *inMax);
            }
        }
        else
        {
            printf("Incorrect format.  Must be [low, high].\n");
        }
    }

    if (!skip)
    {
        *inMin = low;
        *inMax = high;
    }

    return (!skip);
```

```
}

float GetFloat(char *message, int needPositive)
{
    int     ok;
    float   val;

    ok = FALSE;


    while (!ok)
    {
        printf("%s ", message);
        if (scanf("%f", &val) == 1)
        {
            if ((val <= 0) && (needPositive))
            {
                printf("Invalid number.  Needs to be greater than zero.\n");
            }
            else
                ok = TRUE;
        }

        else
        {
            printf("Invalid entry.  Must be a number.\n");
            fflush(stdin);
            fflush(stderr);
            fflush(stdout);
        }
    }
    fflush(stdin);
    fflush(stderr);
    fflush(stdout);
    return (val);
}

int ShortAnswerQuestion(char *message, char trueAns, char falseAns)
{
    char    resp;

    /*resp = getchar();*/
    while(1)
    {
        printf("%s", message);
        resp = getchar();
        if (resp == trueAns)
            return (TRUE);
        else if (resp == falseAns)
            return (FALSE);
        else
        {
            printf("Wrong response.  Must be %c/%c.\n", trueAns, falseAns);
            fflush(stdin);
```

```
            fflush(stderr);
            fflush(stdout);
        }
    }
    fflush(stdin);
    fflush(stderr);
    fflush(stdout);
}

/*int ShortAnswerQuestion(char *message, char trueAns, char falseAns)
{
    char    resp;

    fflush(stdin);

    while(1)
    {
        printf("%s", message);
        fflush(stdin);
        if (scanf("%c", &resp) == 1)
        {
            if (resp == trueAns)
                return (TRUE);
            else if (resp == falseAns)
                return (FALSE);
            else
            {
                printf("Wrong answer.\n");
                fflush(stdin);
            }
        }
        else
        {
            printf("Wrong response.  Must be %c/%c.\n", trueAns, falseAns);
            fflush(stdin);
        }
    }
}
*/

static FILE *GetFile(char *message, char *fileName, char *mode);

static FILE *GetFile(char *message, char *fileName, char *mode)
{
    FILE    *f_file;
    int     ok;

    f_file = NULL;
    ok = FALSE;

    fflush(stdin);

    while (!ok)
    {
```

```
        printf(message);
        if ((scanf("%s", fileName) == 1) && (strcmp(fileName, "q")))
        {
            if (f_file = fopen(fileName, mode))
                    ok = TRUE;
            else
            {
                    if (mode[0] == 'r')
                    {
                    puts("File not found. Try again.");
                    fflush(stdin);
                    }
                    else
                    {
                    puts("Not a valid file name. Try again.");
                    fflush(stdin);
                    }
            }
        }
        else if (!strcmp(fileName, "q"))
        {
            f_file = NULL;
            ok = TRUE;
            fflush(stdin);
        }
        else
        {
            puts("Not a valid file name. Try again.");
            fflush(stdin);
        }
    }
    return (f_file);
}

FILE *AskAndOpen(char *message, char *mode)
{
    char    fileName[128];

    return (GetFile(message, fileName, mode));
}

int GetAReadFileName(char *fileName, char *message, char *mode)
{
    FILE*f_file;

    if ((f_file = GetFile(message, fileName, mode)) != NULL)
    {
        fclose(f_file);
        return (TRUE);
    }
    else
        return (FALSE);
}
```

Appendix B

Hg Fitting Routine

Based on Powell's method for minimizing the figure of merit χ^2. Directional vectors are used to determine fit parameters by minimizing χ^2. The mercury model of Appendix A is included.

Any model parameter may be fit. Most common are: temperature, pressure, broadening co-efficient, zero offset, and frequency stretch.

Notably several routines are called from Numerical Recipies. They are list below, but not included in the complete listing of code.

FILE DPOWELL.C

powell fitting routine

```
void dpowell(double p[], double **xi, int n, double ftol, int *iter, double *fret,
```

FILE DBRENT.C

```
double dbrent(double ax, double bx, double cx, double (*f)(double), double tol,
        double *xmin)
```

FILE DLINMIN.C

line minimizing routine for Powel method

```
void dlinmin(double p[], double xi[], int n, double *fret, double (*func)(double []))
```

FILE: DF1DIM.C

1-d fitting

```
double df1dim(double x)
```

FILE DMNBRAK.C

```
#void dmnbrak(double *ax, double *bx, double *cx, double *fa, double *fb, double *fc,
```

FILE: NRUTIL.C

utilities for powell fitting routine

FILE FIT.C

fitting routine for Hg lineshape

```
#include <stdio.h>
#include <math.h>
#include <stdlib.h>
#include "utility.h"
#include "lineshape.h"
#include "read.h"
#include "chimin.h"
#include "nrutil.h"
#include "dpowell.h"

double freq[10000],data[10000], temp, z, sigma;
int steps;

void main(void)
{
        FILE *g_file;
        double  pres, stretch, offset, lorentz, init[7], sig[4],tst[4],delt1,delt2,delt3;/*temp,*/
        double **dir;
        int num,i;
        double chi;

        dir = dmatrix(1,4,1,4);
        dir[1][1] = .0001;
        dir[1][2] = 0;
        dir[1][3] = 0;
        dir[1][4] = 0;
//      dir[1][5] = 0;
//      dir[1][6] = 0;
        dir[2][1] = 0;
        dir[2][2] = .001;
        dir[2][3] = 0;
        dir[2][4] = 0;
//      dir[2][5] = 0;
//      dir[2][6] = 0;
        dir[3][1] = 0;
        dir[3][2] = 0;
        dir[3][3] = .001;
        dir[3][4] = 0;
//      dir[3][5] = 0;
//      dir[3][6] = 0;
        dir[4][1] = 0;
        dir[4][2] = 0;
        dir[4][3] = 0;
        dir[4][4] = 0.0001;
//      dir[4][5] = 0;
//      dir[4][6] = 0;
//      dir[5][1] = 0;
//      dir[5][2] = 0;
//      dir[5][3] = 0;
//      dir[5][4] = 0;
//      dir[5][5] = 0.0001;
```

```
//              dir[5][6] = 0;
//              dir[6][1] = 0;
//              dir[6][2] = 0;
//              dir[6][3] = 0;
//              dir[6][4] = 0;
//              dir[6][5] = 0;
//              dir[6][6] = 0.01;

                g_file = AskAndOpen("file name: ", "r");

                steps = ffread(g_file, freq, data);

                temp = GetFloat("Temperature (K): ", TRUE);
                pres = GetFloat("Pressure (Torr): ", TRUE);
                stretch = GetFloat("Frequency stretch (e.g 1.02): ", TRUE);
                offset = GetFloat("Freqeuncy offset  (GHz): ", FALSE);
                lorentz = GetFloat("Lorentz Pressure Coeff (GHz/Torr): ", TRUE);
                sigma = GetFloat("Sigma (fraction of datavalue): ", TRUE);
//              z = GetFloat("Cell Length (cm): ", TRUE);
                sig[1] = 0;
                sig[2] = 0;
                sig[3] = 0;
                sig[4] = 0;
                tst[1] = 0;
                tst[2] = 0;
                tst[3] = 0;
                tst[4] = 0;
//              init[1] = temp;
                init[1] = pres;
                init[2] = stretch;
                init[3] = offset;
                init[4] = lorentz;
//              init[6] = z;

// minimization scheme

                dpowell(init, dir, 4, .1, &num, &chi, chimin);

//              temp = init[1];
                pres = init[1];
                stretch = init[2];
                offset = init[3];
                lorentz = init[4];
//              z = init[6];
// calc errors
                for (i = 1; i < 5; i++)
                {
                delt2 = chi;
                init[i] = init[i] - 0.01*init[i];
                delt1 = chimin(init);
                init[i] = init[i] + 0.02*init[i];
                delt3 = chimin(init);
                init[i] = init[i] - 0.01*init[i];
                sig[i] = 0.01*init[i]*sqrt(2*(1/(delt1 -2*delt2 +delt3)));
```

```
                tst[i] = delt1-2*delt2+delt3;
                }
                printf("Done. Chisq: %lf\nTemp =   %lf\nPres =   %lf\tsig: %le\t%lf\nStretch = %lf\tsig:
                    %le\t%lf\nOffset = %lf\tsig: %le\t%lf\nLorentz = %lf\tsig: %le\t%lf\nLength =
                    %lf\nDatapoints: %f\n", chi, temp, pres, sig[1],tst[1], stretch, sig[2], tst[2], offset,
                    sig[3], tst[3],lorentz, sig[4], tst[4], z, (double)steps);
}
```

FILE: CHIMIN.C

mimizing figure of merit

```
#include <math.h>
#include <stdio.h>
#include "chimin.h"
#include "lineshape.h"
#define NUMLINES 10

extern double freq[10000],data[10000], temp, sigma, z;/*pres*/
extern int steps;

double chimin(double *p)
{
        double val, trans, chisq;
        double pres,/* temp,*/ stretch, offset, lorentz, modfreq, os, mass, l_width, g_width, x0[10], a[10],
f[10];
        int i, j, params;
  static int counter = 0;

   params = 4;
//      temp = p[1];
        pres = p[1];
        stretch = p[2];
        offset = p[3];
        lorentz = p[4];
//      z = p[6];

        // cell length [cm]
        z = 5.0;

        // oscillator strength
        os = 0.0241364;

        //calculate lorentz and gauss widths (GHz)
        mass = 200.59;
        l_width = 1/(2*3.14159*120) + lorentz*pres; //should add laser line here ... + laser
        g_width = 0.846354*sqrt(temp/mass); // could add the laser linewidth in here
                        // by doing an RMS of SQRT(glw^2+laser^2)
                        // but the 30 MHz << 1 GHz  -> 1.00045 GHz
                        // not worth it.

        // positions of the lines
/*
        x0[0]=-16.072; /* Hg 199 1/2 *   ***** corrected (thanks Azer) ****** re: Bitter
        x0[0]=-15.391// Hg 199 1/2 a la webster optics communications12/1980
                                        // and Bitter revisited ... check all?
```

```
x0[1]=-15.333; /* Hg 204
x0[2]=-14.679; /* Hg 201 5/2
x0[3]=-10.116; /* Hg 202
x0[4]=-4.812;  /* Hg 200
x0[5]=-0.678;  /* Hg 201 3/2
x0[6]=0;       /* Hg 198
x0[7]=4.1;     /* Hg 196
x0[8]=6.738;   /* Hg 199 3/2
x0[9]=6.882;   /* Hg 201 1/2 */

x0[0]=-15.409; /* Hg 199 1/2 ***** corrected * 9/19 */
x0[1]=-15.313; /* Hg 204 */
x0[2]=-14.662; /* Hg 201 5/2 */
x0[3]=-10.106; /* Hg 202  */
x0[4]=-4.805;  /* Hg 200  */
x0[5]=-0.676;  /* Hg 201 3/2 */
x0[6]=0.0;     /* Hg 198  */
x0[7]=4.107;   /* Hg 196  */
x0[8]=6.728;   /* Hg 199 3/2 */
x0[9]=6.872;   /* Hg 201 1/2 */

// relative population density ... natural abundances //
a[0]=.1684;
a[1]=.0685;
a[2]=.1322;
a[3]=.298;
a[4]=.2313;
a[5]=.1322;
a[6]=.1;
a[7]=.0014;
a[8]=.1684;
a[9]=.1322;

// oscillator strength ... relative to no HF splitting //
f[0]=.3333;
f[1]=1;
f[2]=.5;
f[3]=1;
f[4]=1;
f[5]=.3333;
f[6]=1;
f[7]=1;
f[8]=.6667;
f[9]=.1667;

chisq = 0.0;
modfreq = 0.0;
for (i = 0; i < steps; i++)
{
val = 0.0;
trans =0.0;
modfreq = (freq[i]-offset)*stretch;
for(j=0;j<NUMLINES;j++) val += a[j]*f[j]*lineshape(modfreq, x0[j], g_width, l_width);
trans = exp(-2.65e-11*(pres/temp)*(9.657e+18)*os*z*val);
```

```
        chisq += (trans - data[i])*(trans - data[i])/((sigma*data[i]+0.01)*(sigma*data[i]+0.01));
        }
//      chisq /= (double)(steps-params);

        fprintf(stderr, "chimin called %d\t value %e\tpres %f\n", counter++, chisq,pres);

return chisq;
}
```

FILE LINESHAPE.C

voigt lineshape for fitting

```
#include <math.h>
#include "lineshape.h"


double lineshape(double x, double x0, double g_width, double l_width)
{
    double wv, det, z, norm, p2, p225, val;

    wv = l_width/2 + sqrt(pow(l_width,2)/4 + pow(g_width,2));

    det = x - x0;
    z = l_width/wv;

    norm = wv * (1.065 + 0.447 * z + 0.058 * pow(z,2));
    norm = 1/norm;

    p2 = pow(det/wv,2);
    p225 = pow(fabs(det/wv),2.25);

    val = (1 - z) * exp(-2.772 * p2) + z/(1 + 4 * p2);
    val += 0.016 * (1 - z) * z * (exp(-0.4 * p225) - 10/(10 + p225));
    val *= norm;

    return val;
}
```

FILE READ.C

```
#include <stdio.h>
#include "read.h"

int ffread(FILE *g_file, double *freq, double *data)
        {
        int i=0;
        double a,b;

        while(!feof(g_file))
        {
                fscanf(g_file, "%lf %lf", &a, &b);
                freq[i]=a;
                data[i]=b;
                i ++;
        }
        fclose(g_file);
        return i;
```

Appendix C

Monte Carlo Simulation

Three different incarnations of the simulation are used to capture the flight of photons at an individual frequency (Monte.c), or the flight of photons at a series of different frequencies (Montet.c), or finally a catalog of the duration of flight of each photon as it interacts with the mercury vapor (Monteth.c)

Each of the programs contains a Main subroutine which calls the other listed files: gauss.c (which gives a gaussian distribution of random numbers), and absorb.c (which gives a propagation distance of a photon for a given frequency).

FILE: monte.c

original monte carlo simulation... produces file of
input frequency, and photon count for front (singal), wall, back,held exit conditions.

```
#include <stdio.h>
#include <math.h>
#include "absorb.h"
#include "gauss.h"

static double cellWidth  = 10.0;     /* microns */
static double pathLength = 50000.0;  /* microns */
static double oldalpha   = 0.0004;   /* per micron */

#define LASER -10.106
/* #define PEAK  -10.106 */
#define YWALL 25000.0  /* microns */

/* should be pathlength / cellwidth */
#define NCELL 5000

#define TAU       120.0
#define MAXBOUNCE 25
#define MAXTIME   (MAXBOUNCE * TAU)
#define MAXFREQ 15.0
#define MINFREQ -25.0

static int count[MAXBOUNCE*2];
static FILE *backFile = NULL;
static FILE *wallFile = NULL;
static FILE *monteFile = NULL;

void
initCount()
{
 int i;

 for (i = 0; i < MAXBOUNCE; i++)
   {
    count[i] = 0;
   }
}


void
dumpCount()
{
 int i;

 for (i = 0; i < MAXBOUNCE; i++)
   {
    printf("%d %d\n", i, count[i]);
   }
}
```

```
double
distance(double alpha)
{
 double p,d;

 p = drand48();                    /* double-precision  [0.0,~1.0) */
 p = 1.0 - p;                                          /* (~0.0,1.0] */
 d = (-1.0 / alpha) * log(p);

 return d;
}

double
peakfind(double freq)
{
 double x0[10];
 double p;
 int j;

 /* positions of the lines */
 x0[0]=-15.409; /* Hg 199 1/2 ***** corrected * 9/19 */
 x0[1]=-15.313; /* Hg 204 */
 x0[2]=-14.662; /* Hg 201 5/2 */
 x0[3]=-10.106; /* Hg 202  */
 x0[4]=-4.805;  /* Hg 200  */
 x0[5]=-0.676;  /* Hg 201 3/2 */
 x0[6]=0.0;     /* Hg 198  */
 x0[7]=4.107;   /* Hg 196  */
 x0[8]=6.728;   /* Hg 199 3/2 */
 x0[9]=6.872;   /* Hg 201 1/2 */

 p=x0[0];
 for (j=1; j<10; j++)
  {
   if (fabs(p-freq) > fabs(x0[j]-freq))
                 {
                  p = x0[j];
                 }
  }
 return p;
}

double
delayTime()
{
 double p,d;

 p = drand48();                    /* double-precision  [0.0,~1.0) */
 p = 1.0 - p;                                          /* (~0.0,1.0] */
 d = -TAU * log(p);

 return d;
}
```

```
static int backs = 0;
static int wall = 0;
static int TotalCount = 0;
static int held = 0;

int
bounces(double freq,double pres,double temp)
{
 double alpha;
 double newWidth;
 double dopp;
 double peak;
 int    bounce = 0;
 double dir    = 1.0;
 double x      = 0;
 double y      =  0;
 /*  double pres   = 0.05;
    double temp   = 373.15; */

 do
  {
   alpha = absorb(freq, pres, temp);
   peak = peakfind(freq);
   x    += dir * distance(alpha);
   y    += sin(acos( dir ) ) * distance(alpha);
   dir   = cos( drand48()*M_PI );
   dopp = freq - peak;
   freq  = gaussRandom(gaussAbsorbWidth(temp), peak);
   /* freq = peak + dopp*(dir); */
   /* freq = PEAK; */
   bounce++;
  }
 while (x > 0.0 && x < pathLength && bounce < MAXBOUNCE && y < YWALL);

 if (x >= pathLength)
  {
   backs++;
   /* if (backFile)
                fprintf(backFile, "%d\t%f\t%f\n", bounce-1, freq, peak); */
  }

 if (y >= YWALL)
  {
   wall++;
   /* if (wallFile)
                fprintf(wallFile, "%d\t%f\t%f\n", bounce-1, freq, fabs(peak-freq)); */
  }

 if (x <= 0.0)
  {
   TotalCount++;
  }
 if (bounce >= MAXBOUNCE)
```

```
    {
     held++;
    }
  return --bounce;
}


void
main()
{
  int i, b;
  int steps=1000;
  int photonNumber = 10000;
  int cnt = 0;
  double f;
  double pres   = 1.0;
  double temp   = 420.15;


  monteFile = fopen("monte.freq1.0.g", "w");
   if(monteFile)
   fprintf(monteFile,"press\t%f\ntemp\t%f\tmaxbounce%d\n",pres,temp,MAXBOUNCE);
   fflush(monteFile);
   if(monteFile)
   fprintf(monteFile, "freq\tfront\twall\tback\theld\ttotal number\n");
   fflush(monteFile);

  do
   {
    backs = 0;
    wall = 0;
    TotalCount = 0;
    held = 0;

    f = MAXFREQ - cnt*(MAXFREQ - MINFREQ)/steps;

    /* double f = LASER; */
    /* backFile = fopen("backs.out", "w"); */
    /* wallFile = fopen("wall.out", "w");  */
    /* initCount(); */
    for (i = 0; i < photonNumber; i++)
     {
       b = bounces( f,pres,temp );
       /* count[b]++; */
     }
     cnt ++;
     /*     fprintf(stderr," %d of %d\n", cnt,steps); */

    if(monteFile)
        fprintf(monteFile, "%f\t%d\t%d\t%d\t%d\t%d\n", f,TotalCount,wall,backs,held,photonNumber);
    fflush(monteFile);

    /*dumpCount();*/
    /* fprintf(stderr, "out the back: %d\n", backs); */
```

```
    /* fprintf(stderr, "out the wall: %d\n", wall); */
   }
  while ( cnt < (steps+1) );
 }
```

FILE: montet.c

produces table of freq,and photons in/out/front/back with time duration

```
#include <stdio.h>
#include <math.h>
#include "absorb.h"
#include "gauss.h"

static double cellWidth  = 10.0;     /* microns */
static double pathLength = 50000.0;  /* microns */
static double oldalpha   = 0.0004;   /* per micron */

#define LASER -10.106
#define YWALL 25000.0 /* microns */

/* should be pathlength / cellwidth */
#define NCELL 5000

#define TAU      120.0
#define MAXBOUNCE 25
#define MAXTIME   (MAXBOUNCE * TAU)
#define MAXFREQ 15.0
#define MINFREQ -25.0

static int count[MAXBOUNCE*2];
static FILE *backFile = NULL;
static FILE *wallFile = NULL;
static FILE *monteFile = NULL;

void
initCount()
{
 int i;

 for (i = 0; i < MAXBOUNCE; i++)
  {
   count[i] = 0;
  }
}


void
dumpCount()
{
 int i;

 for (i = 0; i < MAXBOUNCE; i++)
  {
   printf("%d %d\n", i, count[i]);
  }
```

```
}


double
distance(double alpha)
{
 double p,d;

 p = drand48();                    /* double-precision  [0.0,~1.0) */
 p = 1.0 - p;                                          /* (~0.0,1.0] */
 d = (-1.0 / alpha) * log(p);

 return d;
}

double
peakfind(double freq)
{
 double x0[10];
 double p;
 int j;

 /* positions of the lines */
 x0[0]=-15.409; /* Hg 199 1/2 ***** corrected * 9/19 */
 x0[1]=-15.313; /* Hg 204 */
 x0[2]=-14.662; /* Hg 201 5/2 */
 x0[3]=-10.106; /* Hg 202  */
 x0[4]=-4.805;  /* Hg 200  */
 x0[5]=-0.676;  /* Hg 201 3/2 */
 x0[6]=0.0;     /* Hg 198  */
 x0[7]=4.107;   /* Hg 196  */
 x0[8]=6.728;   /* Hg 199 3/2 */
 x0[9]=6.872;   /* Hg 201 1/2 */

 p=x0[0];
 for (j=1; j<10; j++)
  {
   if (fabs(p-freq) > fabs(x0[j]-freq))
                 {
                  p = x0[j];
                 }
  }
 return p;
}

double
delayTime()
{
 double p,d;

 p = drand48();                    /* double-precision  [0.0,~1.0) */
 p = 1.0 - p;                                          /* (~0.0,1.0] */
 d = -TAU * log(p);
```

```
 return d;
}

static int backs = 0;
static int wall = 0;
static int TotalCount = 0;
static int held = 0;

double
wait(double freq,double pres,double temp)
{
 double alpha;
 double newWidth;
 double dopp;
 double peak;
 double delay = 0;
 double dir   = 1.0;
 double x     = 0;
 double y     =  0;


 do
   {
    alpha = absorb(freq, pres, temp);
    peak = peakfind(freq);
    x   += dir * distance(alpha);
    y   += sin(acos( dir ) ) * distance(alpha);
    dir  = cos( drand48()*M_PI );
    dopp = freq - peak;
    freq = peak + dopp*(dir);
    delay += delayTime();
    /* freq  = gaussRandom(gaussAbsorbWidth(temp), freq); */
    /* freq = PEAK; */
   }
 while (x > 0.0 && x < pathLength && delay < MAXTIME && y < YWALL);

 if (x >= pathLength)
   {
    backs++;
    if (backFile)
                    fprintf(backFile, "%d\t%f\t%f\n", delay, freq, peak);
   }

 if (y >= YWALL)
   {
    wall++;
    if (wallFile)
                    fprintf(wallFile, "%d\t%f\t%f\n", delay, freq, fabs(peak-freq));
   }

 if (x <= 0.0)
   {
    TotalCount++;
   }
```

```
 if (delay >= MAXTIME)
  {
   held++;
  }
 return delay;
}


void
main()
{
 int i, b;
 double w;
 int steps=1000;
 int photonNumber = 10000;
 int cnt = 0;
 double f;
 double pres   = 0.1;
 double temp   = 373.15;



   backs = 0;
   wall = 0;
   TotalCount = 0;
   held = 0;

   /* f = MINFREQ + cnt*(MAXFREQ - MINFREQ)/steps; */

   f = LASER;
   backFile = fopen("backs.out", "w");
   wallFile = fopen("wall.out", "w");
   initCount();

   for (i = 0; i < photonNumber; i++)
    {
      w = wait( f,pres,temp );
                    b = (int)((w/TAU)+.5);

      count[b]++;
    }

   dumpCount();
   fprintf(stderr, "out the back: %d\n", backs);
   fprintf(stderr, "out the wall: %d\n", wall);

}
```

FILE: monteth.c

produces a historgram for data... file caputuring time of flight for each photon

```
#include <stdio.h>
#include <math.h>
#include "absorb.h"
#include "gauss.h"

static double cellWidth  = 10.0;      /* microns */
static double pathLength = 50000.0;   /* microns */
static double oldalpha   = 0.0004;    /* per micron */

#define LASER -9.0
#define YWALL 25000.0  /* microns */

/* should be pathlength / cellwidth */
#define NCELL 5000

#define TAU       120.0
#define MAXBOUNCE 25
#define MAXTIME   (MAXBOUNCE * TAU)
#define MAXFREQ 15.0
#define MINFREQ -25.0

static int count[MAXBOUNCE*2];
static FILE *backFile = NULL;
static FILE *wallFile = NULL;
static FILE *monteFile = NULL;

initCount()
{
 int i;

 for (i = 0; i < MAXBOUNCE; i++)
   {
    count[i] = 0;
   }
}


void
dumpCount()
{
 int i;

 for (i = 0; i < MAXBOUNCE; i++)
   {
    printf("%d %d\n", i, count[i]);
   }
}


double
distance(double alpha)
```

```
{
 double p,d;

 p = drand48();                    /* double-precision  [0.0,~1.0) */
 p = 1.0 - p;                                          /* (~0.0,1.0] */
 d = (-1.0 / alpha) * log(p);

 return d;
}

double
peakfind(double freq)
{
 double x0[10];
 double p;
 int j;

 /* positions of the lines */
 x0[0]=-15.409; /* Hg 199 1/2 ***** corrected * 9/19 */
 x0[1]=-15.313; /* Hg 204 */
 x0[2]=-14.662; /* Hg 201 5/2 */
 x0[3]=-10.106; /* Hg 202  */
 x0[4]=-4.805;  /* Hg 200  */
 x0[5]=-0.676;  /* Hg 201 3/2 */
 x0[6]=0.0;     /* Hg 198  */
 x0[7]=4.107;   /* Hg 196  */
 x0[8]=6.728;   /* Hg 199 3/2 */
 x0[9]=6.872;   /* Hg 201 1/2 */

 p=x0[0];
 for (j=1; j<10; j++)
  {
   if (fabs(p-freq) > fabs(x0[j]-freq))
                 {
                  p = x0[j];
                 }
  }
 return p;
}

double
delayTime()
{
 double p,d;

 p = drand48();                    /* double-precision  [0.0,~1.0) */
 p = 1.0 - p;                                          /* (~0.0,1.0] */
 d = -TAU * log(p);

 return d;
}

static int backs = 0;
static int wall = 0;
```

```
static int TotalCount = 0;
static int held = 0;

double
wait(double freq,double pres,double temp)
{
 double alpha;
 double newWidth;
 double dopp;
 double peak;
 double delay = 0;
 double dir   = 1.0;
 double x     = 0;
 double y     =  0;


 do
  {
   alpha = absorb(freq, pres, temp);
   peak = peakfind(freq);
   x   += dir * distance(alpha);
   y   += sin(acos( dir ) ) * distance(alpha);
   dir  = cos( drand48()*M_PI );
   dopp = freq - peak;
   /* freq = peak + dopp*(dir); */
   freq  = gaussRandom(gaussAbsorbWidth(temp), peak);
   delay += delayTime();


   /* freq  = gaussRandom(gaussAbsorbWidth(temp), freq); */
   /* freq = PEAK; */
  }
 while (x > 0.0 && x < pathLength && delay < MAXTIME && y < YWALL);

 if (x >= pathLength)
  {
   backs++;
   if (backFile)
                fprintf(backFile, "%d\t%f\t%f\n", delay, freq, peak);
  }

 if (y >= YWALL)
  {
   wall++;
   if (wallFile)
                fprintf(wallFile, "%d\t%f\t%f\n", delay, freq, fabs(peak-freq));
  }

 if (x <= 0.0)
  {
   TotalCount++;
  }
 if (delay >= MAXTIME)
  {
```

```
    held++;
   }
  return delay;
}


void
main()
{
  int i, b;
  double w;
  int steps=1000;
  int photonNumber = 32640;
  int cnt = 0;
  double f;
  double pres   = 0.1;
  double temp   = 373.15;



    backs = 0;
    wall = 0;
    TotalCount = 0;
    held = 0;

    /* f = MINFREQ + cnt*(MAXFREQ - MINFREQ)/steps; */

    f = LASER;
    backFile = fopen("backs.out", "w");
    wallFile = fopen("wall.out", "w");
    monteFile = fopen("monte.time.out.9.g","w");

    initCount();

    for (i = 0; i < photonNumber; i++)
     {
       w = wait( f,pres,temp );
       if (monteFile)
        fprintf(monteFile, "%f\n",w);
                    b = (int)((w/TAU)+.5);

       count[b]++;
     }

    dumpCount();
    fprintf(stderr, "out the back: %d\n", backs);
    fprintf(stderr, "out the wall: %d\n", wall);

}
```

FILE: monte-dist.c

monte carlo simulation, following photon's distance travelled

```
#include <stdio.h>
#include <math.h>

static double cellWidth  = 10.0;      /* microns */
static double pathLength = 50000.0;   /* microns */
static double alpha      = 0.0004;    /* per micron */

/* should be pathlength / cellwidth */
#define NCELL 5000

static int count[NCELL];

void
initCount()
{
 int i;

 for (i = 0; i < NCELL; i++)
   {
    count[i] = 0;
   }
}


void
dumpCount()
{
 int i;

 for (i = 0; i < NCELL; i++)
   {
    printf("%d %d\n", i, count[i]);
   }
}


double
distanceOld()
{
 int i;
 double p, thresh;

 thresh = cellWidth * alpha;

 for (i = 0; i < NCELL; i++)
   {
    p = drand48();

    if (p < thresh) break;
   }

 return (0.5 + i) * cellWidth;
}
```

```
double
distance()
{
 double p,d;

 p = drand48();
 d = (-1.0 / alpha) * log(p);

 return d;
}


void
main()
{
 int i, cell;
 double d;

 initCount();

 for (i = 0; i < 1000000; i++)
  {
   d    = distance();
   cell = d / cellWidth;

   count[cell]++;
  }

 dumpCount();
}
```

FILE: monte-time.c

time history of photons in Hg cell

```
#include <stdio.h>
#include <math.h>
#include "absorb.h"
#include "gauss.h"

static double cellWidth  = 10.0;      /* microns */
static double pathLength = 50000.0;   /* microns */
static double oldalpha   = 0.0004;    /* per micron */

#define LASER -10.106
#define PEAK  -10.106

/* should be pathlength / cellwidth */
#define NCELL 5000

#define TAU       120.0
#define MAXBOUNCE 50
#define MAXTIME   (MAXBOUNCE * TAU)
```

```
static int count[MAXBOUNCE*2];
static FILE *backFile = NULL;

void
initCount()
{
 int i;

 for (i = 0; i < MAXBOUNCE; i++)
  {
   count[i] = 0;
  }
}


void
dumpCount()
{
 int i;

 for (i = 0; i < MAXBOUNCE; i++)
  {
   printf("%d %d\n", i, count[i]);
  }
}


double
distance(double alpha)
{
 double p,d;

 p = drand48();                    /* double-precision  [0.0,~1.0) */
 p = 1.0 - p;                                          /* (~0.0,1.0] */
 d = (-1.0 / alpha) * log(p);

 return d;
}

double
delayTime()
{
 double p,d;

 p = drand48();                    /* double-precision  [0.0,~1.0) */
 p = 1.0 - p;                                          /* (~0.0,1.0] */
 d = -TAU * log(p);

 return d;
}

static int backs = 0;

int
```

```
bounces(double freq)
{
 double alpha;
 double newWidth;
 int    bounce = 0;
 double dir    = 1.0;
 double x      = 0;
 double pres   = 0.05;
 double temp   = 373.15;

 do
  {
   alpha = absorb(freq, pres, temp);
   x    += dir * distance(alpha);
   dir   = cos( drand48()*M_PI );
   freq  = gaussRandom(gaussAbsorbWidth(temp), freq);
   bounce++;
  }
 while (x > 0.0 && x < pathLength && bounce < MAXBOUNCE);

 if (x >= pathLength)
  {
   backs++;
   if (backFile)
                fprintf(backFile, "%d\t%f\t%f\n", bounce-1, freq, fabs(PEAK-freq));
  }

 return --bounce;
}


int
wait(double freq)
{
 double alpha;
 double newWidth;
 double delay  = 0.0;
 double dir    = 1.0;
 double x      = 0;
 double pres   = 0.05;
 double temp   = 373.15;

 do
  {
   alpha = absorb(freq, pres, temp);
   x    += dir * distance(alpha);
   dir   = cos( drand48()*M_PI );
   freq  = gaussRandom(gaussAbsorbWidth(temp), freq);
   delay+= delayTime();
  }
 while (x > 0.0 && x < pathLength && delay < MAXTIME);

 if (x >= pathLength)
  {
```

```
    backs++;
   }

  return delay;
}


void
main()
{
  int i,b;
  double w;
  double f = LASER;

  /* backFile = fopen("backs.out", "w"); */

  initCount();

  for (i = 0; i < 10000; i++)
   {
    w = wait( f );
    b = (int) (w/TAU) + 1;

    count[b]++;
   }

  dumpCount();

  fprintf(stderr, "out the back: %d\n", backs);
}


#if 0
void
main()
{
  int i,b;
  double w;

  initCount();

  for (i = 0; i < 10000; i++)
   {
    w = delayTime();

    b = (int) (10 * w / TAU);

    if (b < MAXBOUNCE) count[b]++;
   }

  dumpCount();
}
#endif
```

File: absorb.c

absorption profile of mercury, used in the Monte Carlo to determine propigation distance before absorption.

```
#include <stdio.h>
#include <math.h>

#define NUMLINES 10


double lineshape(double x, double x0, double g_width, double l_width)
{
 double wv, det, z, norm, p2, p225, val;

 wv  = l_width/2 + sqrt(pow(l_width,2)/4 + pow(g_width,2));

 det  = x - x0;
 z   = l_width/wv;

 norm = wv * (1.065 + 0.447 * z + 0.058 * pow(z,2));
 norm = 1/norm;

 p2   = pow(det/wv,2);
 p225 = pow(fabs(det/wv),2.25);

 val  = (1 - z) * exp(-2.772 * p2) + z/(1 + 4 * p2);
 val += 0.016 * (1 - z) * z * (exp(-0.4 * p225) - 10/(10 + p225));
 val *= norm;

 return val;
}


double gaussAbsorbWidth(double temp)
{
 double mass = 200.59;

 return 0.846354 * sqrt(temp/mass);
}


double absorb(double freq, double pres, double temp)
{
 double l_width, g_width, lorentz, os, mass;
 double a[10],f[10],x0[10];
 int                 j;
 double val, abs;

 lorentz = 0.003;

 /* oscillator strength */
 os = 0.0241364;

 /* calculate lorentz and gauss widths (GHz) */
```

```
 mass    = 200.59;
 l_width = 1/(2 * M_PI * 120) + lorentz * pres;
 g_width = gaussAbsorbWidth(temp);

 /* positions of the lines */
 x0[0]=-15.409; /* Hg 199 1/2 ***** corrected * 9/19 */
 x0[1]=-15.313; /* Hg 204 */
 x0[2]=-14.662; /* Hg 201 5/2 */
 x0[3]=-10.106; /* Hg 202  */
 x0[4]=-4.805;  /* Hg 200  */
 x0[5]=-0.676;  /* Hg 201 3/2 */
 x0[6]=0.0;     /* Hg 198  */
 x0[7]=4.107;   /* Hg 196  */
 x0[8]=6.728;   /* Hg 199 3/2 */
 x0[9]=6.872;   /* Hg 201 1/2 */

 /* relative population density ... natural abundances */
 a[0]=0.1684;
 a[1]=0.0685;
 a[2]=0.1322;
 a[3]=0.298;
 a[4]=0.2313;
 a[5]=0.1322;
 a[6]=0.1002;
 a[7]=0.0016;
 a[8]=0.1684;
 a[9]=0.1322;

 /* hyper fine degeneracy ... relative to no HF splitting */
 f[0]=0.3333;
 f[1]=1.0;
 f[2]=0.5;
 f[3]=1.0;
 f[4]=1.0;
 f[5]=0.3333;
 f[6]=1.0;
 f[7]=1.0;
 f[8]=0.6667;
 f[9]=0.1667;

 val = 0.0;

 for (j = 0; j < NUMLINES; j++)
  {
   val += a[j]*f[j]*lineshape(freq, x0[j], g_width, l_width);
  }

 abs = 2.65e-15 * (pres/temp) * (9.657e+18) * os * val;

 return abs;
}
```

File: gauss.c

```
/*
 * return a random number with a gaussian probability distibution
 *   centered at center with width width at halfheight
 */
#include <math.h>

#define SCALE 2.35

double
gaussRandom(double width, double center)
{
  double  u1, u2;
  double  x;

  u1 = drand48();
  u2 = drand48();
  x  = pow(-2.0 * log(u1), 0.5) * cos(2.0 * M_PI * u2);

  return ( width * x / SCALE + center);
}
```

IUTAM Symposium on
Variable Density, Low Speed Turbulent Flows
Institut de Recherche sur les Phénomènes Hors Equilibre
Marseille, France
July 8-10, 1996

OPTICAL DIAGNOSTICS FOR FLOWS WITH DENSITY VARIATIONS

R.B. MILES, W.R. LEMPERT, J. FORKEY, N.D. FINKELSTEIN, and S.R. HARRIS
Department of Mechanical & Aerospace Engineering
PRINCETON UNIVERSITY
Princeton, New Jersey 08544 USA

1. Abstract

Two new molecular-based diagnostic methods show great promise for the measurement of turbulence in variable density, low-speed flow fields. The first of these methods is Rayleigh imaging, which is capable of capturing two-dimensional instantaneous cross sections of the flow field density. Through the use of atomic or molecular filters in front of the camera, Rayleigh imaging can be extended to the measurement of temperature and velocity. Flow tagging yields velocity profiles in variable density flow fields and can be used to measure the details of the turbulent structure. These two techniques may be applied simultaneously to capture instantaneous velocity and density fields with high resolution.

2. Introduction

Diagnostic approaches based on molecular scattering and molecular tagging are particularly well suited to the measurement of flows with density fluctuations. This is because the molecules represent a true constituent of the fluid, so molecular scattering and molecular tagging sample the fluid itself. Errors associated with the effects of density variation on a sample probe such as a hot wire or on particle trajectories are not present. Much work has been done using laser-induced fluorescence from molecules such as nitric oxide [1] and OH [2], which are naturally present in hot and combusting flows, but which must be seeded into cold flows. The interpretation of the laser-induced fluorescence signal levels from these molecules is complicated by collisional phenomena, and these effects are particularly troublesome in flows with density fluctuations. Laser-induced fluorescence from oxygen molecules has also been considered for flow diagnostics in air [3]. This approach is attractive since oxygen is strongly predissociative, and, therefore, not subject to quenching. As a result, the oxygen laser-induced fluorescence signal level is a direct measure of the population of oxygen molecules in a particular ground rotational state. Due, in part, to the rapid predissociation, and, in part, to weak absorption, the laser-induced fluorescence signal from oxygen at room temperature is very low. Signals from vibrationally excited oxygen are much stronger because of stronger coupling to the upper electronic level. As a consequence, laser-induced fluorescence from oxygen has been useful in high

temperature flows and as an interrogation step for RELIEF flow tagging, where a line or a pattern of vibrationally excited molecules is created by Raman Excitation (RE) and imaged with oxygen Laser-Induced Electronic Fluorescence (LIEF).

3. Rayleigh Imaging

In order to avoid the problems associated with quenching and seeding, we have explored the application of Rayleigh scattering for quantitative imaging of gaseous flows with density fluctuations. Rayleigh scattering has the advantage of being directly proportional to the density of the gas and lasts only for that period of time during which the gas is illuminated. With high-power, short-pulsed lasers, instantaneous cross-sectional images of the density field can be captured. The drawback of Rayleigh scattering is the low scattering cross section per molecule. For example, oxygen and nitrogen have a scattering cross section of about $3 \times 10^{-27} cm^2$ at 589 nm (orange--the sodium light wavelength) [4]. This cross section is, in effect, the size of the shadow cast by each molecule. At STP (2.69×10^{19} molecules/cc), only one out of every 10^7 photons is scattered per centimeter of path length. Of those photons, only approximately one in 10^4 are usually detected with a camera. This is because of the limited solid angle of the camera collection optics, optical losses in the collection system, and the quantum efficiency of the detector. This scattering can be significantly improved by using ultraviolet light, since the scattering cross section scales as the fourth power of the frequency and as the square of the polarizability. For example, at 193 nm (ArF laser), the total Rayleigh cross section increases to $4 \times 10^{-25} cm^2$ (the differential cross section is $5 \times 10^{-26} cm^2$ /steradian) [5]. High energy laser pulses are also important, since more photons incident produce more photons scattered, and Rayleigh scattering is not subject to saturation. A second drawback of Rayleigh scattering is that the scattered light is at the same frequency or close to the same frequency as the incident source laser. This means that other direct scattering processes, such as scattering from windows, walls, and particles, can obscure the Rayleigh scattering. Thus, the scattering volume must be carefully protected from stray laser light, and the field-of-view of the camera must be masked to minimize the background scattering.

High quality Rayleigh images of compressible flows have been taken in the ultraviolet with argon-fluoride lasers at 193 nm and with frequency-quadrupled Nd:YAG lasers at 266 nm. Figure 1 shows a pair of instantaneous images of the Mach disk region in an underexpanded supersonic air jet taken with an ArF laser. This image clearly show the large increase in density behind the shock, the reflected shock structure, and the turbulent density fluctuations in the free shear layer.

The utility of Rayleigh scattering for density measurements is limited by the low signal level and by interference from background scattering. In the shot noise limit, the signal-to-noise ratio is equal to the square root of the total number of photons collected per resolvable volume element. Thus, for 1% accuracy, at least 10,000 photoelectrons must be collected. This must be done in a single laser shot if the instantaneous density field is to be measured. In essence, this requirement limits the resolution and the field-of-view. For example, a 100 mJ laser at 193 nm, expanded to a 1 cm wide by 100μ thick sheet, gives about 10^4 photoelectrons detected per cubic 100 micron element over a 1 cm by 1 cm field-of-view. Higher resolution will require a smaller field-of-view, a

higher energy laser, or a smaller signal-to-noise ratio. Thus flows with large density gradients, such as the one shown in Fig. 1, are easily imaged. Those with smaller density gradients, including low-speed flows with thermally induced density gradients, are more difficult to see.

An alternative method of enhancing the Rayleigh scattering is by using molecules with large Rayleigh scattering cross sections such as Freon [6], or by using a fog of small particles. In supersonic flows there is a fog of condensate particles which occurs naturally in the cold portions of the flow and arises from the condensation of trace species such as water vapor and CO_2 [7]. Since these particles evaporate in the boundary layer and behind strong shocks, they are useful as tools to observe boundary layer and shock structure. For example, Fig. 2 shows two sequential images of a Mach 3 turbulent boundary layer separated in time by 20 μsec [8]. A large boundary layer feature is clearly evident, and its displacement and evolution during this time interval can be observed. Similar images taken at up to a million frames per second have been captured in a small Mach 2.5 supersonic flow using a new pulsed-burst laser and a MHz rate CCD camera [9]. Figure 3 shows a composite of 25 images, taken sequentially at 2 μsec intervals in this flow. The right-hand side of each image is at the wall, flow is from bottom to top, and the scattering is from a dry ice (CO_2) fog created by introducing a small amount of CO_2 into the air far upstream of the nozzle.

Rayleigh scattering can be augmented through the use of optical filters to remove background scattering. This is especially so for high speed flows where the Doppler shift associated with the average motion of the flow is large compared to the Doppler shifts associated with the thermal and acoustic motion of the individual molecules. In this case, a narrow linewidth laser is tuned to overlap the absorption line of a molecular or atomic vapor. A cell filled with that vapor is placed in front of the camera so that light scattered from non-moving objects such as windows and walls is eliminated from the field-of-view. Light scattering from the flow, on the other hand, is shifted in frequency and passes through the cell. This application is shown in diagrammatic form in Fig. 4, and has been used to suppress background scattering for measurements in supersonic inlets [8] and supersonic free jets [10].

For more quantitative measurements, the filter may be used to discriminate the spectral character and spectral shift of the Rayleigh-scattered light [11]. This is accomplished by tuning the laser and observing the scattered light through the atomic or molecular absorption cell as a function of the laser wavelength. This use of the filter is shown diagramatically in Fig. 5. The laser frequency is carefully monitored with respect to a reference laser. The point of maximum absorption occurs when the Rayleigh-scattered light most completely overlaps the absorption feature in the cell (point #3 on the diagram). By measuring the laser frequency and comparing it with the frequency of the filter, the shift is known and the velocity of the flow is measured. This can be done for each resolvable element in the image, and, so, the velocity field can be captured. In a similar fashion, the line broadening of the scattering is indicative of the temperature of the flow. Thus, by observing the rate at which the scattering is cut-off by the absorption filter as the laser is tuned in frequency, the temperature can be determined. Since the total scattering is proportional to the density, these measurements yield velocity, temperature, and pressure. Images taken in a Mach 2 pressure-matched free jet give the velocity, temperature, and pressure profiles shown in Figs. 6, 7, and 8 [12]. For these experiments, the laser was tuned and therefore the flow fluctuations

were time averaged. For instantaneous measurements, a single pulse laser can be used together with a multiple set of filters observing the same scattering region.

4. Flow Tagging

Molecular flow tagging is another approach to diagnostics and can be used to complement Rayleigh scattering for more accurate measurements of transport properties. In the RELIEF flow tagging process [13], oxygen molecules are "instantaneously" pumped into their vibrationally excited state by stimulated Raman scattering. This is achieved with a high power, short-pulsed, dual-color laser beam, which is focused to a line through the sample volume. Since oxygen is a homonuclear diatomic molecule, the vibrationally excited state cannot easily radiate its energy, and the molecules remain excited for a relatively long period of time. For example, in pure oxygen they will remain excited for tens of milliseconds [14]. In air, the excitation lifetime is usually determined by the partial pressure of water vapor, and in humid air, the vibrational lifetime may be on the order of 10 μsec or so. Figure 9 shows the lifetime as a function of the water mole fraction for atmospheric pressure air at 300 K [15]. A short time after tagging, the displaced molecules are interrogated by laser-induced electronic fluorescence using an argon-fluoride laser (193 nm). This same laser may be simultaneously used to observe Rayleigh scattering for density measurements. The underexpanded supersonic jet shown in Fig. 1 is reproduced in Fig. 10, this time with a line written into it and interrogated after 5 μsec. The displacement of the line is a quantitative measure of the velocity profile across the jet.

This flow tagging approach has been used to measure velocity profiles in supersonic flows as well as in subsonic flows. The displacement of the line gives an immediate visual appreciation of the velocity profile, and as the time interval between tagging and interrogation goes to zero, the displacement is a true measurement of the velocity profile. It is important to recognize that the line is absolutely straight when it is written, so its position can be found to high accuracy. The displaced line center is found using a Gaussian fitting routine and is typically determined to better than a tenth of a pixel resolution, which usually corresponds to on the order of 2-3 microns. Of course, some displacement must occur in order to measure the velocity, so the time interval must be finite. In general, this finite time interval is chosen to be short compared to the fastest eddy roll-over time in the turbulent flow.

As an example of the utility of this line marking approach, a series of experiments were conducted in a free air jet [16]. Table I shows the conditions for three of these experimental runs (A,B,C). Measurements were taken approximately 40 diameters downstream where the Reynolds number, based on the Taylor microscale, was on the order of 575. The approximate eddy roll-over time at this location was 30 μsec, and the time interval between tagging and interrogation was 5 or 7 μsec, less than one-quarter of the eddy turn-over time. A typical image of the initial tagged line and one after 7 μsec is shown in Fig. 11. In this case, the average velocity was 43 m/sec, and the turbulence intensity was 12 m/sec. Approximately 5,000 lines were analyzed for each run and used to compute the first through sixth order structure functions:

$$S_n(\Delta x) = \overline{|u(x) - u(x + \Delta x)|^n} \tag{1}$$

Since odd order transverse structure functions are zero by symmetry, the magnitude of the difference has been used. The first through sixth order structure functions vs. Δx are shown in Fig. 12, where the smallest increment is 30μ, corresponding to the resolution of the optical system. These structure functions have been normalized to one at the inertial scale and they show the characteristic logarithmic slope region in the inertial subrange. The portion of the inertial subrange with a linear logarithmic slope extends over approximately one decade before dissipation steepens the slope at small scales. The logarithmic slopes of the first, second, third, fourth, and sixth order structure functions are shown in Fig. 13. Here it is clear that the low order structure functions are reasonably flat over the range between approximately 700 microns and 7 mm. Higher order structure functions are noisy, since they are very susceptible to low probability events. Application of the extended self-similarity method [17], where other structure functions are plotted against the third order structure function, suppresses this noise and extends the region of linearity over four decades. Figure 14 shows the logarithmic derivatives of the ESS plots for the first, second, fourth, fifth, and sixth order structure functions. The extended linear region and reduced noise are apparent when this plot is compared to Fig. 13. Structure function slopes measured in this manner are consistent with those measured using hot-wire probes under similar conditions.

Since the RELIEF technique observes the transverse velocity profile, vortices have a particularly clear signature: a positive and negative excursion from a straight line. Thus, the scale and strength of violent events, even down to scales on the order of the Kolmogorov scale, can be observed with this technique. The probability density distribution function (PDF) of the transverse velocity increment shows that violent events greater than one-half the RMS fluctuations occur across a distance of 1.8 times the Kolmogorov length with a probability of greater than 10^{-4} (Fig. 15). It seems probable that these events correspond to those cases where the line has been tagged through the core of a vortex filament. The frequency of occurrence of these events is consistent with the view that a volume on the order of the integral scale contains one such filament with a length comparable to the integral scale [16].

A similar technology has been developed for observing velocity and vorticity structure in water. This approach is called the PHANTOMM technique (PHoto-Activated Nonintrusive Tracking Of Molecular Motion) and is accomplished by mixing a small amount (mole fractions of several parts per billion) of a caged dye molecule into water [18]. When illuminated with ultraviolet light, the cage is broken and any time after that, the molecule acts as a normal fluorescent dye. Tagging, therefore, is accomplished by using an ultraviolet laser, such as a frequency-tripled Nd:YAG laser, to write a pattern into the fluid, and subsequently using a blue laser, such as an argon-ion laser or pulsed dye laser, to interrogate. Fluorescence is in the yellowish-orange region of the spectrum and is easily imaged with a standard videocamera. An image of a series of lines written at 1 second intervals into a stationary cylinder filled with water and closed with a rotating top is shown in Fig. 16. The interrogation laser is formed into a sheet containing the initial tagged line. As that line rotates out-of-plane, it appears to become shorter and then longer with a 180° turn. The slowly rotating top draws the fluid up in the center and pushes it out and down on the edges, as is evident from the image. This experimental set-up is being used to study vortex stability and vortex breakdown since the geometry is particularly compatible with cylindrical

computational coordinates [19,20,21]. A comparison of the line displacement with the computed result is shown in Fig. 17.

5. Summary

Rayleigh scattering and molecular line tagging are two approaches which may be utilized in a straightforward manner to generate both qualitative and quantitative images of flows with density variations. A wide range of scales can be simultaneously captured, and the images give unambiguous measurements of density and velocity. For density measurements using Rayleigh scattering and velocity measurements using molecular tagging, the character of the flow field is immediately apparent without further data analysis. High repetition rate laser sources allow this data to be captured at rates which are in excess of the highest frequency fluctuations in the flow. Rayleigh scattering can be further augmented with the use of molecular or atomic filter technologies to extract temperature and velocity fields. These same filters are useful for the suppression of background scattering from windows and walls in high-speed flows. Molecular tagging gives a very precise quantitative measure of velocity, so it is particularly useful for the study of flow physics and the validation and verification of computational codes and fluid models.

6. Acknowledgments

The Rayleigh scattering work was supported by the Air Force Office of Scientific Research (Dr. Julian Tishkoff), NASA-Lewis (Dr. Richard Seasholtz), and NASA-Langley (Dr. Richard Antcliff). The pulse-burst laser technology was supported by the Air Force Office of Scientific Research (Dr. Leonidas Sakell) and the New Jersey Photonics and Opto-Electronics Materials Center (POEM) (Dr. Stephen Forrest). Molecular flow tagging work was supported by the National Science Foundation (Dr. Roger Arndt) and a NATO collaborative research grant (CRG-92-0480).

7. References

1. Lee, M.P., McMillan, B.K., and Hanson R.K., "Temperature Measurements in Gases by use of Planar Laser-Induced Fluorescence Imaging of NO," *Appl. Opt.* **32** (1993) 5370-5396.

2. Palmer, J.L., Hanson, RK., "Temperature Imaging in a Supersonic Free Jet of Combustion Gases with Two-Line OH Fluorescence," *Appl. Opt.* **35** (1996) 485-499.

3. Lee, M.P., Paul, P.H., and Hanson, R.K., "Quantitative Imaging of Temperature Fields in Air Using Planar Laser-Induced Fluorescence of Oxygen," *Opt. Lett.* **12** (1987) 75-77.

4. Shardanand, R., Prasad, and Rao, R.D., "Absolute Rayleigh Scattering Cross Sections of Gases and Freons of Stratospheric Interest in Visible and Ultraviolet Regions," (1977) NASA TN-D-8442.

5. Miles, R.B., Connors, J.J., Howard, P.J., Markovitz, E.C., and Roth, G.J., "Proposed Single-Pulse Two-Dimensional Temperature and Density Measurements of Oxygen and Air," *Opt. Lett.* **13** (1988) 195-197.

6. Yip, B., Schmitt, R., and Long, M.B., "Instantaneous Three-Dimensional Concentration Measurements in Turbulent Jets and Flames," *Opt. Lett.* **13** (1988) 96-98.

7. Shirinzadeh, B., Hillard, M.E., and Exton, R.J., "Condensation Effects on Rayleigh Scattering Measurements in a Supersonic Wind Tunnel," *AIAA J.* **29** (1991) 242-246.

8. Forkey, J., Cogne, S., Smits, A., and Bogdonoff, S., "Time-Sequenced and Spectrally Filtered Rayleigh Imaging of Shockwave and Boundary Layer Structure for Inlet Characterization," AIAA-93-2300 (1993).

9. Lempert, W.R., Wu, P.F., Zhang, B., Miles, R.B., Lowrance, J.L., Mastrocola, V., and Kosonocky, W., "Pulse-Burst Laser System for High-Speed Flow Diagnostics," AIAA 96-0179 (1996).

10. Miles, R., Lempert, W., Forkey, J., Finkelstein, N., and Erbland, P., "Quantifying High-Speed Flows by Light Scattering from Air Molecules," AIAA-94-2230 (1994).

11. Forkey, J.N., Finkelstein, N.D., Lempert, W.R., and Miles, R.B., "Demonstration and Characterization of Filtered Rayleigh Scattering for Planar Velocity Measurements," *AIAA J.* **34** (1996) 442-448.

12. Forkey, J., "Development and Demonstration of Filtered Rayleigh Scattering--A Laser Based Flow Diagnostic for Planar Measurement of Velocity, Temperature, and Pressure," Princeton University, MAE Technical Report #2067 (1996).

13. Miles, R.B., Connors, J.J., Markovitz, E.C., Howard, P.J., and Roth, G.J., "Instantaneous Profiles and Turbulence Statistics of Supersonic Free Shear Layers by Raman Excitation + Laser-Induced Electronic Fluorescence (RELIEF) Velocity Tagging of Oxygen," *Expts. in Fluids* **8** (1989) 17-24.

14. Frey, R., Lukasik, J., and Ducuing, J., "Tunable Raman Excitation and Vibrational Relaxation in Diatomic Molecules," *Chem. Phys. Ltrs.* **14** (1972) 514-517.

15. Diskin, G.S., Lempert, W.R., and Miles, R.B., "Observation of Vibrational Relaxation Dynamics in $X^3\Sigma^-_g$ Oxygen Following Stimulated Raman Excitation to the v=1 Level: Implications for the RELIEF Flow Tagging Technique," AIAA 96-0301 (1996).

16. Noullez, A., Wallace, G., Lempert, W., Miles, R.B., and Frisch, U., "Transverse Velocity Increments in Turbulent Flow Using the RELIEF Technique," (Submitted to J. Fluid Mechanics, May 1996).

17. Benzi, R., Ciliberto, S., Baudet, C., and Ruiz Chavarria, "On the Scaling of Three-Dimensional Homogeneous and Isotropic Turbulence," *Physica D* **80** (1995) 385-398.

18. Lempert, W.R., Magee, K., Ronney, P., Gee, K.R., and Haughland, R.P., "Flow Tagging Velocimetry in Incompressible Flows Using PHoto-Activated Nonintrusive Tracking Of Molecular Motion (PHANTOMM)," *Expts. in Fluids* **18** (1995) 249-257.

19. Harris, S.R., Miles, R.B., and Lempert, W.R., "PHANTOMM Flow Tagging Measurements in Complex 3-D Flows," AIAA 96-1966 (1996).

20. Escudier, M.P., "Observations of the Flow Produced in a Cylindrical Container by a Rotating Endwall," *Expts. in Fluids* **2** (1984) 189-196.

21. Brown, G.L., and Lopez, J.M., "Axisymmetric Vortex Breakdown. Part 2: Physical Mechanisms," *J. Fluid Mech.* **221** (1990) 553-576.

TABLE I: Jet Conditions

Run	Exit Dia. (cm)	Plen Press (psi)	Exit Vel. (m/s)	Tag Loc. Dia.	Time Delay (μs)	Lines Used	Line Lgth pixel	Avg. Vel. (m/s)	Turb. Int. (m/s)	Taylor Micro-scale (μ)	Kol. Scale (μ)	R_λ
A	1	10	278	38	5	5617	344	48.5	12.1	686	14.4	589
B	1	10	278	38	7	5249	344	42.7	11.9	720	14.9	605
C	1	10	278	38	5	5578	344	41.6	12.7	594	13.1	534

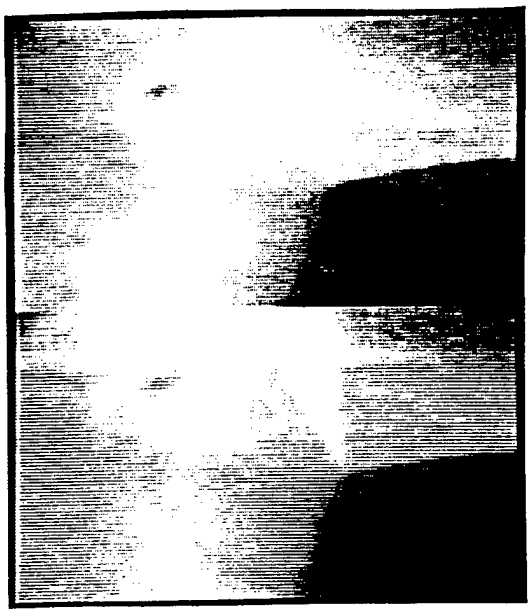

Figure 1.

Rayleigh cross sections of a 6 mm diameter underexpanded free air jet taken with argon-fluoride laser (193 nm) at the edge of the Mach disk.

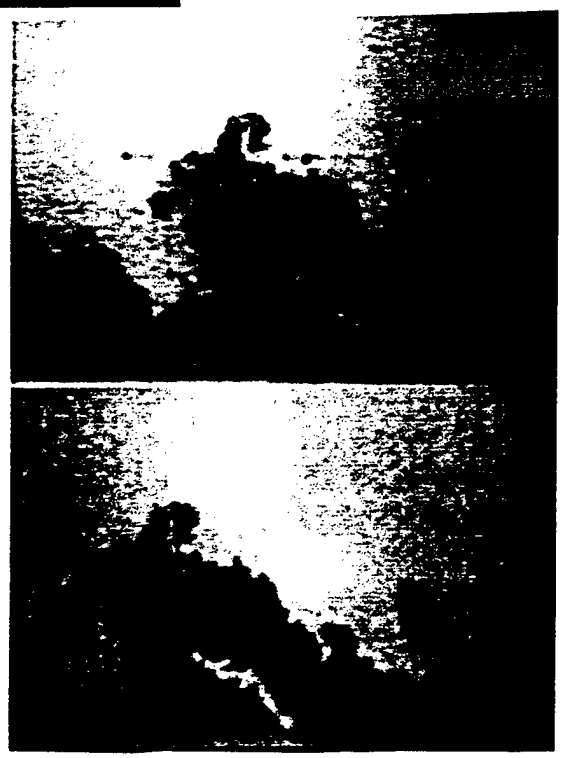

Figure 2.

Sequential Rayleigh images of condensate fog highlighting the boundary layer of a Mach 3 flow. Images are separated by 20 μsec.

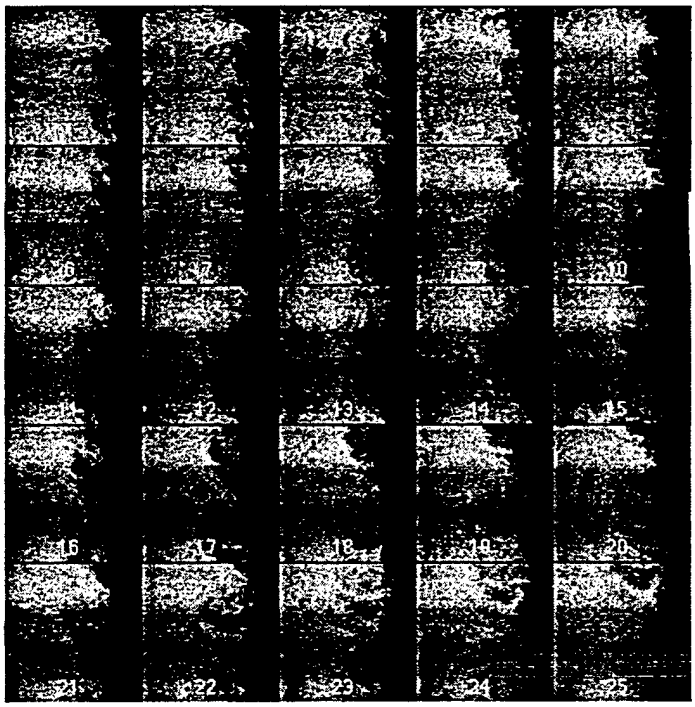

Figure 3.

Images of a Mach 2.5 turbulent boundary layer taken at 500,000 frames per second.

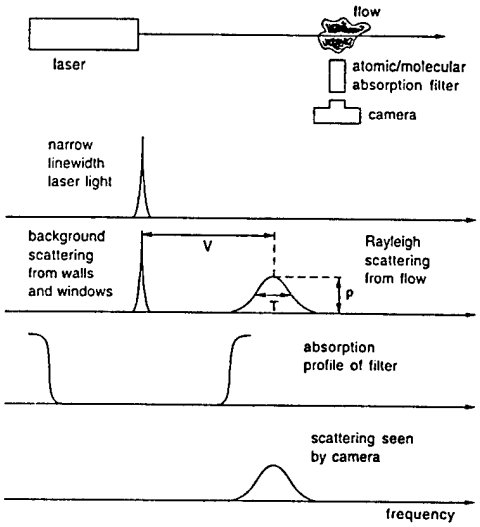

Figure 4. Diagram of background suppression, molecular filter for Rayleigh Scattering.

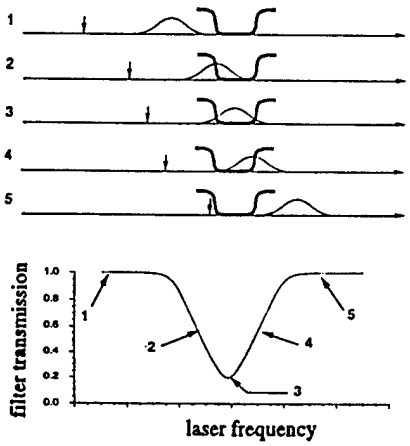

Figure 5. Diagram of velocity, temperature, and pressure measurements with molecular filter.

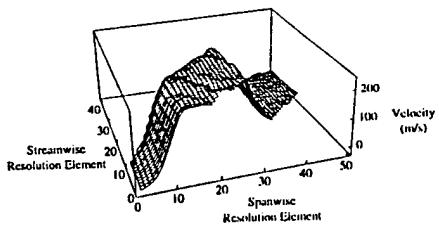

Figure 6. Velocity contour across a Mach 2 pressure-matched free jet.

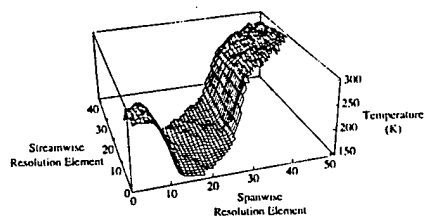

Figure 7. Temperature contour across a Mach 2 pressure-matched free jet.

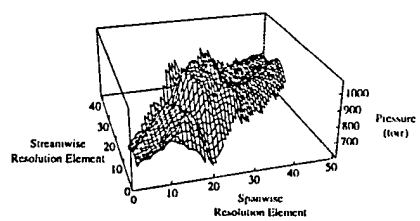

Figure 8. Pressure contour across a pressure-matched Mach 2 free jet.

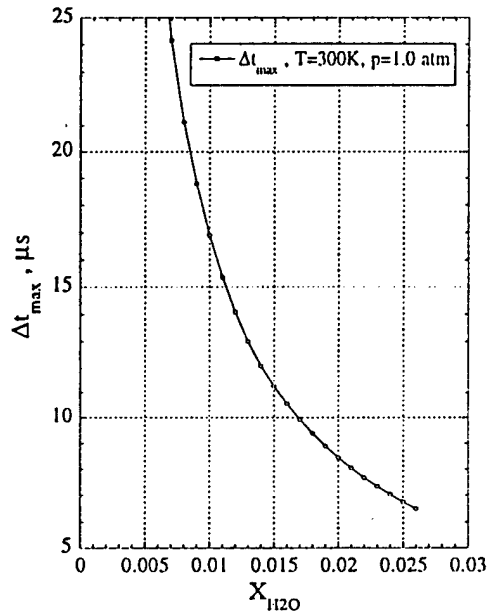

Figure 9. Maximum time between tagging and interrogation for a RELIEF line at 1 atm, 300 K, as a function of water vapor mole fraction. Time is to 10% of maximum signal.

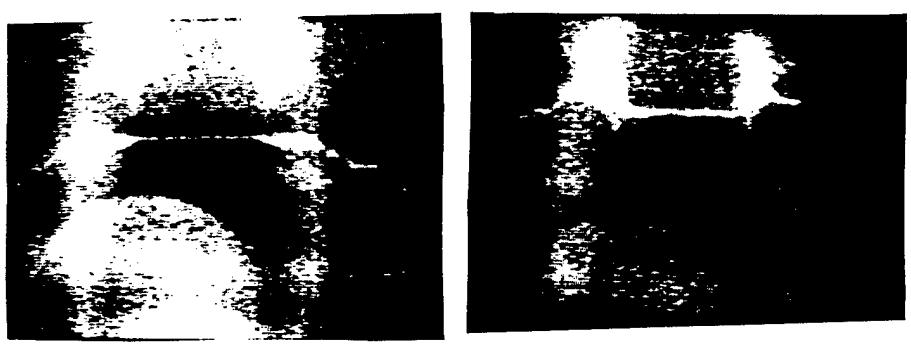

Figure 10. Six millimeter (6 mm) diameter underexpanded free air jet with simultaneous Rayleigh scattering and RELIEF lines. The lines are written into the flow 5 µsec before interrogation.

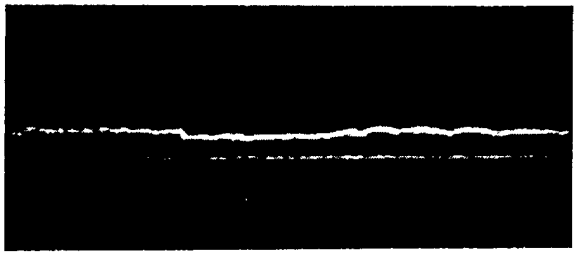

Figure 11.

Original tagged line and line displaced after 7 μsec in a turbulent free air jet.

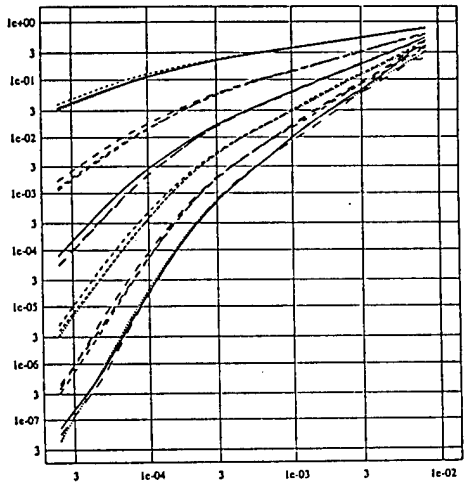

Figure 12.

First (top) through sixth (bottom) order structure functions vs. Δx for the turbulent free air jet.

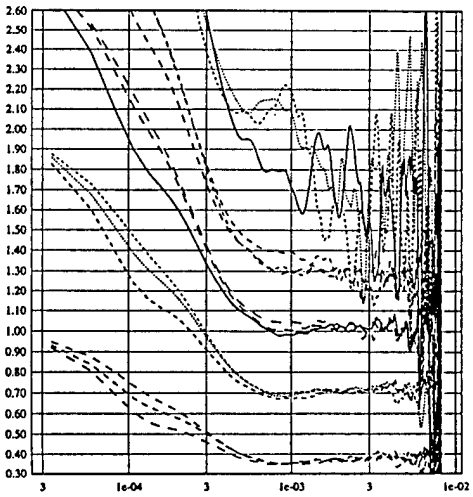

Figure 13. Logarithmic slope of the first, second, third, fourth, and sixth order structure functions.

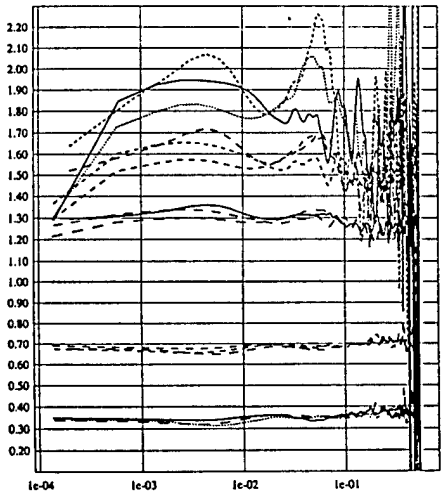

Figure 14. Logarithmic slopes of the first, second, fourth, fifth, and sixth order structure functions plotted against a third order structure function showing extended self-similarity.

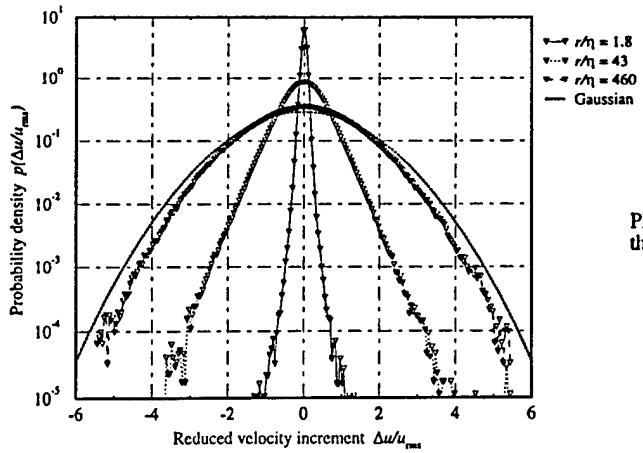

Figure 15.

PDF of the velocity difference at three different transverse spacings.

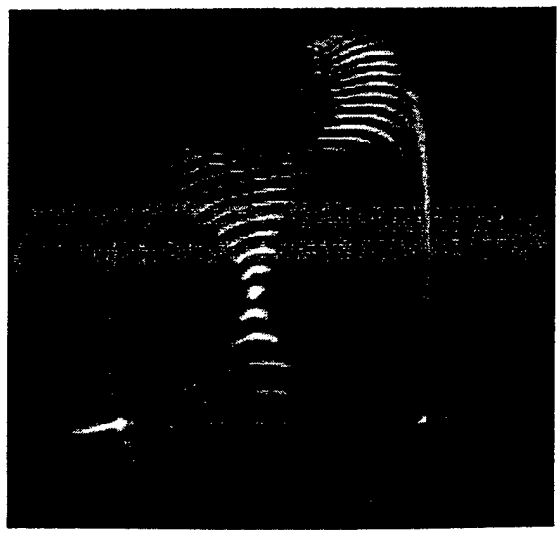

Figure 16.

Set of lines written at 1 second intervals into water contained in a stationary cylinder with a rotating top. Lines are interrogated with a pulsed dye laser focused to a sheet so they appear shorter as they rotate out-of-plane.

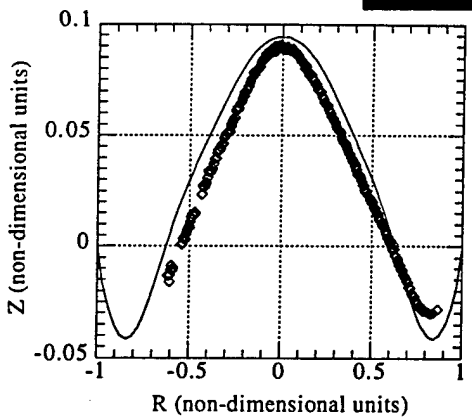

Figure 17.

A comparison of the axial velocity profile with the profile predicted for the cylinder with rotating top. Re = 996, H/R = 2.0.

AIAA 97-0157

Mercury Vapor Filter Technology and Ultraviolet Laser Source for Flowfield Imaging

N.D. Finkelstein, W.R. Lempert, and R.B. Miles

Department of Mechanical and Aerospace Engineering
Princeton University
Princeton, NJ

35th Aerospace Sciences Meeting & Exhibit

January 6-10, 1997 / Reno, NV

For permission to copy or republish, contact the American Institute of Aeronautics and Astronautics
1801 Alexander Bell Drive, Suite 500, Reston, VA 22091

MERCURY VAPOR FILTER TECHNOLOGY AND ULTRAVIOLET LASER SOURCE FOR FLOWFIELD IMAGING

N.D. Finkelstein*, W.R. Lempert**, and R.B. Miles‡

Department of Mechanical and Aerospace Engineering, Princeton University
Princeton, NJ 08544

Abstract

We present a narrow spectral passband filter capable of imaging rotational Raman scattering. The mercury vapor based filter has a spectral passband of less that 1 cm^{-1} and high out-of-band suppression. The filter is coupled with a narrow linewidth ultraviolet laser source. The laser, based on frequency tripling the output of an injection seeded, cavity locked titanium: sapphire resonator achieves in excess of 35 mJ/pulse of tunable single mode light at 250 nm. The filter and laser are used to measure individual lines of pure rotational Raman scattering from room air.

Introduction

The development of narrow linewidth, high power, tunable lasers and accompanying ultra-narrow band spectral filters has enabled advances in non-intrusive flow diagnostic techniques based on molecular Rayleigh and Raman light scattering. We have previously presented simultaneous planar measurements of velocity, temperature, and density in a Mach 2 facility based on spectrally Filtered Rayleigh Scattering (FRS). Those measurements, which utilized the second harmonic of an Nd: YAG laser, in conjunction with a molecular iodine filter, resulted in uncertainties of a few percent.[1] More recently, FRS has been demonstrated for temperature measurement in a sooting flame,[2] and for characterization of flow over a flat plate in a CO_2 seeded Mach 8 wind tunnel.[3] Complementing Rayleigh scattering, techniques based on Raman scattering measure species specific properties, including rotational and vibrational temperature, species mole fraction, and potentially velocity.[4] Because Raman scattering is instantaneous, it is not subject to collisional quenching processes, and is therefore particularly attractive for measurements in high pressure environments.

However, Rayleigh and Raman scattering both suffer from small scattering cross-sections, which lead to weak signals. In general, Raman scattering is two to three orders of magnitude weaker than Rayleigh scattering. Furthermore, the scattering signal is often buried within strong background scattering and luminescence which interferes with detection of the desired signal. As a result, a high power laser source and detection system with a high degree of spectral resolution is utilized.

This paper discusses an ultraviolet, narrow linewidth, tunable laser and accompanying narrow band spectral transmission filter which enable detection of individual rotational Raman lines of nitrogen and oxygen. The laser system, an injection seeded, cavity locked, frequency tripled Ti: sapphire laser, has been used previously to demonstrate UltraViolet Filtered Rayleigh Scattering (UVFRS).[5] A novel filter design, based on mercury vapor absorption and resonant fluorescence, provides the narrow band spectral sensitivity for resolution of individual lines of rotational Raman scattering. The utilization of an ultraviolet light source greatly enhances both the Rayleigh and Raman based diagnostics, because the scattering cross sections scale as the incident frequency to the fourth power, as well as the square of the index of refraction. The narrow spectral linewidth of the source is required for spectral sensitivity (to resolve small Doppler shifts for Filtered Rayleigh Scattering, and to resolve individual rotational Raman lines in the current work). Because the light source is tunable, multiple parameters may be measured, and individual rotational Raman shifts may be detected.

The Laser

The illumination source for our experiments is a single mode ultraviolet laser, which is formed by frequency tripling the output of an injection seeded, cavity-locked Ti: sapphire laser. The seed source, a continuously tunable, cw Ti: Sapphire laser, is tuned by modifying its effective cavity length, and is stabilized via feedback through an intracavity etalon.[6] This seed laser is injected into a pulsed Ti: Sapphire resonator which is pumped by a frequency doubled Nd: YLF. An optical flat placed in the pulsed resonator creates a port to inject the seed laser. The second surface reflection from the optical flat is used to monitor the intensity of the seeded light as it passes through the unstable resonator. The Ramp and Lock cavity locking mechanism is employed to insure single mode

* Graduate Student, Member AIAA
** Research Scientist, Member AIAA
‡ Professor, Associate Fellow AIAA

Copyright © 1997 by N.D. Finkelstein *et al.* Published by the American Institute of Aeronautics and Astronautics, Inc. All rights reserved.

output from the pulsed resonator.[5] Before every laser pulse, the unstable resonator's cavity length is swept by *ramp*ing a piezoelectric transducer (pzt) mounted high reflector. As the pulsed resonator's cavity length is swept, a fringe pattern of the intensity of cw seed light is monitored. Effectively, the pulsed resonator acts as a low finesse etalon for the cw light. When the pulsed cavity length is an integral multiple of half wavelengths of the seed laser, a maximum seed signal passes through the pulsed cavity. For this given cavity length, the pulsed resonator output is single longitudinal mode. A feedback loop insures the pulsed cavity length remains *lock*ed to the cw seed frequency, until the laser is fired. As a result, single mode operation is maintained even if the laser frequency is tuned rapidly and/or discontinuously. The Ti: Sapphire emits 310 mJ in a single longitudinal mode pulse at 761 nm, with a near TEM_{00} transverse mode.

A pair of BBO crystals are used for type I doubling and subsequent type II mixing to generate ultraviolet light. The output is nearly the Fourier transform limit of the 10ns (fwhm) pulse. At 254nm, in excess of 35 mJ/pulse of single mode, tunable output is achieved. The spectral brightness and beam quality of this laser are exceedingly good, making it an excellent tool for diagnostics and spectroscopy.

The Filter

We present a novel ultra-narrow spectral passband filter which features the high spectral discrimination of previously reported Atomic Resonance Filters (ARFs),[7,8] while preserving the imaging capabilities of more conventional filters. It is most similar to the resonance scatter filter presented by Langberg, et. al.[9] The filter is based on absorption and subsequent resonant fluorescence of light by atomic mercury vapor. The strong, and spectrally sharp absorption features of mercury (at 253.7 nm) provide the desired spectral discrimination. The fluorescence process and the long relative lifetime (120ns) of the excited mercury state enable temporal gating which further attenuates background scattering when the sample is interrogated by a nanosecond time scale pulsed laser. Due to the large transition strength of mercury, absorption can be made to occur over a short distance through the vapor, and fluorescence is effectively from a planar sheet. Thus, images may be preserved, despite the absorption and fluorescence processes.

The narrow passband filter acts as the compliment to a previously reported mercury notch absorption filter, used for UltraViolet Filtered Rayleigh Scattering.[5] Light scattered from the sample volume is imaged onto the front surface of a cell filled with mercury vapor, as shown in figure 1. If the incident light is spectrally outside the mercury absorption band, the light passes through the vapor cell

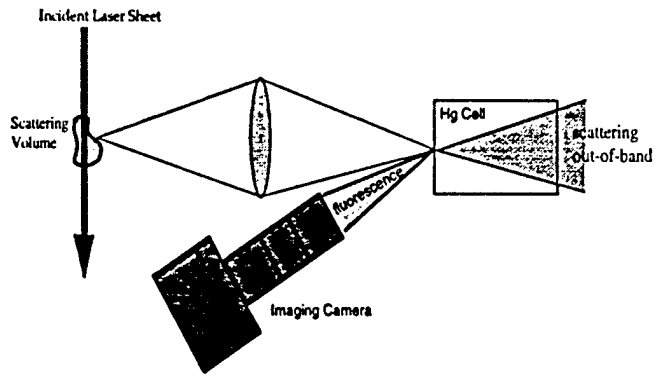

Figure 1: Configuration of Imaging, Narrow Passband Transmission Filter. Scattering from a volume is imaged onto the inside surface of a cell containing mercury vapor. Light coincident with the Hg 253.7nm ground state transition is absorbed, and subsequently fluoresced. Light outside the absorption band passes through the cell and is rejected. Fluorescence is re-imaged onto an intensified camera

and is rejected. If the incident light frequency is coincident with the mercury transition, the light is absorbed. Even with a modest amount of mercury vapor present, incident light is absorbed close to the front surface of the cell. At 0.025 torr, the depth at which the incident radiation is attenuated to e^{-1} of the original value is calculated to be 50 μm. This shallow penetration preserves the filter's imaging capability. Fluorescence is to the ground state, so it is resonant with the incident light and is radiatively trapped in the forward direction. Thus, virtually all the light is reradiated in the backward direction.[10] The fluoresced light is reimaged onto an intensified camera (or photomultiplier tube for non-imaging cases). As a consequence, the only light reaching the camera (or pmt) is from that incident light coincident with the mercury absorption band.

The mercury vapor filter is constructed of an all quartz cell, 5 cm in length with 5 cm diameter widows at each end. A side-arm cold tip, attached to the cell, contains a small amount (1 gm) of mercury. Controlling the temperature of the side arm determines the vapor pressure (and hence number density) of the mercury vapor in the cell. The cell body temperature is kept warmer than the side arm in order to prevent condensation.

Filter Characterization

The temporal, spectral, and spatial response of the mercury vapor filter have been reported previously.[11] The filter response to the short lived (10 ns) laser pulse is a relatively long lived exponential decay. Fits to the filter signal decay yield an e^{-1} lifetime of 630 ns. Since mercury's natural excited state lifetime is 120ns, the longer signal decay time indicates that radiative trapping plays a strong

role in the fluorescence process.[12] The temporal response of the filter is used to enhance suppression of stray laser light scattering. Background scattering from the illuminating source may be temporally filtered, since it only occurs during the 10ns duration of the laser pulse. A detection system gated to observe after the trailing edge of the laser pulse will only capture mercury fluorescence from that light which was spectrally coincident with the mercury vapor absorption. All other scattered light which may enter the detection system will be rejected because of its lack of resonance with mercury. Because of the filter's long temporal decay, gating only minimally reduces the overall fluorescence signal.

The spectral transmission of the narrow passband filter is, to first order, the compliment of the narrow band absorption filter. High resolution transmission scans of the mercury vapor passband filter reveal six peaks corresponding to the naturally occurring isotopes of mercury.[11] As the mercury vapor pressure is increased, the optical depth of the filter is increased, and individual passband peaks are no longer resolved. In both Rayleigh and Raman scattering measurements, the broadened linewidth of the scattering is convolved with the linewidth of the detection instrument (filter). The upper curve in figure 2 plots measured Rayleigh scattering signal transmitted by the filter versus incident laser frequency. The signal measurement is a convolution of the Rayleigh broadening of ambient air (3.8 GHz fwhm, STP, 90°, 254 nm) convolved with the filter transmission profile for a vapor pressure of 0.0015 torr. The filter transmission profile (as measured by the transmission of elastic narrow bandwidth scattering) is plotted on the lower curve of figure 2. The upper plot was obtained by imaging (f/2) ultraviolet scattering from a 1 cm segment of air onto the front surface of the mercury vapor cell. Fluorescence from the mercury was subsequently captured (f/2) on a photomultiplier tube as the incident laser frequency was scanned. Ten shot averages were normalized to incident laser power. As seen in the top of figure 2, individual peaks blend together. For Raman scattering measurements, the scattering linewidth is broader, and the individual passband peaks blend entirely.

Preliminary measurements of spatial resolution yielded 3.4 line pairs/mm (or 295 μm), based on half-width half-maximum resolution, with a filter vapor pressure of 0.02 torr. Higher mercury vapor pressure decreases incident light penetration and therefore increases the resolution. However, at higher optical depths (on the order of 0.1 torr), quenching from the front cell surface is suspected to significantly influence the transmission features of the filter.

The efficiency of the passband filter is limited by the dual collection process, required for the collection of mercury vapor fluorescence. However, while not yet experimentally verified, the fluorescence spatial distribution is presumably Lambertian, because of the high optical depth of the mercury vapor. An f/1 collection lenses imaging Lambertian fluorescence 1:1 would capture six percent of the light impinging on the front of the filter. This calculation neglects surface losses, which may be minimized with anti-reflection coatings at 253.7 nm.

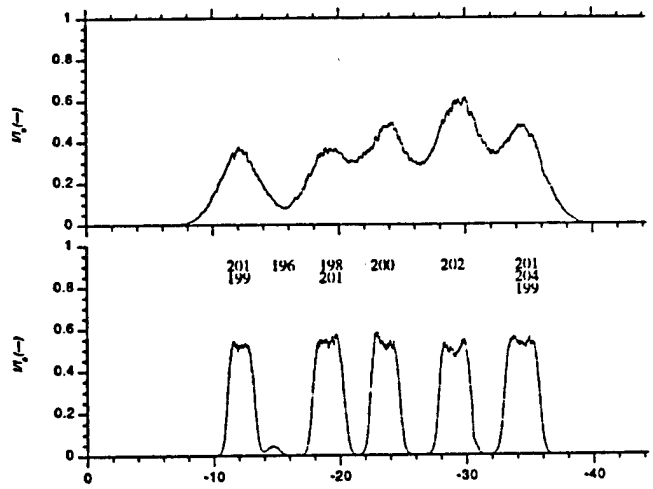

Figure 2: Spectral profile of passband imaging filter. Below, spectral profile of the filter. Above convolution of the spectral profile of the filter with Rayleigh scattering from room air (~ 4 GHz fwhm linewidth, STP). Cell vapor pressure 0.0015 torr. Mercury isotopes listed between plots

Rotational Raman Scattering

An experiment, designed to demonstrate the unique features of the laser/ filter pair, captures the pure rotational Raman scattering spectrum from room air. Light scattering from a 2 cm length of ambient air was 1:1 imaged (f/1 lens) through a vertical slit onto the inside surface of the mercury vapor filter. The mercury vapor fluorescence was re-imaged (f/1) off axis through a mercury line interference filter onto a photomultiplier tube. A boxcar integrator gated the fluorescence signal by capturing a 1.5 μs signal, beginning 50 ns after the initial laser pulse. A photodiode/ boxcar integrator simultaneously measured the laser power. A personal computer and A/D card recorded 100 shot averages of the fluorescence signal, the laser power, and the laser frequency.

By spectrally detuning the laser from the Hg resonance, pure rotational Raman shifted scattering was made spectrally coincident with the 253.7 nm transmission filter. Scattering at the detuned laser frequency was rejected by the filter. Three different data sets, each with the laser scanning over 2.5 cm^{-1}, captured four different Stokes shifted pure rotational Raman lines. Each data set was normalized by incident laser power, so the data sets could

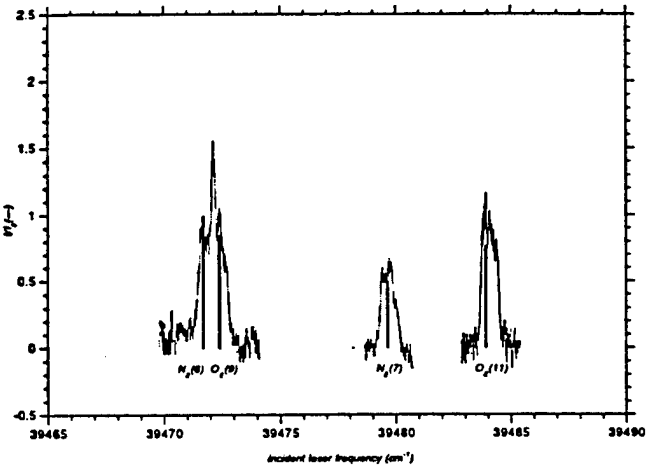

Figure 3: Pure rotational Raman scattering of room air. Three separate scans of different spectral regions, overlapping four separate rotational Raman lines of N_2 and O_2. Simultaneous plots of predicted relative scattering signals and locations of the four lines, given as bar plots beneath.

be weighted relative to each other. The spectral position of each data set was determined with a Burleigh wavemeter which measured the wavelength (±0.01 cm^{-1}) of the cw seed laser.

The three data sets are plotted in figure 3. Predicted location and relative scattering signal strengths of the nitrogen (J=6, 7) and oxygen (J=9,11) rotational lines are illustrated beneath the spectral scans.[13,14] Because the separation of the $N_2(6)$ and $O_2(9)$ rotational lines is small (0.7 cm^{-1}, on the order of the bandpass of the filter itself) the two spectral lines blend together. The other two lines, $N_2(7)$ and $O_2(11)$, appear independently, shifted further apart. The larger rotational Raman scattering cross-section of oxygen (2.7 times that of nitrogen, at 253.7nm) is demonstrated and agrees well with the work of Penny, et. al.[14]

In conclusion, a new narrow passband imaging filter based on mercury vapor absorption and fluorescence has been constructed and initial characterization performed. The spectral width of the passband filter is less than 1 cm^{-1}. The spectral transmission, to first order, acts as the inverse of the well characterized mercury absorption notch filter. The long exponential decay of the fluorescence signal confirms that radiative trapping plays a strong role in the filter dynamics, and temporal gating is an effective means of gating out stray radiation, further suppressing background signal. Individual rotational Raman lines of nitrogen and oxygen have been measured using a unique narrow linewidth, tunable ultraviolet light source.

The authors thank Mike Souza, Princeton University Chemistry department for helpful discussions and his expertise in glassblowing, Andy Finch, Glenn Rines and Richard Schwarz of Schwartz Electro-Optics, Inc. in the development of the laser systems.

This research was supported by an University Research Initiative grant from the Air Force Office of Scientific research and a Small Business Innovative Research grant to Schwartz Electro-Optics, from NASA- Ames.

References

1. J.N. Forkey, "Development and Demonstration of Filtered Rayleigh Scattering - A Laser Based Flow Diagnostic for Planar Measurement of Velocity, Temperature, and Density" NASA Technical Report 2067, and Dissertation Thesis, Princeton University, 2067-T, April 1996.

2. D. Hoffman, K. Münch, and A. Leipertz, "Two-dimensional temperature determination in sooting flames by filtered Rayleigh scattering" Optics Letters, Vol 21, April 1 1996, p.525.

3. P.J. Erbland, M. Baumgartner, A.Yalin, M.Etz, T. Muzas, W.Lempert, R.Miles and L.Smits,"Development of Planar Diagnostics for Imaging Mach 8 Flowfields Using CO_2 and Na seeding,"35th AeroSciences Meeting and Exhibit, Reno, NV, Jan. 1997. AIAA 97-0154.

4. P.A. Skaggs, T.M. Brown, S.P. Nandula, R.W. Pitz and E.P. Hassel, "Multi-Species Measurements in CH_4-Air Flames Using a Narrowband KrF Excimer Laser by UV Raman Scattering," 32nd AeroSciences Meeting and Exhibit, Reno, NV, Jan. 1994. AIAA 94-0613

5. N.D. Finkelstein, W.R. Lempert, R.B. Miles, G.A. Rines, and A.Finch, "Cavity Locked, Injection Seeded, Titanium: Sapphire Laser and Application to UltraViolet Flow Diagnostics," 34th AeroSciences Meeting and Exhibit, Reno, NV, Jan. 1996. AIAA 96-0177.

6. N.D. Finkelstein, J. Gambogi, W.R. Lempert, R.B. Miles, G.A. Rines, A.Finch, and R.A. Schwarz, "Development of a Tunable Single Frequency UltraViolet Laser Source for UV Filtered Rayleigh Scattering," 32nd. AeroSciences Meeting and Exhibit, Reno, NV, Jan. 1994. AIAA 94-0492.

7. J. Menders, K. Benson, S.H. Bloom, C.S. Liu, and E. Korevaar, "Ultranarrow Line Filtering Using a Cs Faraday Filter at 852 nm," Optics Letters, Vol 16, June 1 1991, p.846.

8. J.A. Gelbwachs, "Atomic Resonance Filters," IEEE Journal of Quantum Electronics, Vol 24, No. 7., July 1988, pg 1266.

9. E. Langberg, M. Naylor, and H. Heckscher, Conference on Optical Instruments and Techniques, Chapman and Hall, p. 229 (1962)

10. R.D. Guenard, Y.H. Lee, M. Bolshov, D. Huebuer, B.W. Smith, and J.D. Winefordner, "Characteristics of a Rubidium Metal Vapor Filter for Laser Scatter Rejection in Single Molecule Detection," Applied Spectroscopy, Vol 50, No 2, 188 (1996).

11. N.D. Finkelstein, W.R. Lempert, and R.B. Miles, "A Narrow Passband Imaging Refluorescence Filter for Non-Intrusive Flow Diagnostics," 19th Advanced Measurement and Ground Testing Technology Conference, New Orleans, LA, Jun. 1996. AIAA 96-2269.

12. Holstein, T. "Imprisonment of Resonance Radiation in Gases," Physical Review, Vol 72, No 12, 1974, pg. 1212.

13. Weber, A., Raman Spectroscopy of Gases and Liquids, Springer-Verlag, New York, 1979, pg. 88.

14. C.M.Penny, R.L St. Peters, and M. Lapp, "Absolute rotational Raman cross sections for N_2, O_2 and CO_2" Journal of the Optical Society of America, V64, N2, May 1974, pp. 712.

AIAA 97-0500

FILTERED RAYLEIGH SCATTERING MEASUREMENTS USING A MHz RATE PULSE-BURST LASER SYSTEM

W.R. Lempert, P-F. Wu, and R.B. Miles

PRINCETON UNIVERSITY
Dept. of Mechanical & Aerospace Engineering
Princeton, New Jersey 08544 U.S.A.

35th Aerospace Sciences Meeting & Exhibit

January 6-10, 1997 / Reno, NV

For permission to copy or republish, contact the American Institute of Aeronautics and Astronautics
1801 Alexander Bell Drive, Suite 500, Reston, VA 22091

"FILTERED RAYLEIGH SCATTERING MEASUREMENTS USING A MHz RATE PULSE-BURST LASER SYSTEM"

W.R. Lempert,* P-F. Wu,† and R.B. Miles§

Department of Mechanical & Aerospace Engineering
PRINCETON UNIVERSITY
Princeton, New Jersey 08544 U.S.A.
609/258-2875

ABSTRACT

We present measurements of the spectral characteristics of a MHz rate, Nd:YAG pulse-burst laser system, with particular emphasis on data relevant to spectrally filtered scattering diagnostics which employ molecular iodine vapor filters. The time-averaged laser spectral profile is found to correspond quite well to that predicted from the Fourier transform of the observed temporal profile. The measured maximum extinction value of 5×10^{-5} for the second harmonic output is in good agreement with modeling predictions, based on a 10 cm path length iodine cell under typical operating conditions. Filtered images of time sequences of supersonic flow over a 14° wedge are also presented. The images clearly illustrate the unsteadiness of the oblique shock wave and the correlation of its dynamic behavior with large-scale turbulent boundary layer structure.

*Senior Research Scientist, Mechanical & Aerospace Engineering, Member AIAA.

†Graduate Student, Mechanical & Aerospace Engineering.

§Professor, Mechanical & Aerospace Engineering, Associate Fellow, AIAA.

Copyright © 1997 by Princeton University. Published by the American Institute of Aeronautics and Astronautics, Inc. with permission.

1. INTRODUCTION

The ability to visualize time-evolving high speed flow is severely limited by the modest (order 10's-100's Hz) repetition rates, typical of high power laser systems. We have previously reported[1] a new high-speed imaging system capable of capturing a time sequence of up to 30 images at a maximum rate as high as 1 MHz. The system consists of a "pulse-burst" Nd:YAG laser and a framing CCD camera with integrated, on-chip storage. While it was not stressed in Ref. (1), the laser system has the additional feature that the spectral linewidth is exceedingly narrow, which presents the opportunity to perform spectrally resolved imaging using filtered scattering diagnostic techniques. Filtered scattering[2,3] refers to a class of diagnostic in which an atomic or molecular vapor filter is used to spectrally resolve flow field scattering which is Doppler shifted and/or thermally broadened. The technique has been applied to a wide variety of environments including supersonic jets[4,5] and inlet models,[6] mixing layers,[7] large-scale wind tunnels,[8] flow around automobiles,[9] and sooting flames.[10] Similar approaches have also been reported in the remote sensing community,[11,12] and have been proposed for supersonic inlet mass flux measurement.[13] A detailed discussion of the accuracy limits imposed by constraints of available imaging technology has been presented by McKenzie,[14] and the extension of the technique into the ultraviolet region of the spectrum has recently been presented by Finkelstein.[15]

Forkey[16] has recently presented a detailed measurement of the spectral characteristics of a typical injection-seeded Nd:YAG laser, in which it was shown that the central lasing frequency varies by as much as

+/- 50 MHz across the radial profile of the output beam, greatly affecting the apparent velocity field. In this paper, we present new results which characterize the spectral characteristics of the pulse-burst laser. In particular, measurements of the spectral profile are shown to compare well with the Fourier Transform of the temporal profile. Experimental attenuation of the pulsed second harmonic output in molecular iodine vapor was also measured and agreed well with predictions based on a recently presented iodine absorption model.[17] Finally, images are presented of a supersonic shockwave/boundary layer interaction in which the dynamics of shock unsteadiness and temporal correlation of its motion with large-scale turbulent boundary layer structure are clearly evident.

2. LASER SYSTEM OVERVIEW

A detailed description of the pulse-burst laser system has been given previously.[1] As illustrated in Fig. 1, it consists of the following six elements:

1. Monolithic, single-frequency, diode-pumped, cw Nd:YAG laser.
2. Four -Pass preamplifier #1.
3. Pulse slicer.
4. Two-pass preamplifier #2
5. Three-stage power amplifier chain.
6. Second harmonic crystal.

The single-frequency Nd:YAG laser is a Lightwave Electronics model 120-03, with cw power of approximately 20 mWatts. The output of this laser is polarization-coupled into preamplifier #1, which is a four-pass, 10 Hz repetition rate, flashlamp-pumped, 7 mm diameter by 110 mm long Nd:YAG rod. The net small signal, four-pass gain has been measured to be approximately 1500x, so that the output of preamplifier #1 is a single, approximately 60 microsecond duration, 30 Watt peak power pulse, repeated at a repetition rate of 10 Hz. This 60 microsecond pulse is formed into a "train" using a pulse slicer, custom built by Medox, Inc., Ann Arbor, Michigan. The pulse slicer consists of a pair of fast electro-optic Pockel cells, and is capable of creating a train of between 1 and 99 pulses, with minimum individual pulse duration of 10 nsec, and minimum inter-pulse period of 1 microsecond. The output of the pulse slicer is spatially filtered and double-passed through preamplifier #2. The net, double-pass gain is 20x, so that the output peak power is 600 Watts, corresponding to 12 microjoules for an individual, 20 nsec duration pulse. The power amplifier chain consists of three additional Nd:YAG rods, taken from a commercial laser system. The rods are 6.5, 8, and 9.5 mm diameter, respectively, and there is an optical isolator placed between power amplifiers #2 and #3. The peak gain of the individual stages has been measured to be 10, 10, and 8, respectively, resulting in an overall peak system gain of approximately 2.4×10^7. The corresponding energy is approximately 10 mJ for a single, 20 nsec duration pulse. The temporal evolution of the gain of the amplifier chain is illustrated in Fig. 2, which shows an oscilloscopic trace of a typical burst sequence consisting of 30, 20 nsec duration pulses, separated by 2 microseconds.

The final element of the laser system is the second harmonic generator. To date, we have obtained a maximum conversion efficiency of 10%, corresponding to a single pulse energy of approximately 1.0 mJ at the second harmonic wavelength of 0.532 microns. Preliminary measurements have suggested, however, that the conversion efficiency falls off at the trailing portion of the burst sequence. Figure 3 shows an oscilloscope trace of the fundamental (upper trace) and second harmonic (lower trace) outputs from a single, 30-pulse-burst sequence. This phenomenon has not yet been studied in detail, and its origin is unclear.

3. LASER SPECTRAL CHARACTERISTICS

a. Pulse Temporal Profile

An important feature of the pulse-burst system is that the spectral linewidth is exceedingly narrow. Since the cw, Nd:YAG master oscillator has a time-averaged linewidth of order 1 MHz, the individual pulses are predicted to have a time-average linewidth of order 50 MHz, based on the Fourier transform of a 20 nsec, rectangular temporal profile. ($\Delta\nu\Delta t = 0.88$ for a sinc^2/rectangle Fourier transform pair.)[18] Figure 4 shows a typical oscilloscope trace of a single fundamental pulse (upper trace), obtained with a fast (1 nsec rise time) silicon PIN photodiode. The pulse is approximately rectangular, with a full-width-at-half-maximum of approximately 16 nsec. (The apparent structure in the trailing edge of the pulse is due to "ringing" in the measurement and is not believed to be real.) While it is not obvious from Fig. 4, there is a small (order 1%) dc component to the output pulse due to the finite modulation depth of the pulse slicer. The lower trace in Fig. 4 shows the corresponding temporal profile at the second harmonic frequency. It can be seen that the pulse is also approximately rectangular, with a full-width-at-half-maximum of 14 nsec or approximately 10% less than that of the fundamental. It is worthwhile to point out that, in contrast to a Gaussian pulse, the temporal profile of the second harmonic of a perfectly rectangular pulse, assuming a simple intensity squared law for conversion efficiency, should be identical to that of the fundamental.

b. Pulse Spectral Profile

A 2 GHz, free spectral range, confocal Fabry-Perot spectrum analyzer (Burleigh model RC-46) was used to directly determine the spectral profile of the

fundamental output of the pulse-burst laser. For these measurements, the laser was operated at full gain, with a single pulse per burst, and the output attenuated with a combination of neutral density filters and front surface reflections from uncoated optical quartz flats. As illustrated in Fig. 5, the internal photodiode/mount assembly was removed from the etalon, and replaced with the same fast response time photodiode used to obtain the temporal traces of Fig. 4. The photodiode output was digitized with a commercial boxcar averager (Stanford Research Systems model SR 250) and the output recorded with a laboratory computer. For the data presented below, the boxcar was typically used to average the photodiode voltage over 30 laser shots. The wavelength of the cw master oscillator was slowly scanned (order 2 MHz/sec) by applying a computer generated voltage "staircase" to the input of the laser temperature controller, while holding the voltage to the etalon mirrors constant. (The laser, rather than the etalon, was tuned, because the etalon could not be scanned slowly enough to smoothly capture the profile of the pulsed laser). The tuning rate of the laser was calibrated by observing multiple Fabry-Perot orders as the laser was scanned. The observed scanning rate was 1.6 GHz/volt, and was assumed to be constant over the duration of the scan. The "effective" finesse of the etalon was obtained by identical spectral scans of the laser with the pulse slicer maintained in the "on" position. This produced a nominally 60 microsecond pulse, with corresponding Fourier Transform limited linewidth of 0.02 MHz, which is much less than the manufacturers specification of 1 MHz for the time mean linewidth of the cw master oscillator. The "effective" finesse is lower than the inherent (i.e., that due to reflectivity, etc.) finesse of the etalon due to slow, thermally induced drift in the central transmission wavelength, which occurs over the time scale of the spectral profile measurement. (order 1 minute). The "effective" finesse was measured to be approximately 100, corresponding to a spectral resolution of 2 MHz.

Figure 6 (dotted line) shows the time-averaged spectral profile of the fundamental output of the laser, corresponding to the same, nominally 16 nsec duration, pulse illustrated in Fig. 4. The relatively sharp spectral feature at line center is due to the dc temporal component, as discussed above. The central "lobe" of the pulsed component has a Full-Width-at-Half-Maximum (FWHM) linewidth of approximately 50 MHz, and weak side bands, characteristic of a sinc squared function, can just be discerned. [Note that $\mathrm{sinc}^2(\upsilon)$ is a result of $I(t) = E(t)\,E^*(t)$.] Also shown in Fig. 6 is the discrete Fourier transform of the instantaneous temporal profile of Fig. 4a, convolved with the instrument function measured as described above. While the agreement is not perfect, note particularly the discrepancy in the relative magnitude of the side lobes, it is clear that the spectral profile is "approximately" Fourier transform limited. The discrepancy in the side lobe intensity has not been investigated in detail. Since the second harmonic conversion process is inherently non-linear, the side bands are expected to minimally impact iodine vapor-based filtered scattering diagnostics.

c. Iodine Cell Attenuation

Molecular iodine vapor extinction measurements have been performed in a manner similar to that described by Forkey.[17] The measurement is essentially a simple laser absorption experiment, except that a series of calibrated neutral density filters are used to attenuate the beam prior to spectral tuning into the resonance feature of the vapor. As the laser is tuned into the absorption band, the filters are sequentially removed, boosting the light level reaching the detector. In this way the dynamic range of the attenuation measurement can be increased beyond the limitations imposed by the A/D converter and the linear operating range of the photodiode. The actual experimental apparatus is similar to that shown in Fig. 5, except that the Fabry-Perot etalon is replaced by an iodine vapor cell. The vapor cell, described in detail previously,[17] was 10 cm in length, and operated with a side arm temperature of 313K, which was maintained to within +/- 0.1 K with a temperature controlled water bath. The corresponding iodine vapor pressure is approximately 1 torr.[19] Figure 7 shows a modeled absorption spectrum for the iodine cell over the full tuning range of the laser system. Extinction measurements were made using the strong feature, marked with an arrow, in the vicinity of 18788.5 cm^{-1} and previously referred to as iodine transition "A".[20] Figure 8 shows a typical result, where the laser has been slowly tuned over a range of approximately 2.5 GHz. The detected signal has been arbitrarily normalized in such a way as to set the apparent "transmission" equal to approximately 1 at the endpoints of the scan. At the approximate 1600 MHz point of the laser scan, a 200x neutral density filter was removed from the beam path, resulting in a large increase in signal reaching the detector. This signal decreases as the laser is further tuned into resonance, and a second, 20x filter is removed at the approximate 1800 MHz point. The process is reversed as the laser is tuned out of the iodine resonance. Figure 9 is a blow-up of the central 400 MHz of the experimental data (dotted line) from Fig. 8, overlaid with a modeling prediction (solid line) obtained using the computer code described in Ref. (17). In this case, the experimental data has been converted to absolute transmission by accounting for the attenuation of the neutral density filters. It can be seen that the experimental line center extinction is 5×10^{-5}, as compared to the modeled value of approximately 1.5×10^{-5}. It is important to note, however, that since the absorption is in the highly optically thick regime, it is only weakly dependent on

the actual absorption coefficient. This is most easily seen by noting that the extinction is given by:

$$I/I_0 = \exp\{-\sigma N l\} \quad (1)$$

where σ is the absorption cross-section, N the iodine number density, and l the cell path length. For a cell length of 10 cm, a discrepancy of approximately 10% in the product of σN is sufficient to account for the discrepancy between the measured and the predicted extinction. This is well within the combined uncertainty bounds.[17]

The agreement between the experimental and predicted maximum extinction is in contrast to results presented previously which employed a typical commercial injection-seeded laser system.[20,21] In that work, the maximum extinction measured was of the order of 500, as compared to modeling calculations which predicted as high as 10^{-6}. While the reason for the discrepancy was not known for certain, it was suggested that a laser linewidth significantly greater than the Fourier transform limit could be responsible. Although this has not been explored in detail, it is qualitatively consistent with recent work[16] in which an order 100 MHz variation in laser central frequency was observed across the profile of the second harmonic output beam. The difference between the two measurements appears to confirm the expected improvement in spectral performance inherent to pulsed amplification.

4. IMAGES OF SHOCK WAVE/BOUNDARY LAYER DYNAMICS

In order to demonstrate the ability to capture the dynamics of time-evolving, high speed flow phenomena, time sequences of planar images have been obtained of turbulent Mach 2.5 boundary flow over a 14° wedge. As illustrated in Fig. 10, the second harmonic output of the pulse-burst laser system was formed into an approximately 2 cm high by 100 micron thick sheet, which was incident to a laboratory scale, two-dimensional wind tunnel, at an angle of approximately 45° with respect to the free stream direction. A 14° wedge was attached to a wall of the tunnel at a location where the boundary layer thickness is approximately one third the total span. Images were obtained with the sheet oriented both perpendicular (streamwise view) and parallel (plan view) to the wedge. For the streamwise orientation, (illustrated in Fig. 10) the sheet was brought into the tunnel through a small slot, cut into the wedge at the flow centerline. In order to enhance the scattering signal, gaseous carbon dioxide was seeded into the plenum, which condensed downstream into a finely dispersed "fog" of order 100 nm diameter particles. The enhanced scattering resulting from the condensation more than compensates for the relatively low (order 1 mJ) available second harmonic pulse energy. In the warmer thermal boundary layer, the condensed carbon dioxide sublimes, resulting in very high image contrast. The scattering was captured at 90° to the sheet using a CCD framing camera described in Ref. (1). The CCD camera has a 30-image storage buffer built into the image sensor chip itself, and can frame at rates up to 1 MHz.

Figure 11 shows a typical sequence of nine streamwise view images. The images have been rotated with respect to the geometry of Fig. 10, so that the principal flow direction is from right-to-left. The time between images is 2 microseconds and the correlation of the "kink" in the oblique shock, which is formed in image 3, with the passage of a large-scale boundary layer structure, is clearly evident. Figure 12 shows a representative sequence of images obtained with the sheet incident parallel to the wedge, at a location near the upper edge of the boundary layer. The flow, also from right-to-left, is turned upward as it passes through the oblique shock formed by the wedge. Since the sheet is oriented parallel to the wedge, there appear to be large discontinuities in turbulent structure in the vicinity of the shock location. This is due to structures being turned into the sheet at the shock location. Again, the correlation of the dynamics of the shock with the motion of large-scale structure is readily apparent. (Note, in particular, images 5 - 9.)

The image sequences illustrated in Figs. 11 and 12 were obtained without the use of the molecular vapor filter, which is possible because of the inherently high contrast obtained from the carbon dioxide condensation. In order to demonstrate the potential of high frame rate filtered scattering, we have obtained image sequences, similar to those in Figs. 11 and 12, with the laser tuned to preferentially transmit regions of high/low velocity (i.e., large/small Doppler shift). The iodine filter was as described above (10 cm length, 40° cold tip temperature), and the laser was, again, tuned to the vicinity of the iodine "A" transition. Figure 13 shows three sets of six images each, obtained with a 2 microsecond interframe period. The images in the left column were obtained with the laser tuned far enough from resonance that the images are, effectively, unfiltered. Note that the scattering intensity immediately downstream of the shock, but above the boundary layer, is of the same magnitude as that of the free stream. The images in the center column were obtained with the laser tuned to preferentially transmit the high speed, free stream flow. In this case, the scattering immediately downstream of the shock is attenuated due to the lower flow velocity. Finally, in the images on the right, the laser has been tuned to preferentially transmit the lower velocity fluid, downstream of the shock.

5. CONCLUSIONS

The spectral characteristics of a MHz rate, Nd:YAG pulse-burst laser system have been examined, with particular emphasis on implications for filtered scattering imaging diagnostics. The time-averaged

spectral profile for 16 nsec, near rectangular, pulses was found to agree reasonably well with predictions based on the discrete Fourier transform of the temporal profile. Experimental extinction in molecular iodine was measured to be 5×10^{-5}, which is approximately two orders of magnitude greater than that previously reported[21] using a commercial injection-seeded Nd:YAG system. The difference is possibly attributable to the more ideal spectral characteristics resulting from pulsed amplification of the cw master oscillator. The laser system, and a companion CCD framing camera, were used to obtain image sequences clearly illustrating the temporal correlation between the large-scale structure of a Mach 2.5 turbulent boundary layer, and the curvature and unsteadiness of the oblique shock produced by a 14° wedge.

6. ACKNOWLEDGMENTS

The authors wish to acknowledge John L. Lowrance and Vince Mastrocola of Princeton Scientific Instruments, Inc., for providing the CCD framing camera and for assisting in its operation. The authors also wish to acknowledge Jay H. Grinstead for assistance in the imaging measurements, and Philip Howard for providing technical support.

The pulse-burst laser system has been developed with support from two grants from the United States Air Force Office of Scientific Research, Julian Tishkoff (University Research Initiative) and Leonidas Sakell (External Aerodynamics), technical monitors. Seed money was also provided by AT&T Bell Laboratories, John Bjorkholm, technical monitor, and the Princeton University Center for Photonics and Opto-Electronic Materials. The CCD framing camera has been developed under Small Business Innovative Research (SBIR) grants from the United States Office of Naval Research, Edwin Rood, technical monitor; and the United States Air Force, Wright Laboratory, Charles Tyler, technical monitor.

REFERENCES

1. W.R. Lempert, P-F Wu, B. Zhang, R.B. Miles, J.L. Lowrance, V. Mastrocola, and W.F. Kosonocky, "Pulse-Burst Laser System for High-Speed Flow Diagnostics," Paper #AIAA-96-0179, AIAA 34th Aerospace Sciences Mtg., Reno, NV, Jan. 15-18, 1996.

2. R. Miles and W. Lempert, "Two-Dimensional Measurement of Density, Velocity, and Temperature of Turbulent Air Flows from UV Rayleigh Scattering," Applied Physics B B51., p. 1 (July 1990).

3. H. Komine, S.J. Brosnan, A.B. Litton, and E.A. Stappaerts, "Real-Time Doppler Global Velocimetry, Paper #AIAA091-0337, (1991).

4. J.N. Forkey, W.R. Lempert, and R.B. Miles, "Accuracy Limits for Planar Measurements of Flow Field Velocity, Temperature, and Pressure Using Filtered Rayleigh Scattering," Experiments in Fluids (Submitted December 1996).

5. M.W. Smith and G.B. Northam, "Application of Absorption Filter-Planar Doppler Velocimetry to Sonic and Supersonic Jets," AIAA Paper #95-0299, Jan. 1995.

6. J.N. Forkey, W.R. Lempert, S.M. Bogdonoff, R.B. Miles, and G. Russell, "Volumetric Imaging of Supersonic Boundary Layers Using Filtered Rayleigh Scattering Background Suppression," Paper #AIAA-94-0491, AIAA 32nd Aerospace Sciences Mtg. & Exhibit, Jan. 10-13, 1994, Reno, NV.

7. G.S. Elliott, M. Samimy, and S.A. Arnette, "A Molecular Filter-Based Velocimetry Technique for High-Speed Flows," Experiments in Fluids 18, pp. 107-118 (1994).

8. J. Meyers, "Evolution of Doppler Global Velocimetry Data Processing," Eighth International Symposium on Applications of Laser Techniques to fluid Mechanics, Vol. 1, Lisbon, Portugal, July 8-11, 1996.

9. I. Röehle and R. Schodl, "Doppler Velocimetry in the Flow of a Swirler," Eighth International Symposium on Applications of Laser Techniques to fluid Mechanics, Vol. 1, Lisbon, Portugal, July 8-11, 1996.

10. D. Hoffman, K.-U Münch, and A. Leipertz, "Two-Dimensional Temperature Determination in Sooting Flames by Filtered Rayleigh Scattering," Optics Letters 21, p. 525 (1996).

11. H. Shimizu, S.A. Lee, and C.Y. She, "High Spectral Resolution LIDAR System with Atomic Blocking Filters for Measuring Atmospheric Parameters," Applied Optics 22, pp. 1373-1381 (1983).

12. P. Piironen and E.W. Eloranta, "Demonstration of a High-Spectral-Resolution LIDAR Based on an Iodine Absorption Filter," Optics Letters 19, p. 234 (1994).

13. J.A. Shirley and M. Winter, "Air Mass Flux Measurement System Using Doppler-Shifted Filtered Rayleigh Scattering, "AIAA Paper 93-0513, Jan. 1993.

14. R.L. McKenzie, "Measurement Capabilities of Planar Doppler Velocimetry Using Pulsed Lasers," AIAA Paper 95-0297, Jan. 1995.

15. N.D. Finkelstein, W.R. Lempert, R.B. Miles, A. Finch, and G.A. Rines, "Cavity-Locked, Injection-Seeded, Ti:Sapphire Laser and Application to Ultraviolet Flow Diagnostics," Paper #AIAA-96-0177, AIAA 34th Aerospace Sciences Mtg. & Exhibit, Reno, NV, Jan. 15-18, 1996.

16. J.N. Forkey, W.R. Lempert, and R.B. Miles, "Observation of a 100 MHz Frequency Variation Across the Output of a Frequency-Doubled, Injection-Seeded, Unstable Resonator, Q-Switched Nd:YAG Laser," Optics Letters (Accepted, November 1996).

17. J.N. Forkey, W.R. Lempert, and R.B. Miles, "Corrected and Calibrated I_2 Absorption Model at Frequency Doubled Nd:YAG Laser Wavelengths," Applied Optics (Submitted, November 1996).

18. R. Bracewell, "*The Fourier Transform and Its Applications,*" McGraw-Hill Electrical and Electronic Engineering Series, New York, 1965.

19. *Thermodynamics Research Center (TRC) thermodynamics tables--non-hydrocarbons*, Texas A&M University, p. ka--190 (1975).

20. R.B. Miles, J.N. Forkey, and W.R. Lempert, "Filtered Rayleigh Scattering Measurements in Supersonic/Hypersonic Facilities," Paper #AIAA-92-3894, AIAA 17th Aerospace Ground Testing Conference, Nashville, TN, July 6-8, 1992.

21. J.N. Forkey, "Development and Demonstration of Filtered Rayleigh Scattering--A Laser-based Flow Diagnostic for Planar Measurement of Velocity, Temperature, and Pressure," Ph.D. Thesis, Dept. of Mechanical & Aerospace Engineering, Princeton University, Princeton, New Jersey (June 1996).

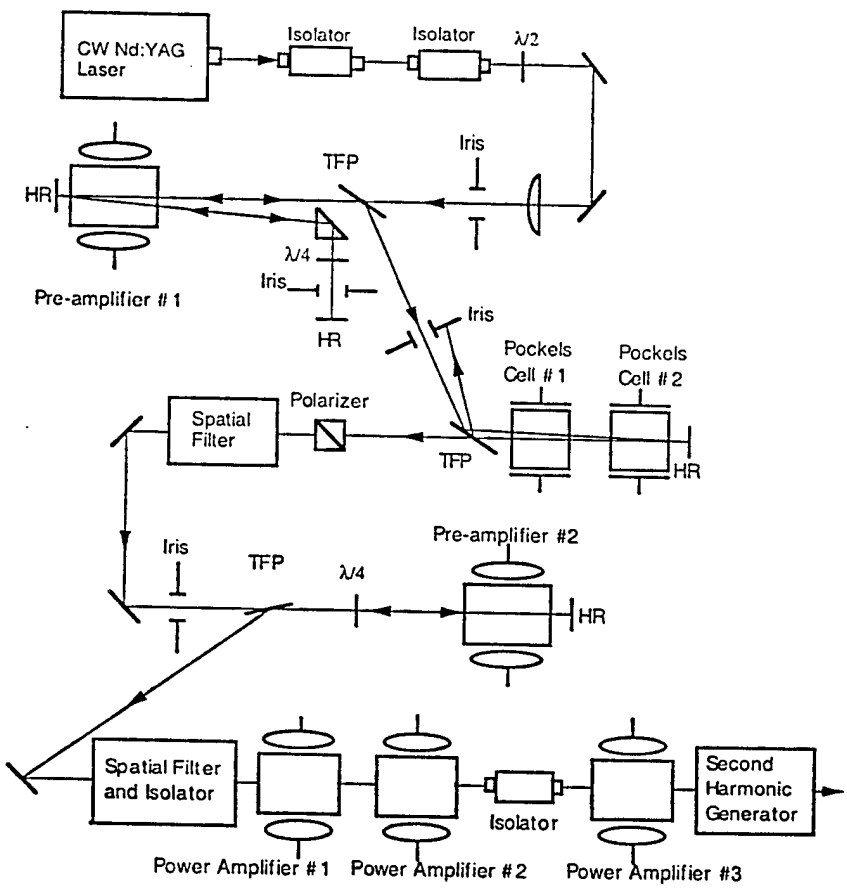

Fig. 1. Schematic diagram of the pulse-burst laser system.

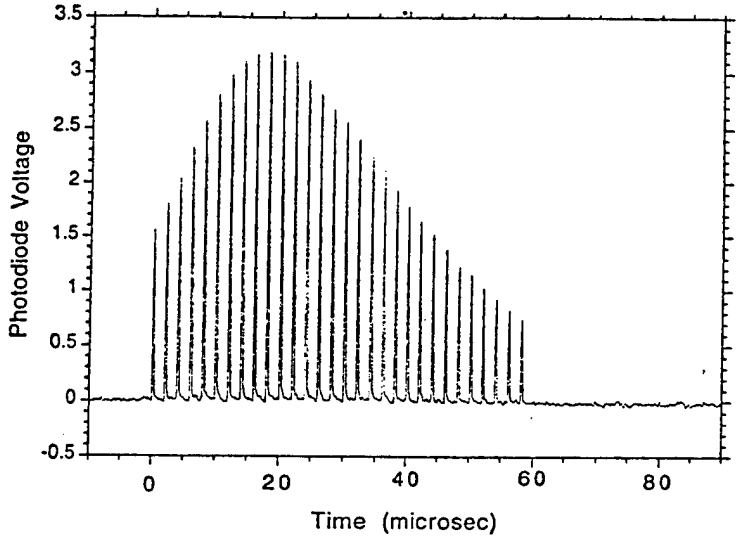

Fig. 2. Oscilloscope trace of typical pulse burst consisting of 30, 20 nsec duration pulses.

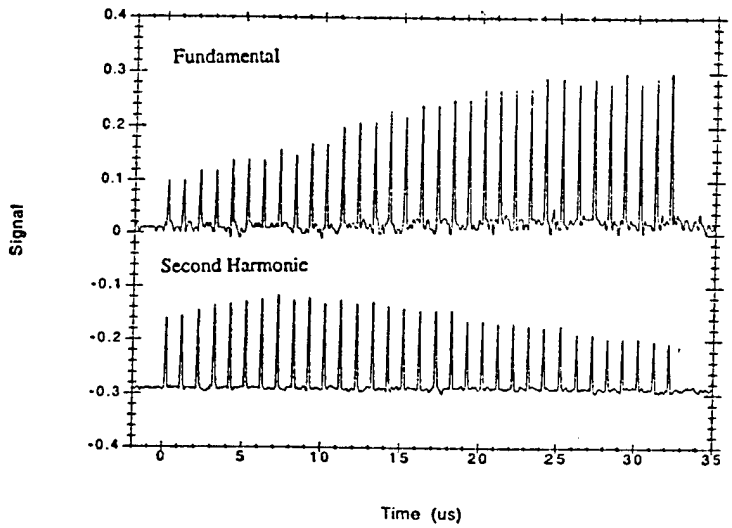

Fig. 3. Comparison of fundamental (upper trace) and second harmonic (lower trace) burst sequences.

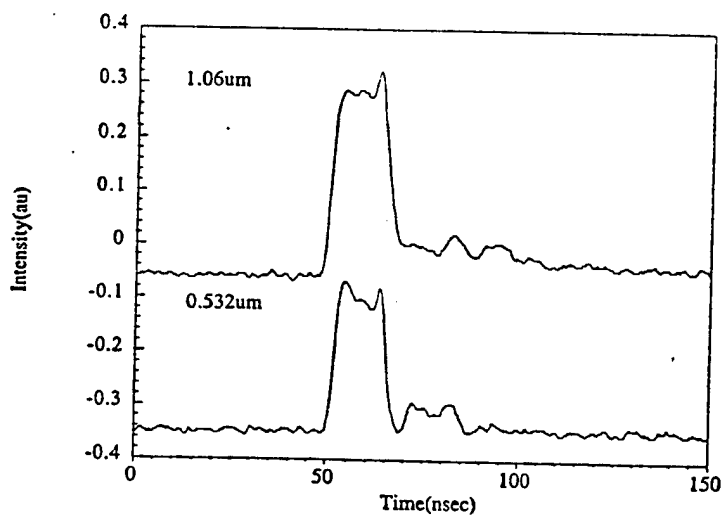

Fig. 4. Temporal profile of typical fundamental (upper trace) and corresponding second harmonic (lower trace) pulses. Fundamental/second harmonic pulse widths are 16/14 nsec, respectively.

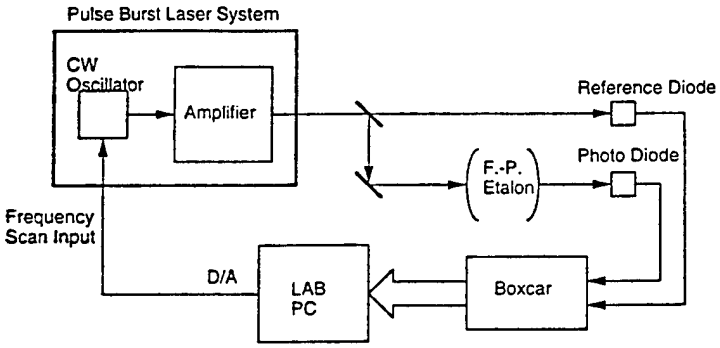

Fig. 5. Schematic diagram of spectral measurement.

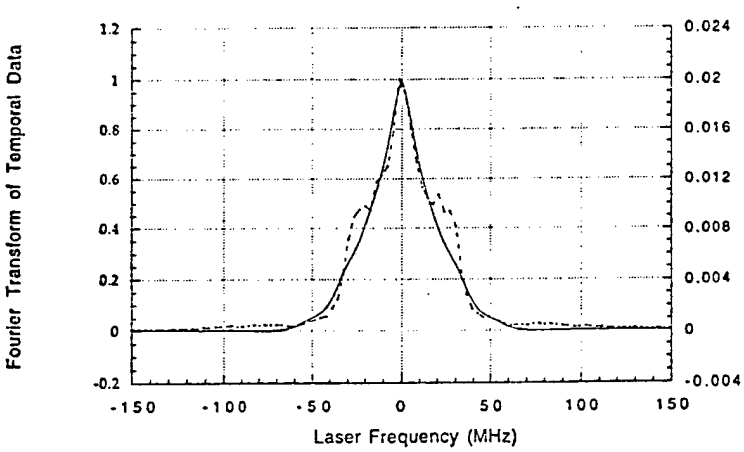

Fig. 6. Time-averaged spectral profile (dotted) of fundamental output of pulse-burst laser overlaid with Fourier transform (solid) of temporal profile from Fig 4.

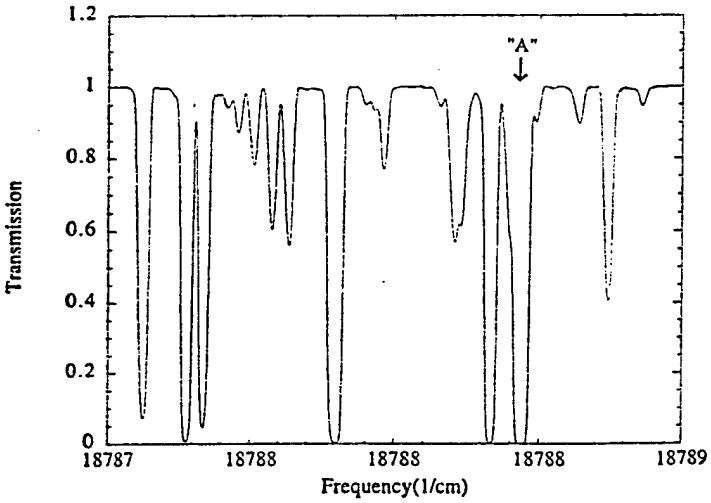

Fig. 7. Modeled iodine absorption over tuning range of Nd:YAG laser. Feature marked with arrow was used for extinction measurements.

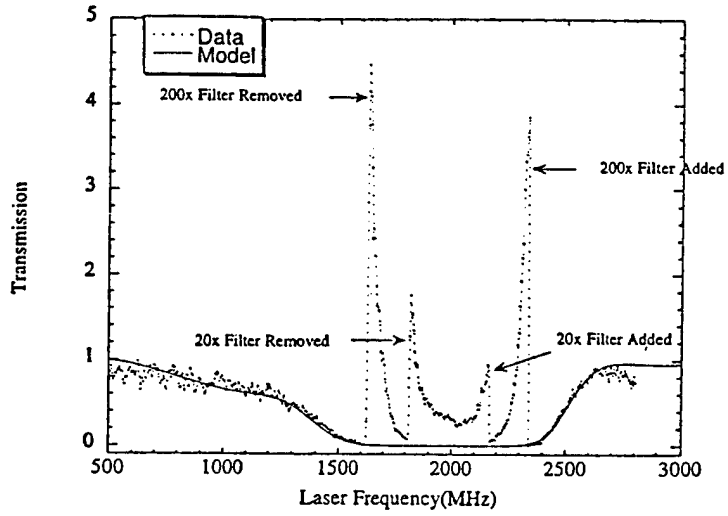

Fig. 8. Experimental (dotted) and modeled (solid) extinction for iodine transition "A". Cell cold tip temperature is 353 K. Cell length is 10 cm.

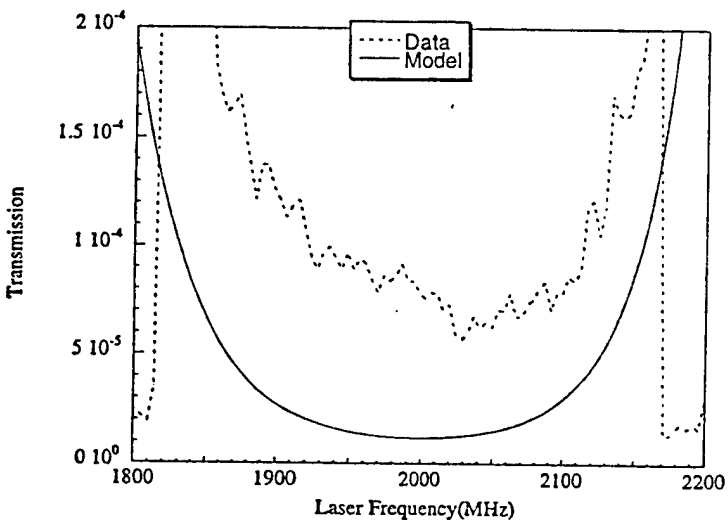

Fig. 9. Blow-Up of central portion of Fig. 8 illustrating absolute extinction near line center of transition "A".

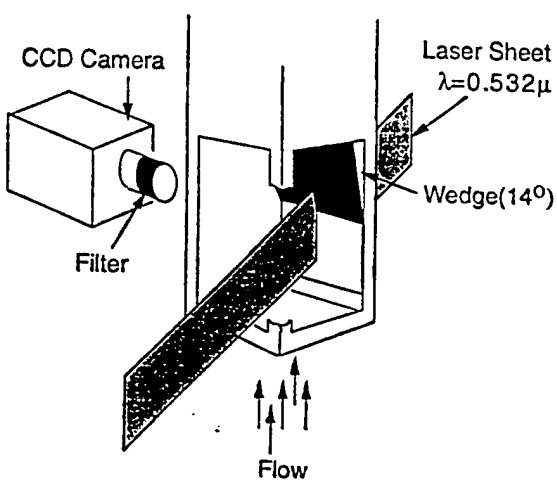

Fig. 10. Schematic diagram illustrating imaging geometry employed for MHz rate visualization of Mach 2.5 flow over 14° wedge.

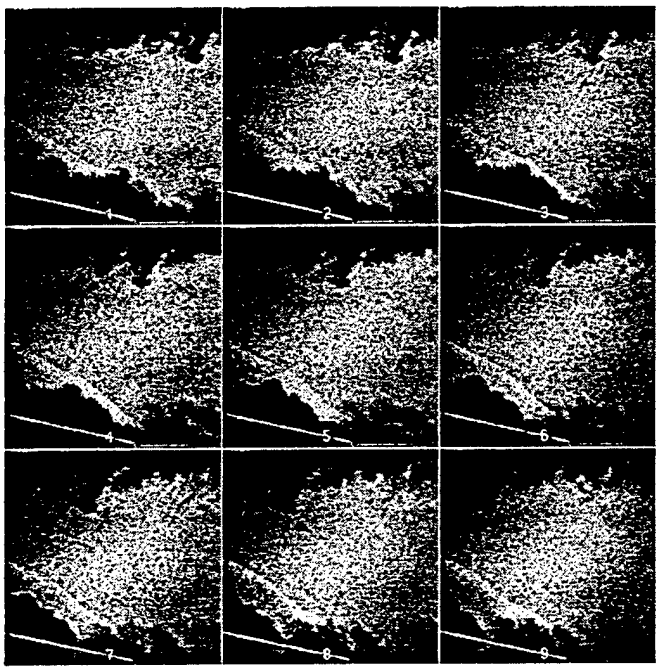

Figure 11
Sequence of 9 streamwise view images of Mach 2.5 flow over
14° wedge. Flow is from right to left. 2 microseconds between images.

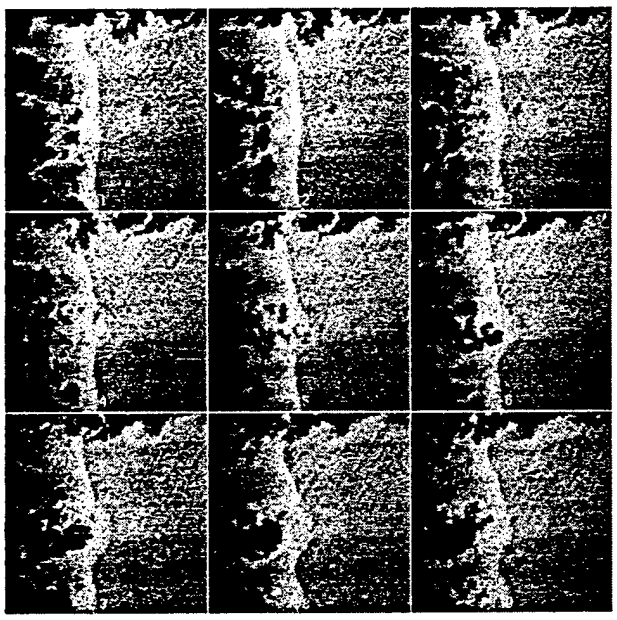

Figure 12
Sequence of 9 parallel view images of Mach 2.5 flow over
14° wedge. Flow is from right to left. 2 microseconds between images.

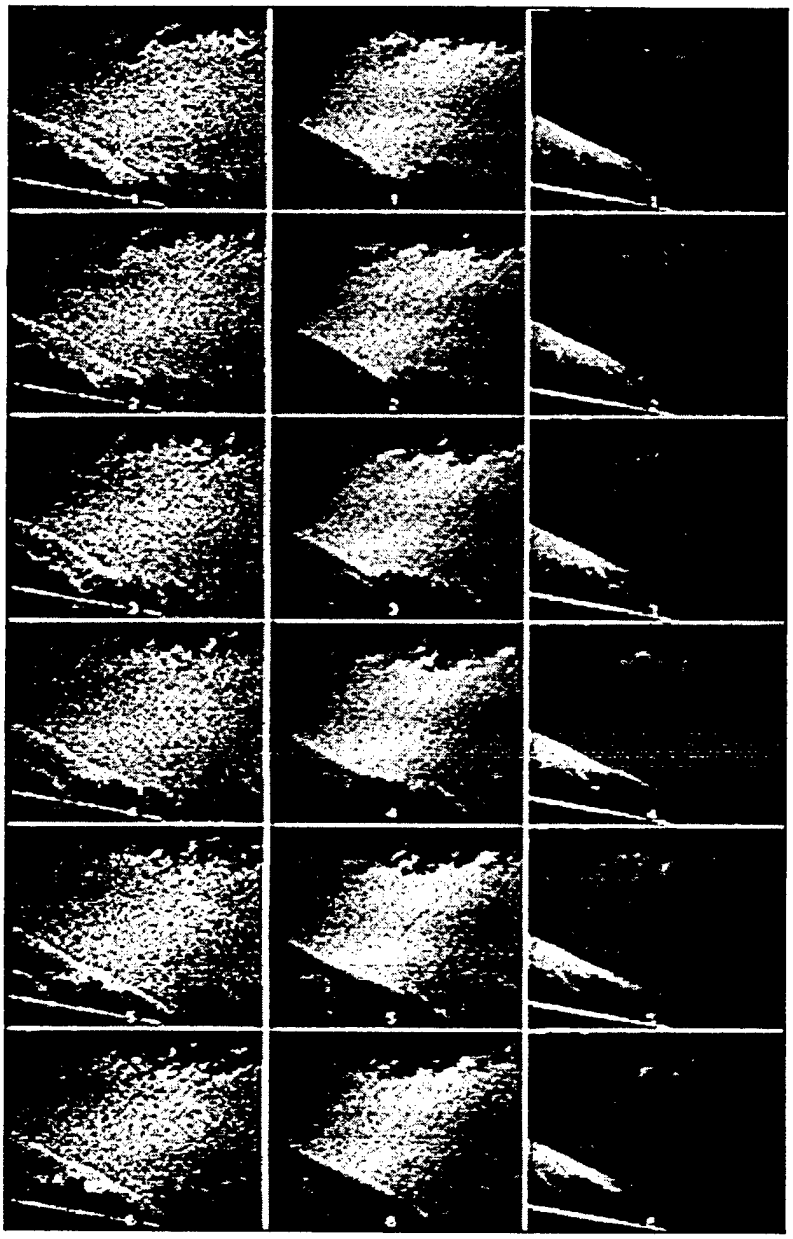

Figure 13
Comparison of filtered and unfiltered streamwise view images.
Flow from right to left. 2 μs interval between images.
left column: unfiltered images.
middle column: filtered to highlight high speed flow.
right column: filtered to highlight low speed flow.

AIAA 97-2520

IMAGING FLUID PHENOMENA WITH ATOMIC AND MOLECULAR VAPOR FILTERS

W.R. Lempert, P. Wu, N. Finkelstein,
P. Erbland, and R.B. Miles

PRINCETON UNIVERSITY
Dept. of Mechanical & Aerospace Engineering
Princeton, New Jersey 08544 U.S.A.

32nd Thermophysics Conference
June 23 - 25, 1997 / Atlanta, GA

For permission to copy or republish, contact the American Institute of Aeronautics and Astronautics
1801 Alexander Bell Drive, Suite 500, Reston, VA 22091

"IMAGING FLUID PHENOMENA WITH ATOMIC AND MOLECULAR VAPOR FILTERS"

W.R. Lempert,* P. Wu,† N. Finkelstein,†
P. Erbland,† and R.B. Miles§

Department of Mechanical and Aerospace Engineering
PRINCETON UNIVERSITY
Princeton, New Jersey 08544 U.S.A.
609/258-2875

ABSTRACT

We present new applications and enhancements to the spectrally Filtered Rayleigh Scattering (FRS) imaging diagnostic. Measurements have been performed in the turbulent boundary layer produced by a zero pressure gradient flat plat at Mach 8 which elucidate the effect of helium injection on large-scale turbulent structure. The technique has also been extended into the ultraviolet regime by pairing the third harmonic output of a new narrow bandwidth Titanium:Sapphire laser with atomic mercury vapor filters. Filters have been demonstrated which work in both absorption and transmission mode. Two different types of narrow band transmission filters have been fabricated and characterized, one based on resonant refluorescence, and the other based on resonance enhanced dispersion. A new "pulse-burst" laser, capable of outputting high power, narrow spectral bandwidth pulses at MHz rates has been paired with a framing CCD camera to obtain high-speed filtered scattering movies of turbulent Mach 2.5 flow over a 14° wedge. The images illustrate the correlation of unsteady oblique shock motion with large-scale boundary layer structure.

*Senior Research Scientist, Mechanical & Aerospace Engineering, Member AIAA.

†Graduate Student, Mechanical & Aerospace Engineering.

§Professor, Mechanical & Aerospace Engineering, Associate Fellow, AIAA.

Copyright © 1997 by Princeton University. Published by the American Institute of Aeronautics and Astronautics, Inc. with permission.

1. INTRODUCTION

In recent years, Rayleigh scattering has emerged as a powerful tool for measurement of two- and three-dimensional density fields in a wide variety of flow and combustion environments.[1-3] From a diagnostic perspective, Rayleigh scattering exhibits both advantages and disadvantages in comparison to other planar imaging techniques, such as Laser-Induced Fluorescence.[4,5] The principal advantages are that the flows to be probed do not need to be seeded (since all flows exhibit Rayleigh scattering), and that for flows of known composition, such as air flows, the scattered intensity is directly proportional to density, a fact which greatly simplifies the extraction of quantitative data. The principal disadvantages are that the collected signal is often quite low, and the scattering frequency is approximately the same as that of the laser source. Background scattering, therefore, can pose a serious interference, in some instances completely overwhelming the desired Rayleigh signal.

In order to overcome this difficulty, as well as to enable measurement of temperature and velocity fields, a number of spectrally Filtered Rayleigh Scattering (FRS) approaches have recently been presented.[6-16] These techniques share the common feature that a narrow linewidth (order MHz) laser is paired with a suitable atomic or molecular resonance filter (or in some cases, an etalon) which is used as a high resolution spectral discriminator. The basic concept is illustrated in Fig. 1. When narrow spectral bandwidth radiation is incident on a sample volume, the detected signal consists of the sum of elastic scattering from stray window and/or wall surfaces and the Doppler-shifted and/or broadened quasi-elastic Rayleigh scattering. If the excitation laser is tuned to the resonance frequency of an atomic or molecular vapor, and, if a cell filled with this vapor is placed between the sample volume and the detector, then the elastic scattering will be highly attenuated while the quasi-elastic scattering will be, at least partially, transmitted. By suitable manipulation of the filter

profile and laser excitation frequency a variety of aims can be realized. The simplest case is to provide enhanced visualization of high-speed flows by employing a highly optically thick filter and positioning the laser near the edge of the cut-off. This is particularly useful at high Mach number, where the static density, and, therefore, the scattering intensity, is generally quite low. Alternatively, velocity and/or temperature can be determined by quantitatively measuring the fractional transmission. The technique has been applied to a wide variety of environments including supersonic jets[7,8] and inlet models,[9] mixing layers,[10] large-scale wind tunnels,[11] flow around automobiles,[12] and sooting flames.[13] Similar approaches have also been reported in the remote sensing community,[14,15] and have been proposed for supersonic inlet mass flux measurement.[16] A recent review has been given by Miles and Lempert.[17]

This paper will focus on recent application of the FRS technique to hypersonic flow using the new Princeton University Mach 8 boundary layer facility and on three recent enhancements of the basic approach currently under development in our laboratory. The first enhancement is the extension of the technique into the ultraviolet region of the spectrum, in order to take advantage of the well-known frequency to the fourth scaling of the Rayleigh scattering cross-section, as well at the more ideal characteristics of atomic mercury vapor. The second is the development of narrow bandwidth transmission filters, which act as compliments to the more traditional absorption filters. Finally, in order to capture the dynamics of high speed, unsteady phenomena, we pair a novel "pulse-burst" laser system with a new framing CCD camera which features integrated on-chip storage. This new system provides the capability to obtain planar images at rates as high as one MHz.

2. MEASUREMENTS IN HYPERSONIC FLOW

We have recently initiated a program to explore the structure of turbulent hypersonic boundary layers using FRS. The measurements have been performed in the new Princeton University Mach 8 wind tunnel located in the Gas Dynamics Laboratory of the Forrestal campus. The facility, which has been described in detail elsewhere,[18] is a blow-down type which operates with a stagnation temperature of 800 K, and a stagnation pressure of between 250 and 1200 psi, depending upon desired Reynolds number. FRS measurements have been performed on a zero-pressure gradient, cold wall, flat plate boundary layer, using the second harmonic of Nd:YAG at 0.532 microns (green light) in combination with a molecular iodine filter. The measurements were performed with the specific goal of elucidating the effect of helium injection on large-scale turbulent structure in the boundary layer. The upper images in Fig. 2, taken from Reference 19, show typical unfiltered instantaneous images obtained with a laser sheet incident 0.50 inches above and parallel to the floor of a 18.75 inch (axial) x 6 inch (span) flat plate. The field-of-view is approximately 4 x 4 inches, centered near the trailing edge of the plate. In these images, approximately 0.1% CO_2 has been seeded into the plenum, which condenses upon expansion to form order 100 nm clusters which exhibit greatly enhanced scattering. The clusters sublime in the warmer, thermal boundary layer, resulting in high image contrast between the free stream and boundary layer fluid. In the upper left/right images, ~100 mgms/sec (out of a total mass flow rate of 1-2 kgms/sec) of nitrogen/helium, respectively, have been injected into the boundary layer through a one-inch long by 1 mm wide slot, oriented transverse to the flow axis, three inches downstream from the leading edge. While it is difficult to see, due to the severe stray scattering which degrades the images, the boundary layer with helium injection is qualitatively different from that with nitrogen injection. The difference is much more apparent in the lower images of Fig. 2, which correspond to filtered images taken at the same location in the boundary layer. These images were taken with a factor of two magnification in order to zoom in on the details of the turbulent structure. Note, in particular, the almost laminar nature of the boundary layer in the lower right (helium) image, as contrasted to the enormous wealth of structure in the corresponding image with nitrogen injection.

3. ULTRAVIOLET FILTERED SCATTERING

With the exception of reference 14, which utilized a single frequency dye laser at 0.589 microns in combination with an atomic sodium cell, all filtered scattering work previously reported has employed molecular iodine in combination with the second harmonic output of Nd:YAG at 0.532 microns or the 0.5145 micron output of an argon-ion laser. The proliferation of diagnostic filtered scattering approaches based on molecular iodine has been driven, primarily, by the convenience and reliability of the laser sources, which need to be high power, somewhat tunable, (over order GHz) and well controlled in frequency. For example, for typical scattering geometries the Doppler shift of air is of order 1 MHz/m/sec in the visible region of the spectrum. Even relatively small uncertainty in mean laser frequency will propagate, therefore, into significant uncertainty in flow velocity. As discussed in more detail by Finkelstein,[20] however, there are significant advantages to be obtained from shifting the measurement into the ultraviolet region of the spectrum. The most obvious advantage is that the Rayleigh scattering cross-section increases as the fourth power of the laser frequency, whereas background scattering from metal surfaces is typically reduced at shorter wavelength. This can result in a simultaneous increase in both

absolute signal and image contrast. A second, somewhat less obvious advantage, is that it is possible to exploit the exceedingly high extinction afforded by atomic mercury vapor. Figure 3, taken from reference 20, shows the experimental absorption profile of a 5 cm long cell with a mercury pressure of 1.50 mtorr, along with a modeling prediction. The six individual features are due to the naturally occurring isotopes, which are labeled on the figure. The line center attenuation is of order 10.[25]

In order to exploit the inherently high extinction of atomic mercury vapor, it is necessary to have a suitable ultraviolet laser source. In collaboration with Schwartz Electro-Optics--Research Division, we have recently reported a "ramp and lock" cavity stabilization scheme for single frequency, injection-seeded Ti:Sapphire.[21] To date, this approach has been used to obtain order 300 mJ/pulse output from the fundamental of Ti:Sapphire at 0.761 microns with a pulse duration of 7-10 nsec and a time-averaged spectral linewidth which is near the Fourier transform limit (order 50 MHz). Conversion to third harmonic at 0.2537 microns, which coincides with a strong absorption of atomic mercury, is approximately 14%. Figure 4 shows a set of instantaneous scattering images obtained from a Mach 2 free jet, which has also been seeded with a small amount of carbon dioxide to enhance the scattering. In Fig. 4a, the laser is tuned such that both the laser and the Doppler-shifted flow scattering fall outside the filter band, so that both are imaged onto the detector. In Fig. 4b, the elastic scatter from the laser is absorbed by the filter while the shifted scatter from the flow is transmitted. In Fig. 4c, the laser is tuned such that the flow scattering is shifted into the filter absorption band while the elastic scatter is outside.

4. TRANSMISSION FILTERS

In many instances it is desirable to have a filter which transmits in a narrow spectral band, and rejects at all over wavelengths. We have been exploring two concepts for achieving such a filter, both employing atomic mercury vapor at 0.2537 microns. The first concept, illustrated in Fig. 5, is based on resonant refluorescence.[22] If the optical density can be made high enough, than scattering which is resonant with the absorption can be imaged onto a thin plane near the front surface of the vapor cell. The absorbed light will subsequently be re-radiated out the front surface and can be re-imaged onto a CCD detector. All light incident on the cell but out of resonance with the vapor will simply pass through the cell and be rejected. Figure 6 (upper trace) shows a measured refluorescence spectrum for a 5 cm path length cell with a mercury pressure of 2.3 mTorr. (There is no buffer gas so the mercury partial pressure is equal to the total pressure). As can be seen from the lower trace, the refluorescence spectrum is essentially the inverse of the absorption spectrum. Note that under these cell conditions, the 1/e extinction length is estimated to be 50 microns. Figure 7 shows a preliminary pure rotational Raman spectrum of room air obtained using the refluorescence transmission filter. In this case, light scattering from a 1 cm length of ambient air was 1:1 imaged (with an f/1 lens) through a vertical slit onto the inside surface of the mercury vapor filter. The Ti:Sapphire laser described above was tuned such that a series of pure rotational Raman transitions from nitrogen and oxygen were sequentially brought into resonance with the mercury absorption. The resonant refluorescence was re-imaged (again f/1) off-axis, through a mercury line interference filter, and onto a S-20 photomultiplier tube. The laser power employed was approximately 10 mJ/pulse and the signal was averaged for 100 shots with a laboratory boxcar integrator.

We have begun an investigation of the spatial resolution of the refluorescence cell. The key parameter is the optical penetration depth which defines the "sharpness" of the image plane formed inside the cell. This is influenced by a variety of factors including the cell vapor pressure, the spectral linewidth of the scattering, and the de-tuning of the scattering from line center of the absorption resonance. Figure 8 shows a schematic of a measurement which was performed to investigate this. The Ti:Sapphire laser was used to illuminate a target with ruled lines varying from 5 lp/mm to 200 lp/mm. The target scattering was imaged (f/8 with 1:2 magnification) onto the inside surface of the mercury vapor cell at 175 mTorr pressure. A sequence of mercury refluorescence images were captured on a microchannel plate intensified CCD video camera as the laser was spectrally tuned through the absorption profile of the mercury cell. The transmitted signal was simultaneously recorded with a photomultiplier tube, and served as a frequency reference. The results are illustrated in Fig. 9 for 2.5, 5.0, 7.5, and 10 lp/mm targets. The lower set of images in Fig. 9 were obtained by replacing the cell with a paper target and yield a baseline resolution of approximately 7.5 lp/mm, defined as a minimum modulation depth of 0.5. This represents the limit of the imaging system and is presumably determined by the microchannel plate intensifier. The upper images in Fig. 9 were obtained using the cell with the laser tuned to the center of the mercury resonance. It can be seen that the overall resolution is essentially unchanged. This can be seen most clearly by comparing the plotted gray scale traces below the images, which were obtained by taking horizontal cuts through the data and digitizing with a laboratory frame-grabber. From these measurements we conclude that, for on-line center scattering where the optical thickness is maximum, the refluorescence cell spatial resolution is greater than 7.5 lp/mm. Additional measurements to quantify other effects, such as spectral de-tuning, and optical diffusion, are in progress.

5. DISPERSION FILTER

The collection efficiency of the refluorescence filter is limited (to order percent) by the dual collection process inherent to its design. For limited light applications, such as Raman imaging, an alternative concept based on resonance enhanced dispersion, is currently being explored. The cell is based on the well known expression for the real part of the index-or-refraction given by:

$$n'-1 = \frac{e^2}{2M_e} Nf \frac{1}{\varepsilon_0} \left(\frac{\left(\omega^2 - \omega_0{}^2\right)}{\left(\omega^2 - \omega_0{}^2\right)^2 + \gamma^2\omega^2} \right) \quad (1)$$

where: e = electron charge
ε_0 = electric permativity
M_e = mass electrons
γ = linewidth
N = number density
ω = radial frequency
f = oscillator strength
ω_0 = resonant frequency

Figure 10 is a schematic diagram of a dispersion filter which has recently be fabricated in our laboratory. It consists of a pair of concentric all quartz cells, the outer of which is surrounded by a large aluminum sheath. The inner cell is a vapor prism which consists of a main body with 2" diameter clear aperture Brewster angle windows, and a side-arm cold tip containing 5 gms of mercury. The main body of the inner cell is jacketed with a copper heat conductor which is used to control the temperature and prevent condensation on the Brewster windows. The combination of inner and outer cell allows heating of the inner Brewster windows, while simultaneously avoiding thermal room currents which would induce additional refraction. Separate heaters and temperature controllers are used to insure that the inner cell body is held at a constant temperature which is slightly warmer than the sidearm cold tip (which controls the vapor pressure). Operating conditions for these experiments were roughly 190 C for the inner cell body temperature, and 170 C for the side-arm. This corresponds to a mercury vapor pressure of 6.3 torr and a thermally-broadened absorption linewidth of 1.18 GHz. It is significant to point out that the line center attenuation for this cell is predicted to be in excess of 10^4/cm, due to the exceedingly high value of the imaginary (or absorptive) part of the index-of-refraction. The cell, therefore, simultaneously achieves high suppression on line center and high dispersion off line center. This can be important for imaging applications in the presence of significant elastic scattering.

In order to provide an experimental verification of the predicted dispersion, the measurement shown schematically in Fig. 11 has been performed. A target was illuminated with the third harmonic output of the Ti:Sapphire laser and the scattering spatially filtered through a slit and then collimated with an f/10 lens. The refracted beam was re-imaged onto the microchannel plate intensified video camera. As the laser was tuned in wavelength, a camera recorded the displaced image of the slit as a function of de-tuning from line center of the mercury vapor resonance. The results are illustrated in Fig 12, along with the prediction from Eq. (1). The agreement is to within the combined uncertainty in the imaging system calibration and the cell pressure.

6. HIGH-SPEED IMAGING

The ability to image the dynamics of high-speed phenomena is severely constrained by existing laser technology. In order to circumvent this, we have embarked on a program to develop a "pulse-burst" laser, which, when paired with a new CCD framing camera, has been used to capture scattering images of turbulent flows at a rate of up to 1 MHz.[23,25] The laser system, illustrated schematically in Fig. 13, consists of the following six elements:

1. Monolithic, single-frequency, cw Nd:YAG laser.
2. Four-pass preamplifier # 1.
3. Pulse slicer.
4. Two-pass preamplifier # 2.
5. Three-stage power amplifier chain.
6. Second harmonic crystal.

The single-frequency Nd:YAG laser is a Lightwave Electronics model 120-03 with a cw power of approximately 20 mWatts. The output of this laser is pre-amplified and "sliced" into a train of pulses using a pulse slicer custom built by Medox, Inc., Ann Arbor, Michigan. The pulse slicer consists of a pair of fast electro-optic Pockel cells, and is capable of creating a train of between 1 and 99 pulses, with minimum individual pulse duration of 10 nsec, and minimum inter-pulse period of 1 microsecond. The train is further amplified, with an overall system gain of 2 x 10^7. The corresponding energy is ~10 mJ for a single, 20 nsec duration pulse. The second harmonic conversion is approximately 10%.

As discussed in some detail in Reference 24, the spectral linewidth of the individual pulses in the burst is approximately Fourier transform-limited (order 50 MHz), so that the system is well matched to a molecular iodine filter. As a demonstration, time sequences of planar images have been obtained of turbulent Mach 2.5 flow over a 14° wedge. The second harmonic output of the pulse-burst laser was formed into a 2 cm high by 100 micron thick sheet, which was incident to a laboratory-scale wind tunnel at an angle of 45°. A 14° wedge was

attached to a wall of the tunnel at a location where the boundary layer thickness is approximately one-third the total span. Once again, in order to enhance the scattering signal, gaseous carbon dioxide was seeded into the plenum. The scattering was captured at 90° to the sheet using a CCD framing camera developed by Princeton Scientific Instruments, Inc., Monmouth Junction, New Jersey.[23,25] The CCD camera has a 30-image storage buffer built into the image sensor chip itself, and can frame at rates up to 1 MHz.

Figure 14 shows three sets of images obtained using a 10 cm long molecular iodine filter, operated in a manner very similar to that described above for the Mach 8 measurements. Images obtained with a 2 microsecond interframe period. The images in the left column were obtained with the laser tuned far enough from resonance that the images are, effectively, unfiltered. Note that the scattering intensity immediately downstream of the characteristic oblique shock but above the boundary layer, is of the same magnitude as that of the free stream. The images in the center column were obtained with the laser tuned to preferentially transmit the high-speed, free stream flow. In this case, the scattering immediately downstream of the shock is attenuated due to the lower flow velocity. Finally, in the images on the right, the laser has been tuned to preferentially transmit the lower velocity fluid, downstream of the shock.

7. CONCLUSIONS

Spectrally Filtered Rayleigh Scattering (FRS) is a powerful diagnostic technique which has been applied in a variety of disciplines, including supersonic flow, combustion, and remote sensing. We have presented recent measurements obtained from the turbulent boundary layer produced on a zero pressure gradient flat plate at Mach 8. The effect of helium injection on large-scale structure was clearly evident in the filtered images. The FRS technique has also been extended into the ultraviolet regime by combining an atomic mercury vapor filter with a new, cavity-locked Titanium:Sapphire laser, which produces order of 300 mJ/pulse output in the near IR with near Fourier transform-limited spectral linewidth. Narrow bandwidth, mercury vapor notch, transmission filters have also been demonstrated, using both refluorescence and resonance enhanced dispersion. For measurement of high-speed, unsteady flow phenomena, a "pulse-burst" laser has been developed, which, when paired with a molecular iodine filter and a framing CCD camera provides the capability to capture FRS images at rates as high as one MHz.

8. ACKNOWLEDGMENTS

The authors acknowledge Mr. Mike Souza for his expertise in fabricating the vapor cells; Andy Finch, Glenn Rines, and Richard Schwarz of Schwartz Electro-Optics, for the development of the Titanium:Sapphire laser system; John Lowrance and Vince Mastrocola of Princeton Scientific Instruments, for providing the framing CCD camera; and Marcel Bouvier, of Medox Electro-Optics, for design of the high-speed pulse slicer. We also acknowledge Alexander Smits, Mike Etz, Mark Huntley, and Tom Magruder of the Princeton University Gas Dynamics Laboratory for their collaboration in performing the Mach 8 measurements; Jay Grinstead for assistance in many of the imaging measurements; and Phil Howard and Bob Bogart for providing expert technical support. The work has been supported by grants from the Air Force Office of Scientific Research, Julian Tishkoff (University Research Initiative) and Leonidas Sakell (External Aerodynamics), technical monitors; and a Small Business Innovative Research grant to Schwartz Electro-Optics from NASA Ames Research Center, John Cavolowsky, technical monitor. The CCD framing camera has been developed under Small Business Innovative Research grants from the U.S. Office of Naval Research, Edwin Rood, technical monitor, and the U.S. Air Force, Wright Laboratory, Charles Tyler, technical monitor.

REFERENCES

1. M.C. Escoda, M.B. Long: AIAA J. 21, 81 (1983).

2. J.A. Lock, R.G. Seasholtz, and W.T. John, "Rayleigh-Brillouin Scattering to Determine One-Dimensional Temperature and Number Density Profiles of a Gas Flow Field," Applied Optics 31, pp. 2839-2848, 1992.

3. M. Smith, A. Smits, and R. Miles, "Compressible Boundary Layer Density Cross Sections by UV Rayleigh Scattering," Optics Letters 14, 1989.

4. R.K. Hanson, "Planar Laser-Induced Fluorescence Imaging," J. Quant. Spectrosc. Radiat. Transfer 40, pp. 343-362, 1988.

5. J. Grinstead, T. Quagliaroli, G. Laufer, and M.C. McDaniel, Jr., "Single-Pulse Temperature Measurements in a Turbulent Flame Using KrF Laser-Induced O_2 Fluorescence," AIAA Journal 34, pp. 624-626, 1996.

6. R. Miles and W. Lempert, "Two-Dimensional Measurement of Density, Velocity, and Temperature of Turbulent Air Flows from UV Rayleigh Scattering," Applied Physics B B51, p. 1, July 1990.

7. J.N. Forkey, W.R. Lempert, and R.B. Miles, "Accuracy Limits for Planar Measurements of Flow Field Velocity, Temperature, and Pressure Using Filtered Rayleigh Scattering," Experiments in Fluids (Manuscript Accepted March 1997).

8. M.W. Smith and G.B. Northam, "Application of Absorption Filter-Planar Doppler Velocimetry to Sonic and Supersonic Jets," AIAA Paper #95-0299, January 1995.

9. J.N. Forkey, W.R. Lempert, S.M. Bogdonoff, R.B. Miles, and G. Russell, "Volumetric Imaging of Supersonic Boundary Layers Using Filtered Rayleigh Scattering Background Suppression," Paper #AIAA-94-0491, AIAA 32nd Aerospace Sciences Mtg. & Exhibit, Jan. 10-13, 1994, Reno, NV.

10. G.S. Elliott, M. Samimy, and S.A. Arnette, "A Molecular Filter-Based Velocimetry Technique for High-Speed Flows," Experiments in Fluids 18, pp. 107-118 (1994).

11. J. Meyers, "Evolution of Doppler Global Velocimetry Data Processing," Eighth International Symposium on Applications of Laser Techniques to Fluid Mechanics," Vol. 1, Lisbon, Portugal, July 8-11, 1996.

12. I. Röehle and R. Schodl, "Doppler Velocimetry in the Flow of a Swirler," Eighth International Symposium on Applications of Laser Technique to Fluid Mechanics, Vol. 1, Lisbon, Portugal, July 8-11, 1996.

13. D. Hoffman, K.-U Münch, and A. Leipertz, "Two-Dimensional Temperature Determination in Sooting Flames by Filtered Rayleigh Scattering," Optics Letters 21, p. 525 (1996).

14. C.Y. She, H. Latifi, J.R. Yu, R.J. Alvarez, R.E. Bills, and C.S. Gardner, "Two-frequency lidar technique for mesospheric Na temperature measurements," Geophys. Res. Lett. 17, p. 929 (1990).

15. P. Piironen and E.W. Eloranta, "Demonstration of A High Spectral Resolution LIDAR Based on an Iodine Absorption Filter," Optics Letters 19, p. 234 (1994).

16. J.A. Shirley and M. Winter, "Air Mass Flux Measurement System Using Doppler-Shifted Filtered Rayleigh Scattering," AIAA Paper 93-0513, Jan. 1993.

17. R.B. Miles and W.R. Lempert, "Quantitative Flow Visualization in Unseeded Flows," Annu. Rev. Fluid Mechanics 29, pp. 285-326, 1997.

18. M.L. Baumgartner, "Turbulence Structure in a Hypersonic Boundary Layer," Report #2077T, Ph.D. Thesis, Princeton University, Department of Mechanical & Aerospace Engineering, June 1997.

19. M. Etz, P. Erbland, M. Huntley, T. Magruder, A.J. Smits, "Turbulent Boundary Layer Control at Mach 8 Using Helium Injection," (Manuscript in Preparation, 6/97).

20. N.D. Finkelstein, W.R. Lempert, R.B. Miles, A. Finch, and G.A. Rines, "Cavity-Locked, Injection-Seeded, Titanium:Sapphire Laser and Application to Ultraviolet Flow Diagnostics," Paper #AIAA-96-0177, AIAA 34th Aerospace Sciences Meeting & Exhibit, Jan. 15-18, 1996, Reno, NV.

21. N.D. Finkelstein, W.R. Lempert, and R.B. Miles, "Narrow Linewdith Passband Filter for Ultraviolet Rotational Raman Imaging," Optics Ltrs. 22, p. 537, April 15, 1997.

22. N.D. Finkelstein, W.R. Lempert, and R.B. Miles, "Mercury Vapor Filter Technology and Ultraviolet Laser Source for Flow Field Imaging," Paper #AIAA-97-0157, AIAA 35th Aerospace Sciences Meeting & Exhibit, Jan. 6-10, 1997, Reno, NV.

23. W.R. Lempert, P.F. Wu, B. Zhang, R.B. Miles, J.L. Lowrance, V. Mastrocola, and W.F. Kosonocky, "Pulse-Burst Laser System for High-Speed Flow Diagnostics," Paper #AIAA-96-0179, AIAA 34th Aerospace Sciences Mtg., Jan.. 15-18, 1996, Reno, NV.

24. W.R. Lempert, P-F. Wu, and R.B. Miles, "Filtered Rayleigh Scattering Measurements Using a MHz Rate Pulse-Burst Laser System," Paper #AIAA-97-0500, AIAA 35th Aerospace Sciences Meeting & Exhibit, Jan. 6-10, 1997, Reno, NV.

25. W.F. Kosonocky, G. Yang, R.K. Kabra, C. Ye, Z. Pektas, J.L. Lowrance, V. Mastricola, F.V. Shalleross, and V. Patel, "360 x 360 3-Phase Very High Frame Rate Burst Image Sensor: Design, Operation, and Performance," to be published in IEEE Transactions of Electron Devices, Special Issue on Solid State Image Sensors, Oct., 1997.

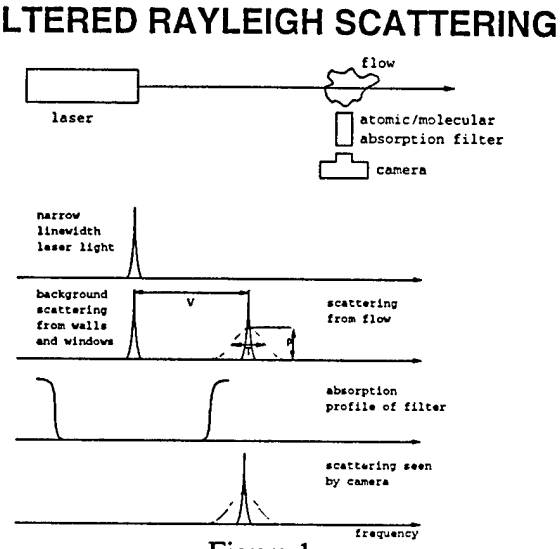

Figure 1
Basic Filtered Rayleigh Scattering Concept

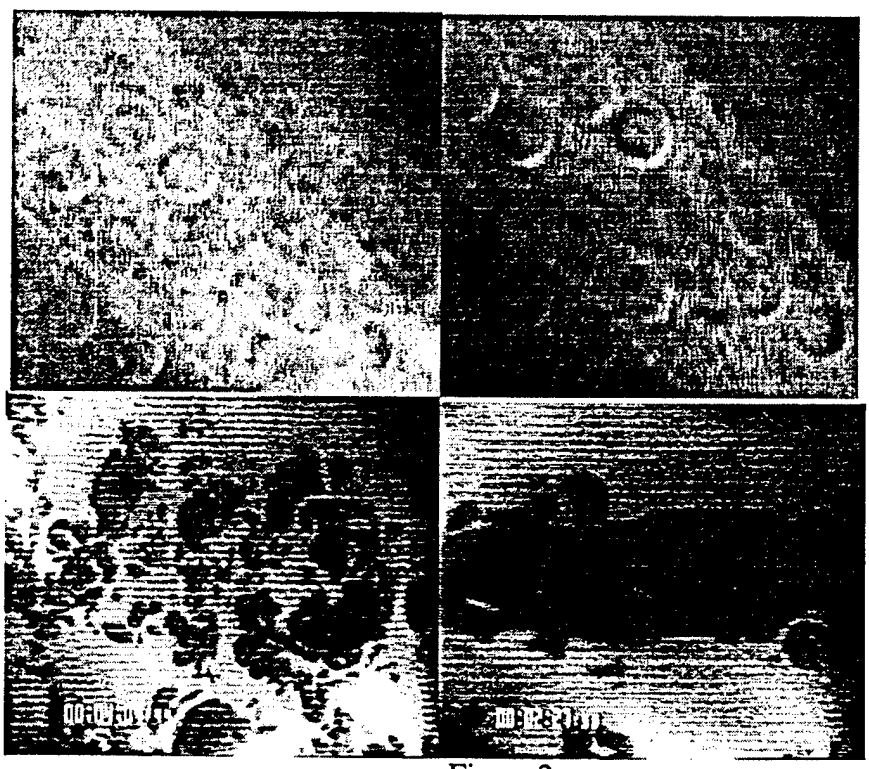

Figure 2
Collage of instantaneous boundary layer scattering images from flat plate at Mach 8.
Flow from left to right.
Upper Left: Nitrogen injection, no iodine filter.
Upper Right: Helium injection, no iodine filter.
Lower Left: Nitrogen injection with iodine filter.
Lower Right: Helium injection with iodine filter.

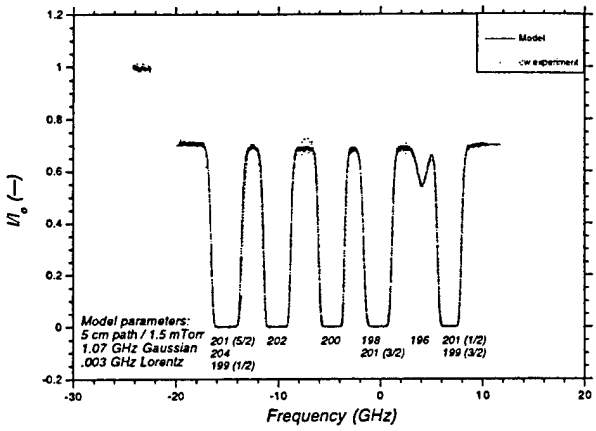

Figure 3. Mercury Cell Absorption Profile.

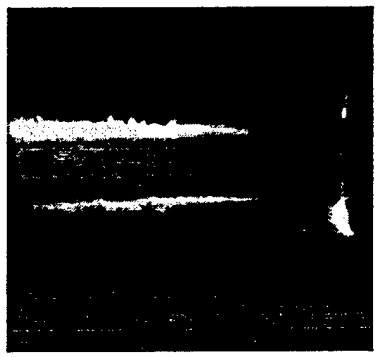

Figure 4a. UV Filtered Scattering Image Laser Tuned to transmit flow and background scattering.

Figure 4b. UV Filtered Scattering Image Laser Tuned to transmit flow only.

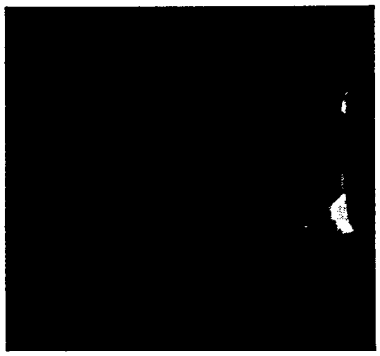

Figure 4c. UV Filtered Scattering Image Laser Tuned transmit only background.

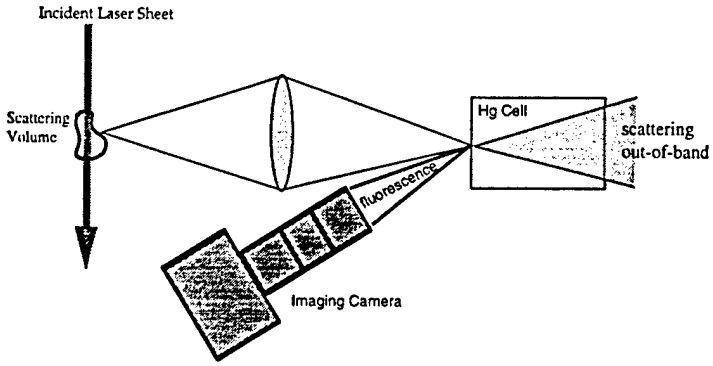

Figure 5. Refluorescence-based Narrow Band Transmission Filter.

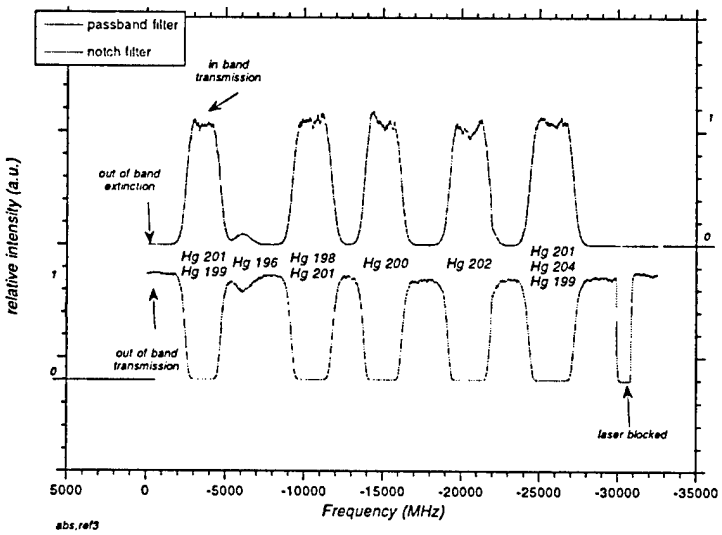

Figure 6. Transmission (upper) and Absorption (lower) profile of mercury vapor cells.

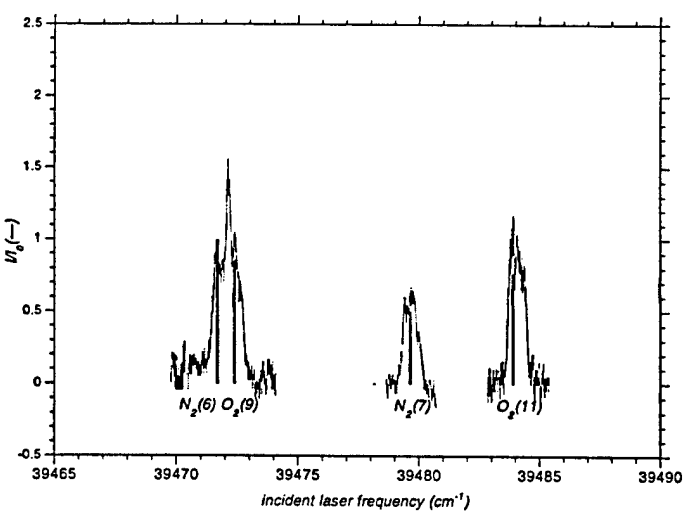

Figure 7. Rotational Raman Spectrum obtained using refluorescence transmission filter.

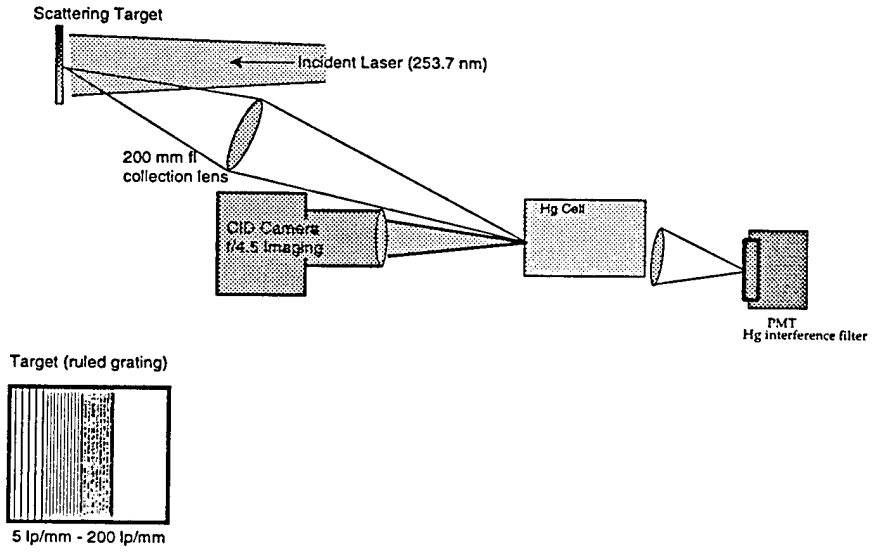

Figure 8
Schematic of Refluorescence Cell Spatial Resolution Measurement

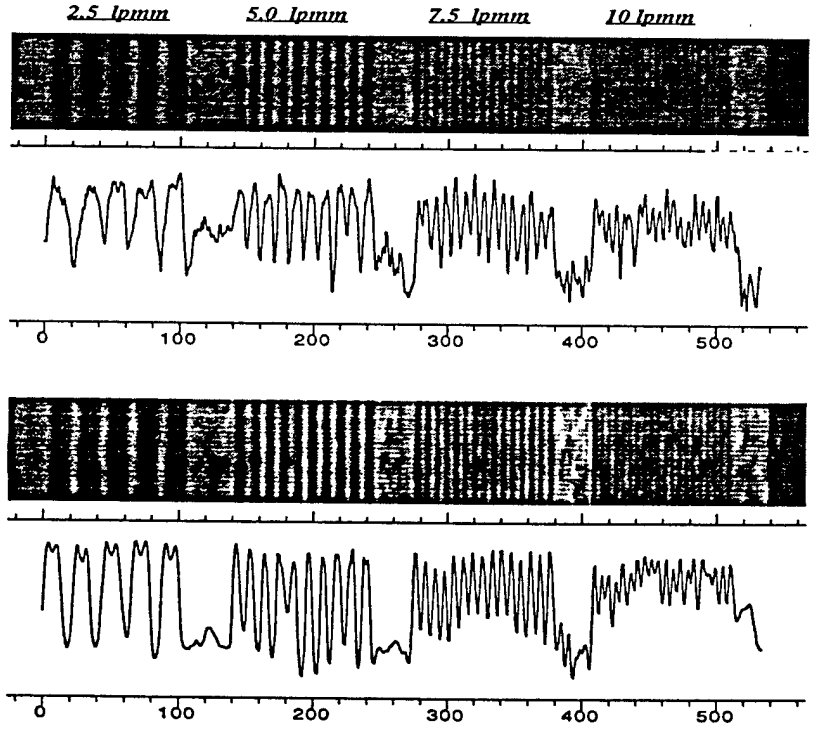

Figure 9
Refluorescence Cell Spatial Resolution Results
Upper Trace: Mercury Cell
Lower Trace: Target Baseline

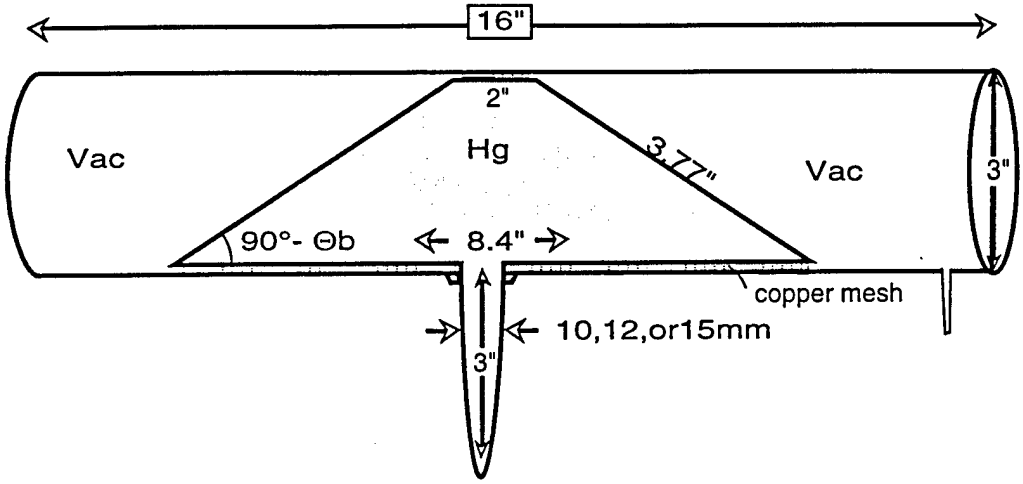

Figure 10
Mercury Vapor Dispersion Filter

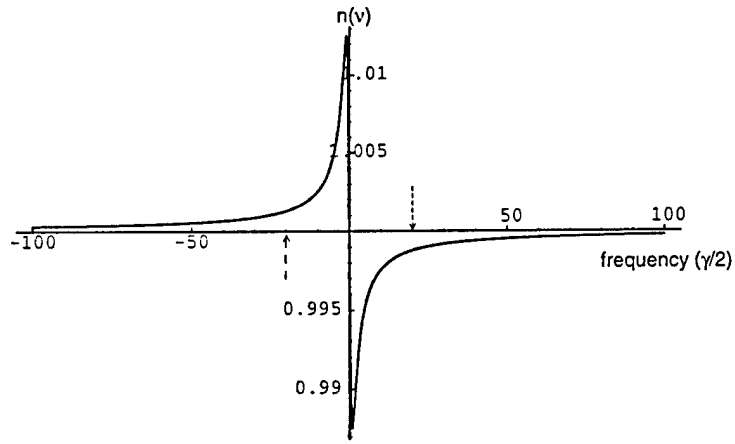

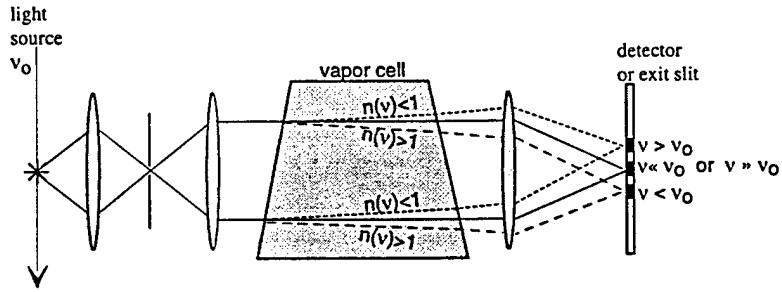

Figure 11
Dispersion Filter Basic Concept

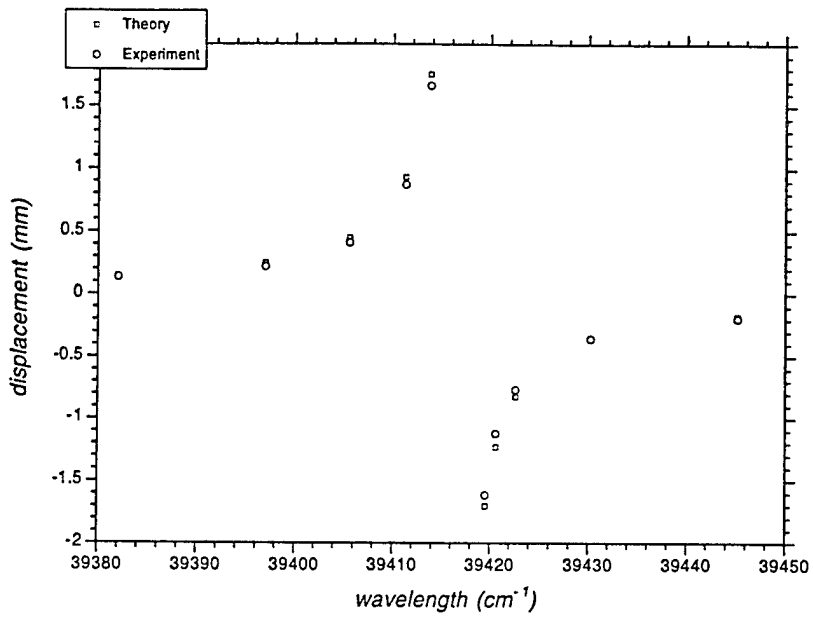

Figure 12
Experimental (circles) and predicted (squares) Linear Dispersion from Vapor Filter

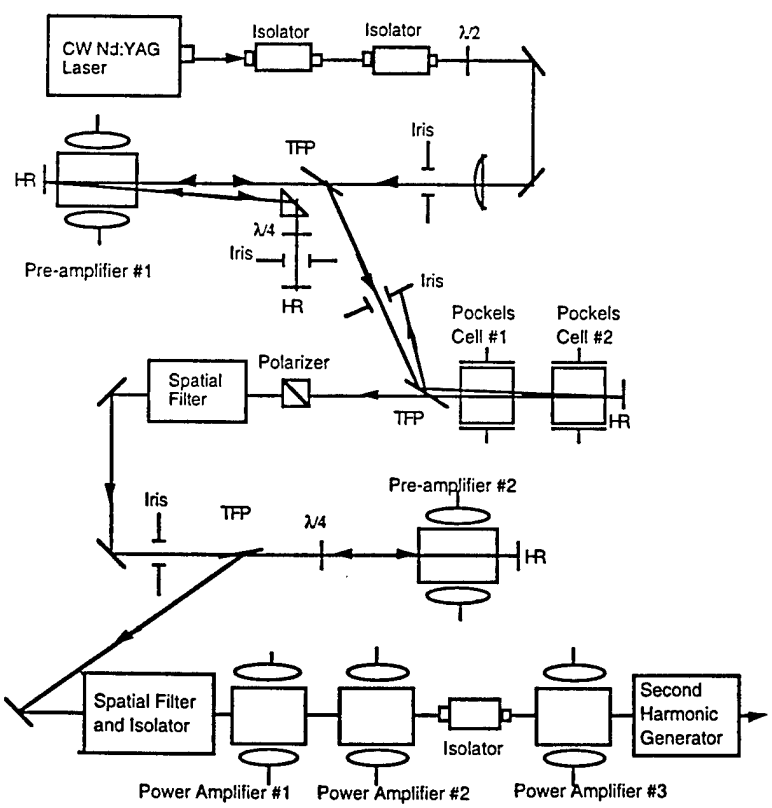

Figure 13
Pulse Burst Laser Schematic Diagram

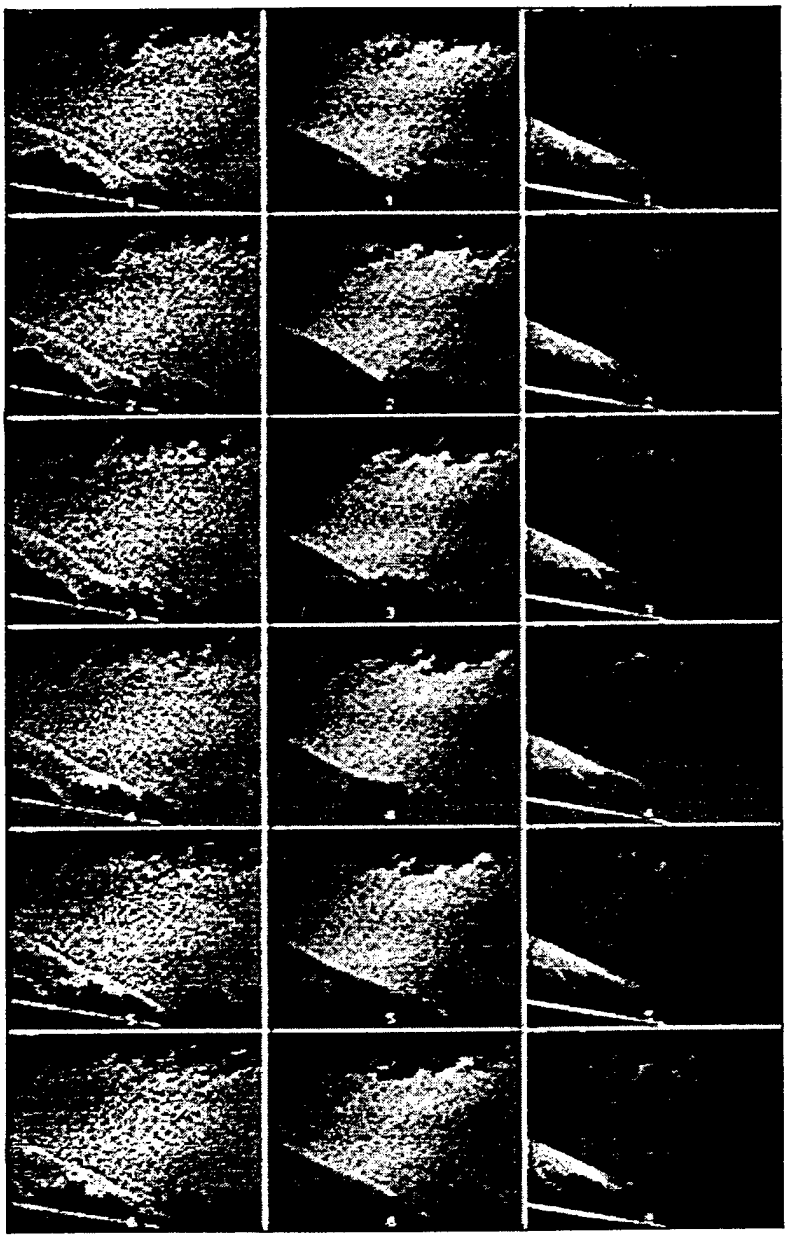

Figure 14
Comparison of filtered and unfiltered streamwise view images.
Flow from right to left. 2 μs interval between images.
left column: unfiltered images.
middle column: filtered to highlight high speed flow.
right column: filtered to highlight low speed flow.

AIAA 98-0311

UltraViolet Rotational Raman Spectroscopy with an Atomic Resonance Filter

A.P. Yalin, N.D. Finkelstein, W.R. Lempert, R.B. Miles

Department of Mechanical and Aerospace Engineering, Princeton University, Princeton, NJ 08544

36th Aerospace Sciences Meeting & Exhibit

January 12–15, 1998 / Reno, NV

For permission to copy or republish, contact the American Institute of Aeronautics and Astronautics
1801 Alexander Bell Drive, Suite 500, Reston, Virginia 20191-4344

UltraViolet Rotational Raman Spectroscopy with an Atomic Resonance Filter

A.P. Yalin, N.D. Finkelstein*, W.R. Lempert**, and R.B. Miles****
Department of Mechanical and Aerospace Engineering, Princeton University
Princeton, NJ 08544

Abstract

A new approach for pure rotational Raman imaging based on a dispersive filter paired with a tunable narrow line-width laser source has been developed. The dispersive filter simultaneously captures multiple rotational Raman lines while maintaining capabilities for 1-D spatially resolved measurements. A theoretical model for the filter has been developed and verified and preliminary 1-D images of rotational Raman scattering from CO_2 have been obtained.

Introduction

In recent years, significant developments in non-intrusive, optically based diagnostics of complex flow fields have been realized. A recent review highlights measurement techniques aimed at quantitative flow field measurements of temperature, density, and velocity[1]. The development of narrow line width, high power, tunable lasers and accompanying ultra-narrow band spectral filters enables advances in many of these non-intrusive flow diagnostic techniques based on molecular Rayleigh and Raman light scattering. We have previously presented simultaneous planar measurements of velocity, temperature, and density in a Mach 2 facility based on spectrally Filtered Rayleigh Scattering (FRS). Those measurements, which utilized the second harmonic of an Nd: YAG laser, in conjunction with a molecular iodine filter, resulted in uncertainties of a few percent.[2] Complimenting Rayleigh scattering, techniques based on Raman scattering measure species specific properties, including rotational and vibrational temperature, density, species mole fraction, and potentially, velocity.[3] We present here a new approach towards making Raman measurements. The ability to obtain species selective measurements makes Raman scattering particularly desirable for reactive flows. As with Rayleigh scattering, the Raman signal is linearly proportional to both scatterer number density and input laser intensity. Further, due to the instantaneous nature of the scattering, the signal is not affected by the collisional quenching processes which can complicate interpretation of LIF signals.[4] Also, Raman scattering compliments LIF in high pressure environments where one may have low fluorescent yields.

The limiting factor in most Raman measurements is the small scattering cross-section, which leads to weak signals. In general, Raman scattering is two to three orders of magnitude weaker than Rayleigh scattering. The vibrational and rotational Raman spectra are determined by the spacings of the corresponding energy levels of the scattering molecules. The rotational scattering cross-section is typically an order of magnitude larger than the vibrational. However, because the spacing of the rotational levels is very small (~1000 times less than the vibrational spacing), and because the manifold of rotational lines lies very near the much stronger Rayleigh line, most Raman measurements have focused on vibrational scattering. The general requirement for observing Raman scattering is a detector with high spectral resolution, as well as a light source with high energy in a narrow spectral band.

The goal of our work is to resolve individual rotational Raman lines so that temperature measurements may ultimately be made. The strengths of the different rotational lines depend on the Boltzmann fractions and are

* Graduate Student, Member AIAA
** Professor (Ohio State University), Member AIAA
*** Professor, Associate Fellow AIAA

Copyright © 1998 by A.P.Yalin *et al.* Published by the American Institute of Aeronautics and Astronautics, Inc. All rights reserved.

thus temperature dependent. In order to make measurements of rotational Raman scattering we have developed a high power, narrow line-width UV laser source, as well as a detection system with high spectral resolution and strong out of band rejection. The laser source, an injection-seeded, cavity-locked, frequency-tripled Ti:Sapphire laser, has been previously presented [5]. The development of a mercury vapor dispersion filter with high spectral discrimination forms the basis of the current work. A filter has been constructed and modeled, and its operation demonstrated. The mercury vapor filter acts as a prism or dispersive element - It spatially disperses small spectral shifts in the light passed through it. The most dramatic dispersion occurs at frequencies near the mercury resonance. The interrogation laser is tuned to a frequency near the resonance, and the scattered light is passed through the filter so that spectral variations in the scattered light become spatial variations on the detector. The second dimension on the detector remains for imaging in one dimension. As a demonstration of the capabilities of the dispersion filter we present images of pure rotational Raman scattering.

Filter Operation and Design

The mercury vapor dispersion filter is based on the resonance enhanced variation of the index of refraction (near the 253.7 nm transition). Essentially, the filter consists of a controlled amount of mercury vapor contained between two angled windows. The concept of operation is analogous to that of a prism and is illustrated, along with the variation in the real part of the index of refraction, in Fig.1. Light passing through the cell is variably refracted according to Snell's Law and the index. The strong dependence of the index of refraction near the mercury resonance causes significant spatial dispersion of small spectral shifts (as is typical of rotational Raman lines) yielding high spectral sensitivity. In our experiments light scattered from a 1-dimensional beam (a line) is imaged through the filter. The different spectral components of the scattered light have different indices of refraction in the filter, so that they are differently refracted at the two filter interfaces, and thus exit the filter at different angles. The light exiting the filter passes along the second lever arm and is refocused onto a detector. The deviation on the detector is proportional to the length of the lever arm. However, the magnification also increases with the lever arm length, so that changing the lever arm does not affect the ability to resolve individual lines. In one dimension spatial information is preserved allowing for 1-D imaging, while the signal in the second detector dimension is a measure of the spectral content of the scattered light. The most dramatic dispersive effects occur for light close to the resonance. Light of frequency slightly above the mercury transition frequency is refracted up, while light of slightly lower frequency is refracted down. Light on resonance is undeviated and absorbed. Light far off resonance is almost undeviated.

The frequency profile of the scattered light is given by the inelastically scattered Raman spectrum and the elastically scattered Rayleigh line, and the imaged light on the detector echoes this. The pattern of the Raman scattered light observed on the detector has a temperature dependence due to the Boltzmann fractions of the rotational energy levels. By comparing the signal strengths of the individual rotational lines a measurement of the rotational temperature is possible. An obstacle to such a measurement is the presence of the nearby and much stronger Rayleigh line. A salient feature of the filter is its strong attenuation of light at the transition line center (due to a peak in the imaginary index of refraction). By tuning the laser frequency near the resonant frequency, one may image the comparatively weak rotational lines in the presence of the dominant Rayleigh line and any other elastic scatter. Detuning from line center allows one to control the fraction of Rayleigh scattering observed.

A resonant dispersion prism filter has been fabricated in our laboratory, fig.2 [6]. It consists of a pair of concentric all quartz cells, the outer of which is surrounded by a large aluminum sheath. The inner cell consists of a main body with 2" diameter clear aperture Brewster angle windows, and a side arm cold tip containing 5 gms of mercury. The main body of the inner cell is jacketed with a copper heat conductor which is used to control the temperature and prevent condensation on the Brewster windows. The combination of inner and outer cells allows heating of the inner Brewster windows while simultaneously avoiding thermal room currents which would induce additional refraction. Separate heaters and temperature controllers are used to insure that the inner cell body is held at a constant temperature which is slightly warmer than the sidearm cold tip (which controls the vapor pressure). Operating conditions for these experiments were roughly 210C for the inner cell body temperature and 190C for the side arm. This corresponds to a mercury vapor pressure of 12 torr and a

thermally broadened absorption line width of 1.2 GHz. An analysis of the dispersive properties shows that at these condition one has a dispersion of ~30 microns/cm^{-1} (for a 1 m lever arm) in the spectral region of interest. The absorption coefficient for this cell is predicted to be in excess of 104/cm, due to the exceedingly high value of the imaginary (or absorptive) part of the index-of-refraction. The cell, therefore, simultaneously achieves high suppression on line center and high dispersion off line center.

Theoretical Analysis

A model for the operation of the dispersion filter and prediction of Raman signals has been developed. The dispersive behavior of the filter is due to the well known variation of the real part of the refractive index around a transition given by

$$n = 1 - \Sigma\, (e^2/2m_e)\, Nf/\varepsilon_0\, [(\omega^2-\omega_0^2)\,/\,((\omega^2-\omega_0^2)^2+\omega^2\gamma^2)] \qquad (1)$$

where:
- e is the electron charge
- m_e is the electron mass
- N is the number density
- f is the oscillator strength
- ε_0 is the electric permittivity
- γ is the line width
- ω is the radial frequency
- ω_0 is the resonant frequency

The sum reflects the contributions from the six mercury isotopes, whose relative abundances, strengths and locations are part of the code. The overall mercury number density is determined from the vapor pressure, which has a known variation with temperature. From eqn. (1) and applying Snell's Law at the two filter interfaces, it is possible to predict the angular deviation of light rays through the cell. Incorporating the lens geometry gives the spatial deviation on the detector. Thus, knowing the laser frequency and the spacing of the Raman spectrum, one can predict the spatial deviation on the detector of the different rotational lines.

In order to model rotational Raman signal levels, one must determine the signal strengths of the individual lines. The signal level is dependent upon the laser energy, scattering cross-section (including Plazcek-Teller coefficient), Boltzmann population fraction, scattering volume, solid angle, detector efficiency, as well as an attenuation factor to account for cell absorption. A value of 1.49 10^{-28} cm^2/sr at 488 nm was taken as the rotational Raman scattering cross-section for CO_2, from [7]. (The cross-section scales with frequency to the fourth power). The cell attenuation is found using Beer's Law. The absorption line shape is determined using a Whiting approximation [8] to the Voigt profile.

Test cases have been run for rotational Raman scattering from various species. Figure 3 models the deviation, and signal strength in a 200 micron pixel for N_2 and CO_2 scattering. The modeled laser intensity is 30 mJ/pulse; laser frequency is on the mercury line-center; the cell vapor pressure is 10 Torr, collection is f/10, with a 1 meter imaging length and 0.2 quantum efficiency. Plotted are the predicted Stokes shifted rotational Raman scattering lines for N_2 and CO_2 at STP. As expected, the different spectral signatures of the two species yield different spatial signatures. The profile gives a means of measuring temperature (from the Boltzmann distribution), species identification and detection (from the spatial/spectral signature), and density (from the signal strength). The thickness of the bars corresponds to the resolution a typical detector would offer. Non-overlapping bars therefore indicate cases where the individual lines would be clearly resolvable (provided the system resolution is detector limited). For the first three CO_2 lines there is some absorption by the mercury vapor. This is denoted by an asterix, and the original, unattenuated signal levels are plotted as vertical bars. Work is underway to incorporate a fitting routine into the model. This would allow extraction of parameters (such as scatterer temperature) from experimental data.

Verification

In order to provide an experimental verification of the predicted dispersion, a target was illuminated with the third harmonic output of the Ti:Sapphire laser and the scattering collected with f/10 optics through the vapor prism. The side-arm temperature was 170C giving a vapor pressure of 6.3 Torr. A slit was placed near the scattering source, and the refracted beam reimaged onto a microchannel plate intensified video camera. As the laser was tuned in wavelength, a camera recorded the displaced image of the slit as a function of detuning from line center of the mercury vapor resonance. The results are illustrated in figure 4, along with the model prediction. A better model fit is obtained using a temperature of 168C, suggesting a roughly two degree offset in the measurement of the cell temperature. The

agreement is to within the combined uncertainty in the imaging system calibration and the cell pressure.

Experimental Configuration

Measurements of Rayleigh and rotational Raman scattering from room air and CO_2 were performed. The experimental set-up used in these experiments is shown in Fig.5. The third harmonic output of the Ti:Sapphire laser was focused to a waist of approximately 100 microns. The pulse duration was ~ 10 ns and breakdown limited the energy to about 20 mJ per pulse.

In order to look at scattering from CO_2, a low-speed flow from a 2 cm diameter tube (connected to a cylinder) was used. The outlet of the tube was 2 cm above the beam, and flow was vertically down across the beam waist in the imaging volume. The collection lens was an f/5.8, 29 cm focal length spherical lens, while the final refocusing lens had a focal length of 90 cm. This ratio gave a magnification of 3.1. A Princeton Instruments intensified camera (Pentemax model) connected to a microcomputer was used without a lens as the detector. The detector width was 9.2 mm so that 3.0 mm of the beam was imaged. The side-arm of the cell was held at 190C giving a vapor pressure of 12.4 Torr.

Experimental Results & Discussion

Rayleigh Scattering

Rayleigh scattering from room air was observed by detuning the laser from the mercury resonance. The deviation and attenuation of the imaged Rayleigh beam were recorded.

Rayleigh imaging was performed as a preliminary step towards the imaging of rotational Raman scattering. Due to its larger cross section, the Rayleigh signal is, of course, much easier to image. The Rayleigh imaging allowed additional confirmation of the model as well as calibration of the imaging system. Images were taken at a series of different spectral positions around the filter resonance. On resonance the Rayleigh scattering is not observed because of strong absorption, but if it could be seen it would be undeflected. As the laser frequency is tuned away the resonance, the transmission through the cell increases, and the deviation rapidly increases and then decreases. When the laser is on transition line center (Fig. 6c) the Rayleigh line is undeviated and completely suppressed so that nothing is visible. Slightly off line-center (Fig. 6b,6d) the Rayleigh line is deviated and partially transmitted. As one moves yet further from line-center (Fig. 6a,6e)the deviation decreases while the transmission increases.

Rotational Raman Scattering

Preliminary images of rotational Raman scattering from CO_2 were obtained. CO_2 was chosen because it has a comparatively high rotational Raman scattering cross-section as well as tightly spaced lines (small B coefficient). A molecule whose spectrum has tightly spaced lines is advantageous because by tuning the laser judiciously several of the lines may undergo significant deviation. The image obtained in Fig.7b is a 50 shot average. Figure 7a shows the spectral location of the laser and Raman spectrum relative to the predicted filter deviation and attenuation. The laser frequency is slightly below transition line center. It is far enough from line-center to allow some transmission of the Rayleigh line, yet near enough for significant deviation (about 1.2 mm down). The Stokes lines are at lower frequencies than the Rayleigh/laser line so that they are further from transition line-center. Therefore, the Stokes lines are deviated in the same direction as the Rayleigh line (down), though less so. The situation with the Anti-Stokes lines (which are at higher frequencies than the Rayleigh line) is more complex. The first two Anti-Stokes lines (2-0 and 4-2) are on the same side of the transition line-center as the Rayleigh and Stokes lines, but closer in. These lines undergo large downward deviations but are too weak to be detected due to their small Boltzmann fractions and large cell attenuation. The next two Anti-Stokes lines (6-4 and 8-6) are just on the other side of transition line-center. These lines undergo significant deviation in the opposite direction (up), but the absorption so close to line-center is too strong for them to be detected. The higher Anti-Stokes lines are located progressively further and further from line-center (on the opposite side from the Rayleigh and Stokes). These lines are deviated up, and are visible as they are far enough from line-center to be unattenuated. Therefore, in this configuration, the Rayleigh line is deviated down, the Stokes lines are less deviated in the same direction, and the detected Anti-Stokes lines are deviated up. The Rayleigh line appears not between the Stokes and Anti-Stokes bands but rather on the outside. This configuration was chosen in order to highlight the Anti-Stokes side. The strongest Anti-Stokes lines (10-8, 12-10, 14-12, and 16-14) lie in a spectral region which

undergoes substantial deviation at attenuations of less than 50%.

Figure 7c plots average pixel intensity (20 pixels in horizontal direction) versus deviation on the detector. The Rayleigh line as well as Stokes and Anti-Stokes bands are clearly visible. The system resolution is not sufficient to clearly resolve the individual rotational lines. Each line showing up on the detector has a width of about 300 microns due to the beam waist and system magnification, while modeling predicts that the most separated lines should have a separation of about 150 microns on the detector. Although the lines are not fully resolved it is possible to identify some of their peaks. Figure 7c also includes the predicted line locations and good agreement exists between the experimental and predicted peak locations. For example, in the Stokes band one can see the peaks of the 2-4, 4-6 and 6-8 lines. -convolution-

Any residual scattered light far from the mercury resonance will be undeviated on the detector. One source of such light is the vibrational Raman lines and it is believed that they constitute the bulk of the signal at the zero position. Note that the signal from all of the vibrational lines combined is insufficient to overwhelm the signal from the rotational lines, indicating that the vibrational lines are of significantly lower intensity.

Filter Performance

Comparison of dispersive prism with diffraction spectrometer

Because of their similarities in application and implementation, it is fruitful to compare the dispersion prism to a more conventional spectrometer. First, worthy of note is the similarity that in both cases angular dispersion results in a spatial deviation after some imaging distance; the greater the distance the greater the deviation and hence resolution. Second, both feature identical trade-offs between fast collection and increased imaging distance for spectral resolution. The most notable difference is the inverted deviation of the dispersive prism. As evident from the index-of-refraction, those spectral features closest to the resonant absorption are deviated the most. A spectrometer deviates monotonically — the higher the frequency the greater the deviation. The dispersion prism deviates non-monotonically (as seen with the non-linear behavior of the index of refraction), and only close to resonance; whereas the spectrometer/diffraction grating has a broadband dispersion.

The dispersive prism near resonance out performs the state-of-the-art commercial spectrometer both in spectral sensitivity (linear dispersion) and throughput efficiency. The model predictions of the dispersive prism were compared to the specifications of an Acton Research Corporation AM512 2-meter monochrometer with 3600 groves/mm grating.[9] At two meters, the linear dispersion of the spectrometer is 0.138 nm/mm. The dispersion of the vapor prism is non-linear with frequency and vapor pressure. Comparisons were made at two vapor pressures, at spectral locations close to resonance (80% transmission through the cell), and further from resonance. The results are listed in Table 1. Close to resonance, the dispersion of the vapor prism exceeds the spectrometer from 5 to 25 times. Farther from resonance, the dispersion of the vapor prism matches and eventually drops below that of the diffraction grating. Aside from common imaging loss (collection f/#), the vapor prism throughput is reduced by surface reflections and transmission through the mercury vapor. Surface reflection loss is about 8% per surface (8 surfaces) and may be reduced with surface coatings. The trade-off between high vapor pressure (large dispersion) and reduced transmission depends upon precise operating conditions. However, 80% transmission was used as the 'near resonance' operating condition of Table 1. Furthermore, minimizing the vapor path length further increases transmission without affecting the deviation (as this arises at the mercury- air interface). In the case of spectrometers, the dispersive element itself is lossy due to higher orders of diffraction. By optimizing the grating for a particular wavelength region by blazing, efficiencies of 50-70% can be achieved for first order diffraction.[9]

System Resolution

In order to make a temperature measurement it would be desirable to have increased resolution of the individual rotational lines. The quantity one needs to maximize is the ratio of the deviation between two lines to the detected width of an individual line. This may be accomplished in various manners. The imaging system may be modified by increasing the focal length of the collimating lens (to reduce magnification) or by decreasing the size of the beam (limited by breakdown). Alternatively, a smaller effective beam size may be achieved by imaging through a slit. The above options enhance resolution at the expense of losing light. The fundamental limit on these parameters is the

diffraction limit. The diffraction limit gives the smallest useful slit size for a spectrometer as:

$$s_m = f/D\,\lambda \qquad (2)$$

where s_m is the smallest useful slit, f is focal length between slit and lens, D is the diameter filled on the lens, and λ is the wavelength of light. Applying this formula with our geometry gives a smallest useful slit size of 6 microns. Such a slit, however, would exceed the detector resolution limit (about 80 microns). Work is underway to incorporate a 25 micron slit into the imaging system. It is also interesting to consider the limit on resolving capability imposed by diffraction. The diffraction equations [10] for a prism give:

$$f / \delta f = L\, dn/d\lambda \qquad (3)$$

is the length of the prism, and $dn/d\lambda$ is the slope of the index of refraction versus wavelength. Our filter has a resolution limit of $\sim 10^5$ which is an order of magnitude higher than the separation of rotational lines (39000 cm^{-1} / 3.2 cm^{-1} ~ 10^4).

An alternative means of increasing the ability to resolve lines is by raising the cell vapor pressure, giving a higher mercury number density. However, with increased number density comes increased absorption such that the absorption notch effectively widens. Thus, at higher temperatures one is forced to work farther away from the mercury resonance where the dispersion is less. Modeling indicates that working at higher mercury vapor pressure would be beneficial though significant gains will be not achieved in this manner.

Future Work

In order to further improve the temperature and species measurements via atomic resonance filters several other ideas are being explored. One approach under consideration is the use of a temperature gradient filter to significantly increase the dispersion. Such a filter would be differentially heated with the top and bottom being held at different temperatures in a manner that produces a uniform temperature gradient in the vertical direction. The temperature gradient filter could have normally incident windows and would create dispersion by the refraction of light *within* the filter. This is just as Robert Wood demonstrated with sodium vapor in a cell placed over a flame.[11] The temperature gradient causes a gradient in index of refraction, which in turn causes refraction of light rays through the cell. To first order, the angular deviation of a light ray through such a cell is found as the product of the index of refraction gradient and the cell length. The design of such a filter is an area of active work.

Conclusion

A filter for rotational Raman scattering diagnostics has been constructed and demonstrated. The filter spatially separates (1-D) small spectral shifts by creating a vapor prism near the mercury resonance. Spectral shifts are mapped into one dimension onto a detector, while the second dimension remains for spatial resolution. A model for the filter operation has been developed and verified. The filter has been used to image Rayleigh scattering, and preliminary rotational Raman images have been obtained.

Acknowledgments

The authors thank Michael Souza, Princeton University Chemistry department for helpful discussions and fabrication of the filter cells, Glenn Rines of IR.. Sources, Andy Finch, Richard Schwartz of Schwartz Electro-Optics, Inc. in the development of the laser systems, and Phil Smith of Princeton Instruments for the loan of a Pentemax camera. This research was supported by the Air Force Office of Scientific Research.

References

1. R.B. Miles and W.R. Lempert, "Quantitative Flow Visualization in Unseeded Flows," *Annual Review of Fluid Mechanics*, V 29, pp. 285-326, 1997.

2. J.N. Forkey, "Development and Demonstration of Filtered Rayleigh Scattering - A Laser Based Flow Diagnostic for Planar Measurement of Velocity, Temperature, and Density" *NASA Technical Report 2067, and Dissertation Thesis*, Princeton University, 2067-T, April 1996.

3. P.A. Skaggs, T.M. Brown, S.P. Nandula, R.W. Pitz and E.P. Hassel, "Multi-Species Measurements in CH4-Air Flames Using a Narrowband KrF Excimer Laser by UV Raman Scattering," 32nd AeroSciences Meeting and Exhibit, Reno, NV, AIAA 94-0613, Jan. 1994.

4. A.C. Eckbreth, Laser Diagnostics for Combustion Temperature and Species Abacus Press, 1988

5. N.D. Finkelstein, W.R. Lempert, R.B. Miles, A. Finch, and G.A. Rines, "Cavity Locked, Injection Seeded, Titanium:Sapphire Laser and Application to UltraViolet Flow Diagnostics", 34th Aerospace Sciences Meeting

and Exhibit, Reno, NV, AIAA 96-0177, Jan. 1996.

6. N.D. Finkelstein, W.R. Lempert, and R.B. Miles, "Narrow Linewidth Passband Filters and UV Laser Source for Rotational Raman Imaging," *SPIE*, Vol. 3172, pp. 656-665, 1997.

7. C.M. Penney, R.L. St. Peters, and M. Lapp, "Absolute rotational Raman cross sections for N_2, O_2, and CO_2," *Journal of the Optical Society of America*, Vol 64, Number 5, pp. 712-716, 1974.

8. E.E. Whiting, "An Empirical Approximation to the Voigt Profile," *J. Quant. Spectrosc. Radiat. Transfer*, Vol. 8, pp.1379-1384, 1968.

9. Acton Research Corporation, Monochrometer Systems and Accessories Catalog, Acton Mass, 1997.

10. R. Kingslake, Applied Optics and Optical Engineering, Vol.5 Optical Instruments, Academic Press, New York, 1969.

11. R.W. Wood, Physical Optics, Dover Publications, New York, 495, 1967.

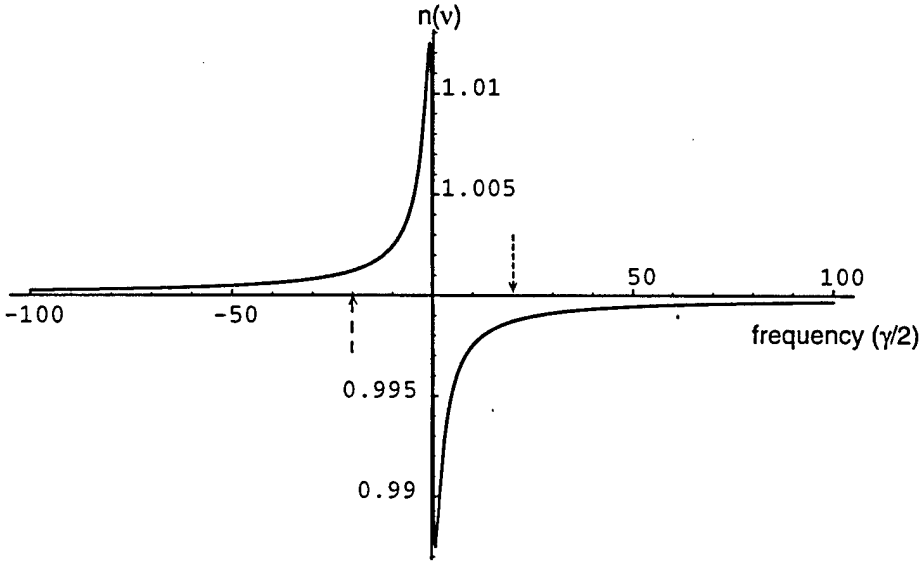

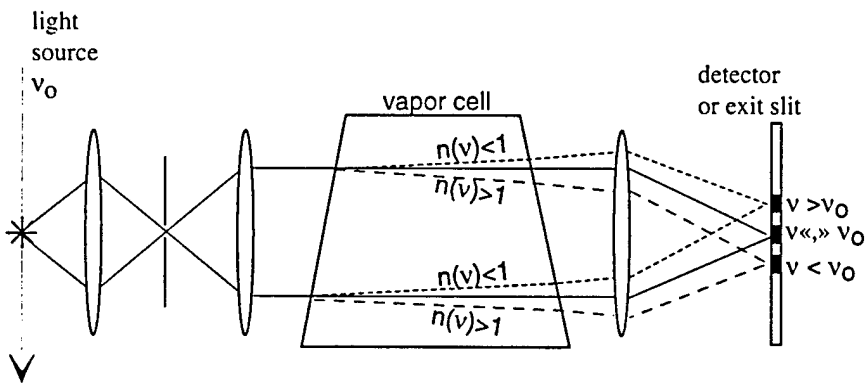

Figure 1: Schematic diagram of the dispersive vapor prism. Above (1a), plot of the change in index of refraction near resonance. The frequency axis is normalized by $\gamma/2$, the linewidth of the resonant transition. Below (1b), concept of filter. Light scattering is imaged through a spatial filter, through a vapor prism, onto a detector or exit slit. Light far from the vapor resonance is undeviated. Light on resonance is absorbed. Light spectrally higher than resonance is shifted up (due to an index of refraction less than one). Light at lower frequencies is shifted down.

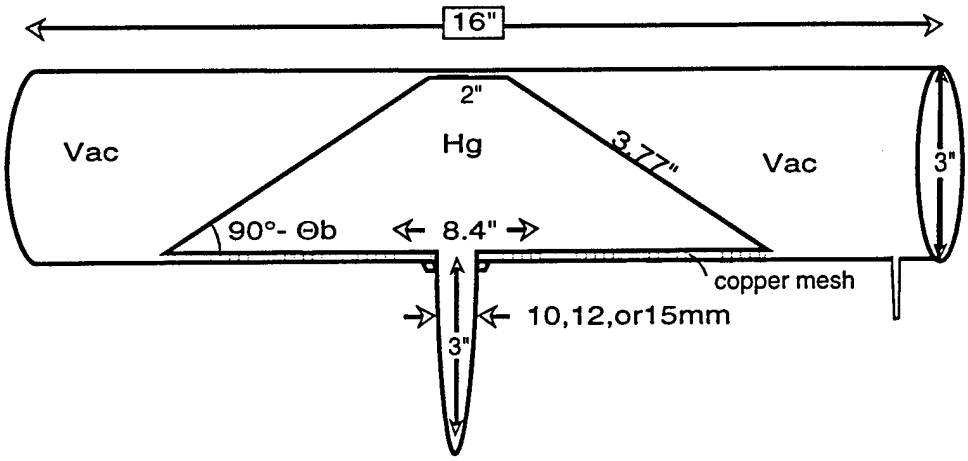

Figure 2: Schematic of the Hg vapor prism. Concentric quartz cylinders allow for heating of the inner Brewster cut windows, while keeping the outer flat windows cool.

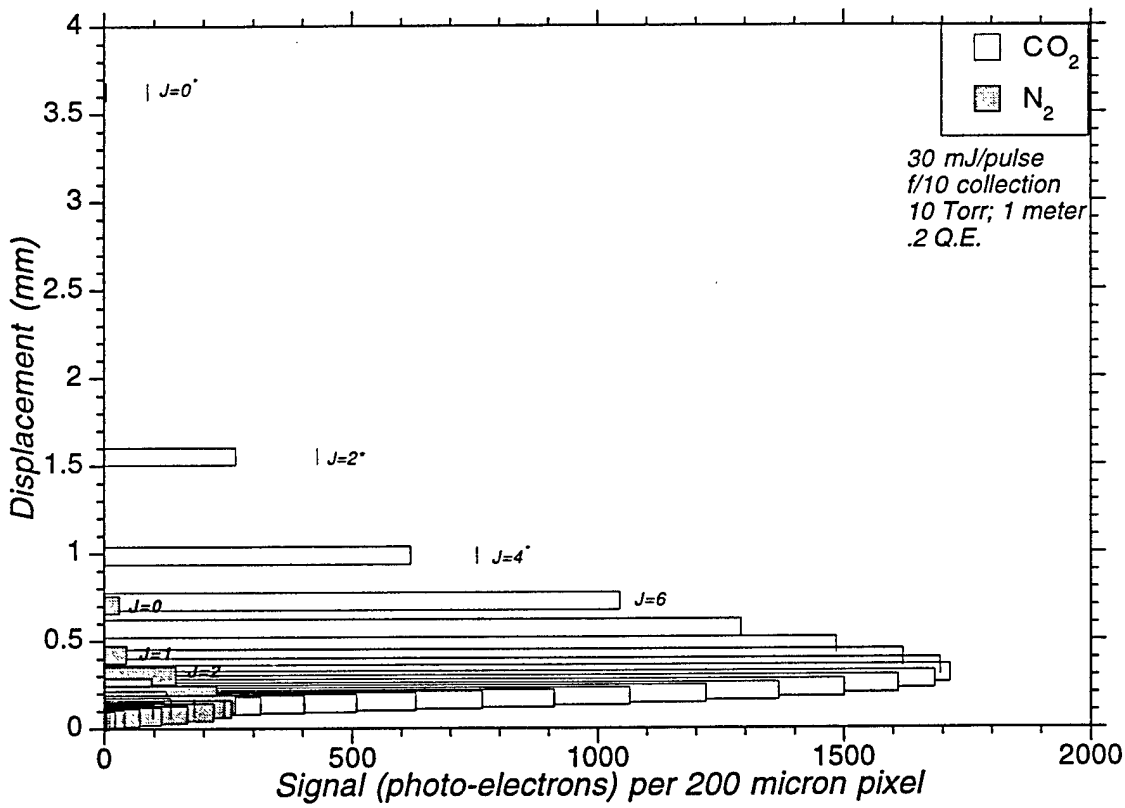

Figure 3: Model prediction for signal level and deviation of CO_2 and N_2 rotational Raman lines. The * indicates absorption of some fraction of incident radiation.

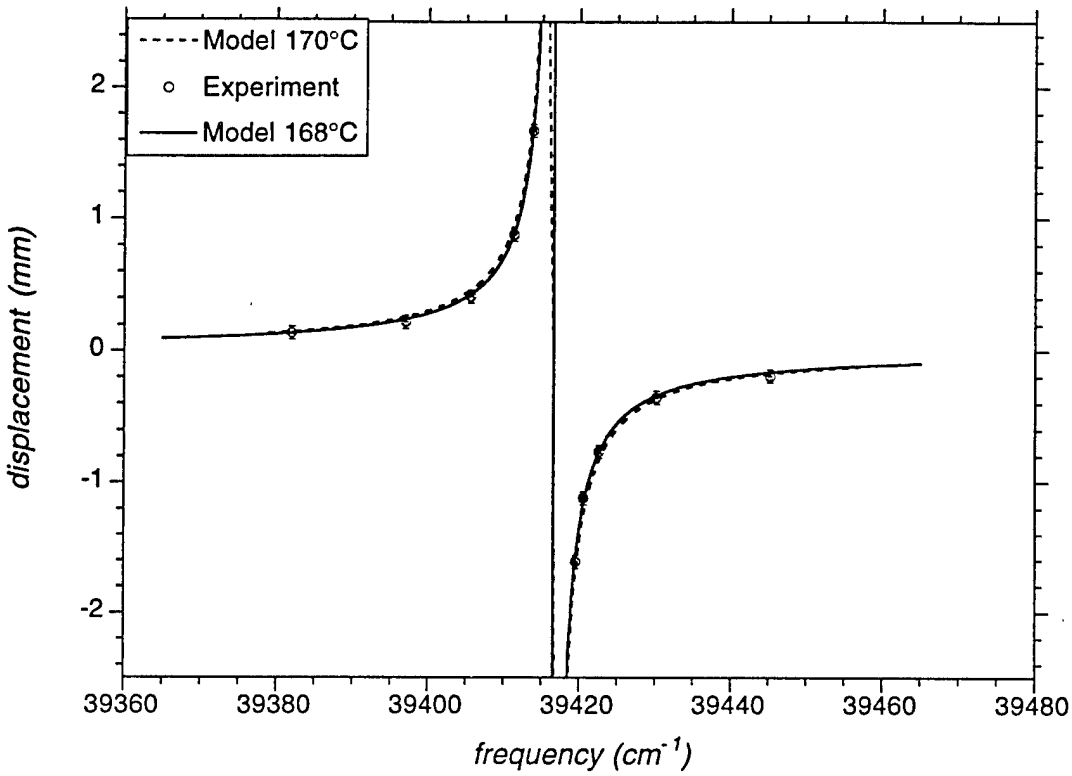

Figure 4: Measured and predicted deviation of light through the dispersive filter as a function of incident frequency.

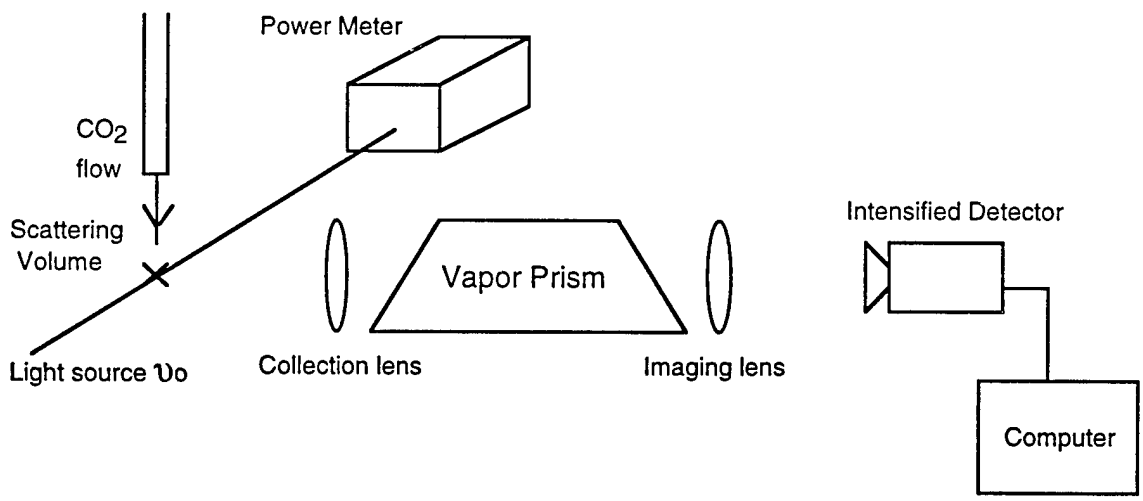

Figure 5: Experimental set-up. Scattered light is imaged through the vapor filter onto detector. Imaging parameters: collection f/5.8 (29 cm focal length), imaging f/18 (90 cm focal length)

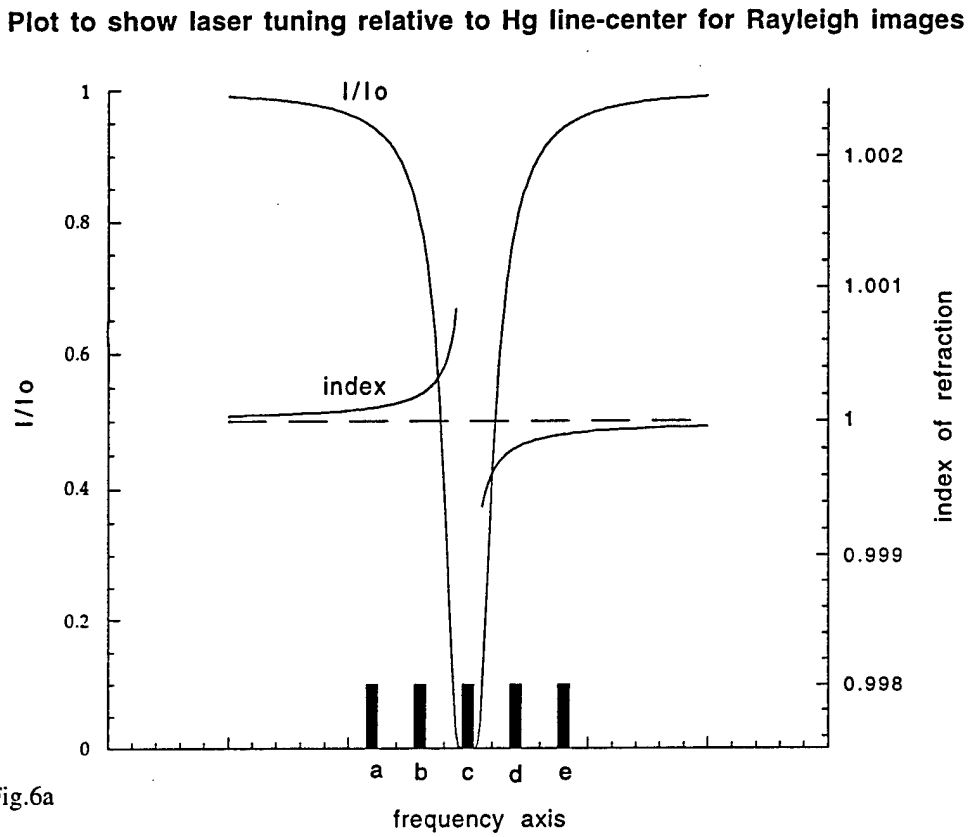

Fig.6a

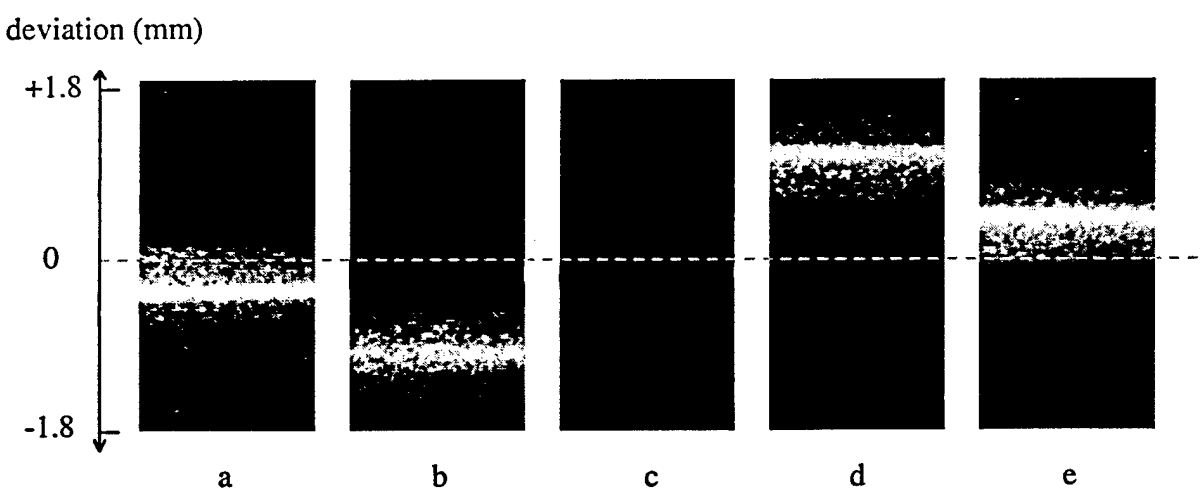

Fig.6b

Figure 6: Images of Rayleigh line obtained at different frequencies relative to transition line center. Figure 6a gives the relative laser tuning for the 5 images. Figure 6b shows the images of the Rayleigh line. Note that on line-center (c) all the light is absorbed. Near the resonance (b,d) one has strong dispersion. As one moves away from resonance (a,e) the dispersion decreases while the transmission increases.

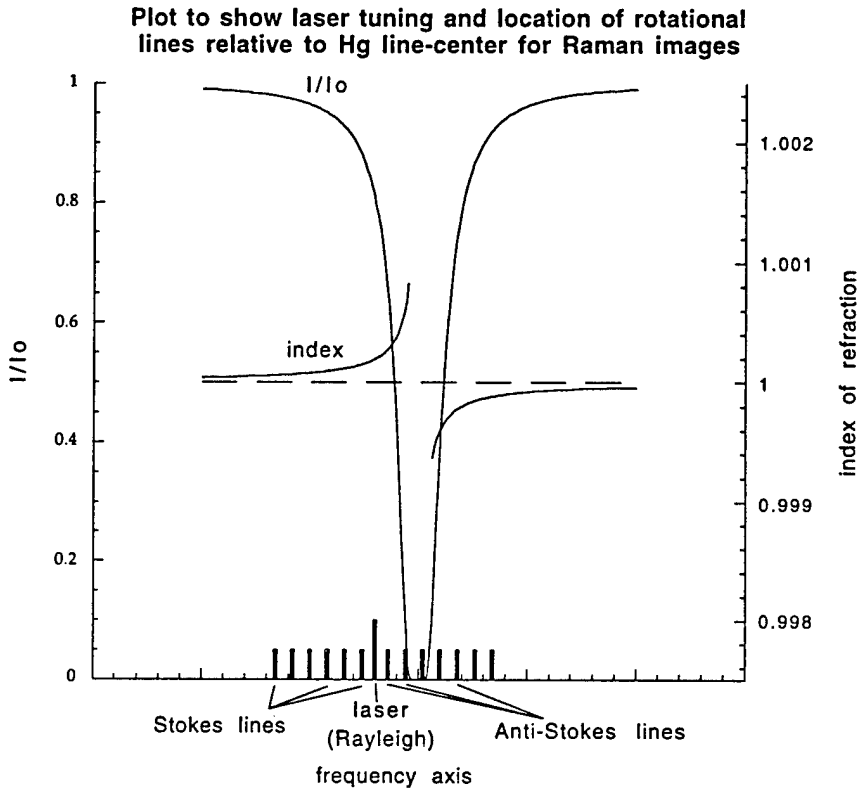
Plot to show laser tuning and location of rotational lines relative to Hg line-center for Raman images
I/Io
index
1
0.8
0.6
0.4
0.2
0
1.002
1.001
1
0.999
0.998
index of refraction
Stokes lines
laser
(Rayleigh)
Anti-Stokes lines
frequency axis

Fig. 7a

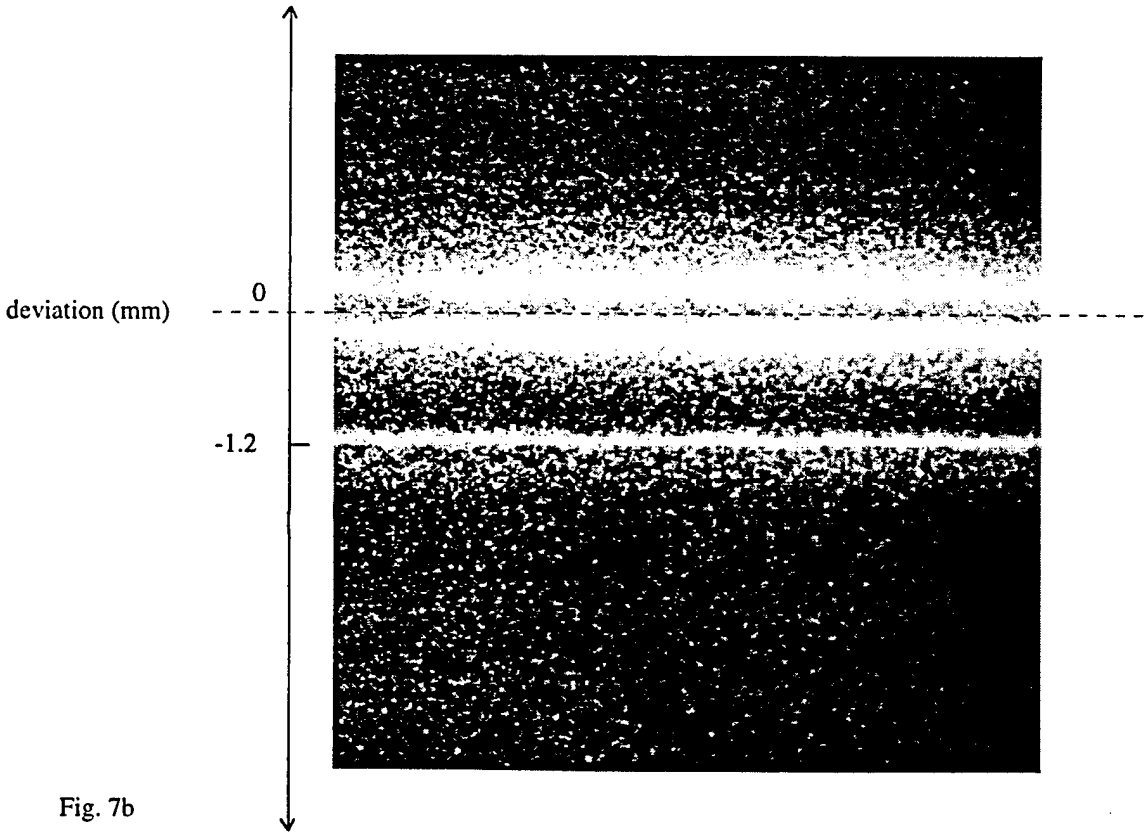
deviation (mm)
0
-1.2

Fig. 7b

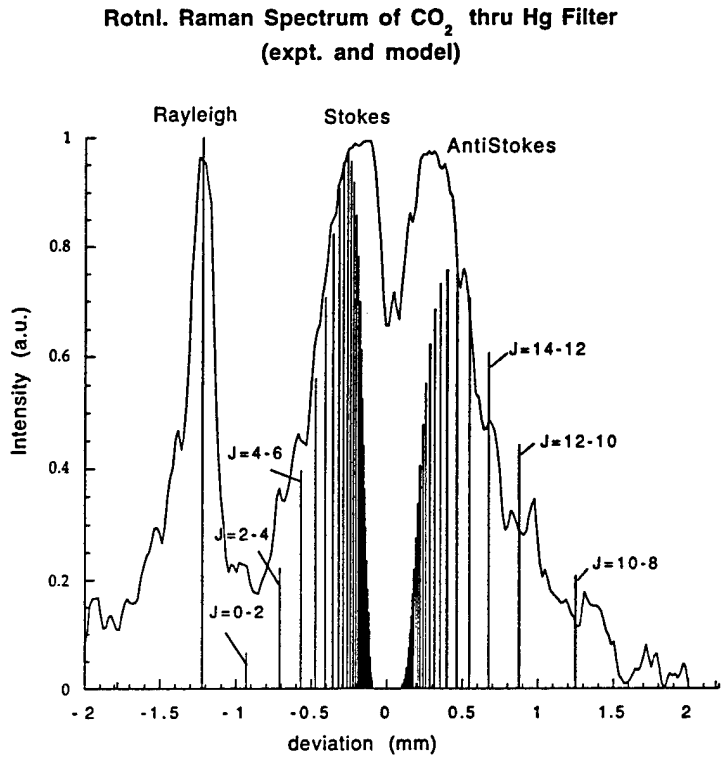

Fig.7c

Figure 7 Preliminary images of rotational Raman scattering from CO_2. Fig.7a shows the location of the laser tuning and rotational lines relative to transition line center. Fig.7b is the image obtained. The Rayleigh line is deviated down. The Stokes lines are spectrally located further from line-center and are therefore less deviated. The Anti-Stokes lines are on the other side of line-center and are deviated up. Fig.7c is an average cross-section obtained across 20 pixels. Also shown is the model prediction of the line locations. Individual lines are not well resolved however some of the peaks are visible.

pressure (Torr)	ν_0 (cm^{-1})	ν_1 (cm^{-1})	Δy (mm)	dispersion (nm/mm)
10	39424*	39430	1.0	0.039
10	39425*	39426	0.26	0.025
10	39440&	39441	0.03	0.22
1	39417.4*	39418.1	1.0	0.0045
1	39425&	39426	0.257	0.251

Table 1: Comparison of spectrometer and dispersive vapor prism. Dispersion at two vapor pressures: near resonance * and far from resonance &, for a 2 meter image length. Compare with 0.138 nm/mm dispersion of an ARC 2m monochrometer. (The lower the number for dispersion, the higher the spectral sensitivity).

AIAA-98-3932

Laser Propulsion Using a Molecular Absorber

Vincent P. Chiravalle, Richard B. Miles, and Edgar Y. Choueiri

Mechanical and Aerospace Engineering Department
Princeton University, Princeton NJ 08544
USA

34th AIAA/ASME/SAE/ASEE
Joint Propulsion Conference & Exhibit
July 13-15, 1998 / Cleveland, OH

For permission to copy or republish, contact the American Institute of Aeronautics and Astronautics
1801 Alexander Bell Drive, Suite 500, Reston, VA 20191

Laser Propulsion using a Molecular Absorber

V.P. Chiravalle*, R.B. Miles†, and E.Y. Choueiri‡
MAE Dept.
Princeton University
Princeton, New Jersey 08544

AIAA-98-3932§

Abstract

Unlike the conventional approach of using a laser sustained plasma to heat a propellant, molecular absorption of laser energy makes it possible to avoid the frozen flow losses associated with the high temperature and complex chemistry of a plasma. The molecular absorption concept is developed by exploring several thermodynamic pathways using a 1-D fluid theory for energy addition in the supersonic regime and different pathways are shown in H-K coordinates. The absorption physics of a promising molecular absorber, SF_6, is described at arbitrary laser beam intensities using a two-temperature non-equilibrium model, which is then applied to calculate the nozzle length required to achieve a specific impulse of 250 sec through a 300 K isothermal expansion in the supersonic section. The results of this conversative example case for energy addition illustrate that over a length of less than 1 m laser power on the order of 20 kW can be absorbed in the supersonic region of a 10 g/sec H_2 flow without creating a plasma.

1 Introduction

As high-power laser technology continues to mature the possibility of using a laser to generate rocket thrust for propulsion applications grows more feasible. The laser propulsion concept was first introduced by Kantrowitz[1] , more than twenty five years ago, and was experimentally demonstrated by Krier et. al.[2] and by Myrabo[3] . As with any thermal propulsion system, the efficiency of conversion of laser beam energy into the kinetic energy of propellant gas is a critical figure of merit. In addressing laser thruster performance it is useful to consider both the absorption efficiency as well as the the propulsion efficiency. In the context of laser thrusters, the propulsion efficiency is a measure of how much absorbed energy appears as kinetic energy of the propellant at the nozzle exit.

The established approach for achieving energy conversion is to create a laser sustained plasma (LSP) in the flowing propellant. The plasma is localized near the focal point of a laser beam, and laser energy is absorbed through the electron inverse bremsstralung process. As the propellant gas flows through and around the stationary plasma high bulk temperatures are sustained which can be in excess of 10,000 K in gases such as argon. Stable LSPs have been created and observed in the laboratory[4, 5]. Absorption efficiencies as high as 86 % for LSPs in argon have been reported by Keefer et. al.[4]. Several attempts have been made to model the physical interactions occurring in laboratory LSPs using two dimensional numerical simulations[6, 7]. Although the coupling of laser energy to a plasma has been found to be quite high, the overall propulsion efficiency is not as good. There are several processes that degrade the efficiency. In general, plasma radiation is a significant contributor, and in the case of molecular propellants such as hydrogen, dissociative frozen flow losses are also important. The equilibrium fraction of dissociated hydrogen is known to vary exponentially with temperature, and the reduction of frozen flow losses in hydrogen thermal thrusters necessitates

*Graduate Student. Mechanical & Aerospace Engineering. AIAA

†Professor. Mechanical & Aerospace Engineering. Associate Fellow AIAA

‡Assistant Professor. Mechanical & Aerospace Engineering. Senior Member AIAA

§This work was supported by an AASERT award from the Air Force Office of Scientific Research (AFOSR). Copyright © 1998 by Princeton University. Published by the American Institute of Aeronautics and Astronautics, Inc., with permission.

finding a way to add significant amounts of energy without completely dissociating the propellant. The dissociation fraction of hydrogen for various temperatures and densities is shown in Fig. 1.

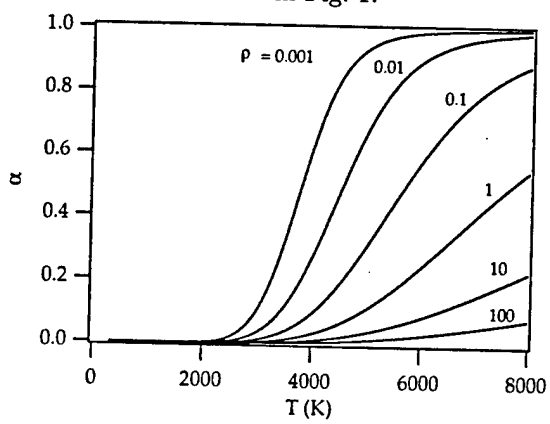

Figure 1: The calculated equilibrium dissociation fraction of H_2, as a function of temperature and density. The units of ρ are kg/m^3.

A different approach for energy addition, one that does not utilize a plasma, is the molecular absorption of radiation in the supersonic regime. Adding energy using a molecular absorber involves the excitation of an internal mode such as rotation or vibration of a seed molecule, the seed molecule subsequently transfers its energy to the propellant gas by relaxation collisions. The molecular absorption approach for laser propulsion was previously identified by Caledonia et. al.[8] in 1975. More recently, molecular absorption has been considered as an energy addition mechanism in the supersonic region for air in a proposed hypersonic wind tunnel and has been the focus of an ongoing research effort[9, 10].

The central issues with this approach involve the choice of the thermodynamic path over which energy is added and the choice of the seed molecule, with its associated set of physical parameters. Fig. 2 illustrates the conventional approach of energy addition in the plenum and the concept of energy addition in the supersonic region using a molecular absorber. The goal of this paper is to explore relatively simple pathways, such as a constant temperature expansion, to gain insight into the more complicated cases that may be of use to laser propulsion. The interaction between the seeded propellant mixture and the laser beam is described in general terms, using a familiar quasi-one dimensional model. It is understood that this approach is useful in a restricted sense, and is intended as a starting point for more realistic numerical simulations. This formalism is then applied using absorption data for SF_6 to calculate the length of the energy addition region in a laser thruster with molecular absorption.

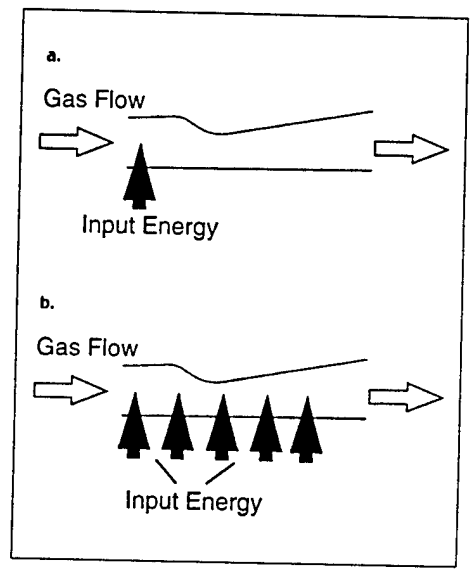

Figure 2: Laser rocket propulsion concepts : a: Energy addition using a laser sustained plasma in the plenum region. b: Energy addition in the supersonic region using a molecular absorber.

2 Fluid Model for Energy Addition

Within the constraints of one dimensional theory, the physics of an absorbing fluid in steady state is expressed by the fluid conservation equations,

$$\frac{1}{A}\frac{dA}{dx} + \frac{1}{\rho}\frac{d\rho}{dx} + \frac{1}{u}\frac{du}{dx} = 0 \quad (1)$$

$$\frac{dp}{dx} + \rho u\frac{du}{dx} = 0 \quad (2)$$

$$c_p\frac{dT}{dx} + u\frac{du}{dx} = c_p\frac{dT_0}{dx}. \quad (3)$$

It is assumed also that the gas is ideal and perfect i.e. with $p = \rho RT$ and constant c_p. T_0 is the total temperature of the fluid and

$$\dot{m}c_p\frac{dT_0}{dx} = -\frac{dP_w}{dx}. \quad (4)$$

The laser power, P_w, which is assumed to be uniform across the beam cross section is described by Beer's law written in conversation form,

$$\frac{dP_w}{dx} = -\kappa P_w. \tag{5}$$

The absorption coefficient, κ, is in general a function of the gas thermodynamic variables T and ρ and the laser intensity, I. There are more variables in this system than equations relating them. When the nozzle area, A, is specified everywhere and when the laser power incident to the energy addition region, P_{w0}, is known, the above equations uniquely determine the thermodynamic and mechanical state of a gas with a given set of initial conditions.

If a transformation is performed, expressing all quantities in terms of the optical length, $\tau = \int \kappa dx$, the conservation equations can be solved without reference to the properties of the absorbing species[8, 11]. The solution in physical space is recovered, for a chosen absorber, by reversing the transformation. There are limitations to the effectiveness of this approach since the radius of the nozzle is now a function of τ. Choosing $A(\tau)$ to give a specific shape in physical space is not intuitively obvious.

This difficulty can be removed, if instead of constraining the nozzle to have a given profile in space, an additional relation among the fluid variables is specified. The enlarged system of equations is solved with A as a variable. In this way the nozzle size and shape, consistent with a specified thermodynamic constraint, such as the isothermal condition, are found. The additional relation can be chosen as

$$\frac{dH}{dK} = \chi, \tag{6}$$

with kinetic energy, $K = \frac{u^2}{2}$, and enthalpy, $H = c_p T$. Going a step further, all the variables that describe the fluid, A, T_0, ρ, T, and u, can be written in terms of M^2, γ and χ,

$$\begin{aligned}
\frac{1}{A}\frac{dA}{d\tau} &= \frac{((\gamma-1)\chi+\gamma)M^2 - 1}{2-\chi(\gamma-1)M^2}\frac{dM^2}{d\tau}, \\
\frac{1}{T_0}\frac{dT_0}{d\tau} &= \frac{(\gamma-1)(\chi+1)}{(1+\frac{\gamma-1}{2}M^2)(1-\chi(\gamma-1)M^2)}\frac{dM^2}{d\tau}, \\
\frac{1}{\rho}\frac{d\rho}{d\tau} &= -\frac{(\gamma-1)\chi+\gamma}{2-\chi(\gamma-1)M^2}\frac{dM^2}{d\tau}, \\
\frac{1}{T}\frac{dT}{d\tau} &= \frac{\chi(\gamma-1)}{2-\chi(\gamma-1)M^2}\frac{dM^2}{d\tau}, \\
\frac{1}{u}\frac{du}{d\tau} &= \frac{1}{M^2(2-\chi(\gamma-1)M^2)}\frac{dM^2}{d\tau},
\end{aligned} \tag{7}$$

where for the moment χ is an unspecified function of M^2. The above equations trace curves in a five dimensional space parametized by M^2.

Another way to visualize the above relations is to look at their trajectories in H-K coordinates[12] . In the H-K plane each horizontal line, $\chi = 0$, corresponds to a constant temperature process and each vertical line, $\chi \to \infty$, corresponds to a constant pressure process. Three other basic cases are heat transfer with constant area, adiabatic, isentropic expansion and constant Mach number heating of the gas. The appropriate χ functions for these three cases are given below

$$\chi = (1-\gamma M^2)/M^2(\gamma-1), \tag{8}$$

$$\chi = -1, \tag{9}$$

$$\chi = 2/(\gamma-1)M^2, \tag{10}$$

where Eq. 8 refers to the constant area heat transfer case, Eq. 9 refers to the adiabatic, isentropic expansion case and Eq. 10 refers to the constant Mach number case. The example cases just discussed are illustrated in Fig. 3, and do not exhaust the set of

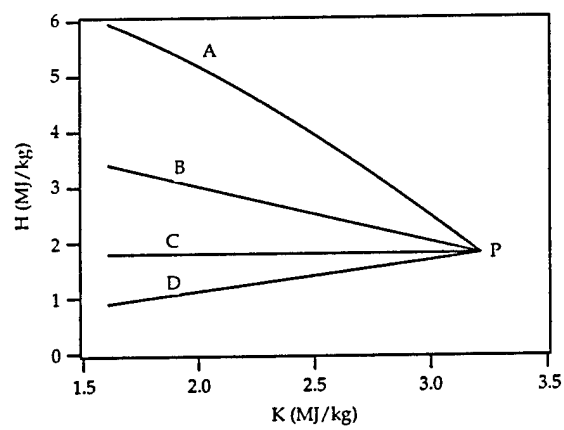

Figure 3: H-K coordinates of four trajectories in the supersonic regime that converge at point P. The conditions at P represent a fluid at T=300 K with M=3.0 and $\gamma = 1.39$. (A) cooling with constant area, (B) adiabatic, isentropic expansion, (C) isothermal expansion, and (D) heating at constant Mach number.

possible curves in H-K space. Any function $\chi(M^2)$ defines a path for the thermodynamic and mechanical parameters of the fluid to traverse. The task with regard to laser propulsion is to identify the χ function or set of functions which achieve a required

exhaust velocity, while having desirable characteristics in terms of efficiency of laser energy addition and nozzle size.

An attempt is made in the following sections to do this by solving the case of $\chi = 0$, isothermal flow, using a realistic model of a molecular absorber, SF_6. An isothermal energy pathway was selected for the examples in this work to ensure that the temperature would remain below the dissociation limit everywhere in the nozzle. The solution is obtained for the fluid variables in τ-space first, then the results are transformed back into physical space by computing the SF_6 absorption coefficient at each point in the nozzle. SF_6 was chosen because of its exceptionally high absorption coefficient at 10.6μm, the wavelength of commercial CO_2 lasers. As discussed later the required SF_6 absorption data exist in a narrow temperature range around 300 K, and for this reason 300 K was used in all the example cases computed here.

3 Study Case: Isothermal Expansion

Consider an isothermal expansion taking place in the supersonic region of a laser thruster. The laser enters at the nozzle exit and propagates in the direction of the throat, as seen in Fig. 4.

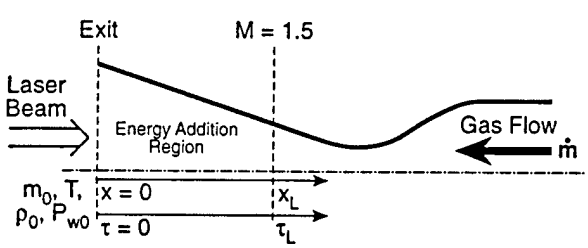

Figure 4: The orientation of the laser beam propagation relative to the fluid flow in the examples considered in this study. The non-dimensional optical length, τ, and the physical axial length are measured relative to the nozzle exit where the laser beam enters and the fluid conditions are specified.

The energy addition term of Eq. 3 is related to the power extracted from the laser beam. In τ-space Eq. 5, describing the evolution of the beam power, can be written as

$$\frac{dP_w}{d\tau} = -P_w. \tag{11}$$

The solution is an exponential function of τ. τ is measured relative to the nozzle exit, and the direction of increasing τ corresponds, in physical space, to marching upstream toward the throat, Fig. 4. With this expression for P_w and the isothermal condition, analytic solutions for M^2 and ρ can be obtained as a functions of τ and of the conditions at the nozzle exit. These are used to compute the flow properties at each section of the nozzle and are given below

$$M^2 = M_0^2 + \frac{2\Gamma}{\gamma}\left[1 - \exp -\tau\right], \tag{12}$$

$$\rho = \rho_0 \exp \Gamma \left[1 - \exp -\tau\right]. \tag{13}$$

The non-dimensional parameter Γ has the form $\Gamma = P_{w0}/\dot{m}RT$ and in physical terms it is proportional to the ratio of incident laser beam power to flow enthalpy.

4 SF_6 Absorption Physics

Gaseous SF_6 is a strong absorber of infrared radiation at the $C0_2$ laser wavelength of 10.6μm. A spherical top molecule, SF_6 has six fundamental vibrational modes, one of these, designated by the ν_3 quantum number, corresponds to an infrared active band. In addition to vibrational motion the SF_6 molecule also has rotational energy components, described collectively by the quantum number J. The excitation of SF_6 by radiation at 10.6μm can be understood in terms of a transition from a state where none of the vibrational modes are excited, the vibrational ground state, to a state of higher energy where the ν_3 mode is excited, $\nu_3 = 1$. Let N_1 be the number density of SF_6 in the vibrational ground state with a rotational quantum number, J_1. Let N_2 be the corresponding number density for a state with only the ν_3 vibrational mode excited, $\nu_3 = 1$, and with rotational quantum number J_2. The values of the rotational quantum numbers are found to be $J_1 = 67$ and $J_2 = 66$ using the theory presented by Herzberg[13] together with the appropriate molecular constants for the ground and excited states, determined by Bobin[14]. The absorption coefficient can be expressed as a function of N_1 and N_2 according to the equation below,

$$\kappa = \sigma(N_1 - \frac{g_1}{g_2}N_2). \tag{14}$$

σ is the absorption cross section for the transition described above and is a function of the gas properties, T and ρ. The ratio of degeneracies, g_1/g_2 for large

J is approximately 1/3. Based on the measurements by Anderson[15] in pure SF_6 at 100 torr and 300 K, the value of κ is 3500 m^{-1}. σ was determined by computing N_1 and N_2 at these conditions and solving Eq. 14 using the experimental value for κ. At 300 K available data for the absorption coefficient of SF_6-air mixtures[15] show that κ varies linearly with ρ over several orders of magnitude. This implies that the dependence of σ on ρ is negligible. Therefore in this paper it is assumed that σ for the transition at 10.6μm in a SF_6-H_2 mixture is a constant at 300 K. With σ known, the absorption coefficient can be extrapolated to high laser beam intensities using Eq. 14.

To understand the effect of laser intensity on κ, it is necessary to explore the physics contained in the N_1 and N_2 terms. At equilibrium conditions N_2 and N_1 are determined by the Boltzmann relation and depend entirely on the thermodynamic temperature. Situations may arise when the translational and vibrational modes of the fluid become uncoupled, for instance when a fluid is perturbed by a tightly focused laser or when a shock wave passes through the fluid. In such a case N_1 and N_2 are described in terms of two temperatures, a translational temperature, T, and a vibrational temperature, T_{vib}. Energy transfer from one mode of vibration to another occurs on a short time scale relative to energy transfer to a translational mode. The evolution of the fluid vibrational energy, e_{vib}, is described by a conservation equation which in steady-state is

$$\dot{m}\frac{de_{vib}}{dx} = \frac{\rho A(e^*_{vib} - e_{vib})}{\beta} + \kappa P_w. \qquad (15)$$

β, the characteristic time for vibrational relaxation, was measured for pure SF_6 by Burak et. al.[16] and was found to approximately 140 μsec torr. This value was adopted in this work, although one would expect the relaxation time to be shorter for an SF_6-H_2 mixture than for pure SF_6 because, as a consequence of the smaller molecular mass of H_2, the collision frequency between SF_6 and H_2 is greater than the corresponding collision frequency for pure SF_6. Eq. 15 can be transformed from physical space into τ-space in the same way as the other fluid conservation equations. When this is done a coefficient, $1/u\kappa$ appears, which is the characteristic flow residence time. The flow residence time is the time required for the fluid to travel a distance equal to the distance over which the laser beam intensity drops by a factor of $1/e$. de_{vib}/dx can be neglected in Eq. 15 when two criteria are met simultaneously, the flow residence time, σ, is much longer than the vibrational relaxation relaxation time, β, and the difference between the vibrational energy that the flow would have at equilibrium, e^*_{vib}, and the flow vibrational energy, e_{vib}, is the same order of magnitude as e_{vib}. e_{vib} is a function of T_{vib} and e^*_{vib} is a function of T. The conditions for neglecting de_{vib}/dx are summarized below,

$$\sigma \gg \beta,$$
$$e^*_{vib} - e_{vib} \sim e_{vib}. \qquad (16)$$

The functional forms of the terms, N_1, N_2, e_{vib} and e^*_{vib}, are given in Ref. [15].

A two-temperature approach was put forth by Anderson[15] to treat saturation absorption in SF_6 at high laser intensities. The model presented in that work is applied here to compute the SF_6 absorption coefficient and is strictly valid at room temperature, 300 K, where absorption data was collected. The present implementation of the model differs from the one used by Anderson in one way, only absorption from the ground state is considered here for the sake of simplicity. The original model considered absorption from both the ground state and an excited state. The present model is more conservative in the sense that at high laser beam intensities the absorption coefficient is less because absorption by excited states is not considered.

5 Results for a Supersonic Isothermal Expansion with SF_6 as an Absorber

To assess the potential of laser propulsion using a molecular absorber it is necessary to get a rough answer to some basic questions regarding how much energy can be deposited in the supersonic region of an expanding nozzle flow, whether the expansion can begin at a low enough temperature to avoid hydrogen dissociation and if the nozzle size in such a system is so large as to be impractical. As discussed in the previous sections, one possible way of introducing the laser into the supersonic energy addition region is to direct the beam from downstream through the nozzle exit. For nozzles where the supersonic expansion ratio is sufficiently gradual the one dimensional theory developed in this paper may not be a bad approximation.

The fluid conditions and laser beam power are specified at the nozzle exit. Using Eq. 12 and Eq. 13 the conditions at all other points upstream of the

exit in the energy addition region are uniquely determined. The nozzle exit conditions were chosen to be reasonable values for an expanded supersonic flow, such as $M_0 = 3.0$ and $\rho_0 = 0.001$ kg/m^3. T was set to 300 K for reasons discussed earlier and the mass flow rate was selected as 10 g/sec to keep the required nozzle exit diameter in the 5-10 cm range. The propellant mixture consisted of H_2 with an SF_6 concentration of 2 %. The conditions at the nozzle exit correspond to a specific impulse of 250 sec. The laser beam power incident to the nozzle exit was a parameter to be specified for each run. The computation marched forward toward the throat from the exit, and was concluded when the flow achieved $M = 1.5$. For a given run, the first step was to find the point in τ-space where $M = 1.5$, this was accomplished using Eq. 12. Then for all points in the energy addition region, Eq. 15 was solved numerically for T_{vib} assuming, $de_{vib}/dx \approx 0$, and the absorption coefficient was calculated using Eq. 14. Knowing κ at all points in the energy addition region, the nozzle radial profile and all the fluid conditions were determined as functions of axial length.

Twenty two runs were made with the nozzle exit conditions discussed above, varying the laser beam power for each run. For a given value of laser power, the non-dimensional optical length at the position where $M = 1.5$, denoted τ_L, was calculated and the corresponding position, x_L, was then determined. Fig. 5 shows how x_L varies with laser power. The laser beam power, Γ, is non-dimensionalized in terms of $\dot{m}RT$. The absorption coefficient, κ, at the point where $M = 1.5$, is used to non-dimensionalize x_L. The largest nozzle size of 0.72 m occurs when $\Gamma = 5.0$. This case is also the case where most of the laser beam power is absorbed in the supersonic region. The fraction of laser beam power absorbed in the supersonic region to the incident laser beam power is shown in Fig. 7. As the laser beam power is increased two trends occur, the required nozzle size in the supersonic energy addition region decreases and the fraction of absorbed power decreases, i.e. more of the laser power passes through the intended energy addition region into the throat region. Looking at Fig. 5 and Fig. 7, it is evident that there is a limit for Γ, which can be found by solving Eq. 12 for Γ as $\tau \rightarrow \infty$. For the specified Mach number at the nozzle exit, $M_0 = 3.0$, the limit is $\Gamma = 4.72$. The laser beam power corresponding to $\Gamma = 4.72$ is 24 kW ($\dot{m} = 10$g/sec) and represents the minimum amount of input power, $\dot{m}c_p dT_0/dx$, required to satisfy the isothermal condition from $M = 1.5$ to $M = 3.0$. Laser beams of greater power propagate through the supersonic energy addition region without being completely attenuated, i.e. $\eta < 1$.

Among the cases computed the results for Γ of 5.63, 9.67 and 23.12 are presented. The ratio of flow residence time to vibrational relaxation time is plotted in Fig. 8, and it is seen that σ is at least an order of magnitude larger than β. The ratio of vibrational temperature to translational temperature is given in Fig. 6, and is everywhere greater than 1. It is evident, therefore, that the criteria for neglecting de_{vib}/dx are satisfied in the cases considered. As the laser beam power is increased, T_{vib} increases, raising N_2 and lowering N_1. The net effect is to decrease κ.

The computed nozzle profile for the case with $\Gamma = 5.63$ is shown in Fig. 9. At the nozzle exit the radius is 3.5 cm. The right most point on the graph corresponds to the $M = 1.5$ point, where the radius is 0.47 cm. The total length is 68 cm with an area expansion ratio of 56.

6 Conclusions

The concept of laser propulsion using a molecular absorber was studied by choosing a simple isothermal pathway for energy addition, and by implementing a model of SF_6 absorption. The results indicate that significant amounts of energy can be deposited in the supersonic region without paying too unreasonable a penalty in terms of nozzle length. Although one energy addition pathway was explored in depth in this paper, other traditional cases such as constant Mach number energy addition, and other less familiar χ functions should also be studied. To do so with SF_6, however requires additional absorption data to describe how σ varies in the high T regime, since data of this type are not available. For an isothermal expansion over a given density range the amount of energy added to the flow is directly proportional to the temperature. The specific impulse of the example cases studied here was 250 sec, operation at a higher temperature, although not high enough to cause dissociation, would produce a significantly higher specific impulse.

References

[1] A. Kantrowitz. Propulsion to orbit by ground-based lasers. *Astronautics and Aeronautics*, 10:74–76, 1972.

[2] H. Krier, J. Black, and R.J. Glumb. Laser propulsion 10 kw thruster test program results. *Journal of Propulsion and Power*, 11:1307–1316, 1995.

[3] L.N. Myrabo, D.G. Messitt, and F.B. Mead Jr. Ground and flight tests of a laser propelled vehicle. In *AIAA* 36th *Aerospace Sciences Meeting*, Reno, NV, January 1998. AIAA 98-1001.

[4] R. Welle, D. Keefer, and C. Peters. Laser-sustained plasmas in forced argon convective flow, part 1: Experimental studies. *AIAA Journal*, 25:1093–1099, 1987.

[5] A. Mertogul, D. Zerkle, and H. Krier. Investigation of CO_2 laser-sustained hydrogen plasmas. *Journal of Propulsion and Power*, 8:1123–1125, 1992.

[6] S. Jeng and D. Keefer. Theoretical investigation of laser sustained argon plasmas. *Journal of Applied Physics*, 60:2272–2279, 1986.

[7] A. Mertogul and H. Krier. Two-temperature modeling of laser sustained hydrogen plasmas. *Journal of Thermophysics and Heat Transfer*, 8:781–790, 1994.

[8] G.E. Caledonia, P.K.S. Wu, and A. N. Pirri. Radiant energy absorption studies for laser propulsion. Final Report NASA-CR-134809, NASA Lewis Research Center, 1975.

[9] R.B. Miles, G.L.Brown, W.R. Lempert, R. Yetter, G.J. Williams Jr., S.M.Bogdonoff, D. Natelson, and J.R. Guest. Radiatively driven hypersonic wind tunnel. *AIAA Journal*, 33:1463–1469, 1995.

[10] R.B. Miles and G.L. Brown. Energy addition mechanisms for radiatively-driven wind tunnel: Predictions & experiments. In *AIAA* 29th *Plasmadynamics and Lasers Conference*, Albuquerque, NM, June 1998. AIAA 98-2748.

[11] W.G. Vincenti and C.H. Kruger. *Introduction to Physical Gas Dynamics.* John Wiley & Sons, 1965.

[12] D.T. Pratt and W.H. Heiser. Isolator-combustor interaction in a dual-mode scramjet. In *AIAA* 31th *Aerospace Sciences Meeting*, Reno, NV, January 1993. AIAA 93-0358.

[13] G. Herzberg. *Molecular Spectra and Molecular Structure II. Infrared and Raman Spectra of Polyatomic Molecules.* D. Van Nostrand Co., 1945.

[14] B. Bobin, C.J. Borde, J. Borede, and C. Breant. Vibration-rotation molecular constants for the ground and ($\nu_3 = 1$) states of SF_6 from saturated absorption spectroscopy. *Journal of Molecular Spectroscopy*, 121:91–127, 1987.

[15] J.D. Anderson Jr. and J.L. Wagner. CO_2 laser radiation absorption in SF_6-air boundary layers. In *AIAA* 11th *Aerospace Sciences Meeting*, Washington, D.C., January 1973. AIAA 73-262.

[16] J.I. Steinfeld, I. Burak, D.G. Sutton, and A.V. Nowak. Infrared double resonance in sulfur hexafluoride. *Journal of Chemical Physics*, 52:5421–5434, 1969.

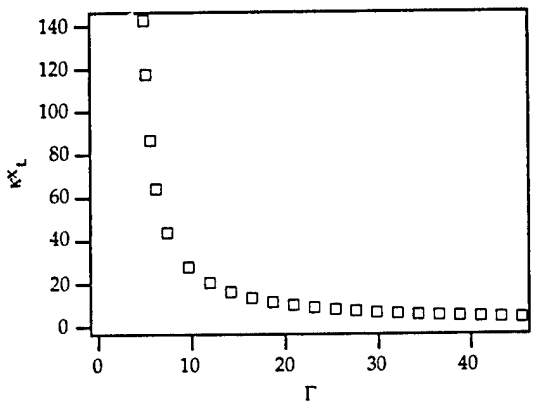

Figure 5: The calculated nozzle length for supersonic energy addition versus the laser beam power incident at the nozzle exit. 22 cases were considered. The left most point corresponds to having $\Gamma = 5.0$.

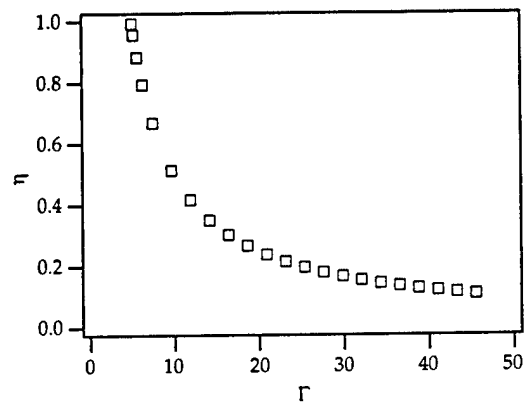

Figure 7: The fraction of laser beam power absorbed in the supersonic region, η, versus the laser beam power incident at the nozzle exit.

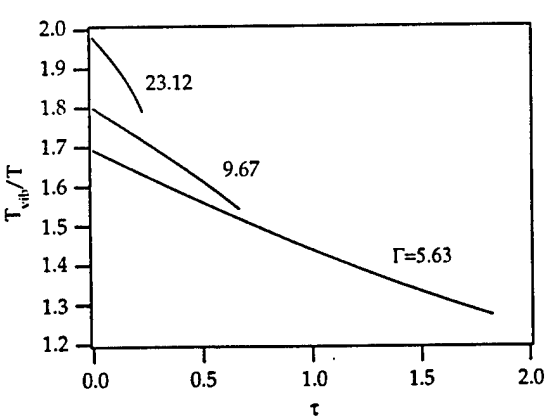

Figure 6: The ratio of SF_6 vibrational temperature to the fluid translation temperature, 300 K, as a function of the non-dimensional optical length, τ.

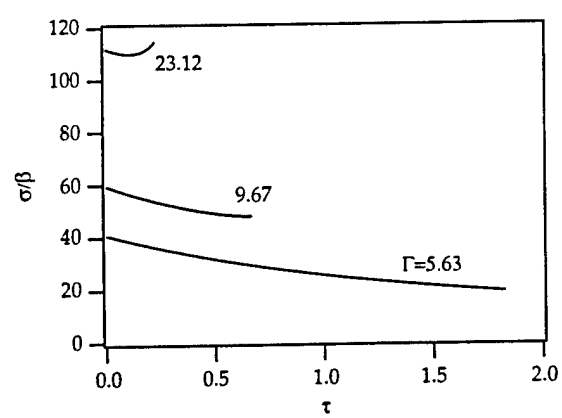

Figure 8: The ratio of the characteristic flow residence time to the vibrational relaxation time of SF_6 as a function of the non-dimensional optical length.

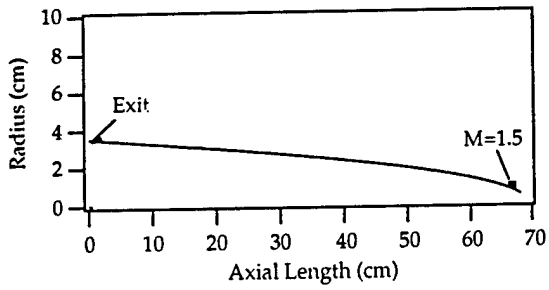

Figure 9: The computed nozzle profile, nozzle radius versus axial length, for supersonic energy addition with $\Gamma = 5.63$.

Dispersion filter for spectral and spatial resolution of pure rotational Raman scattering

Noah D. Finkelstein, Azer P. Yalin, Walter R. Lempert, and Richard B. Miles

Department of Mechanical and Aerospace Engineering, Princeton University, Princeton, New Jersey 08544

Received June 15, 1998

A new filtering technique for Raman spectroscopy utilizes atomic vapor to suppress strong elastic and Rayleigh scattering while simultaneously resolving individual rotational Raman lines. Filtered images capture high-resolution spectral information in one dimension and spatial resolution in the other dimension. The filter is based on resonance enhanced dispersion, where the index of refraction varies dramatically. In a simple prism geometry the vapor disperses incident radiation according to frequency. A mercury-vapor-based dispersion filter has been fabricated, modeled, and demonstrated to capture pure rotational Raman scattering from CO_2.
© 1998 Optical Society of America
OCIS codes: 230.5480, 330.6180, 300.6540, 330.6130, 280.2470.

A novel filtering concept for imaging pure rotational Raman scattering has been developed and characterized. The filter suppresses background radiation from the nearby Rayleigh line while simultaneously resolving multiple rotational Raman lines. The filter is based on resonant enhanced dispersion of atomic or molecular vapor. As demonstrated by Wood, near resonance one can use the strong variation in index of refraction to refract light.[1] Notably, the strongest variation in index occurs near resonance, which makes a device based on resonant enhanced dispersion particularly sensitive to small spectral shifts, as is typical of rotational Raman scattering. In one dimension, different spectral signatures become different spatial signatures, whereas spatial information is preserved in the other dimension. The profiles give one a means of measuring temperature (from the Boltzmann distribution), species identification and detection (from the spatial–spectral signature), and density (from the signal strength). Furthermore, aside from imaging losses, the filter possesses no other inherent inefficiencies, so the quantum efficiency of detection can be quite high. The high throughput near resonance, the high background suppression on resonance, and the spectral and spatial resolution of multiple rotational lines make this device uniquely attractive for Raman-based diagnostics.

The concept is illustrated in Fig. 1. For incident-light scattering at a higher frequency than the vapor resonance the index of refraction of the vapor is less than that of air [given by Eq. (1) below]. As this scattered light is imaged through the vapor cell, it is deviated upward (away from the input normal) on the detector. For light at a lower spectral frequency (the long-dashed lines) the index is greater than that of air, and the light is bent toward the input normal and shifted downward on the detector. For light far from resonance the index of refraction is 1, and the propagation path is undeviated (solid lines). Light on resonance, of course, is suppressed owing to absorption.[2] Notably, the light that deviates most significantly is that which is closest to resonance, making this device particularly sensitive to small spectral shifts.

The use of the index of refraction variation near resonance has long been exploited for spectroscopic measurements. A review of the *hakenmethode* (the hook, or dispersion, method) is given by Marlow.[3] Traditionally, this method has been used for spectroscopic measurements such as highly accurate oscillator strengths; however, shock waves have also been studied.[3] In a study more closely related to the present one, Wood demonstrated the feasibility of using anomalous dispersion for differently refracting light of different wavelengths.[1]

More recently, spectrometers were employed for high-sensitivity spectral measurements. Their high spectral resolution combined with their one-dimensional imaging capability allowed for Raman measurements in combustion environments. Not until relatively recently were rapid measurements imaging combustion environments made. Vibrational Raman scattering was used to image combustion in jet flames.[4] The weaker vibrational Raman scattering was used because of its larger energy shift, which simultaneously allows for discrimination from the Rayleigh line and a coarser spectral window on the spectrometer. Recently, Rothe and Andresen reported what is believed to be the first one-dimensional images of rotational Raman scattering with hydrogen.[5] By use of a modified KrF laser to produce narrow-band highly polarized output, rotational Raman scattering through a spectrometer onto an intensified CCD camera was observed. They achieved attenuation of the Rayleigh line by viewing depolarized scattering and dispersion through the spectrometer. Nonetheless, the imaging detector was

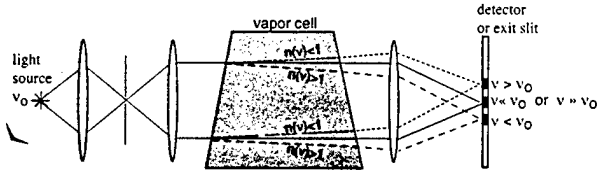

Fig. 1. Dispersive vapor prism: Scattering is vertically deviated according to frequency and is spatially resolved (in the plane perpendicular to this page).

0146-9592/98/201615-03$15.00/0 © 1998 Optical Society of America

saturated for several hundred wave numbers about the Rayleigh line. Rotational Raman scattering is feasible because of hydrogen's large B_0 coefficient (61 cm^{-1}).

Our dispersion filter is based on the well-known expression for the real part of the index or refraction,[6]

$$n' = 1 - \left(\frac{e^2}{2M_e}\right) Nf \frac{1}{\epsilon_0}\left[\frac{(\omega^2 - \omega_0{}^2)}{(\omega^2 - \omega_0{}^2)^2 + \omega^2\gamma^2}\right], \quad (1)$$

where e is the electron charge, M_e is the electron mass, N is the number density, f is the oscillator strength, ϵ_0 is the electric permittivity, γ is the linewidth, ω is the radial frequency, and ω_0 is the resonant frequency. Using the strong variation in index of refraction, one can construct a prism from a vapor near resonance. In the simplest incarnation a controlled amount of vapor is contained between two angled windows. Incident light imaged through this cell is refracted according to its input frequency, Eq. (1), and Snell's law. Geometric analysis yields the resulting spatial deviation. Effects of isotopic variation, hyperfine splitting, and signal attenuation (the imaginary component of the index) must be included for a given atomic or molecular vapor. We developed a detailed computer model to describe a mercury-vapor dispersion filter operating at the $^3P-^1S$ transition at 253.7 nm.

For model verification and CO_2 Raman imaging a dispersion prism filter based on the mercury resonance was fabricated. The filter consists of a pair of concentric all-quartz cells, with the outer cell surrounded by a large aluminum sheath. The inner cell consists of a main body with 5-cm-diameter clear aperture Brewster angle windows, and a sidearm cold tip containing 5 g of mercury. We selected Brewster's angle as the angle of incidence to minimize surface reflection and maintain significant angular deviation. The main body of the inner cell is jacketed with a copper heat conductor that is used to control the temperature and prevent condensation on the Brewster windows. Evacuating the space between the inner and outer quartz shells allows for heating of the inner cell while keeping the outermost windows at room temperature. The combination of inner and outer cells allows heating of the inner Brewster windows while simultaneously avoiding the creation of thermal room currents near the hot windows, which would induce additional refraction. Separate heaters and temperature controllers are used to ensure that the inner cell body is held at a constant temperature, which is slightly warmer than a sidearm cold tip (which controls the vapor pressure). Four resistive cartridge heaters are used to heat the aluminum housing of the sidearm cold tip, and eight identical heaters (two sets of four in parallel) are used to heat the upper aluminum housing. Sea sand is used to increase coupling from the aluminum sheath to the sidearm. Omega Engineering temperature controllers (Model 7600) and resistive temperature devices are used to assess and control the temperature (to ±0.1°C) at four locations on the cell. The entire cell and housing unit is wrapped with a 2.54-cm-thick ceramic fiber blanket surrounded by Fibercon insulating tape. Operating conditions for the cell range from room temperature to roughly 500 K (1-mTorr–40-Torr vapor pressure).

We experimentally verified the model by illuminating a target with a high-power tunable narrow-band ultraviolet laser.[2] Operating conditions were roughly 190 °C for the inner cell-body temperature and 170 °C for the sidearm. These temperatures correspond to a mercury-vapor pressure of 6.3 Torr and a thermally broadened absorption linewidth of 1.2 GHz.[2] It is significant that the line-center attenuation for this cell is modeled to be in excess of 10^4/cm, owing to the exceedingly high value of the imaginary (or absorptive) part of the index of refraction. The cell, therefore, simultaneously achieves high suppression on the line center and high dispersion off the line center. Similar to the configuration shown in Fig. 1, a 300-μm slit was illuminated by a diffuse scattering source, and scattering through the slit was collimated with an $f/10$ lens through the vapor prism. The refracted beam was reimaged (at 895 mm) directly onto the microchannel plate of an intensified CCD camera that captured images to video. As the laser was tuned in wavelength, the camera recorded the displaced image of the slit as a function of spectral detuning from the line center of the mercury-vapor resonance. The scattering wavelength was determined with a Burleigh wavemeter (±0.3 cm^{-1}). We calibrated the camera pixel displacement to yield spatial deviation. The results are illustrated in Fig. 2, along with model predictions. The agreement is within the combined uncertainty of the imaging-system calibration and the cell pressure (denoted by error bars).

In Fig. 3 we demonstrate the filter's imaging capability by showing its spectral resolution of rotational Raman scattering from CO_2. The small spectral separation of the CO_2 rotational Raman lines ($B_0 = 0.39$ cm^{-1}) simulates the heavier hydrocarbons of combustion environments. The incident laser energy of 30 mJ/pulse was focused to a 100-μm line, and a 3-mm length of scattering was collimated (roughly $f/5.8$ collection) through the vapor prism. An 895-mm imaging lens refocused light passing through the prism (held at 12-Torr vapor pressure) onto an intensified CCD camera (Princeton Instruments, Pentamax). The image shown in Fig. 3 captures

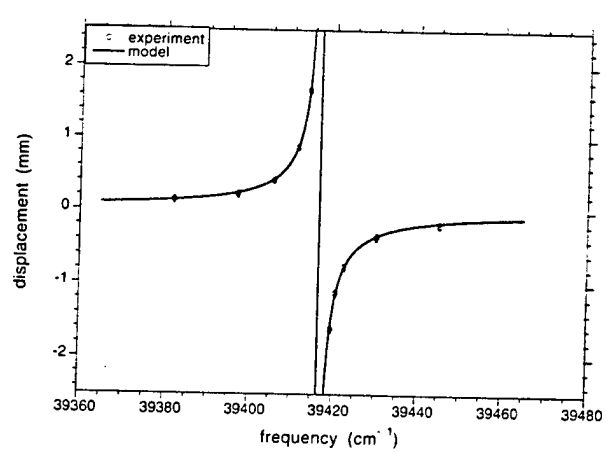

Fig. 2. Vapor prism: measured and predicted deviation as a function of incident scattering frequency.

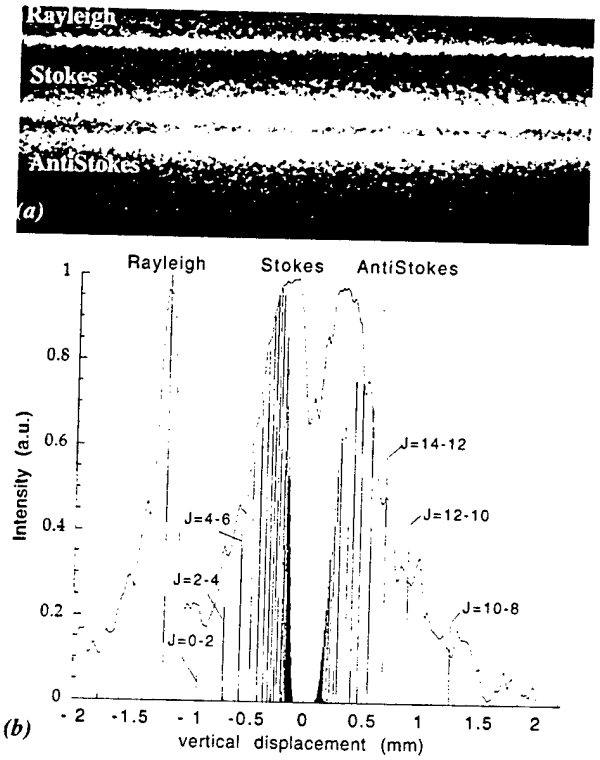

Fig. 3. CO_2 rotational Raman scattering imaged with the mercury-vapor prism. (a) Raman-scattering images of CO_2. (b) Intensity versus location for vertical cut through (a).

roughly 3 mm × 3 mm in the object plane, with a magnification of 3.1. The ultraviolet laser was tuned to 39 404.7 cm^{-1}, which corresponds to roughly a 7.7-cm^{-1} shift down from the center of the absorption band of the mercury cell. An average of 50 laser shots cropped (to 4.5 mm × 9 mm in the image plane) is imaged in Fig. 3(a). At this laser frequency the Rayleigh line is significantly attenuated and deviated, whereas the Stokes lines (further from the resonance) are less deviated in the same upward direction. The anti-Stokes branch is deviated downward because it is spectrally located on the opposite side of the resonance. Although the Rayleigh line can be completely suppressed with appropriate laser tuning, it is shown to give a measure of the filter's spatial resolution. Although experimental limitations in focusing and laser beam size (to avoid breakdown) constrained resolution to several hundred micrometers, individual rotational Raman lines are observed. Figure 3(b) plots pixel intensity versus displacement in a vertical cut through the image. Modeled scattering intensity and location appear beneath the measured intensity profile. Individual pure rotational Raman lines are discernible and in good agreement with the model predictions.

The dispersive prism near resonance outperforms state-of-the-art commercial spectrometers in both spectral sensitivity (linear dispersion) and throughput efficiency. The model predictions of the dispersive prism were compared with the specifications of an Acton Research Corporation AM512 2-m monochromator with a 3600-groove/mm grating.[7] At 2 m the linear dispersion of the spectrometer is 0.138 nm/mm. The dispersion of the vapor prism is nonlinear with frequency and vapor pressure; however, near resonance the linear dispersion of the vapor prism exceeds that of the spectrometer 5 to 25 times. We used 80% transmission as the near-resonance operating condition of the vapor prism. For spectrometers, optimizing the grating for a particular wavelength region by blazing allows one to achieve efficiencies of 50–70% for first-order diffraction.[7]

A variety of mechanisms can be used to increase the dispersion, and hence the sensitivity, of this filter. Because the filter relies on the index variation at the Brewster window interface and not on the path length through the vapor, a multipass or series of vapor prisms additively improves the dispersion. Alternatively, a filter can be fabricated by creation of a vapor-density gradient that is perpendicular to the input radiation (i.e., a vertical gradient in Fig. 1). This variation in the number density is analogous to the volume effects observed in *schlieren* or shadow graphs. The longer the traversed path, the greater the angular deviation. This is just as Wood demonstrated with sodium vapor in a cell placed over a flame.[1]

In conclusion, we have developed, modeled, and demonstrated a new spectral filter for spatial and spectral resolution of pure rotational Raman scattering. The filter is capable of simultaneous resolution of multiple rotational lines while suppressing strong elastic Rayleigh and background scattering. In the spectral region of interest, nearest the filter resonance, the filter outperforms state-of-the-art imaging spectrometers. Because of its high resolution and flexible operating parameters, this filter holds great potential for spatially resolved species identification and for imaging species-specific temperature profiles in high-pressure environments.

The authors are grateful to Phil Howard and Michael J. Souza of Princeton University for their expertise in the design and fabrication of the vapor cell. This research was supported by the U.S. Air Force Office of Scientific Research.

References

1. R. W. Wood, *Physical Optics* (Dover, New York, 1967), p. 495.
2. N. D. Finkelstein, W. R. Lempert, R. B. Miles, G. A. Rines, and A. Finch, in *34th AIAA Aerospace Sciences Meeting* (American Institute of Aeronautics and Astronautics, Washington, D.C., 1996), paper 96-0177.
3. W. C. Marlow, Appl. Opt. **6,** 1715 (1967).
4. S. P. Nandula, T. M. Brown, and R. W. Pitz, Opt. Lett. **19,** 414 (1994).
5. E. W. Rothe and P. Andresen, Appl. Opt. **36,** 3971 (1997).
6. R. S. Longhurst, *Geometrical and Physical Optics* (Longman Group, London, 1967), p. 458.
7. *Monochromators Systems and Accessories Catalog* (Acton Research Corporation, Acton, Mass., 1997).

Narrow-linewidth passband filter for ultraviolet rotational Raman imaging

N. D. Finkelstein, W. R. Lempert, and R. B. Miles

Department of Mechanical & Aerospace Engineering, Princeton University, Princeton, New Jersey 08544

Received November 26, 1996

We present a narrow-passband spectral filter capable of frequency-resolved imaging of rotational Raman light scattering with strong spectral rejection of out-of-band Raman, Rayleigh, and Mie scattering. The filter is based on mercury-vapor absorption, and subsequent resonant fluorescence and has a passband of less than 1 cm^{-1}. It is paired with an injection-seeded, cavity-locked, frequency-tripled Ti:sapphire laser that produces >30 mJ/pulse of single-mode, tunable light in the vicinity of 253.7 nm. The laser and filter are combined to spectrally resolve scattering from individual rotational Raman lines of nitrogen and oxygen. © 1997 Optical Society of America

Many optically based diagnostic techniques require, or are enhanced by, ultranarrow-linewidth spectral filters. In their simplest incarnation, narrow-bandwidth notch-absorption filters can be used to suppress elastic background scattering, while simultaneously imaging Doppler-shifted or thermally broadened Rayleigh scattering.[1–3] Spectral absorption filters using atomic or molecular transitions can provide high attenuation, sharp spectral cutoff, and spectral absorption bands of the order of gigahertz. However, such notch filters absorb over only a small spectral band and transmit light everywhere else. In many cases, a filter with a narrow passband is preferable. Diagnostic techniques in which background scattering at multiple frequencies must be suppressed, or where weakly scattered spectral lines are to be observed, require the use of a narrow-passband filter.

We present a novel ultranarrow spectral passband filter that features the high spectral discrimination of previously reported atomic resonance filters,[4,5] while preserving the imaging capabilities of more conventional filters. It is most similar to the resonance-scatter filter presented by Langberg *et al.* [6] The filter is based on absorption and subsequent resonant fluorescence of light by atomic mercury vapor. The strong and spectrally sharp absorption features of mercury (at 253.7 nm) provide the desired spectral discrimination. The fluorescence process and the long relative lifetime (120 ns) of the excited mercury state make possible temporal gating, which further attenuates background scattering when the sample is interrogated by a nanosecond-time-scale pulsed laser. Because of the large transition strength of mercury, absorption can be made to occur over a short distance through the vapor, and fluorescence is effectively from a planar sheet. Thus images can be preserved despite the absorption and fluorescence processes.

The narrow-passband filter acts as the compliment to a previously reported mercury notch-absorption filter.[7] Light scattered from the sample volume is imaged onto the front surface of a cell filled with mercury vapor, as shown in Fig. 1. If the incident light is spectrally outside the mercury absorption band, the light passes through the vapor cell and is rejected. If the incident light frequency is coincident with the mercury transition, the light is absorbed. At 0.025 Torr, the depth at which the incident radiation is attenuated to e^{-1} of the original value is calculated to be 50 μm. This shallow penetration preserves the filter's imaging capability. Fluorescence is to the ground state, so it is resonant with the incident light and is radiatively trapped in the forward direction. Thus virtually all the light is reradiated in the backward direction.[3] The fluoresced light is reimaged onto an intensified camera (or photomultiplier tube for nonimaging cases). As a consequence, the only light reaching the camera (or photomultiplier tube) is from that incident light that is coincident with the mercury absorption band.

The mercury-vapor filter is constructed of an all-quartz cell, 5 cm in length with 5-cm-diameter windows at each end. A sidearm cold tip, attached to the cell, contains a small amount (1 gm) of mercury. Controlling the temperature of the sidearm determines the vapor pressure (and hence the number density) of the mercury vapor in the cell. The cell body temperature is kept warmer than the sidearm to prevent condensation.

The illumination source for our experiments is a single-mode ultraviolet laser beam that is formed by frequency tripling the output of an injection-seeded, cavity-locked Ti:sapphire laser. The seed source, a

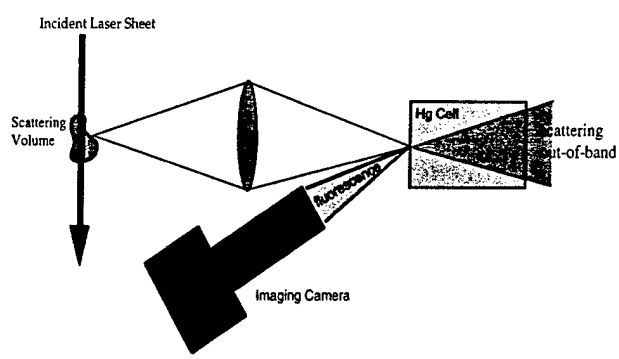

Fig. 1. Orientation of narrow-passband imaging filter. The only light reaching the imaging camera is spectrally coincident with the mercury-vapor transition.

0146-9592/97/080537-03$10.00/0 © 1997 Optical Society of America

continuously tunable, cw Ti:sapphire laser, is tuned by modification of its effective cavity length and is stabilized by feedback through an intracavity étalon.[7] This seed laser is injected into a pulsed Ti:sapphire resonator that is pumped by a frequency-doubled Nd:YLF. The ramp-and-lock cavity-locking mechanism is used to ensure single-mode output from the pulsed resonator.[8] Before every laser pulse, the unstable resonator acquires a lock to the cw seed frequency. As a result, single-mode operation is maintained even if the laser frequency is tuned rapidly. The Ti:sapphire emits 245 mJ in a single-longitudinal-mode pulse at 761 nm. A pair of β-barium borate crystals are used for type I doubling and subsequent type II mixing to generate ultraviolet light. The output is nearly the spectral transform limit of the 10-ns (FWHM) pulse. At 254 nm, in excess of 30 mJ/pulse of single-mode, tunable output is achieved.

We determined the temporal response of the narrow-passband filter by illuminating the mercury cell with the narrow-band ultraviolet laser source. The laser frequency was tuned to the peak of the Hg 202 resonance and the mercury-cell vapor pressure held at 0.05 Torr. The laser power was attenuated to nominally 100 pJ/pulse by a combination of several front-surface reflections, neutral-density filters, and finally a polarizer as a variable attenuator. The beam was attenuated until the passband fluorescence signal varied linearly with incident laser power. Fluorescence from the mercury vapor was imaged ($f/2$) through a 10-nm passband mercury-line interference filter, onto a photomultiplier tube. The photomultiplier tube (30-ns response time) response versus time was recorded on a digital oscilloscope.

The filter response to the short-lived (10-ns) laser pulse is a relatively long-lived exponential decay. Fits to the filter signal decay yield an e^{-1} lifetime of 630 ns. Since mercury's natural excited-state lifetime is 120 ns, the longer signal decay time indicates that radiative trapping plays a strong role in the fluorescence process.[9] The temporal response of the filter is used to enhance suppression of stray laser light scattering. Background scattering from the illuminating source can be temporally filtered, since it only occurs during the first 10 ns (the laser pulse width). Because of the filter's long temporal decay, gating only minimally reduces the overall fluorescence signal.

The spectral transmission of the narrow-passband filter was determined with a similar experimental setup. In this case, simultaneous measurements of the fluorescence signal and laser transmission through the mercury cell were captured, while the incident laser was scanned in frequency. In this way, measurem of the mercury-vapor cell acting as a narrow passband and a narrow-blocking band filter were made simultaneously. Ten pulse averages, with a variety of collection gate times, were collected with a boxcar integrator, digitized, and stored on a personal computer.

Figure 2 shows the measure of intensity versus laser frequency for both the notch-blocking and the passband filtering modes of the mercury-vapor cell. The sidearm is held at 27.5 °C (corresponding to 0.0023 Torr). The cell temperature is 67 °C. The laser is spectrally scanned over approximately 1 cm^{-1} in 12-MHz steps. The upper trace is the fluorescence passband signal, in which the integrator gate time was 4 μs and began 60 ns after the laser pulse. The lower trace is the absorption notch-filter profile with an integrator gate time of roughly 50 ns, centered on the laser pulse. Six features can be identified, corresponding to the naturally occurring isotopes of mercury. Note that the Hg 196 line is optically thin (because of its low 0.14% natural abundance), whereas all other isotopes are optically thick. As the mercury-vapor pressure is increased to 0.05 Torr (sidearm temperature of 70 °C), the individual peaks blend together, yielding a passband of approximately 0.8 cm^{-1}.

While the imaging capability of the passband filter has been demonstrated previously,[10] we made preliminary measurements of spatial resolution by measuring the filter's point spread function. Scattering from a target was imaged 1:1 by an $f/3$ lens onto a diffuse reflector (a sand-blasted metal plate). The scattering for the diffuse reflector was then reimaged by an $f/4.5$ lens onto the intensified charge-injection device camera. In the object plane of the camera, the spot size was measured to be 540 μm (FWHM). This measured the resolution of the imaging system. Next the diffuse scattering source was replaced by the passband filter operating at a mercury-vapor pressure of 0.022 Torr. The imaged spot size was measured to be 800 μm in the object plane. This measurement is a convolution between the imaging-system resolution and the filter resolution at this vapor pressure. Deconvolving the linewidths, assuming Gaussian profiles, yields 3.4-line/mm (or 295-μm) resolution, based on half-width at half-maximum resolution.

The efficiency of the passband filter is dominated by the dual-collection process. The low density of mercury vapor ensures that collisional-quenching time scales are longer than the fluorescence lifetime, yielding a high fluorescence efficiency. At higher vapor

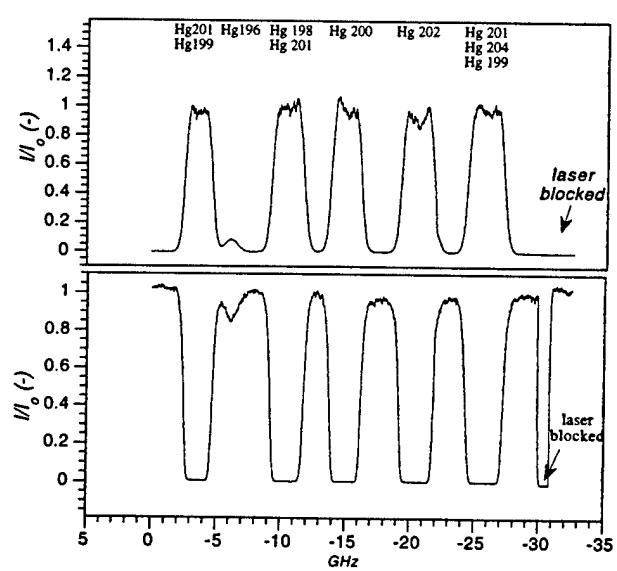

Fig. 2. Spectral profiles of the narrow-passband imaging filter (top) and the narrow-band notch-absorption filter (bottom).

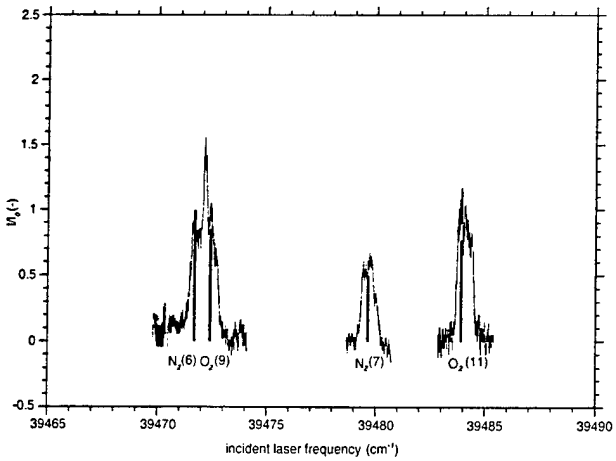

Fig. 3. Pure rotational Raman spectrum of room air. Experimental scans of $N_2(6)$, $N_2(7)$, $O_2(9)$, $O_2(11)$ lines with predicted relative position and strength illustrated beneath.

pressure (0.1 Torr), quenching by the front window can reduce fluorescence yield. However, the collection of mercury-vapor fluorescence requires a second imaging step. The fluorescence is presumed to be Lambertian, because of the high optical depth of the mercury vapor. An $f/1$ collection lens imaging the fluorescence 1:1 is calculated to capture 6% of the light impinging upon the front of the filter. This calculation neglects surface losses, which may be minimized with antireflection coatings at 253.7 nm.

An experiment, designed to demonstrate the unique features of the laser and filter pair, measured a rotational Raman scattering spectrum from room air. The incident laser was focused to a 200-μm-diameter beam, and a 2.5-cm segment of light scattering from ambient air was 1:1 imaged ($f/2$) through a vertical slit onto the inside surface of the mercury-vapor filter. The mercury-vapor fluorescence was reimaged ($f/3$) off axis through a mercury-line interference filter onto a photomultiplier tube. A boxcar integrator gated the fluorescence signal by capturing a 4-μs signal, beginning 50 ns after the initial laser pulse. A personal computer recorded 100 shot averages of the fluorescence signal, the laser power, and the laser frequency.

By spectrally detuning the laser from the mercury resonance, pure rotational Raman-shifted scattering was made to overlap the 253.7-nm passband filter. Scattering at the detuned laser frequency was rejected by the filter. Three different data sets, each with the laser scanning over 2.5 cm^{-1}, captured four different Stokes-shifted rotational Raman lines. Each data set was normalized by incident laser power, so the data sets could be weighted relative to each other. The spectral position of each data set was determined with a Burleigh wavemeter, which measured the wavelength (± 0.01 cm^{-1}) of the cw seed laser.

The three data sets are plotted in Fig. 3. Predicted location and relative scattering signal strengths of the nitrogen ($J = 6, 7$) and oxygen ($J = 9, 11$) rotational lines are illustrated beneath the spectral scans.[11] Because the Raman separation of the $N_2(6)$ and $O_2(9)$ rotational lines is small (0.7 cm^{-1}, of the order of the bandpass of the filter itself) the two spectral lines blend together. The other two lines, $N_2(7)$ and $O_2(11)$, appear independently, shifted further apart. The larger rotational Raman scattering cross section of oxygen (2.7 times that of nitrogen, at 253.7 nm) is demonstrated and agrees well with the research of Penny *et al.*[11]

In conclusion, a new narrow-passband imaging filter based on mercury-vapor absorption and fluorescence has been constructed, and initial characterization has been performed. The spectral width of the passband filter is less than 1 cm^{-1}. The spectral transmission, to the first order, acts as the inverse of the well-characterized mercury absorption notch filter. The long exponential decay of the fluorescence signal confirms that radiative trapping plays a strong role in the filter dynamics, and temporal gating is an effective means of gating out stray radiation, further suppressing background signal. Individual rotational Raman lines of nitrogen and oxygen have been measured with a unique narrow-linewidth, tunable ultraviolet light source.

The authors thank Mike Souza, Department of Chemistry, Princeton University, for helpful discussions and his expertise in glassblowing and Andy Finch, Glenn Rines, and Richard Schwarz of Schwartz Electro-Optics, Inc., for the development of the laser systems. This research was supported by an University Research Initiative grant from the U.S. Air Force Office of Scientific Research and a Small Business Innovative Research grant to Schwartz Electro-Optics, from NASA-Ames.

References

1. J. N. Forkey, N. D. Finkelstein, W. R. Lempert, and R. B. Miles, AIAA J. **34,** 442 (1996).
2. H. Shimizu, S. A. Lee, and C. Y. She, Appl. Opt. **22,** 1373 (1983).
3. R. D. Guenard, Y. H. Lee, M. Bolshov, D. Huebuer, B. W. Smith, and J. D. Winefordner, Appl. Spectrosc. **50,** 188 (1996).
4. J. Menders, K. Benson, S. H. Bloom, C. S. Liu, and E. Korevaar, Opt. Lett. **16,** 846 (1991).
5. J. A. Gelbwachs, IEEE J. Quantum Electron. **24,** 1266 (1988).
6. E. Langberg, M. Naylor, H. Heckscher, *Conference on Optical Instruments and Techniques* (Chapman and Hall, London, 1962), p. 229.
7. N. D. Finkelstein, J. Gambogi, W. R. Lempert, R. B. Miles, G. A. Rines, A. Finch, and R. A. Schwarz, AIAA paper 94-0492 (American Institute of Aeronautics and Astronautics, Washington, D.C., 1994).
8. N. D. Finkelstein, W. R. Lempert, R. B. Miles, G. A. Rines, and A. Finch, AIAA paper 96-0177 (American Institute of Aeronautics and Astronautics, Washington, D.C., 1996).
9. T. Holstein, Phys. Rev. **72,** 1212 (1974).
10. N. D. Finkelstein, W. R. Lempert, R. B. Miles, AIAA paper 96-2269 (American Institute of Aeronautics and Astronautics, Washington, D.C., 1996).
11. C. M. Penny, R. L. St. Peters, and M. Lapp, J. Opt. Soc. Am. **64,** 712 (1974).